

JULIUS-MAXIMILIANS-UNIVERSITÄT-WÜRZBURG

MASTER THESIS

High-frequency polarization studies of high-energy emitting AGN jets

Author:

Jonas Heßdörfer

Supervisor:

Prof. Dr. Matthias Kadler



*A thesis submitted in fulfillment of the requirements
for the degree of Master of Science*

in the group of

Prof. Dr. Matthias Kadler
Chair of Astronomy

Zusammenfassung

Materie akkretierende supermassereiche schwarze Löcher in den Zentren von aktiven Galaxien, genannt aktive Galaxienkerne (AGN), gehören zu den leuchtkräftigsten Objekten des Universums. Blazare sind eine Unterklasse der AGN, deren hochrelativistische Jets unter einem kleinen Winkel beobachtet werden. Sie emittieren Strahlung über das gesamte elektromagnetische Spektrum vom Radio- bis hin zum γ -Bereich, wobei ihre spektrale Energiedichte eine charakteristische Doppelhöckerstruktur aufweist. Das Maximum im nieder-energetischen Bereich wird dabei Synchrotronstrahlung zugeschrieben, die durch die Bewegung von geladenen Teilchen im Magnetfeld entsteht. Ein starkes Argument dafür ist die gemessene Polarisation in Radiobeobachtungen, die in dieser Arbeit im Vordergrund steht. Während intrinsische Polarisationsgrade bis zu 70% möglich sind, werden typischerweise deutlich niedrigere Werte gemessen. Dies liegt unter anderem an den Effekten der Faraday-Rotation und Depolarisation, die entstehen, weil sich links- und rechts-zirkular polarisierte Wellen unterschiedlich schnell in einem Medium bewegen. Beobachtungen mit einem Einzelteleskop können die dadurch leicht gegeneinander verdrehten Polarisationswinkel nicht auflösen, sondern detektieren nur die vektorielle Addition der einzelnen Winkeln, was zu einer niedrigeren Polarisation führt.

Im Rahmen dieser Arbeit wurden TELAMON Daten (Kadler et al., 2021), die zwischen September 2021 und Mai 2022 mit dem Effelsberg 100 m Teleskop aufgenommen wurden, hinsichtlich ihrer Polarisation untersucht. Dabei wurden Messungen bei sechs unterschiedlichen Frequenzen zwischen 14 GHz und 39 GHz durchgeführt und mit der SPECPOL-Version des Empfängers zusätzlich die vier Stokes-Parameter I, Q, U und V aufgezeichnet, wobei in dieser Arbeit die zirkulare Polarisation nicht weiter untersucht wird. Allerdings stellte sich heraus, dass das SPECPOL bei den beiden mittleren Frequenzen technische Probleme hat, die eine Verwendung unmöglich machen. Durch die Beobachtung von Quellen mit bekannter Polarisationscharakteristik können über den Müller-Formalismus die instrumentellen Effekte auf die beobachtete Strahlung beschrieben und korrigiert werden.

Insgesamt wurden zu den Polarisationsdaten auch die Daten für die totale Flussdichte aufgenommen, letztere sogar mit zwei verschiedenen Empfängerversionen, da das OPTOCBE standardmäßig verwendet wird und das SPECPOL nebenbei zusätzlich misst. Um einen Vergleich zwischen den beiden Empfängerversionen zu erhalten, wurden die Detektionsstatistiken und die Unterschiede in den gemessenen Flussdichten untersucht. Dabei fiel auf, dass die Daten sehr gut übereinstimmen.

Im Rahmen dieser Arbeit wurden 87 unterschiedliche Quellen beobachtet, von denen 46 als polarisiert betrachtet werden, die also, nach eigener Definition, eine linear polarisierte Flussdichte aufweisen, die mehr als doppelt so groß ist wie der damit assoziierte Fehler. Die Majorität der Quellen weist dabei einen Polarisationsgrad $m_l < 5\%$ auf.

Einige der Quellen, die im Rahmen dieser Arbeit beobachtet wurden, finden sich auch in anderen

Studien wieder. Im Vergleich mit der MOJAVE-Studie ([Lister et al., 2018](#)), die die Methode der Very Long Baseline Interferometry, also der Zusammensetzung von mehreren Einzelteleskopen zu einem virtuellen größeren Teleskop, verwenden, zeigt sich, dass die meisten Quellen in TELAMON eine geringere Polarisierung aufweisen, was durch den Effekt der Depolarisation erklärt werden kann. Im Gegensatz dazu verwendet das F-GAMMA Programm ([Myserlis, 2015](#); [Angelakis et al., 2019](#)) ebenfalls das Effelsberg Teleskop, allerdings bei niedrigeren Frequenzen. Hier zeigt ein Vergleich, dass in TELAMON die Quellen typischerweise höher polarisiert sind, was sich mit der Erwartung deckt, dass die Polarisierung mit der Frequenz anwächst ([Agudo et al., 2014](#)).

Über die beobachtete Drehung der Polarisationswinkel durch die Faraday-Rotation, beschrieben durch das Rotationsmaß RM, lassen sich Rückschlüsse auf das Magnetfeld in der Sichtlinie zwischen Beobachter und Quelle schließen. Für die beobachteten Quellen ergeben sich durchschnittliche Rotationsmaße von $RM \approx 470 \text{ rad m}^{-2}$ bei einer Wellenlänge von 20 mm, die sich nicht ausschließlich durch galaktische Phänomene beschreiben lassen können ([Taylor et al., 2009](#)).

Abstract

Accreting supermassive black holes, so-called active galactic nuclei (AGN), are among the most luminous objects in the entire Universe. Blazars, a subclass of AGN, exhibit highly relativistic jets that are observed under a small angle to the line-of-sight. They emit radiation over the entire electromagnetic spectrum, ranging from radio- to γ -rays. Their spectral energy distribution shows two prominent peaks, where the low-energy hump is attributed to Synchrotron radiation that is produced by charged particles moving in a magnetic field. A strong argument in favor of this association is the observed polarization in the radio band. This is the main focus of this thesis. While intrinsic polarizations can be as high as 70%, in real observations, way smaller values are detected. This can be attributed to Faraday rotation and depolarization effects. In a medium, left- and right-circularly polarized waves travel with slightly different velocities, leading to a rotation of the polarization angle. Since single-dish telescopes cannot resolve the individual angles, only the vectorial sum is measured that is typically lower.

In the framework of this thesis, TELAMON data (Kadler et al., 2021), taken between September, 2021, and May, 2022, with the Effelsberg 100 m telescope were studied with a special focus on their polarization characteristics. Data were recorded at six distinct frequencies between 14 GHz and 39 GHz for all four Stokes parameters I, Q, U and V with the SPECPOL backend of the receiver. However, the circular polarization was not further investigated. Also, due to technical problems with the SPECPOL at the middle frequencies, their data cannot be used. By observing sources with known polarization properties, using the Müller formalism, instrumental effects of the telescope can be characterized and corrected.

Next to the polarization data, the total intensity flux densities were recorded by two backend versions, the OPTOCBE that is used for total intensity measurements and the SPECPOL that also measures this property. A comparison of their detection statistics and the derived flux densities from their measurements shows that their data are in very good agreement.

For this thesis, a total of 87 different sources were observed, with 46 of them being polarized. Here, a source was defined to be significantly polarized if its linearly polarized flux density is greater than twice its associated error. The majority of all polarized sources exhibit a fractional polarization $m_l < 5\%$.

Other studies also observed some of the sources in the TELAMON sample. In the Very Long Baseline Interferometry study MOJAVE (Lister et al., 2018), most sources are found to be polarized at a higher level than in TELAMON, as would be expected due to depolarization. The F-GAMMA project (Myserlis, 2015; Angelakis et al., 2019), on the contrary, also used the Effelsberg telescope, albeit at slightly lower frequencies. They find, in most cases, lower polarizations than in TELAMON. This is expected in the assumption that the polarization increases with increasing frequency (Agudo et al., 2014).

From the observed rotation of the polarization angle due to Faraday rotation, conclusions about

the magnetic field in the line-of-sight can be drawn. The property characterizing the rotation, the rotation measure RM, for the sources in the sample is found to be $RM \approx 470 \text{ rad m}^{-2}$ at 20 mm. Such values cannot be fully explained by Galactic effects ([Taylor et al., 2009](#)).

Contents

Zusammenfassung	iii
Abstract	v
1 Motivation	1
2 Scientific Context	3
2.1 Active Galactic Nuclei	3
2.1.1 Unification of AGN	5
2.1.2 Blazars	7
2.2 Synchrotron Radiation	8
2.3 Polarization and Stokes Parameters	12
2.4 Faraday Rotation and Depolarization	14
2.5 How to Correct Measured Polarized Fluxes for Instrumental Influences	14
2.5.1 The Rotation Matrix \mathcal{R}	15
2.5.2 The Müller Matrix \mathcal{M}	16
2.6 What a Radio Telescope Measures	17
3 Observations and Data Reduction	19
3.1 The Effelsberg 100m Telescope	19
3.2 Data Taking and Sample	21
3.3 Data Reduction of Total Intensity Flux Densities	23
3.4 Data Reduction of Polarized Flux Densities	26
4 Results	29
4.1 Comparing OPTOCBE and SPECPOL Backends	29
4.1.1 Detection Differences	31
4.1.2 Flux Density Differences	33
4.2 Polarization Data	41
4.2.1 General Results	41
4.2.1.1 Müller Matrix and Instrumental Properties	41
4.2.1.2 Polarization Distribution	43
4.2.2 Some Selected Results	48
4.2.2.1 TXS 0215+015	48
4.2.2.2 PG 1553+113	50
4.2.2.3 PKS 0735+17	52
4.2.2.4 PKS 1725+123	54

5 Discussion	55
5.1 Comparison With Other Studies	55
5.1.1 MOJAVE Polarization Study	55
5.1.2 F-GAMMA Polarization Study	58
5.2 Rotation Measures	59
6 Summary and Outlook	63
Bibliography	65
A List of All Observed Sources	69
B Evolution of the Müller Matrix Elements and Average Müller Matrices	73
C Polarization Properties Distributions	79
D Overview-Plots and Overview-Table of All Sources	83
E Rotation Measures	141
Acknowledgments	159
Declaration of authorship	160

1 | Motivation

In the summer of 2020, a proposal for a monitoring program of TeV-emitting blazars was handed in to the program committee of the Effelsberg 100 m telescope, as these sources make up a poorly studied and quite faint sample. Ever since then, more than 60 observational sessions were conducted in the name of the TELAMON program (Kadler et al., 2021) on these sources. The first results were presented in Heßdörfer (2021). Soon after, Eppel (2021) provided a more sophisticated overview of the data obtained between August 2020 and October 2021 at multiple frequencies between 19 GHz and 44 GHz, and developed a semi-automatic data reduction pipeline. In the meantime, two lower frequencies, namely 14 GHz and 17 GHz were added to the observation setup to improve the detection rate of the sources.

In the original proposal, it was suggested to test the weakly polarized signals of the sample sources, using the spectropolarimeter (SPECPOL) backends available for certain receivers of the telescope. This was motivated mainly by two factors. One of them is the fact that polarization can give insight into the physical conditions of the source such as the magnetic field. Another reason is that previous studies (e.g., Aller et al., 1996; Agudo et al., 2018) found the variability of the polarized intensity to be faster and the fractional amplitude to be higher than for the total intensity. This allows for a super-resolution of potential flares and an overall better modeling of the variability.

After ~ 1 year of observations, in which the observer team got more experienced and the data was confirmed to be of high quality and self-consistent, the SPECPOL backends were gradually involved into the observations as well.

Studying the polarimetric properties of TeV blazars at high radio frequencies is not easy, as these sources are generally faint at these frequencies. On top of that, they typically are not highly polarized, meaning that their polarized flux is even fainter than their already weak total flux density. In the optical regime, polarimetric monitoring of TeV blazars is done by, e.g., Hiriart et al. (2019), using the 84 cm telescope at the San Pedro Martir Observatory. At short millimeter radio wavelengths, the POLAMI program (Agudo et al., 2018) observes bright radio-loud active galactic nuclei (AGN) with the IRAM 30-m telescope, although their source sample mainly consists of quasars and low-peaked blazars. In the F-GAMMA program, Angelakis et al. (2019) monitored GeV blazars between 2.64 GHz and 43 GHz, using the Effelsberg 100 m telescope. Myserlis (2015) published the analysis of a temporal subsample of their data, recovering linear and circular polarization for four different frequencies between 2.64 GHz and 10.45 GHz. The goal of this thesis was to test whether the Effelsberg 100 m telescope is capable of detecting polarized signals of typically even fainter TeV blazars at higher radio frequencies, and therefore has to be understood as a kind of feasibility study.

It is structured as follows: In Chapter 2, the scientific background is given. This includes a short introduction into the sources of interest, synchrotron radiation and its polarization properties,

effects that reduce this polarization as well as a way of correcting the measured polarization information for instrumental effects. The process of data taking and analysis is described in Chapter 3. In Chapter 4, the two receivers that were used in the data taking process are compared. Also, some general information on the source sample and some interesting individual sources are presented. The results are put into context in Chapter 5 by comparing them to two other studies of a partly overlapping source sample. Finally, Chapter 6 includes a summary of the results as well as a few remarks on possible future studies that could be done using the presented data.

2 | Scientific Context

For millennia, the night sky has fascinated humankind. In its early days, phenomena were investigated using photographic plates, but after the first telescopes were used in the 17th century, new fields of study appeared and more and more discoveries were made. However, roughly 300 years had to go by until the birth of radio astronomy, when [Jansky \(1935\)](#) noticed that the Milky Way was an emitter of radio waves, with the strongest signals coming from the Galactic center. One of the most fundamental discoveries for this thesis, namely quasars, happened, when [Schmidt \(1963\)](#) examined the spectrum of the radio source 3C 273, an object that appeared to be star-like at first. He noticed, more or less by coincidence ([Kellermann & Sheets, 1984](#), p.171), that the emission lines at unfamiliar wavelengths seen in its spectrum could be identified by redshifted ($z = 0.158$) Balmer lines. [Schmidt \(1963\)](#) also realized that in order to explain his finding, the stellar object could potentially be identified with the nuclear region of a galaxy that would be less than 1 kiloparsec across. Nevertheless, this small region would still be brighter than all of the radio sources that were identified with galaxies up until that point in time, at least in the optical regime. This discovery laid the foundation for further revolutionary findings in the field of extragalactic astronomy.

Nowadays, such objects are referred to as active galactic nuclei (AGN). In the following sections, their properties that are relevant for this thesis will be explained.

While this was only a very short introduction into the history of AGN, [Kellermann \(2014\)](#) and [Shields \(1999\)](#) provide great and more complete overviews over their discovery and its implications.

2.1 Active Galactic Nuclei

It does not come as a surprise that AGN were only discovered relatively late in the history of astronomy, as they appear to be very faint in the optical sky. In fact, there are millions of stars brighter than even the brightest AGN. However, the situation completely changes when observing the sky in the γ -ray or radio band, where they are amongst the brightest objects outside the Galactic plane.

As was already suggested by [Schmidt \(1963\)](#), AGN are the innermost region of so-called active galaxies. In contrast to „regular“ galaxies that emit most of their radiation in the optical regime due to thermal radiation of stars in the galaxy, AGN emit their radiation across the entire electromagnetic spectrum from radio to γ -rays. With bolometric luminosities of up to $L_{\text{bol}} \approx 10^{48} \text{ erg s}^{-1}$, AGN are one of the most powerful non-explosive objects known in the Universe ([Padovani et al., 2017](#)). To reach such high luminosities, other radiation producing processes than nuclear fusion or thermal emission have to be at work.

This can be shown by a short thought experiment. The lifetime of the active phase of an AGN ranges between $10^7 - 10^9$ years (Martini & Weinberg, 2001; Marconi et al., 2004). Assuming realistic moderate values of $L_{\text{bol}} = 1 \times 10^{47} \text{ erg s}^{-1}$ and $t_{\text{life}} = 1 \times 10^8 \text{ yr}$, an AGN would produce $E = L_{\text{bol}} \cdot t_{\text{life}} \approx 3 \times 10^{62} \text{ erg}$ of energy in its lifetime. Variability arguments, based on the fact that AGN emission can vary on timescales as short as minutes (Albert et al., 2007), restrict the bulk of the emission to lie in a region of a linear scale of $\lesssim 0.1 \text{ pc}$. Nuclear fusion in stars, especially the proton-proton chain, converts rest mass into radiated energy with an efficiency of $\epsilon_{\text{nuc}} \sim 0.7\%$. In order to produce the required $\sim 10^{62} \text{ erg}$ to power an AGN over its lifetime with this reaction, a total mass of $\sim 2 \times 10^{10} M_{\odot}$ is needed. This would mean that on average $\sim 200 M_{\odot} \text{ yr}^{-1}$ are turned into energy. As this number is very high, a more efficient way of liberating energy is needed to explain AGN. A process that is capable of liberating energy more efficiently is the accretion of material, reaching $\epsilon_{\text{acc}} \sim 5.7\%$ to $\sim 42\%$, for a non-rotating and a maximally rotating black hole, respectively (Gammie, 1999). However, these values are only valid in the case where no magnetic fields are present. With that, accretion of material onto a central object is the most efficient astrophysical source of energy. The theoretical maximal luminosity an object can produce via accretion is given by the Eddington luminosity

$$L_{\text{Edd}} = \frac{4\pi GcMm_p}{\sigma_T} \approx 1.3 \times 10^{38} \frac{M}{M_{\odot}} \text{ erg s}^{-1} \quad (2.1)$$

that is found by imposing equilibrium between the inward pulling gravitational force and the outward pushing radiation force due to radiation pressure. Here, G is the gravitational constant, c is the speed of light, m_p is the mass of a proton and $\sigma_T = 6.65 \times 10^{-29} \text{ m}^2$ is the Thomson scattering cross-section. Using the above equation and the bolometric luminosity from the example, an estimate of the mass of the central object in such an AGN can be derived to be $M \approx 7.7 \times 10^8 M_{\odot}$. This matches with the expected masses that range from $10^6 M_{\odot}$ to $10^9 M_{\odot}$ (Woo & Urry, 2002). Such high masses are explained by the presence of a supermassive black hole (SMBH) in the center of an AGN.

The SMBH is surrounded by an accretion disk of hot plasma that is created due to the conservation of angular momentum, perpendicular to the net angular momentum vector. In the disk, dissipation processes lead to matter being transported inwards, while angular momentum is transferred to greater distances from the center, meaning the inner part of the disk can be accreted (Shakura & Sunyaev, 1973). Due to these processes, the disk heats up, causing it to emit radiation. The emission from the disk can be approximated by assuming a black body spectrum with a certain temperature and integrating over the entire disk. While the exact spectrum depends on the relative strengths of ν and $k_B T/h$, to first order it appears to be a stretched black body curve, peaking in the UV- and X-ray regimes. The emission of the accretion disk is, however, not of prime importance for this work.

Rather, the emission of so-called jets, highly collimated outflows of relativistic plasma, is the source of interest in this thesis. While the exact origin of these jets is still up for debate (e.g., Blandford et al., 2019), it is known that they appear in up to 10% of all AGN (Padovani, 2011) and are characteristic for radio-loud AGN. This classification goes back to Kellermann et al. (1989) and is defined as the ratio of 5 GHz radio flux to 4400 Å optical flux, such that the radio-loudness R_L reads

$$R_L = \frac{S_R}{S_O}, \quad (2.2)$$

with S_R and S_O being the fluxes in the radio and optical band, respectively. By their definition, sources with $R_L > 10$ are considered radio-loud (RL), while sources with $R_L \lesssim 1$ are considered radio-quiet (RQ). Over the years, different studies (see, e.g., Shastri et al., 1993; Zhang et al.,

2021) argued for distinct dividing values between the two classes. [Padovani et al. \(2017\)](#) even suggested to get rid of these labels and rather use „jetted“ and „non-jetted“, as they better describe the fundamental physical difference between the two types. Despite the controversy about the labeling of the source types, for the sake of consistency with most of the literature, the historical RL and RQ distinction will be used here. In this thesis, only RL AGN are considered. Nevertheless, in the following, a short overview of different types of RQ and RL AGN will be given.

2.1.1 Unification of AGN

As different types of AGN were discovered at distinct points in time at various frequencies, they appeared to be due to different phenomena. Other than the already introduced classification into RQ and RL, it is possible to characterize AGN by their emission lines, or, to be more precise, by the presence or absence of broad emission lines. While sources that show both narrow and broad lines are type I AGN, those that only exhibit narrow lines are type II AGN. Interestingly, even classically forbidden narrow lines can be observed, as the mean free path in the clouds of gas that are responsible for the production of the emission lines is large enough for the low probability transitions to occur.

According to the currently widely accepted AGN unification model ([Antonucci, 1993](#); [Urry & Padovani, 1995](#)), these properties can all be explained by the same underlying object: a supermassive black hole accreting matter onto an accretion disk. Near the SMBH are clouds of gas, called the „broad line region“, where the broad emission lines are produced. As they are close to the black hole and therefore under the influence of its strong gravitational potential, the atoms in them each experience a peculiar Doppler shift, resulting in the broadening of the lines. These constituents are surrounded by a dusty absorber that was, originally, assumed to be a torus. With newer studies, evidence is piling up that the actual shape of the absorber is not that simple, but rather clumpy ([Nenkova et al., 2008](#)) or even conical ([Hönig, 2019](#)). However, the exact shape is not critical to explain the unification model. Outside of the absorber, the „narrow line region“ is situated. These clouds of gas have to have a lower density than the ones in the broad line region to explain the presence of the forbidden lines. Also, since they are farther away from the black hole, its gravitational potential is not as strong and the emitted lines are narrow and not broadened. Additionally, if the source is RL, relativistic jets are ejected perpendicular to the accretion disk. The exact mechanism that is responsible for the launching of the jets is, as was already mentioned before, not yet fully understood, but it appears to be connected to the presence of strong magnetic fields (e.g., [Blandford et al., 2019](#)). Of course, the above mentioned properties are true for both „sides“ of the black hole. A schematic overview is given in [Fig. 2.1](#). The classification of the observed AGN depends on the viewing angle, its intrinsic power as well as the presence or absence of a jet. Radio-quiet AGN are mainly made up of Seyfert I/II galaxies ([Seyfert, 1943](#)). Here the division happens based on the type I/II criterion introduced earlier. Since the broad emission lines originate from close to the black hole, they are absorbed by the dusty absorber when observed nearly edge-on, thus resulting in a Seyfert II galaxy. When increasing the viewing angle, more and more of the broad line region is visible, so that the observed AGN is classified as a Seyfert I. Radio-loud AGN, on the other hand, do show a broader spectrum of different classes. In an analogous way to dividing the Seyferts, radio galaxies (RG) are also classified according to their emission line profile. Narrow line radio galaxies (NLRG) are observed nearly edge-on and therefore only exhibit narrow lines, while broad line radio galaxies (BLRG) are observed more face-on. Furthermore, RGs are also subdivided into two distinct groups depending on their radio-emission morphology, according

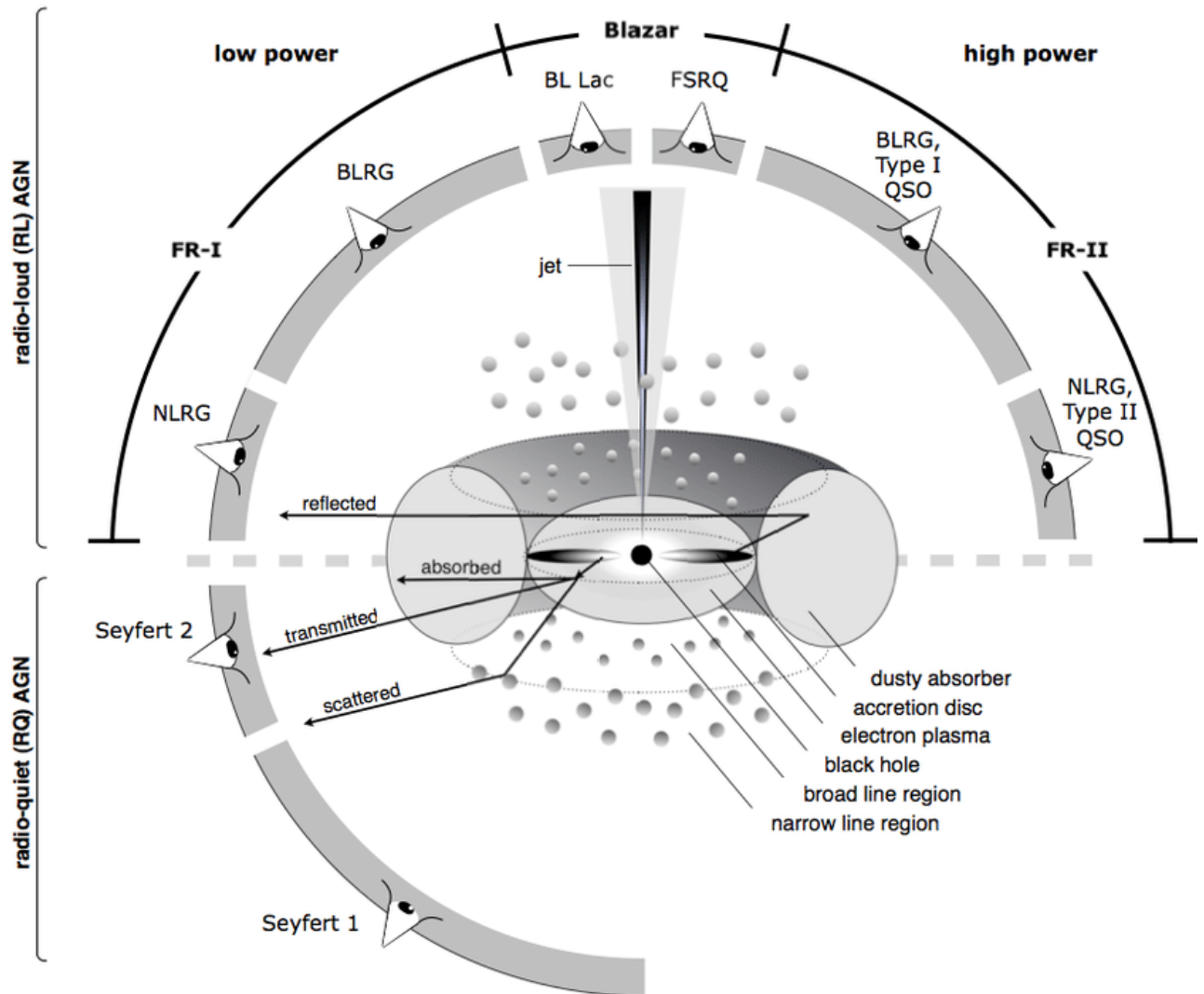


Figure 2.1: A schematic representation of the unified model of AGN, as illustrated by [Beckmann & Shrader \(2012\)](#). According to the unification scheme, AGN are classified depending on them being radio-loud or radio-quiet, their power and the viewing angle.

to [Fanaroff & Riley \(1974\)](#). Those radio galaxies with low power, a bright nucleus and two jets whose power declines with increasing distance from the nucleus, resulting in plumes, are classified as FR1 AGN. On the contrary, FR2 AGN are of higher power than FR1s, displaying prominent radio lobes with hot spots, usually only showing a one-sided jet. The one-sidedness can be explained by Doppler boosting. As the luminosity of the jet moving towards the observer is boosted, it is dampened by the same amount for the jet that is facing away from the observer. A more detailed description this effect is given by, e.g., [Rybicki & Lightman \(1979\)](#). There is one more type of RL AGN that does not directly fit the classification introduced up until now. These sources are called blazars and will be further investigated in the following section, as they are of prime interest for this thesis.

2.1.2 Blazars

While all of the previously introduced types of AGN are observed at an angle with respect to the jet, blazars are more or less observed face-on, meaning that the jet emission is heavily Doppler-boosted. As a direct consequence of the Lorentz transformation in special relativity, the intensity I of the radiation transforms as

$$I(\nu) = \mathcal{D}^3 I'(\nu'), \quad (2.3)$$

where \mathcal{D} is the relativistic Doppler factor, ν is the frequency and the primed quantities correspond to the rest frame of the source. They can also be divided into two subclasses, namely BL Lac objects, named after their prototype BL Lacertae, and flat-spectrum radio quasars (FSRQ). The former are characterized by the absence of emission lines, while the latter are generally more luminous and do show emission lines (Urry & Padovani, 1995).

Blazar emission spans across the entire electromagnetic spectrum, from radio- to γ -rays. In a spectral energy distribution (SED) plot, where the product of the frequency and the luminosity is plotted with respect to the frequency, they exhibit a characteristic double-humped structure. An example is shown in Fig. 2.2 on the right for several possible behaviors. The figure itself will be explained later on. While the low energy hump is attributed to non-thermal synchrotron emission, the origin of the high energy hump is not yet ascertained. In leptonic models, inverse Compton scattering of low energy synchrotron photons is used to explain the high energy emission (Ghisellini & Tavecchio, 2009), while hadronic models predict that the pion decay into neutrinos and photons is responsible for producing this emission (Mannheim, 1993). Since the high energy emission is not of primary interest in this thesis, no further introduction is given. The synchrotron emission, on the other hand, will be investigated in detail in Sect. 2.2.

Coming back to Fig. 2.2, on both sides there are six distinct SEDs that are representative for different blazar samples, forming the so-called blazar sequence. Focusing on the right side of the figure for now, the original („old“) blazar sequence was first proposed by Fossati et al. (1998) and Donato et al. (2001). Average SEDs were computed for groups of blazars binned together according to their radio luminosity. This showed that for increasing luminosity, the peak frequencies shift to lower frequencies, while the γ -dominance increases as well. A „new“ blazar sequence was proposed by Ghisellini et al. (2017), who binned the blazars according to their γ -ray luminosity rather than their radio luminosity; their result is shown on the left of Fig. 2.2. It has to be noted that the two studies used different γ -ray data. While the Ghisellini et al. (2017) study used *Fermi*-LAT data, the original blazar sequence was based on EGRET that mainly detected flaring blazars. Comparing the two blazar sequences some obvious differences become apparent, although there are still many similarities such as the increasing γ -dominance and the shift of the peaks to lower frequencies for higher luminosities.

Since the peak frequencies depend on the luminosity of a blazar, Padovani & Giommi (1995) introduced a way to distinguish them according to their synchrotron peak frequency. Blazars that peak below $\nu_{\text{peak}} < 10^{14}$ Hz are regarded as low-peaked (LBL), while those with peak frequencies 10^{14} Hz $< \nu_{\text{peak}} < 10^{15}$ Hz are called intermediate-peaked blazars (IBL). The highest peaked sources are the ones with $\nu_{\text{peak}} > 10^{15}$ Hz and are therefore called high-peaked blazars (HBL). In a recent publication, Giommi & Padovani (2021) suggest that categorizing these sources according to their properties leads to only two classes, namely the LBLs and the IHBLs (intermediate-high-energy peaked). In extreme cases, as was shown by Biteau et al. (2020), the peaks can be shifted upwards by up to two orders of magnitude. Such sources are called

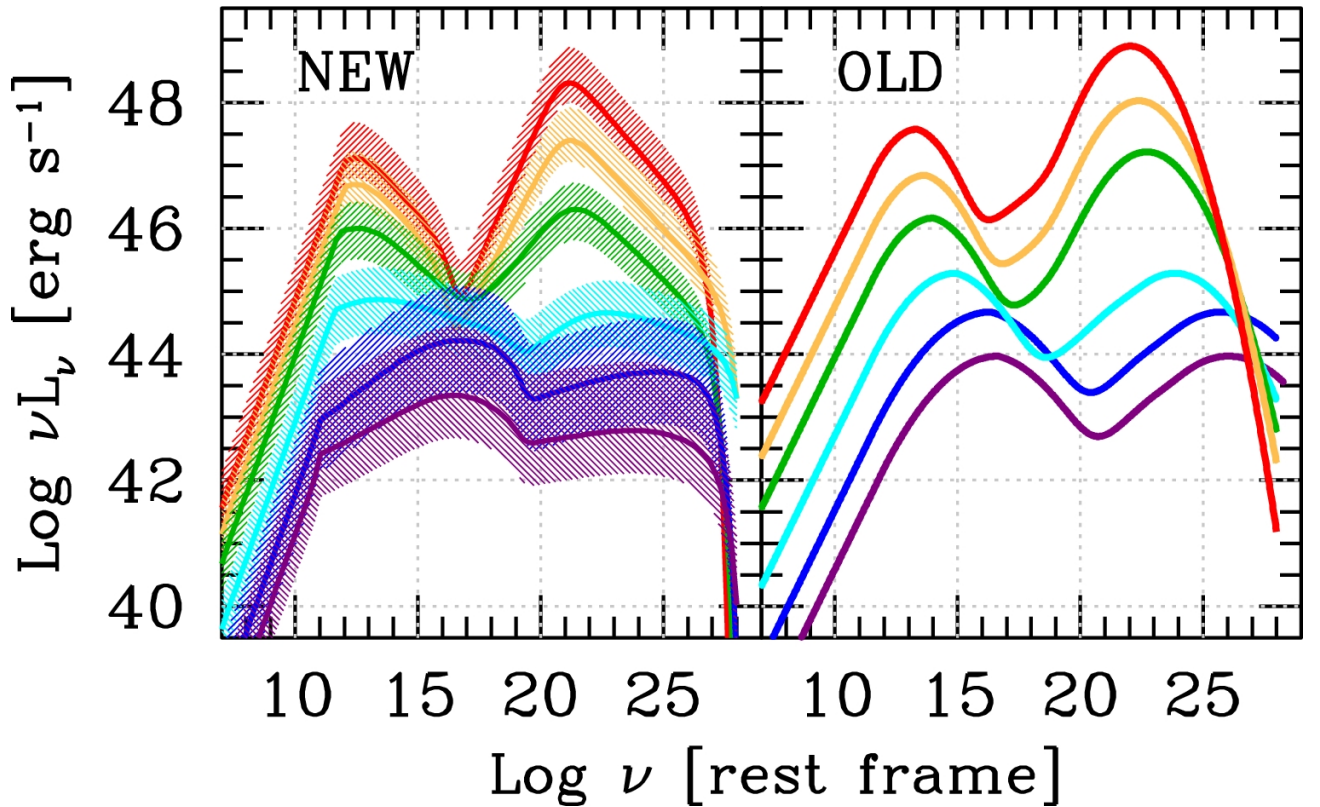


Figure 2.2: Comparison of the „old“, original (Fossati et al., 1998; Donato et al., 2001) and „new“ blazar sequence (Ghisellini et al., 2017). While the original one binned the blazars according to their radio luminosity, in the new study, γ -ray bins were used. With some apparent differences, the similarities remain: the shift of the peaks to lower frequencies and the increasing γ -dominance for higher luminosities. Taken from Ghisellini et al. (2017).

„extreme blazars“.

As HBLs and extreme blazars have their emission peaks at very high frequencies, they are typically very faint radio sources (see Fig. 2.2). This is why they are hard to detect by regular radio telescopes. In order to detect them, very large telescopes, like the Effelsberg 100 m telescope, have to be used.

2.2 Synchrotron Radiation

In the previous section it was mentioned that the low frequency peak of a blazar SED is explained by synchrotron radiation. In this section, an introduction to this emission type is given, closely following Rybicki & Lightman (1979) and Longair (2010). Vector quantities are written in bold face.

Synchrotron radiation is produced when charged relativistic particles of mass m and charge q are moving in a magnetic field \mathbf{B} . The Lorentz force acting upon this particle is given by

$$\frac{d}{dt}(\gamma m \mathbf{v}) = \frac{q}{c}(\mathbf{v} \times \mathbf{B}), \quad (2.4)$$

where $\gamma = (1/(1 - \beta))$ is the Lorentz factor with $\beta = v/c$ and \mathbf{v} is the velocity of the particle. The velocity of the particle can be split into two components, one parallel, $|\mathbf{v}_{\parallel}| = v_{\parallel}$, and one

perpendicular, $|\mathbf{v}_\perp| = v_\perp$, to the magnetic field. Doing so, the Lorentz force is now characterized by

$$\frac{dv_\parallel}{dt} = 0, \quad \frac{dv_\perp}{dt} = \frac{q}{\gamma mc} (v_\perp \times \mathbf{B}). \quad (2.5)$$

From the first equation it is clear that the velocity parallel to the magnetic field has to be constant. Since the Lorentz force is always perpendicular to \mathbf{v} and to \mathbf{B} , γ and $|\mathbf{v}| = v$ have to be constant. This constrains the velocity perpendicular to the magnetic field $v_\perp = \sqrt{v^2 - v_\parallel^2}$ to also be constant. Combining the constant motions parallel and perpendicular, i.e., circular, to the magnetic field into one results in a net helical motion. The gyration frequency of this motion is given by

$$\omega_B = \frac{qB}{\gamma mc} = \frac{\omega_L}{\gamma}, \quad (2.6)$$

with the Larmor frequency $\omega_L = qB/mc$. The radius of this orbit is found to be

$$R_L = \frac{\gamma v_\perp}{\omega_L} \approx 300 \text{ km} \cdot \frac{E}{1 \text{ GeV}} \cdot \left(\frac{B}{1 \text{ G}} \right)^{-1}, \quad (2.7)$$

where $E = |\mathbf{E}|$ is the electric field and $1 \text{ G} = 10^{-4} \text{ T}$. Using typical orders of magnitude for the electric and magnetic field¹ shows that this radius is small on cosmological scales.

As the particle moves around the magnetic field lines, it is accelerated and therefore, according to Larmor's formula, its radiated power is

$$P = \frac{2q^2}{3c^3} \dot{\mathbf{v}}^2 = \frac{2q^2}{3c^3} \gamma^4 [a_\perp^2 + \gamma^2 a_\parallel^2], \quad (2.8)$$

where the acceleration $\dot{\mathbf{v}}' = \mathbf{a}'$, in an instantaneous electron rest frame, was split into perpendicular and parallel components a'_\perp and a'_\parallel and then Lorentz transformed to $a'_\perp = \gamma^2 a_\perp$ and $a'_\parallel = \gamma^3 a_\parallel$. Because $\mathbf{a} \perp \mathbf{v}$, $a_\parallel = 0$, while, for circular motion, $a_\perp = \omega_B v_\perp = \omega_B v \sin \varphi$, where φ is the pitch angle between \mathbf{B} and \mathbf{v} . Plugging this, along with the definition of the gyration frequency (Eq. 2.6), into Eq. 2.8 results in

$$P = \frac{2q^4 \gamma^2 B^2 v^2}{3c^5 m^2} \sin^2 \varphi. \quad (2.9)$$

Since $P \propto m^{-2}$, heavier particles than electrons (and positrons) are less efficient in producing synchrotron radiation. Therefore, in the following, only electrons will be considered, i.e., $q = e$ and $m = m_e$. Assuming an isotropic velocity distribution ($\beta \sim 1$) and averaging over the emitted power results in

$$\langle P \rangle = \frac{4}{3} \sigma_T \beta^2 c \gamma^2 U_B, \quad (2.10)$$

using the magnetic field energy density $U_B = B^2/8\pi$ and the Thomson cross-section $\sigma_T = 8\pi e^4/(3m_e^2 c^4)$.

In the electron's rest frame, its emission pattern is that of a dipole, with the two lobes being perpendicular to the direction of the acceleration. However, performing a Lorentz transformation into the observer's frame results in the emission being forward beamed into a cone with an

¹Close to the centers of AGN, the magnetic field is assumed to be of the order of $B \sim 1 \text{ G}$; Matthias Kadler, University of Würzburg, Lecture on Multiwavelength Astronomy, summer term 2020.

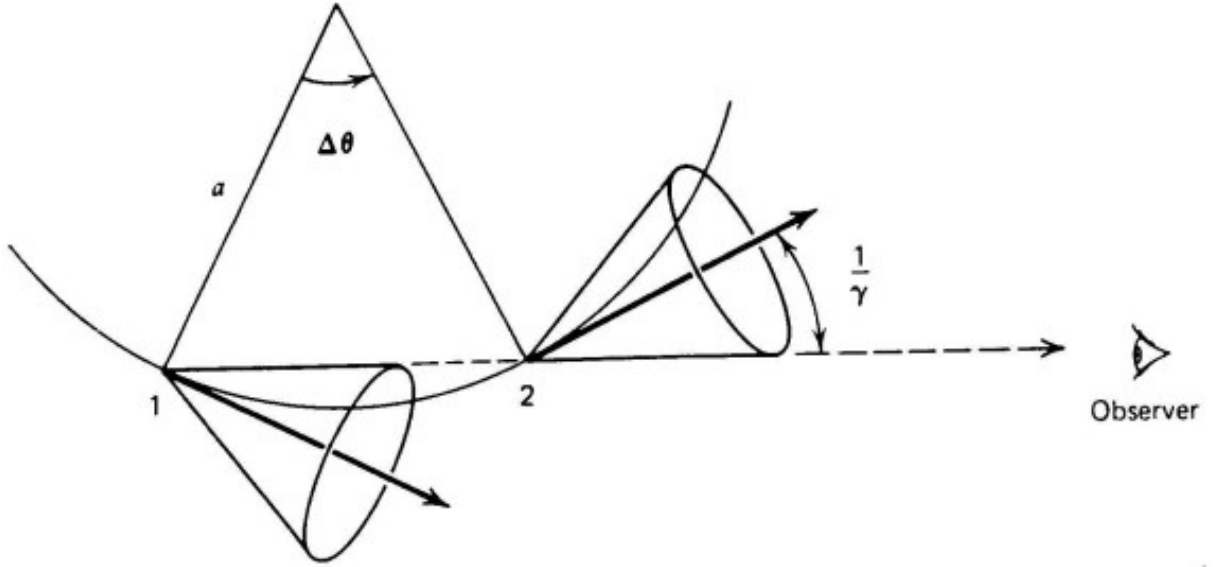


Figure 2.3: Synchrotron emission of a relativistic electron in circular motion. Taken from [Rybicki & Lightman \(1979\)](#).

opening angle of $\vartheta \sim 1/\gamma$ (and $\Delta\theta = 2\vartheta = 2/\gamma$), as is sketched in Fig. 2.3. Coming back to the electron's frame of rest for a moment, its beam passes the observer in a time interval

$$\Delta t = \frac{\Delta\theta}{\omega_B} = \frac{\gamma\Delta\theta}{\omega_L} = \frac{2\gamma}{\omega_L\gamma} = \frac{2}{\omega_L}. \quad (2.11)$$

Due to the Doppler effect, as the electron is assumed to travel with $\beta \sim 1$, the duration τ of the pulse is shortened to

$$\tau = (1 - \beta) \Delta t, \quad (2.12)$$

as the electron is closer to the observer at position 2 than it is at position 1 in Fig. 2.3. Assuming a highly relativistic Lorentz factor $\gamma \gg 1$, the approximation

$$\frac{1}{\gamma^2} = 1 - \frac{v^2}{c^2} = (1 + \beta)(1 - \beta) \approx 2(1 - \beta) \quad (2.13)$$

is valid. With the above approximation, Eq. 2.12 can be rewritten as

$$\tau = (1 - \beta) \Delta t = \frac{\Delta t}{2\gamma^2} = \frac{2}{2\gamma^2\omega_L} = \frac{1}{\gamma^2\omega_L}. \quad (2.14)$$

The characteristic frequency ν_c of the synchrotron radiation is then given by

$$\nu_c = \frac{\omega_c}{2\pi} = \frac{1}{2\pi}\gamma^2\omega_L = \frac{eB}{m_e c} \left(\frac{E}{m_e c^2} \right)^2 \simeq 280\gamma^2 \left(\frac{B}{10^{-4} \text{ G}} \right) \text{ Hz}. \quad (2.15)$$

For typical magnetic field strengths of $B \sim 1 \text{ G}$ near the center of AGN, radio emission of $\nu \sim 10^9 \text{ Hz}$ can therefore readily be explained by a modest Lorentz factor of $\gamma \sim 10$. Similarly, even X-ray emission with $\nu \sim 10^{17} \text{ Hz}$ can be produced by this process, requiring $\gamma \sim 10^6$; a realistic value in the extreme environments of AGNs.

It is typically assumed that non-thermal synchrotron radiation is produced by electrons whose energy distributions are described by a power-law

$$n(\gamma)d\gamma = n_0\gamma^{-p}d\gamma, \quad (2.16)$$

with $n(\gamma)d\gamma$ being the number of electrons per unit volume and n_0 and p being constants. Possible explanations for the power-law distribution lie in the acceleration mechanisms that are thought to be responsible for electron energy distribution, namely first and second order Fermi acceleration or diffusive shock acceleration (Fermi, 1949; Blandford & Eichler, 1987; Bell, 1978). In the case where an electron with energy $E = \gamma m_e c^2$ emits its average power only at a single frequency $\gamma^2 \nu_L$, its emitted power spectrum P_ν is given by

$$P_\nu = \int_1^\infty \langle P_\nu(\gamma) \rangle n(\gamma) d\gamma. \quad (2.17)$$

Here, $P_\nu(\gamma)$ is its spectral energy distribution

$$P_\nu(\gamma) = \frac{4}{3} \sigma_T \beta^2 c \gamma^2 U_B \phi_\nu(\gamma), \quad (2.18)$$

where $\phi_\nu(\gamma)$ is the spectral shape that is constrained by

$$\int \phi_\nu(\gamma) d\gamma = 1 \quad (2.19)$$

in order to ascertain that Eq. 2.10 still holds true. The assumption that photons are only emitted at the mentioned frequency is valid, as the synchrotron radiation can be seen as a series of narrow pulses (Eq. 2.14). This also fixes the spectral shape to be

$$\phi_\nu(\gamma) \sim \delta(\nu - \gamma^2 \nu_L). \quad (2.20)$$

Combining all these equations (Eq. 2.16, 2.17, 2.18, 2.19) generates the expression

$$P_\nu = \int_1^\infty \frac{4}{3} \sigma_T \beta^2 c \gamma^2 U_B \delta(\nu - \gamma^2 \nu_L) n_0 \gamma^{-p} d\gamma. \quad (2.21)$$

Applying the already introduced constraint of $\gamma \gg 1$, it can be rewritten to

$$P_\nu = \frac{4}{3} \sigma_T c U_B n_0 \int_1^\infty \gamma^{2-p} \delta(\nu - \gamma^2 \nu_L) d\gamma. \quad (2.22)$$

Introducing the substitution $\nu' = \gamma^2 \nu_L$, and with that $d\gamma = d\nu' / (2\nu_L \gamma)$, leads to

$$P_\nu = \frac{2}{3\nu_L} \sigma_T c U_B n_0 \int_{\nu_L}^\infty \gamma^{1-p} \delta(\nu - \nu') d\nu'. \quad (2.23)$$

Resubstituting γ and solving the integral then finally results in

$$P_\nu = \frac{2}{3\nu_L} \sigma_T c U_B n_0 \left(\frac{\nu}{\nu_L} \right)^{-\frac{p-1}{2}}. \quad (2.24)$$

Remarkably, this is again a power-law, meaning that the spectrum of an electron power-law distribution is a power-law itself. In radio astronomy, the exponent is usually called the spectral

index $\alpha = -(p - 1) / 2$.

The above calculations all rely on approximations to increase the flow of reading. [Rybicki & Lightman \(1979\)](#) carry out the calculations without many of the approximations and find for the highly relativistic case

$$P(\nu) = \frac{\sqrt{3}e^3 B \sin \varphi}{m_e c^2} \left(\frac{\nu}{\nu_c} \right) \int_{\nu/\nu_c}^{\infty} K_{5/3}(\xi) d\xi, \quad (2.25)$$

where $K_{5/3}(\xi)$ is the modified Bessel function of the second kind of order $5/3$ and $\nu_c = (5/3) \gamma^2 \nu_L \sin \varphi$ is the critical frequency.

At this point it has to be noted that the described power-law distribution is only valid in the case of an optically thin medium. A medium is said to be optically thin, if its optical depth

$$\tau_\nu(s) = \int_{s_0}^s \alpha_\nu(s') ds' \quad (2.26)$$

is $\tau_\nu < 1$. In Eq. 2.26, s is the path of the photon and α_ν the absorption coefficient. If the optical depth is $\tau_\nu > 1$, then the medium is said to be optically thick or opaque. The turning point between optically thin and thick happens at a specific frequency ν_t , where $\tau_\nu = 1$. In the latter case, where $\nu < \nu_t$, synchrotron self-absorption occurs, as low frequency photons interact with electrons and get absorbed. Here, the emitted power spectrum

$$P_\nu \propto \nu^{\frac{5}{2}} \quad (2.27)$$

is completely independent of p . For large frequencies $\nu > \nu_t$, i.e., an optically thin medium, the power spectrum remains the same as already derived above

$$P_\nu \propto \nu^{-\frac{p-1}{2}} = \nu^\alpha. \quad (2.28)$$

2.3 Polarization and Stokes Parameters

A strong argument in favor of the low energy emission being produced by synchrotron radiation is the observation of polarization in radio measurements.

Based on Eq. 2.25, considering the two polarization components of the radiation that are linearly polarized perpendicular and parallel to the magnetic field, the emitted power per frequency can be expressed by

$$P_\perp(\nu) = \frac{\sqrt{3}e^3 B \sin \varphi}{2m_e c^2} \left[\left(\frac{\nu}{\nu_c} \right) \int_{\nu/\nu_c}^{\infty} K_{5/3}(\xi) d\xi + \left(\frac{\nu}{\nu_c} \right) K_{2/3} \left(\frac{\nu}{\nu_c} \right) \right] \quad (2.29)$$

$$P_\parallel(\nu) = \frac{\sqrt{3}e^3 B \sin \varphi}{2m_e c^2} \left[\left(\frac{\nu}{\nu_c} \right) \int_{\nu/\nu_c}^{\infty} K_{5/3}(\xi) d\xi - \left(\frac{\nu}{\nu_c} \right) K_{2/3} \left(\frac{\nu}{\nu_c} \right) \right] \quad (2.30)$$

([Rybicki & Lightman, 1979](#)). The total emitted power is then the sum of Eq. 2.29 and Eq. 2.30, $P(\nu) = P_\perp(\nu) + P_\parallel(\nu)$. For a power-law electron distribution in an optically thin medium, the degree of polarization is defined as

$$\Pi = \frac{P_\perp - P_\parallel}{P_\perp + P_\parallel} = \frac{p + 1}{p + 7/3}. \quad (2.31)$$

Assuming a typical $p = 2 - 3$, the degree of polarization is as high as $\Pi \sim 70\%$. In real observations, however, such values are basically never observed. A few reasons for this are given in Sect. 2.4.

Another description of the polarization state of radiation is given by the Stokes parameters I, Q, U, V . Here, I represents the total intensity of the wave, V the circular and Q together with U the linear polarization. In the simplest case, a monochromatic plane wave, the electric field E of the wave can be expressed as

$$E(t) = E_0 e^{i\omega t}, \quad (2.32)$$

where E_0 is the amplitude and ω the angular frequency of the wave. Planar waves can be understood as the superposition of two orthogonal waves. These orthogonal waves can be expressed either in a linear or a circular base, where the choice depends on whether the measurement system uses linear or circular polarizing receivers. As the Effelsberg 100 m telescope measures left- and right-handed circular polarization (LCP and RCP) with the used receivers², this base will also be used for the following introduction. Therefore, Eq. 2.32 can be split into

$$E_l(t) = E_L e^{i\omega t} \quad (2.33)$$

$$E_r(t) = E_R e^{i(\omega t + \delta)}, \quad (2.34)$$

with δ being the phase difference between the two waves, following Myserlis et al. (2018). Using this description, the Stokes parameters are then defined as

$$I = \langle E_L^2 \rangle + \langle E_R^2 \rangle \quad (2.35)$$

$$Q = 2 \langle E_L E_R \cos \delta \rangle \quad (2.36)$$

$$U = 2 \langle E_L E_R \sin \delta \rangle \quad (2.37)$$

$$V = \langle E_R^2 \rangle - \langle E_L^2 \rangle, \quad (2.38)$$

where the $\langle \rangle$ denote time averaging in order to account for the fact that the waves are not actually monochromatic, causing variations in E_L , E_R and δ . The Stokes vector \mathbf{S} is then the four-dimensional vector

$$\mathbf{S} = \begin{pmatrix} I \\ Q \\ U \\ V \end{pmatrix}. \quad (2.39)$$

Through the Stokes parameters, the polarization properties of the received signal can be further quantified, defining the intensity of linear polarization p_{lin} , the fractional polarization m_l and the polarization angle (or the electric vector position angle, EVPA) χ as

$$p_{\text{lin}} = \sqrt{Q^2 + U^2} \quad (2.40)$$

$$m_l = \frac{p_{\text{lin}}}{I} \quad (2.41)$$

$$\chi = \frac{1}{2} \arctan \frac{U}{Q}, \quad (2.42)$$

with $0^\circ \leq \chi \leq 180^\circ$, meaning that a full azimuth rotation corresponds to a 180° change in the EVPA.

²See https://eff100mwiki.mpifr-bonn.mpg.de/doku.php?id=information_for_astronomers:rx_list

2.4 Faraday Rotation and Depolarization

In theory, the observation of an EVPA, produced by synchrotron radiation in an optically thin medium, gives insight into the orientation of the magnetic field, as in this case $\chi \perp \mathbf{B}$. However, in reality, this connection cannot be drawn that easily, as Faraday-rotation occurs when the radiation travels through a plasma with a magnetic field. Again using the circular base, due to their polarization (either LCP or RCP), the two waves experience different permittivities of the plasma and therefore propagate at different phase velocities, leading to a rotation of the EVPA. This rotation is quantified by

$$\Delta\chi \text{ [rad]} = 8.1 \times 10^5 \lambda^2 \int_L n_e B \cos \theta dL = \text{RM} \cdot \lambda^2, \quad (2.43)$$

where λ is the wavelength in meters, L is the path length traveled by the wave through the medium in parsec, n_e is the electron density in cm^{-3} , B is the magnetic field in Gauß and θ is the angle between the magnetic field and the propagation direction (Saikia & Salter, 1988), and with the definition of the so-called rotation measure

$$\text{RM} \text{ [rad m}^{-2}\text{]} = 8.1 \times 10^5 \int_L n_e B \cos \theta dL. \quad (2.44)$$

The rotation of the EVPA is then given by

$$\chi_{\text{obs}} = \chi_0 + \text{RM} \cdot \lambda^2, \quad (2.45)$$

where χ_{obs} is the observed and χ_0 the source intrinsic EVPA. Faraday rotation can either occur in the medium that is emitting the radiation or in an external medium.

On top of that, Faraday rotation can also introduce a depolarization of the radiation. Magnetic fields and electron densities in a medium are not uniformly distributed but rather vary on small scales. In a simple model, it can be assumed that both B and n_e are constant in a cell of a certain size. However, the radiation passing through the cells will experience different rotation measures, meaning that the EVPAs are not rotated evenly. If there is more than one such cell inside a telescope beam, the polarization adds vectorially, resulting in a reduced EVPA amplitude and therefore in a lower polarization degree.

Of course, source intrinsic depolarization can occur as well, when different source components that are not resolved by the telescope do, in fact, exhibit different polarization properties, as they are added vectorially as well.

2.5 How to Correct Measured Polarized Fluxes for Instrumental Influences

Measuring polarized flux densities is not as easy as measuring total (Stokes I) flux densities, as the receiving system does not actually measure the true, source intrinsic Stokes parameters for two main reasons. The first one is the parallactic rotation that occurs due to the azimuthal mount of the Effelsberg 100 m telescope, causing the source to rotate with respect to a default reference frame, leading to a rotation of the EVPA. The second reason is attributed to the imperfect receiving system that introduces spurious polarization. Turlo et al. (1985) developed a calibration scheme to account for both of these effects. Their method was used on the data

in this thesis and thus this section is based on their work. Also, it is based on Kraus (1997), who established the analysis scripts that are, in parts, still used today. The Turlo et al. (1985) method reproduces the true Stokes parameters \mathbf{S}_{true} from the observed ones \mathbf{S}_{obs} via two matrices

$$\mathbf{S}_{\text{obs}} = \mathcal{M} \cdot \mathcal{R} \cdot \mathbf{S}_{\text{true}}. \quad (2.46)$$

Here, \mathcal{R} represents the parallactic rotation and \mathcal{M} is the Müller matrix of the instrument that corrects for the instrumental effects.

At this point it has to be noted that throughout this thesis, circular polarization is neglected, i.e., $V \sim 0$, as the sources of interest typically only show considerable linear polarization. On top of that, the Stokes V signal is very noisy and developing an analysis tool to extract the weak signal exceeds the means of this thesis. With that, the Stokes vector \mathbf{S} is effectively reduced to a three-dimensional quantity.

2.5.1 The Rotation Matrix \mathcal{R}

The parallactic angle q is defined to be the angle between the hour circle and the great circle, i.e., the circle through the source and the zenith. In Fig. 2.4, this is shown in more detail. From here it is possible to see that the parallactic angle is the angle between the elevation and the declination δ of the source. The parallactic angle can then be calculated as

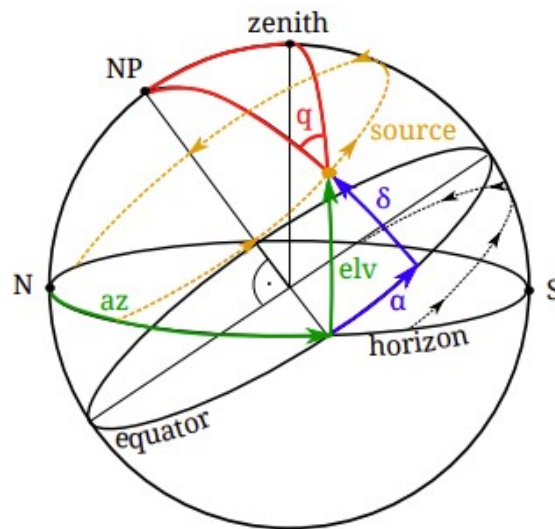


Figure 2.4: The green lines represent the azimuth and elevation system of the telescope. α is the right ascension and δ the declination of a source. The parallactic angle q is defined as the angle between the elevation and the declination of the source. Taken from Beuchert (2013).

$$q = \arctan \left(\frac{\pm \cos \phi \sin H}{\sin \phi \cos \delta - \cos \phi \sin \delta \cos H} \right), \quad (2.47)$$

with ϕ being the geographical latitude of the telescope and H being the hour angle of the source.

For the Effelsberg 100 m telescope, the rotation of the EVPA is given by $2q$ and thus the rotation

matrix can be expressed as

$$\mathcal{R} = \begin{pmatrix} 1 & 0 & 0 \\ 0 & \cos 2q & \sin 2q \\ 0 & -\sin 2q & \cos 2q \end{pmatrix}, \quad (2.48)$$

with q being the parallactic angle of the source at the time of the observation. From this it can be seen that Stokes I is not affected by this rotation, only Q and U . Of course, q changes over the time of an observation, resulting in an uncertainty in the rotation. However, the measurements done by TELAMON are short enough for this effect to be negligible.

2.5.2 The Müller Matrix \mathcal{M}

Various effects in the receiving system lead to the imperfections that introduce the spurious polarization. In the used formalism, these effects are described by the Müller matrix

$$\mathcal{M} = \begin{pmatrix} M_{11} & M_{12} & M_{13} \\ M_{21} & M_{22} & M_{23} \\ M_{31} & M_{32} & M_{33} \end{pmatrix}. \quad (2.49)$$

With that, the components of Eq. 2.46 read

$$\begin{pmatrix} I \\ Q \\ U \end{pmatrix}_{\text{obs}} = \begin{pmatrix} M_{11} & M_{12} & M_{13} \\ M_{21} & M_{22} & M_{23} \\ M_{31} & M_{32} & M_{33} \end{pmatrix} \begin{pmatrix} 1 & 0 & 0 \\ 0 & \cos 2q & \sin 2q \\ 0 & -\sin 2q & \cos 2q \end{pmatrix} \begin{pmatrix} I \\ Q \\ U \end{pmatrix}_{\text{true}}. \quad (2.50)$$

While \mathcal{R} can easily be determined by measuring the parallactic angle simultaneously with the actual data, \mathcal{M} cannot be ascertained that easily. To find the components of \mathcal{M} , polarization calibrators, i.e., sources of known \mathbf{S}_{true} , have to be observed during a measurement campaign. From Eq. 2.50 it is obvious that at least three individual and independent observations of such a source need to be done in order to find a unique solution to the system of equations.

Certain entries of the Müller matrix give an overview of the instrumental properties. For example, the instrumental polarization p_{inst} , describing the overflow of Stokes I to polarized intensity, is given by

$$p_{\text{inst}} = \frac{\sqrt{M_{21}^2 + M_{31}^2}}{|M_{11}|}. \quad (2.51)$$

Therefore, only Müller matrices that have a small value of p_{inst} can be used in a meaningful way. Contrarily, the so-called depolarization p_{depol} gives an estimate of how much the polarized intensity influences the total intensity and is defined as

$$p_{\text{depol}} = \frac{\sqrt{M_{12}^2 + M_{13}^2}}{|M_{11}|}. \quad (2.52)$$

As the polarization in blazars is typically rather low, depolarization effects do not have a significant impact on the results. Finally, the instrumental polarization angle χ_{inst} is given by

$$\chi_{\text{inst}} = \arctan \frac{M_{31}}{M_{21}}. \quad (2.53)$$

2.6 What a Radio Telescope Measures

In this section, the technical background of measuring with a radio antenna will be given. Only aspects relevant for this work will be discussed and some steps will be skipped. For a more in-depth introduction, it is referred to [Kraus \(1966\)](#) and [Burke et al. \(2019\)](#).

Assuming a realistic radio telescope of effective area A_{eff} that observes a source of brightness $B_\nu(\theta, \phi)$ at a certain frequency ν in a solid angle Ω , its received power P_ν is given by

$$P_\nu = \frac{1}{2} A_{\text{eff}} \int_{\Omega} B_\nu(\theta, \phi) \Pi(\theta, \phi) d\Omega, \quad (2.54)$$

where $\Pi(\theta, \phi)$ is the power pattern of the telescope and θ, ϕ are the angle to the zenith and the azimuth, respectively. The power pattern of an antenna can be understood as a way to describe its sensitivity, depending on the direction of the incident radiation.

When talking about radio sources, the quantity of interest mostly is the flux density

$$S = \int_{\Omega} B_\nu(\theta, \phi) \Pi(\theta, \phi) d\Omega \quad (2.55)$$

of the source. In radio astronomy, the flux density is usually given in units of *Jansky*, in honor of Karl Jansky, where

$$1 \text{ Jy} = 10^{-26} \text{ W m}^{-2} \text{ Hz}^{-1}.$$

Considering the antenna to be sensitive to a range of frequencies $\Delta\nu$, Eq. 2.54 can be written as

$$P = \frac{1}{2} A_{\text{eff}} S \Delta\nu. \quad (2.56)$$

Assuming the antenna to be a black body, its received power is governed by Planck's law. For radio waves, it is sufficient to use the Rayleigh-Jeans approximation and write

$$B_\nu = \frac{2\nu^2 k_B T}{c^2}, \quad (2.57)$$

where k_B is the Boltzmann constant, T the temperature and c the speed of light. With that, Eq. 2.54 becomes

$$P_\nu = \frac{1}{2} A_{\text{eff}} \int_{\Omega} \frac{2\nu^2 k_B T}{c^2} \Pi(\theta, \phi) d\Omega = A_{\text{eff}} \frac{\nu^2 k_B T}{c^2} \Omega_A = A_{\text{eff}} \frac{k_B T}{\lambda^2} \Omega_A, \quad (2.58)$$

where $\Pi(\theta, \phi) \approx 1$ was assumed, as is valid for point sources, and $\lambda = c/\nu$ was used. From antenna theory ([Rohlf & Wilson, 2013](#)) it is known that

$$A_{\text{eff}} \Omega_A = \lambda^2 \quad (2.59)$$

holds. Using this on Eq. 2.58, the received power reduces to

$$P_\nu = A_{\text{eff}} \frac{k_B T}{\lambda^2} \Omega_A = \lambda^2 \frac{k_B T}{\lambda^2} = k_B T, \quad (2.60)$$

meaning that the power can be expressed as a temperature. This temperature is called the antenna temperature T_A and the received power is thus

$$P_\nu = k_B T_A. \quad (2.61)$$

Note that the antenna temperature does not correspond to the physical temperature of the antenna, but is rather an equivalent temperature a black body would have if it emitted a spectral power P_ν .

The observed flux density can now be related to the measured antenna temperature, by integrating Eq. 2.61 over a frequency range $\Delta\nu$ and equating it with Eq. 2.56. Doing so, the relation is found to be

$$S = \frac{2k_B}{A_{\text{eff}}} T_A. \quad (2.62)$$

With this equation, in theory, the flux density of a source could be calculated by recording the antenna temperature. In Chapter 3, the usefulness of this formula will be elucidated.

3 | Observations and Data Reduction

Radio waves are generally able to pass through most matter, as it is optically thin for them. This also includes Earth's atmosphere, giving radio astronomy the critical advantage that it can be done from the ground, rather than needing telescopes in space. For most parts of the electromagnetic spectrum, Earth's atmosphere presents an opaque barrier, with the exception of two main atmospheric windows in the optical and radio regime, where radiation can pass through without being absorbed. The radio window is bound by molecules such as CO_2 , O_2 or H_2O in the atmosphere absorbing incoming radiation on the one end and by the reflective properties of the ionosphere on the other, roughly ranging from $1 \text{ mm} \leq \lambda \leq 30 \text{ m}$.

In this chapter, the Effelsberg 100 m telescope (Fig. 3.1) will be introduced, as it was used for all of the observations performed in the framework of this thesis. Furthermore, the observational setup as well as the reduction of total intensity flux densities will be explained shortly. As the main analysis part of this thesis, the reduction of polarized flux densities will be described in more detail.

3.1 The Effelsberg 100m Telescope

This section is based on information from [Bach & Kraus \(2020\)](#) and the [data sheet](#)¹ of the telescope, provided by the Max-Planck-Institut für Radioastronomie (MPIfR), who also operates the telescope. Located in a protected valley in Effelsberg, Germany, it is one of the largest fully steerable single-dish radio telescopes in the world. Its instruments can detect radiation in a large range of frequencies, from 90 GHz ($\sim 3.5 \text{ mm}$) down to 300 MHz ($\sim 90 \text{ cm}$), while its parabolic dish has a very high surface accuracy of $\sigma \sim 0.5 \text{ mm}$ (rms). To add onto that, it is built using the principle of homology, meaning that, even though gravity acts on it, its dish will always stay in a parabolic shape with a well-defined (but shifted) focal point.

An important property of a telescope is its angular resolution θ that describes its ability to distinguish between two small features of an object. The angular resolution is limited by the Rayleigh criterion

$$\theta \approx \frac{\lambda}{D}, \quad (3.1)$$

with λ being the wavelength of the observation and D being the diameter of the telescope. For the Effelsberg telescope, $D = 100 \text{ m}$, and an observing wavelength of $\lambda = 20 \text{ mm}$, the angular resolution amounts to $\theta \sim 0.7 \text{ arcmin}$. To set this into relation, the resolution of the human eye

¹<https://www.mpifr-bonn.mpg.de/231173/specs>

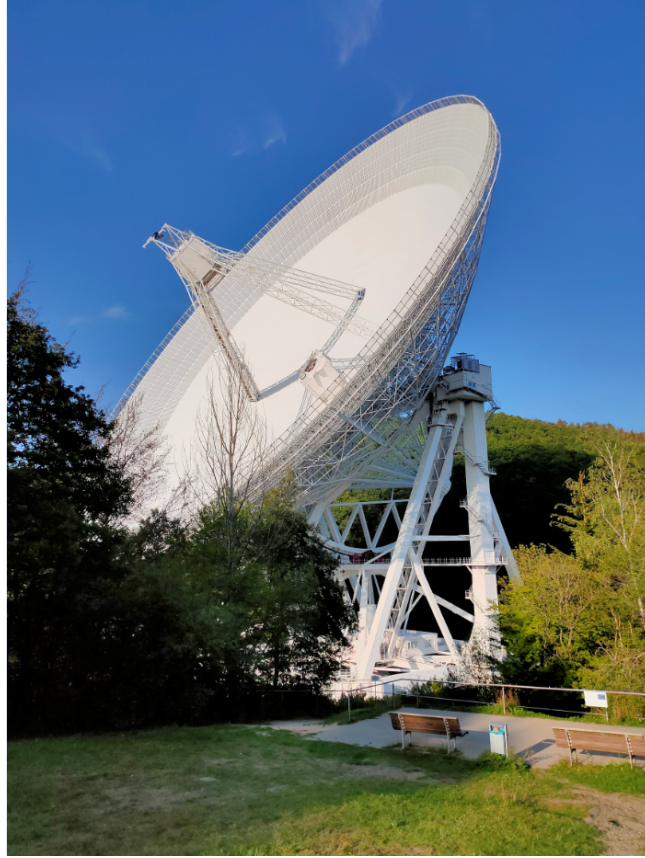


Figure 3.1: The Effelsberg 100 m telescope, located in Effelsberg, Germany, is one of the largest steerable single dish radio telescopes on Earth. With its 100 m dish it achieves high sensitivities and high angular resolutions.

Credit: Jonas Heßdörfer, 2020

in the green part of the visible spectrum, where it is most sensitive, is just as big. The main beam B of the telescope is well described by a Gaussian of the form

$$B = \exp\left(-4 \ln 2 \left(\frac{\vartheta}{\theta}\right)^2\right), \quad (3.2)$$

where ϑ is the angular distance from the beam center.

Another property of a telescope is its sensitivity Γ . Re-writing Eq. 2.62 to

$$T_A = \frac{SA_{\text{eff}}}{2k_B} = \frac{S\eta_A A_{\text{geom}}}{2k_B} = S \cdot \Gamma, \quad (3.3)$$

with $A_{\text{eff}} = \eta_A A_{\text{geom}}$, where A_{geom} is the geometric area of the telescope and η_A its aperture efficiency, the sensitivity of the Effelsberg 100 m telescope is given by

$$\Gamma [\text{K/Jy}] = \frac{T_A}{S} = \frac{\eta_A A_{\text{geom}}}{2k_B} = \eta_A \frac{\pi D^2}{8k_B} = \eta_A \cdot 2.844 \text{ K/Jy}. \quad (3.4)$$

The aperture sensitivity can be calculated via Ruze's formula (Ruze, 1966)

$$\eta_A = \eta_0 \exp\left(-0.78 \left(\frac{4\pi\sigma}{\lambda}\right)^2\right). \quad (3.5)$$

Here, σ is the rms of the reflector and η_0 is a constant. Bach et al. (2007) determined $\eta_0 = 0.55$ for the Effelsberg telescope, resulting in $\Gamma \sim 1.4 \text{ K/Jy}$ for $\lambda = 20 \text{ mm}$.

3.2 Data Taking and Sample

As already mentioned in the introduction, this thesis is based on data taken as part of the TELAMON program. Therefore, the observing procedure and the sample are the same as for TELAMON, described in full detail in Heßdörfer (2021) and Eppel (2021), as well as in Kadler et al. (2021). Here, only a short summary will be given. Eppel (2021) focused his studies on TeV-detected and neutrino-candidate AGN at different 14 mm and 7 mm frequencies. In contrast to his work, this thesis focuses on *all* sources that were observed in the scope of TELAMON between 19.09.2021 and 17.05.2022². Table A.1 in Appendix A gives the names and J2000 coordinates of all those sources. Additionally, a third receiver was used, taking data at two 20 mm frequencies. For the observations in TELAMON, the OPTOCBE backend of the receivers is used to take total intensity (Stokes I) flux density data. All of the used receivers are also equipped with a second horn that is offset with respect to the primary horn by $\sim 100'' - 200''$ in azimuthal direction. Due to this offset, the second horn monitors the atmosphere near the source, making it possible to subtract weather effects from the primary data. This is especially useful for cloudy conditions, as then, according to Kirchhoff's law on thermal radiation, Earth's atmosphere emits more thermal radiation that corrupts the data, especially at higher frequencies.

To measure polarization data, a second backend, the SPECPOL, was used that runs simultaneously (in „piggyback“ mode) with the OPTOCBE backend. In addition to the Stokes I data, the SPECPOL also collects Stokes U, Q (and V). Therefore, doing a scan on a source yields five sets of data: Stokes I taken by the OPTOCBE, Stokes I taken by the SPECPOL and Stokes Q, U, V , also taken by the SPECPOL. Since the sources in this sample are expected to have $V \sim 0$ and the extraction of a Stokes V signal is way harder than for the other Stokes parameters, circular polarization will be ignored throughout the thesis and when „polarization“ is said, linear polarization (Stokes Q and U) is meant. The two backends provide data in several frequency bands that are centered around slightly different values, shifted by 0.25 GHz. The center frequencies are 14 GHz (14.25 GHz), 17 GHz (16.75 GHz), 19 GHz (19.25 GHz), 21.4 GHz (21.15 GHz), 36 GHz (36.25 GHz) and 39 GHz (38.75 GHz) for the SPECPOL (OPTOCBE) backend. Technically, the OPTOCBE takes data in four more bands, but since they are not covered by the SPECPOL, they will not be considered in this thesis. Also, it has to be noted that the frequency range of the OPTOCBE is 2.5 GHz, while it is only 2 GHz for the SPECPOL. For the sake of simplicity, when talking about these frequencies in the rest of the thesis, they will be referred to as 14 GHz, 17 GHz, 19 GHz, 21 GHz, 36 GHz and 39 GHz, always implying the „correct“ frequencies for the corresponding backend. Compared to the OPTOCBE, the SPECPOL has one critical disadvantage, namely the lack of a second horn, meaning that bad weather has a larger influence on the data quality, as will be discussed later on in this section. However, the SPECPOL also has an advantage, as it is possible to manually set the frequency range to be integrated. This is particularly helpful, as some of the data are corrupted by disturbances or radio-frequency interference. An example of this is shown in Fig. 3.2, for a 14 GHz scan on NGC 7027. Here, the entire frequency range recorded by the SPECPOL is plotted with respect to the measured power and temperature. For both plots, a vast drop at $\sim 13 \text{ GHz}$ is visible and a central peak can be made out in the temperature plot. To get rid of these effects,

²See <http://telamon.astro.uni-wuerzburg.de/> for an overview

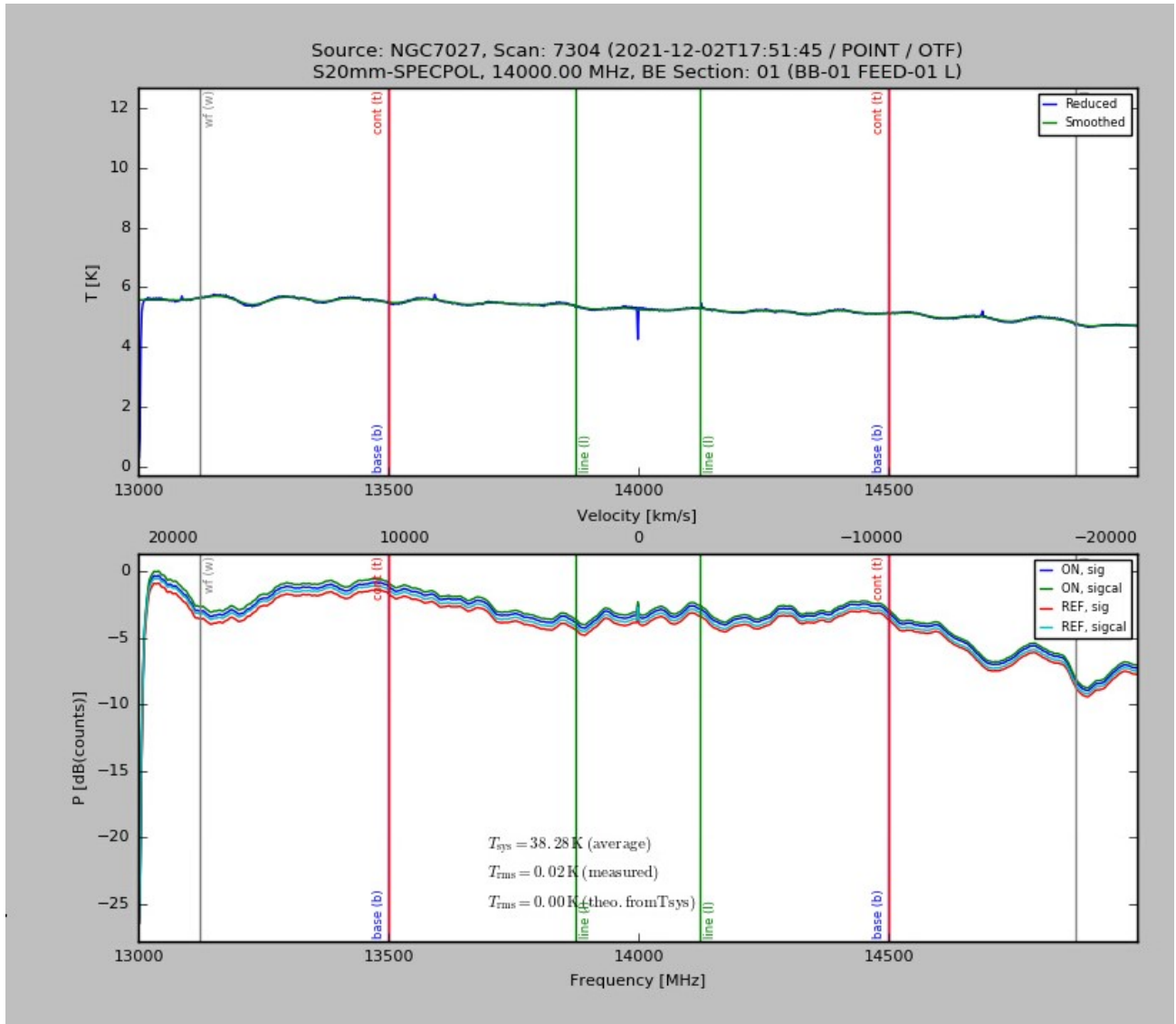


Figure 3.2: Shown are the temperature (top) and the power (bottom) of a 14 GHz scan on NGC 7027 for the entire frequency range of the SPECPOL backend. In both plots a steep drop at ~ 13 GHz is discernible and in the temperature plot also a central peak can be seen. In other scans, this peak can be even more pronounced. Small frequency ranges around these disturbances are therefore excluded from the integrated frequency range of the data.

a frequency mask (fmask) is applied to the data, limiting the range of the integrated signal. Throughout this thesis, the fmask given in Table 3.1 are used for the respective frequencies.

SPECPOL frequency [GHz]	fmask
14	13.05-13.95,14.05-14.95
17	16.10-16.95,17.05-17.90
19	18.20-19.50
21.4	20.45-22.35
36	35.05-36.95
39	38.05-39.95

Table 3.1: Frequency masks used for the different frequencies.

As all observed sources appear point-like to the telescope beam at the used frequencies, their flux densities can be measured using „cross-scans“, where the antenna response is measured while repeatedly slewing the telescope over the source position in two orthogonal directions, azimuth and elevation. This technique allows to find possible offsets between the expected source position and the maximum of the telescope response, due to, e.g., deformations of the telescope, and to correct for them before doing the next scan.

For the calibration of the data, calibrator sources are observed regularly. In contrast to the total intensity data, in order to get meaningful polarization data, three distinct calibrator measurements need to be done in one observing session (see Sect. 2.5). Moreover, at least one polarized calibrator needs to be observed as well. For this thesis, 3C 286 was used as the polarization calibrator and NGC 7027 and W3(OH) were used as unpolarized calibrators.

In total, 23 long TELAMON observation sessions are considered in this thesis. Of them, 12 cannot be used for the polarization analysis due to various reasons, while the other 11 session can be used at least in parts. Also, not in all distinct epochs the SPECPOL was collecting data for all six frequencies, again due to several reasons. Since only frequencies can be compared that were recorded for both backends, in epochs were certain SPECPOL frequencies did not work, the OPTOCBE data for them are not used in this thesis. In Table 3.2, all the relevant information for the epochs are given.

3.3 Data Reduction of Total Intensity Flux Densities

After the data taking process, in order to arrive at the unit of interest, flux density, they need to be reduced. While the main focus of this work lies on the polarization data, to get them, the total flux densities need to be reduced first. This is done using the semi-automated analysis tool developed by Eppel (2021). The exact steps taken to correct the data for various effects are explained in his work, as well as in Heßdörfer (2021) and Angelakis et al. (2019). Here, only a short summary will be given.

In Sect. 2.6, the antenna temperature was introduced as the observable that the telescope measures. However, this is not completely true, since the telescope actually measures the signal T_{obs} in counts. To convert the counts into the antenna temperature, they are multiplied with

Date	Polarization data?	OPTOCBE and SPECPOL frequencies [GHz]	Reason
19.09.21	Y	14, 17	a
07.10.21	Y	14, 17, 19, 21	a
24.10.21	Y	14, 17, 19, 21	a
05.11.21	N	—	b
22.11.21	N	—	b
27.11.21	N	—	c
28.11.21	N	—	c
02.12.21	N	14, 17, 19, 21, 36, 39	d
08.12.21	N	14, 17, 19, 21, 36, 39	e
20.12.21	Y (N for 7 mm)	14, 17, 19, 21, 36, 39	e
06.01.22	N	17, 19, 39	b, d
24.01.22	Y	14, 17, 19, 21, 36, 39	
08.02.22	N	—	c
12.02.22	Y	14, 17, 19, 21, 36 (, 39)	f
27.02.22	N	14, 21, 36	b, d
05.03.22	N	14, 21, 36	b, d, e
06.03.22	N	14, 21, 36	b, e
23.03.22	Y	14, 17, 19, 21, 36, 39	
09.04.22	Y	14, 17, 19, 21, 36, 39	
26.04.22	Y	14, 21, 36	b
30.04.22	N	17, 19	c, e
02.05.22	Y (N for 7 mm)	14, 17, 19, 21, 36, 39	d
17.05.22	Y	14, 17, 19, 21, 36, 39	

Table 3.2: Dates of all observations conducted in the framework of this thesis. The second column gives information if polarization data could be reconstructed (Y) or not (N). In the third column, all frequencies for which data could be evaluated for both receivers are given. Reasons: *a*: in the beginning, the SPECPOL was not used at all frequencies, *b*: SPECPOL did not work (at certain frequencies), *c*: SPECPOL scans are not of good quality, *d*: Not enough usable calibrators were observed, *e*: Müller matrix is not reasonable, *f*: one OPTOCBE channel did not work

the temperature of the noise diode T_{cal} that is well documented on the [receiver page](#)³ of the telescope. Then, the desired antenna temperature in Kelvin is found via

$$T_A = T_{\text{cal}} \cdot T_{\text{obs}}. \quad (3.6)$$

Quality checks of the scans are performed to make sure they fulfill certain criteria. This is done using the method presented in [Eppel \(2021\)](#). Afterwards, the scans are corrected for pointing offsets due to imperfect centering of the cross-scan. The corrected antenna temperature $T_{A,\text{corr},i}$

³https://eff100mwiki.mpifr-bonn.mpg.de/doku.php?id=information_for_astronomers:rx_list

is calculated using the pointing offset Δp_j , with i, j being the two scanning directions in azimuth and elevation, and found to be

$$T_{A,\text{corr},i} = T_{A,i} \exp \left(4 \ln 2 \left(\frac{\Delta p_j}{\theta} \right)^2 \right). \quad (3.7)$$

Here, θ is the half-power beam width of the telescope beam at the used frequency and $T_{A,i}$ is the antenna temperature before the correction. Then, a correction to account for the attenuation of the observed signal in Earth's atmosphere is applied. To do this, the zenith opacity τ is measured simultaneously by a water-vapor radiometer in the vicinity of the telescope, utilizing the strength of the 22 GHz water-vapor line. Together with the airmass AM , defined via the sine of the elevation of the source $AM = 1/\sin ELV$, the corrected antenna temperature then is

$$T_{A,\text{corr}2} = T_{A,\text{corr}} \cdot \exp(\tau \cdot AM). \quad (3.8)$$

A last adjustment happens in form of an elevation-dependent gain correction, using a second-order polynomial G that depends on the elevation of the source. The final corrected antenna temperature T_f then is

$$T_f = T_{A,\text{corr}2} \cdot G^{-1}. \quad (3.9)$$

Applying the aforementioned corrections to the initial data results in an antenna temperature amplitude in Kelvin. Arriving at the flux density should then simply be a matter of rearranging Eq. 3.3. However, in practice, it is not that easy to calculate the aperture efficiency a priori needed to evaluate Eq. 3.4. Another possibility to calculate the sensitivity Γ of the telescope arises through the observed calibrators. As their flux densities S_{cal} are known, Γ can be expressed as the ratio of the observed antenna temperature and the theoretical flux density

$$\Gamma = \frac{T_{A,\text{corr}2}}{S_{\text{cal}}}. \quad (3.10)$$

Throughout the observation, the sensitivity changes, as environmental and telescope effects occur. To model the continuous change of the sensitivity, the simple moving average interpolation, introduced by Eppel (2021) is used.

Finally, to make the interpretation of the data possible, the associated errors need to be investigated. Throughout the correction process described above, the linked errors are propagated according to Gaussian error propagation. Here, the largest error is usually due to the uncertainty in the derived sensitivity. Typically, two scans are done on one source per receiver. If only one scan remains after going through the analysis, its associated Gaussian error is assumed to be its final error. On the contrary, when two (or more, in rare cases) scans are left over, their average is used. The final flux densities S , with their errors σ , are then calculated as the weighted mean and the weighted error of the individual scans for the source and the frequency as

$$S = \sum_{i=1}^n \left(\frac{S_i}{\sigma_i^2} \right) / \sum_{i=1}^n \left(\frac{1}{\sigma_i^2} \right) \quad (3.11)$$

$$\sigma = \sqrt{\left(\sum_{i=1}^n \sigma_i^{-2} \right)^{-1}}, \quad (3.12)$$

following Taylor (1997). In some rare cases, the flux density values of the individual scans are farther apart than appears to be reasonable, making the weighted error somewhat unmeaningful. To handle such cases, the standard deviation of the flux densities is assumed as the error, while the mean is still calculated as the weighted mean.

In the following, whenever mean- and error-calculation are mentioned, this process is implied, if not noted otherwise.

3.4 Data Reduction of Polarized Flux Densities

While the analysis procedure explained in the previous section works for both the OPTOCBE and the SPEC POL, the latter, as already mentioned before, also includes Stokes Q , U , V . Up until this point, they are treated just as the Stokes I flux density is, except no flagging of subscans takes place. Nevertheless, when subscans of Stokes I are excluded, they are also excluded from the polarization analysis. To give an illustration of how a scan looks at different Stokes parameters, Fig. 3.3 shows all four of them for the source 1ES 1440+122 (J1443+2501), a moderately polarized source, at 14 GHz, taken on September 19, 2021. From the figure it is

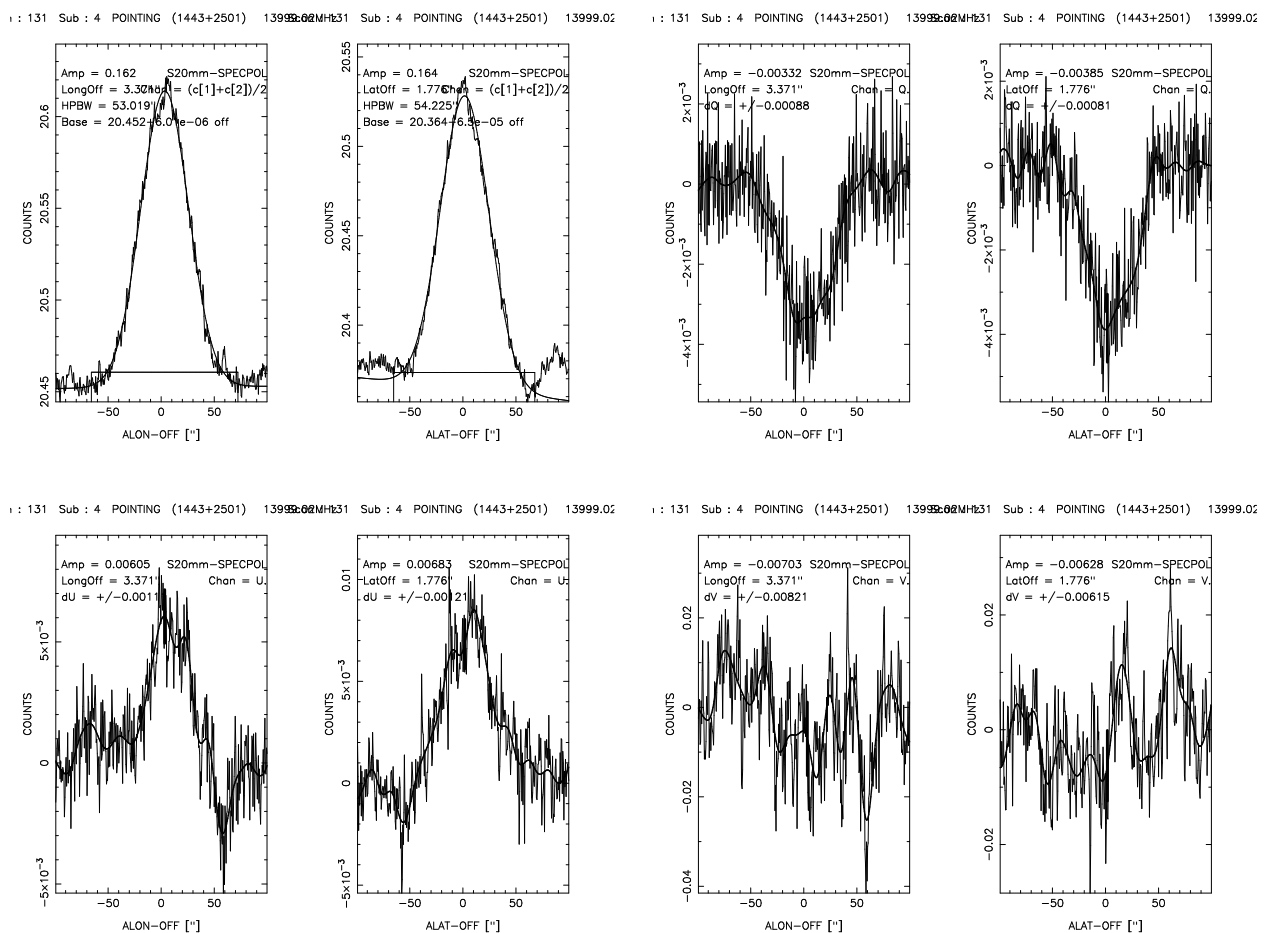


Figure 3.3: 1ES 1440+122 (J1443+2501) at 14 GHz on September 19, 2021. *Top left:* Stokes I , *top right:* Stokes Q , *bottom left:* Stokes U , *bottom right:* Stokes V . These scans are typical for a well detected, moderately polarized source.

clear that Stokes I , Q and U do show good signals, while V does not show any signal at all.

Also, the amplitudes of Q and U are far less than the one of I , while their noise is much higher. Of course this makes sense, as the polarization is only a small fraction of the total intensity and therefore the noise that is always present is more significant. To keep things consistent, it is assumed that Q and U have the same offset as I , therefore, their amplitudes are read off at the position of the Stokes I peak, rather than their maximum.

In principle, the calibration of Stokes I and polarization data works similarly. For total intensity, 3C 286 and NGC 7027 are modeled according to Perley & Butler (2017) and Zijlstra et al. (2008), respectively. The model for W3(OH) is based on Effelsberg data and assumes free-free emission (Alex Kraus, priv. comm.). However, the only polarized calibrator is 3C 286, where the model of Perley & Butler (2013) is used. The planetary nebula NGC 7027 and the star forming region W3(OH) are not expected to emit any polarized radiation. Therefore, their fractional polarization m_l and polarization angle χ are set to $m_l = 0\%$ and $\chi = 0^\circ$.

In practice, the calibration of the polarization data is done by inverting Eq. 2.50. Before doing that, the Stokes parameters of the calibrators need to be calculated from the known I , m_l and χ values. This is done using the relations

$$Q = Im_l \cos 2\chi = p_{\text{lin}} \cos 2\chi \quad (3.13)$$

$$U = Im_l \sin 2\chi = p_{\text{lin}} \sin 2\chi, \quad (3.14)$$

where $V = 0$ was assumed. Applying the rotation matrix \mathcal{R} (Eq. 2.48) to the Stokes parameters of the calibrators, the rotated parameters then read

$$I_{\text{rot}} = I_{\text{cal}} \quad (3.15)$$

$$Q_{\text{rot}} = Q_{\text{cal}} \cos 2q + U_{\text{cal}} \sin 2q \quad (3.16)$$

$$U_{\text{rot}} = -Q_{\text{cal}} \sin 2q + U_{\text{cal}} \cos 2q, \quad (3.17)$$

with q being the parallactic angle of the source at the time of the observation, as defined in Eq. 2.47. Fitting the observed values to the expected, rotated values using `scipy.optimize.curve_fit`, the elements of the Müller matrix (Eq. 2.49) and their associated errors are determined. However, these errors are not used in the analysis, as the overall error is assumed to be dominated by the uncertainty in the calibration.

Finally, the inverse Müller matrix

$$\mathcal{M}^{-1} = \begin{pmatrix} m_{11} & m_{12} & m_{13} \\ m_{21} & m_{22} & m_{23} \\ m_{31} & m_{32} & m_{33} \end{pmatrix} \quad (3.18)$$

is applied to Eq. 2.50 so that the true Stokes parameters of all sources can be calculated. The components of this equation are

$$I_{\text{true}} = m_{11}I_{\text{obs}} + m_{12}Q_{\text{obs}} + m_{13}U_{\text{obs}} \quad (3.19)$$

$$Q_{\text{true}} = m_{21}I_{\text{obs}} + m_{22}Q_{\text{obs}} + m_{23}U_{\text{obs}} \quad (3.20)$$

$$U_{\text{true}} = m_{31}I_{\text{obs}} + m_{32}Q_{\text{obs}} + m_{33}U_{\text{obs}}. \quad (3.21)$$

Here, the lower right 2×2 matrix acts as a rotation matrix between the true and observed polarization.

Throughout this thesis, the Stokes I correction was not performed, due to two reasons. The first one being the fact that the effect of the polarized flux density on the total flux density is assumed to be negligible. The second reason, as will be seen later on, being that the instrument apparently suffers from a strong depolarization (Eq. 2.52) that cannot be explained thoroughly.

4 | Results

In this chapter, the results of the data analysis, as introduced in the previous chapter, are presented. To begin with, a comparison between the two receiver backends OPTOCBE and SPECPOL is given in Sect. 4.1. Since both backends record total intensity flux densities, the coincidence of the respective results is checked. Differences in the detection of sources and the reduced flux densities are investigated. Sect. 4.2 then gives an overview of the polarized flux densities, the fractional polarization and the EVPA distributions in the studied sample. Also, some interesting individual sources are investigated in further detail.

4.1 Comparing OPTOCBE and SPECPOL Backends

A first step to confirm the validity of the derived polarization information is to check whether the Stokes I fluxes measured by the SPECPOL are in agreement with the ones obtained using the OPTOCBE. Since the OPTOCBE is the main backend for continuum flux density measurements at Effelsberg for the used receivers, its performance is monitored on a regular basis, and therefore making it safe to assume that its results are reliable in almost all cases. On the other hand, the SPECPOL is not often used for this type of measurement, especially not at such high radio frequencies. Furthermore, the exact mode of operation of this backend is not known in its entirety to the responsible for continuum flux density observations at Effelsberg, making it some kind of a „black box“¹. These reasons alone demand a cross-check between the results of the two backends. On top of that, there are two other factors that make it worth to investigate the potential differences, as the SPECPOL does not have a second horn to subtract weather effects and also has a smaller frequency range.

Therefore, in this section, potential differences and similarities between the results of the two backends are examined. At this point it has to be noted again that they are not centered around the same frequencies, but rather around frequencies that lie 0.25 GHz apart. However, no vast flux density jumps are expected to occur in such a frequency range, making the comparison of the two frequencies possible. Three exemplary OPTOCBE and SPECPOL spectra are presented in Fig. 4.1, showing the reduced Stokes I flux densities for three different sources at different dates, as measured by the two backends. Comparing the spectra, three different scenarios are possible. In scenario 1 (Fig. 4.1 top), both backends detect all measured frequencies and the resulting flux densities coincide well within their respective errors. It can happen that both backends detect the same frequencies, but, after the data reduction, the flux density values do not coincide for one or more frequencies (scenario 2, Fig. 4.1 center). Finally, scenario 3 (Fig. 4.1 bottom) occurs when one of the backends does not detect a source at a certain frequency that the

¹Alex Kraus, priv. comm.

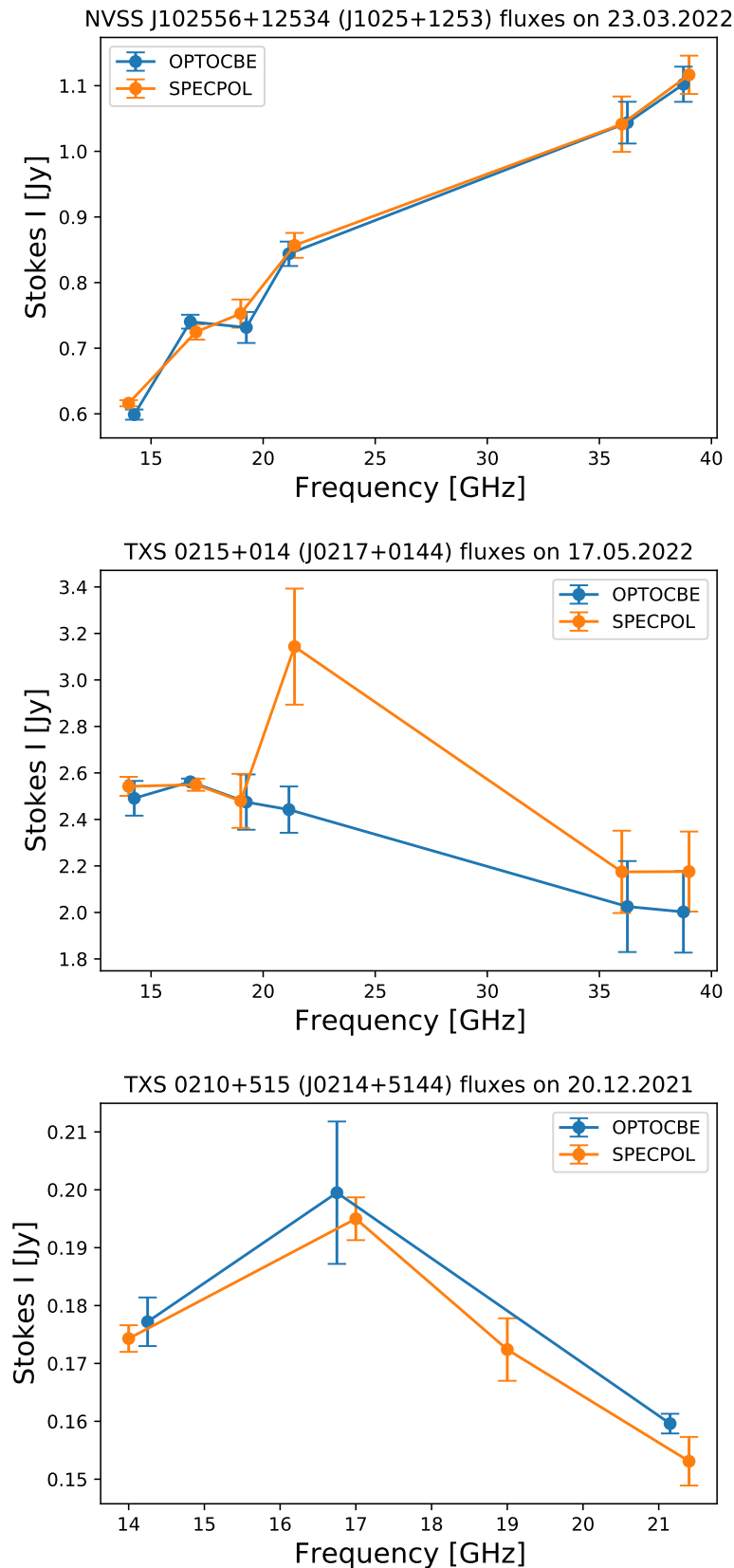


Figure 4.1: Example spectra of three different sources taken in the framework of this thesis. Shown are the three possible scenarios when comparing the OPTOCBE and SPECPOL spectra. *Top:* All frequencies are detected by both backends and coincide well within their respective errors. *Center:* All frequencies are detected by both backends, but not all flux densities coincide with their error regions. *Bottom:* Not all frequencies are detected by both backends. All other possibilities arise as combinations of these three scenarios.

other backend detected. Other scenarios are then just combinations of these three possibilities. Of course, scenario 1 is the optimal case. However, as is obvious from the figure, this does not always happen. In the following, scenario 2 (Sect. 4.1.2) and scenario 3 (Sect. 4.1.1) are further investigated to see how often they occur and how severe the differences are.

4.1.1 Detection Differences

To get an overview of the detection statistics of the two backends, Table 4.1 shows the amount of total detections at each frequency, representing the number of scans that lead to a detection of a source for at least one backend. Across all frequencies, in more than 80% of all cases,

Frequency [GHz]	Total detections	Detected by		
		Both	Only OPTOCBE	Only SPECPOL
14	274	272	1	1
17	228	209	6	13
19	284	246	18	20
21	318	296	16	6
36	127	113	6	8
39	90	75	5	10

Table 4.1: Detection differences between the two backends. Total detections refers to all observations conducted in the framework of this thesis, as presented in Table 3.2, where a flux density value could be derived for a frequency.

both backends did significantly detect the source, meaning that at least one of the scans done on it did not get flagged in the data reduction process. Conversely, a non-detection by one backend implies that all its scans on a source were flagged, while a minimum of one scan did yield a significant detection for the other backend. This can happen for various reasons, such as slightly changing offsets or scan amplitudes possibly due to, among other things, the different frequency ranges and therefore center frequencies. However, probably the biggest factor in most of the „OPTOCBE-only“ detections is the weather, or, to be more precise, the subtraction of the weather effects through its second horn. This is exemplarily demonstrated in Fig. 4.2 for the source NVSS J102556+12534 (J1025+1253), using data from 17.05.2022 at 39 GHz. In the top row, a scan of the source is shown for the SPECPOL (left) and for the OPTOCBE backend without the weather subtraction (right). Both scans appear to be very similar and do not exemplify valid detections, at least in the latitude scans. However, when subtracting the second horn (bottom), and thereby getting rid of the negative impact of weather effects, both scan directions are now much clearer and do resemble a good detection. As can be seen from Table 4.1, the SPECPOL does, in fact, detect at least as many sources as the OPTOCBE, if not more, with the exception of 21 GHz. This implies that either the smaller frequency range or the exclusion of disturbances in the data have a larger positive effect than the absence of the second horn has a negative effect. This makes sense, as typically TELAMON observations are only performed for good weather conditions and in such cases, the second horn does not have a huge impact on the data quality. The detection statistic is also illustrated in Fig. 4.3. Here it can be seen that the SPECPOL does slightly more single-detections than the OPTOCBE, although the numbers are very well comparable.

As a side note, the single non-detection of the SPECPOL at 14GHz appears to be due to a random malfunction of the backend during the two scans performed on the source, leading to some data getting lost. Since this did not happen for any other scan in this epoch, the non-detection was not excluded from the list.

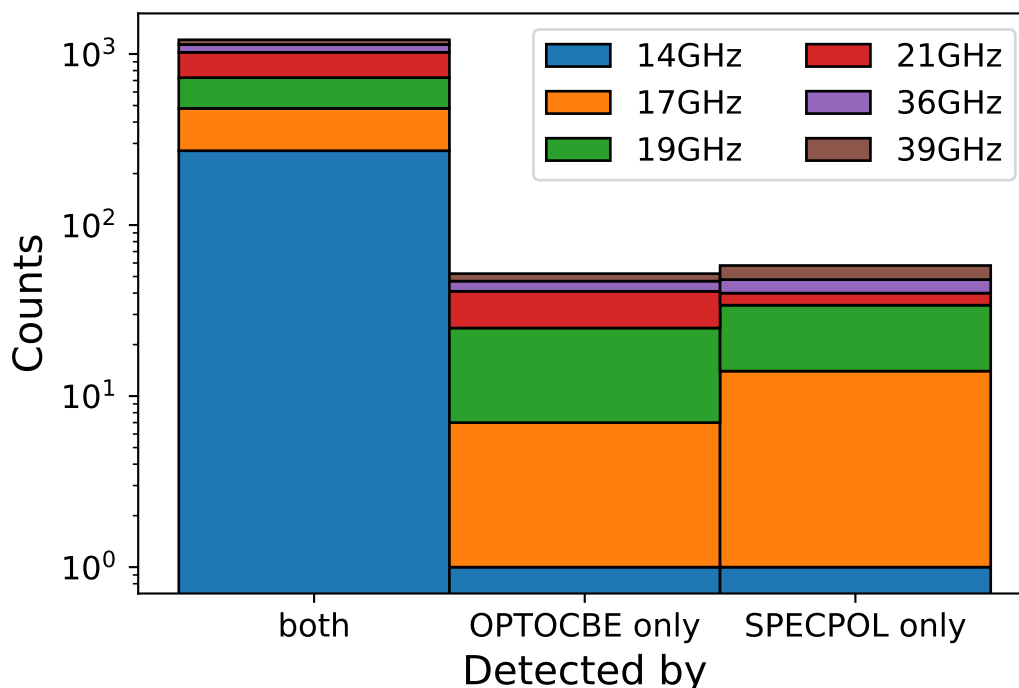


Figure 4.3: Detection differences between the two backends.

An interesting question to ask is whether the non-detection of a source depends on its flux density or not. Intuitively, weaker sources should make up the largest amount of detections by only one backend, as for them, the noise is more significant and therefore the aforementioned effects influence the scan quality more than for brighter sources. To check this assumption, Fig. 4.4 shows the derived flux densities of the respective other backends for all sources that were only detected by one backend at a time. For the 20 mm and 14 mm receivers, the vast majority of these flux densities lies below 0.25 Jy, and a majority even under 0.125 Jy. At 7 mm, most sources have a flux density lower than 0.5 Jy, although there are some outliers toward higher fluxes and no flux densities as low as for the other two receivers. The latter has to do with the fact that at 7 mm no sources below ~ 0.2 Jy were observed. Additionally, it is generally harder to detect sources with this receiver, due to a lower telescope sensitivity and higher atmospheric attenuation at these frequencies. Nevertheless, while most of the single-detected flux densities are at the lower end of all flux densities in the sample at the corresponding frequencies (see Fig. 4.15), there are also single-detections toward the higher end of the flux density values. This indicates that the assumption is mostly true, although also higher flux density values can be affected by random offset changes and other effects between the two backends.

4.1.2 Flux Density Differences

Knowing that the detection statistics for both backends are practically the same, the next step is to compare their derived flux densities. Of course, only the scans on sources for which flux densities could be calculated for both backends can be compared (Table 4.1 third column).

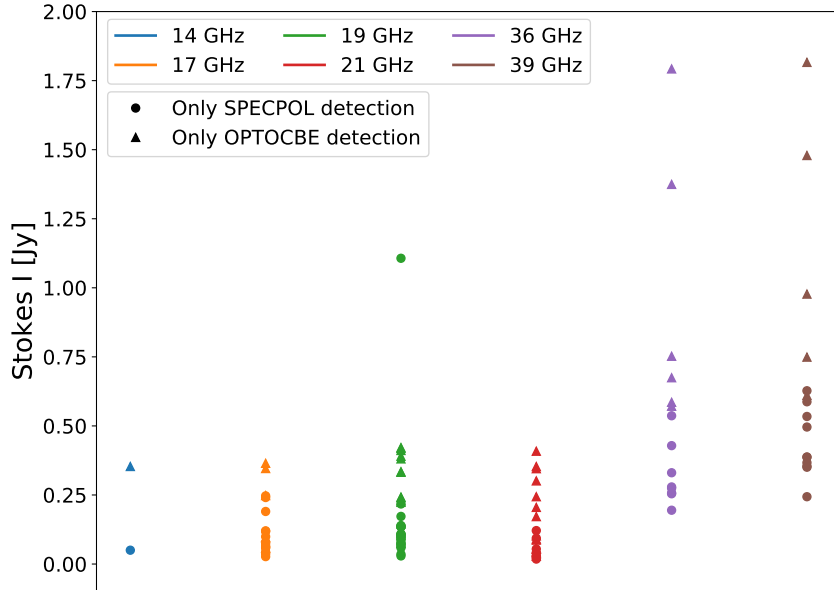


Figure 4.4: Flux densities of sources that were only detected by one backend. Shown are the fluxes measured by the respective other backend for the observation.

When doing this, the important information is the difference in the two flux densities and whether they coincide within their respective errors. In Fig. 4.1 on the top, all flux densities agree within their errors, but, of course, there are some minor differences in the exact values. On the contrary, scenario 2 in the middle shows one exception at 21 GHz, where a vast gap between the two values is apparent. For now, only the differences between the best fit values are considered, in order to do a statistical analysis of their distribution in the collected data. Doing this for all sources, dates and frequencies results in the distribution shown in Fig. 4.5. From this figure, several important conclusions can be drawn. First of all, a clearly visible peak occurs around a difference of 0, indicating a good agreement between the flux densities derived by the two backends. The vast majority of the differences lie in the range -0.1 Jy to 0.1 Jy (note the logarithmic scale of the y -axis) and nearly all lie in the range -0.2 Jy to 0.2 Jy with only a few outliers, signifying that very large differences only occur seldom. To get a better overview, Fig. 4.6 shows the difference distributions for the individual frequencies. In theory, assuming no systematic influences, a Gaussian distribution of the differences would be expected for each frequency. However, by eye, they do not seem to be normally distributed and generally they do not have a similar shape. While at 14 GHz, 17 GHz and 19 GHz the distributions are centered more around zero, for the higher frequencies the distributions are skewed more to positive differences. This means that for high frequencies, on average, the OPTOCBE flux is higher than the SPECPOL flux. Performing Shapiro-Wilk tests (Shapiro & Wilk, 1965) on the individual frequencies to see if they are normally distributed results in p -values < 0.01 , indicating that actually none of them are normally distributed. In an ideal case, again assuming no systematic effects, the distributions of the frequencies should be the same. Although, in reality, this does not hold, as the flux density errors are larger for higher frequencies and therefore, according to probability theory, the observed values are expected to vary by larger amounts. Nevertheless,

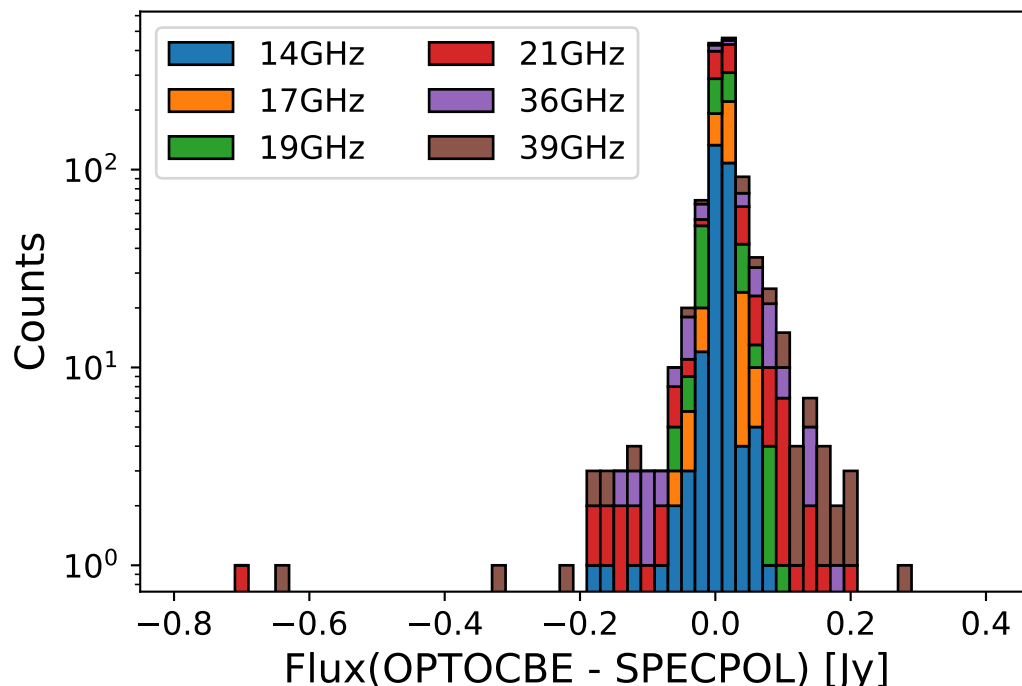


Figure 4.5: Differences in the flux densities derived using the two backends, considering only the best fit values.

the similarity of the distributions is tested by performing Kolmogorov–Smirnov tests (KS tests, e.g., Massey Jr, 1951) on the data. These tests are used to probe the agreement between two data sets, i.e., two distinct frequencies, with the underlying assumption that both distributions are drawn from the same parent population. Performing the KS tests on all possible combinations of frequencies results in p -values smaller than $p = 0.01$ for all combinations except 17GHz-21GHz, having $p = 0.14$. Therefore, excluding the one exception, the distributions are not the same, meaning that the differences between the two flux values behave differently for the individual frequencies.

A way to verify whether the found distributions are reasonable is by comparing the standard deviations of the distributions with the arithmetic mean flux density errors. This was done for the individual frequency distributions as well as for the entire distribution (Fig. 4.5) of only the best fit values. The results are presented in Table 4.2. As the mean errors and the standard deviations of the distributions are highly comparable, this suggests that the observed distributions are consistent with respect to the derived flux errors.

While the physically relevant property is the difference between the best fit values, it is worth to look at the coincidence of the values within their respective errors. For this thought, when the error bars of the OPTOCBE and SPEC POL fluxes overlap, their difference is set to zero, indicating that they are in agreement. In the other cases, the difference between the smallest and largest values compatible with their errors are used to calculate the „distance“ between the two flux densities. Doing this and plotting the results for the individual frequencies results in the distributions shown in Fig. 4.7 that has to be compared with Fig. 4.6. Including the error bars into the calculation clearly sharpens the peak around a difference of zero, indicating that most of the measured flux densities by the two backends are coincident within their errors.

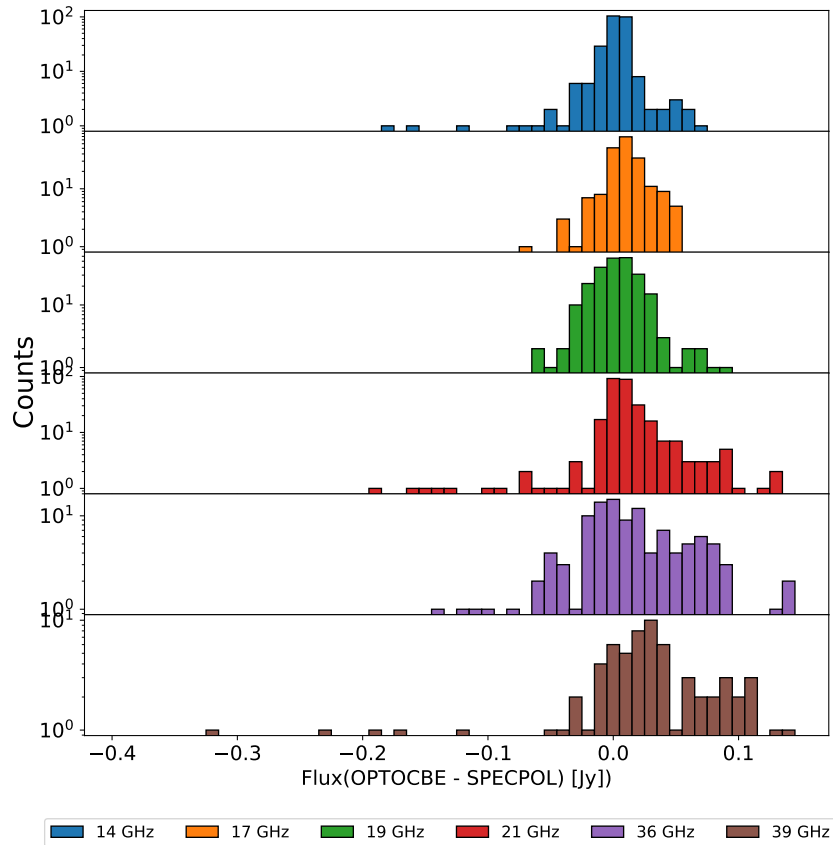


Figure 4.6: Differences in the flux densities derived using the two backends, divided into the individual frequencies for the best fit values only.

Frequency [GHz]	Standard deviation [Jy]	Mean error [Jy]
All	0.046	0.034
14	0.023	0.014
17	0.016	0.021
19	0.020	0.029
21	0.055	0.034
36	0.051	0.067
39	0.117	0.093

Table 4.2: Given are the standard deviations and the arithmetic mean flux density errors for the difference distributions shown in Fig. 4.6.

Performing KS tests to check for similarities between the individual distributions now results in p -values no smaller than $p = 0.18$. Therefore, the null-hypothesis of the distributions being the same cannot be rejected. This also shows that, when including the errors, the differences between the two flux values behave similarly, as expected.

Plotting the OPTOCBE versus the SPECPOL flux densities gives another way of checking for

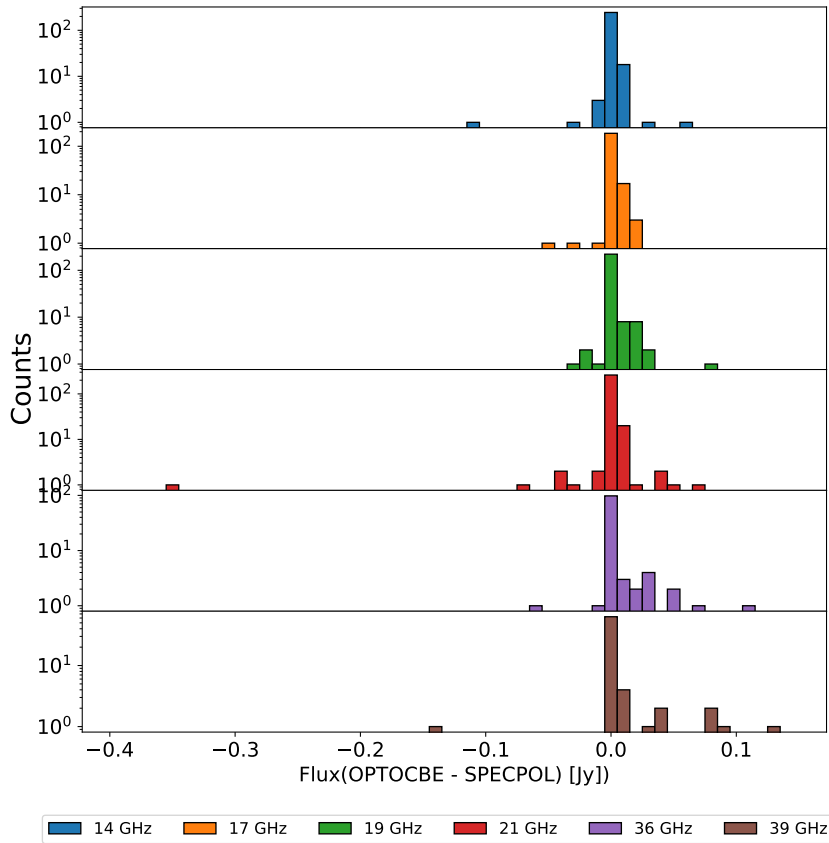


Figure 4.7: Differences in the flux densities derived using the two backends, divided into the individual frequencies. In comparison to Fig. 4.6, the error bars of the flux densities are also taken into account. When they overlap, the difference is set to 0.

differences between the two backends. In an ideal case, the slope m of a linear fit of the form

$$y = mx + t \quad (4.1)$$

to the data would be $m = 1$, marking no difference between them. A physically motivated boundary condition is to set $t = 0$. This is a sensible condition for two reasons. First, the fluxes are expected to be the same for both backends, meaning that no systematic differences should occur between them, reducing the problem to $y = x$. Additionally, when no source is observed, both backends cannot detect a source and $y(0) = 0$ is forced. In Fig. 4.8, this scatter plot is shown and the results of the fit, using `scipy.optimize.curve_fit`, are given in the legend. Although the slopes are all very close to 1, only the 36 GHz and 39 GHz values are coincident with the optimal case within one standard deviation. However, performing χ^2 -tests on the data indicate that they are well described by the fits, as the p -values are all similar to 1. Also, the performed KS tests to check whether the ideal case $y = x$ and the real case $y = m_{\text{fit}}x$ come from the same parent population all result in p -values greater than 0.998 and therefore the null-hypothesis cannot be ruled out. In other words, it is likely that the observed fit values might only be due to the limited sample size.

Overall, the agreement between OPTOCBE and SPEC POL fluxes is therefore very good and the minor differences can probably be explained by statistical effects as well as the slightly different center wavelengths and frequency ranges.

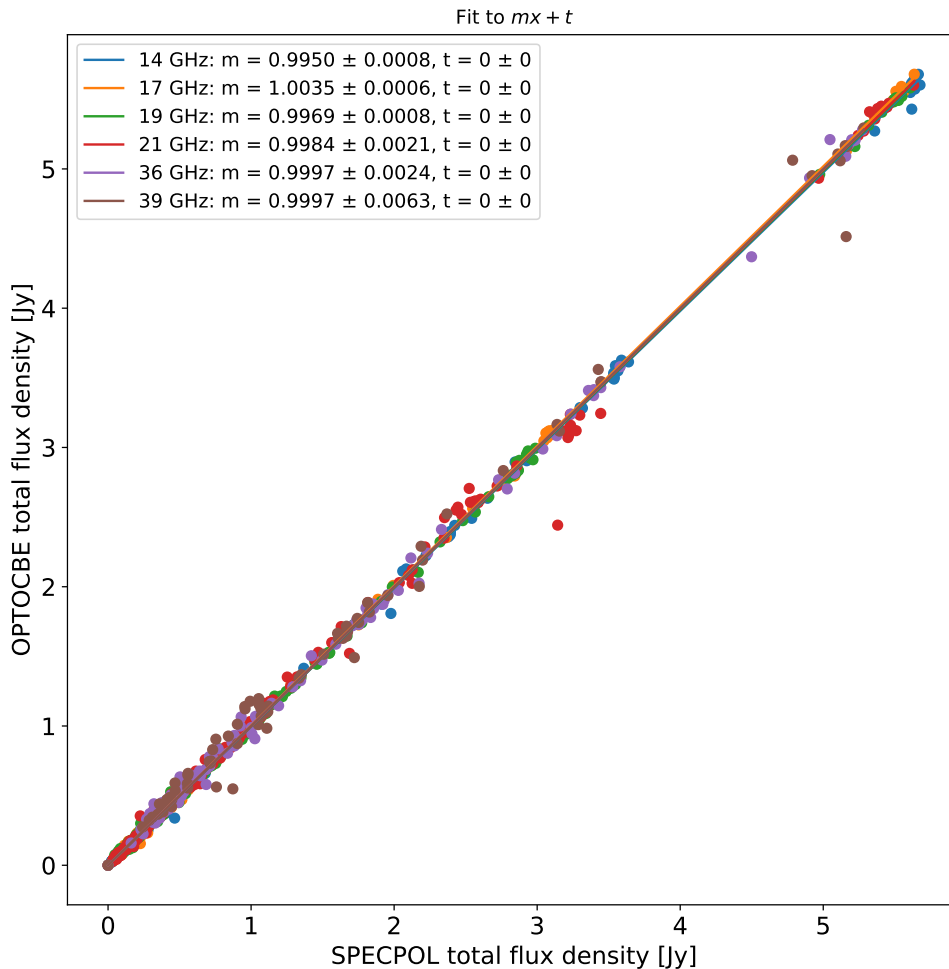


Figure 4.8: Scatter plot of OPTOCBE and SPECPOL fluxes. The legend gives the fit results to a linear function of the form $y = mx + t$.

A last comparison drawn between the OPTOCBE and SPECPOL in this thesis is the signal-to-noise ratio (SNR) that the two backends exhibit. Here, the SNR is defined as

$$\text{SNR} = \frac{S}{\sigma}, \quad (4.2)$$

the ratio of signal S to noise σ , i.e., the error of the respective flux density, as defined in Eq. 3.11, and is therefore the inverse of the relative error of the measurement. The SNR distributions of the different frequencies are plotted in histograms, depicted in Fig. 4.9. It was already shown in Table 4.1 that the backends did not detect the same amount of scans, which is why there are slightly different amounts of SNR values in these plots. However, the numbers are still very similar, making the comparison between the backends possible. By eye, only the 20 mm and 14 mm SNR distributions look different, while the 7 mm distributions appear to be quite similar. To check this assumption, KS tests were performed on the signal-to-noise ratios for the individual frequencies. It turns out that for 14 GHz, 17 GHz, 19 GHz and 21 GHz, the null

hypothesis of the two distributions being the same can be rejected on a 5% significance level with p -values of $p = 2 \times 10^{-18}$, $p = 0.014$, $p = 0.0019$ and $p = 1 \times 10^{-9}$, respectively. On the contrary, the null hypothesis cannot be rejected for 36 GHz and 39 GHz, as the respective p -values are $p = 0.071$ and $p = 0.74$, as the visual impression already suggested. While the

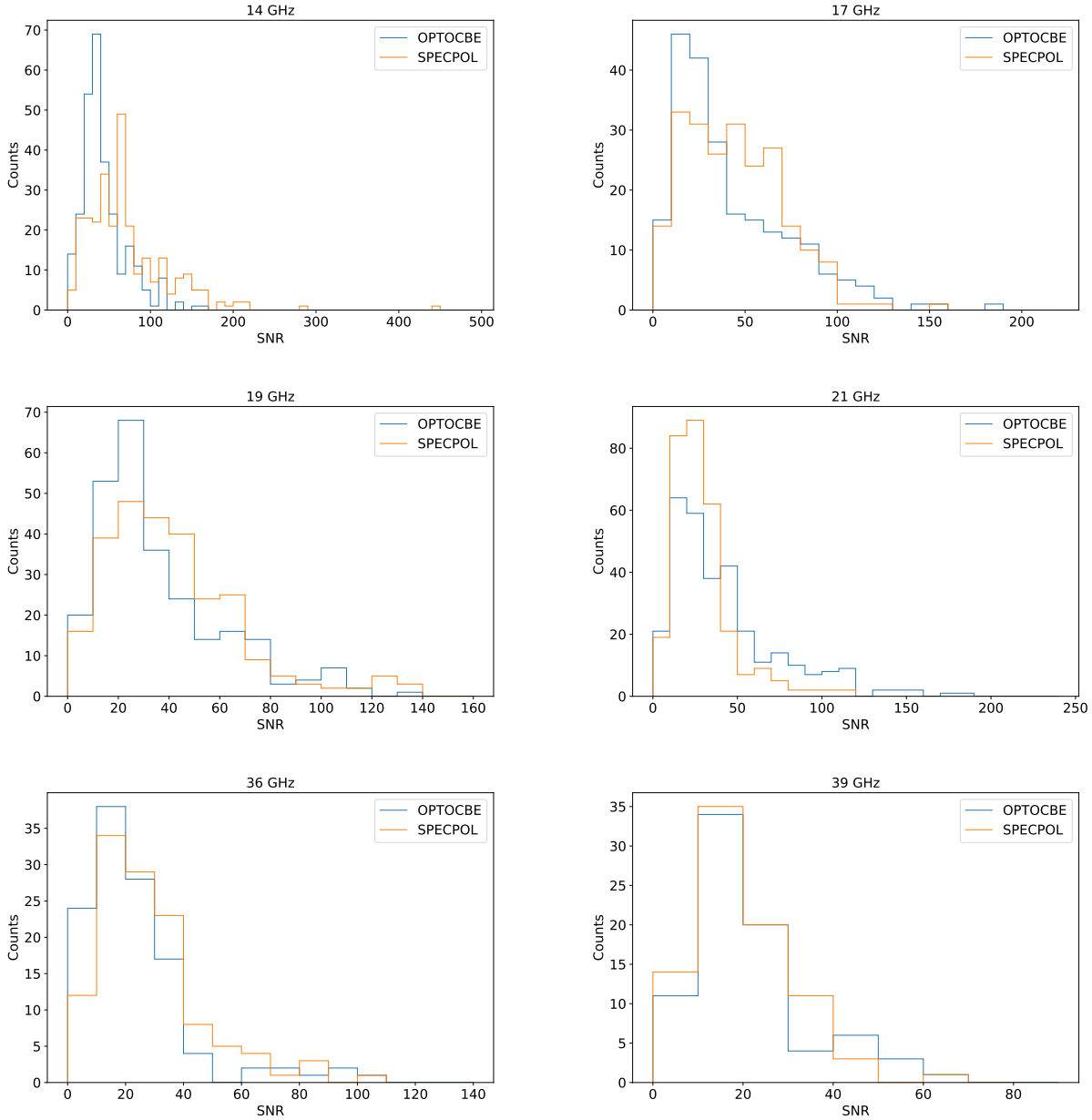


Figure 4.9: Signal-to-noise ratios (SNR) of the two backends for all frequencies. SNRs were calculated for all sources and scans that were detected by at least one backend.

shape of the distributions are different, this does not necessarily infer that the mean SNRs are actually different. In Table 4.3, the mean and median SNRs of the individual frequencies for both backends are shown. Here it becomes obvious that the SNRs of the two backends are approximately similar, with two exceptions in the form of the 14 GHz and 21 GHz data. While the SPECPOL SNR is higher by a factor $\sim \sqrt{2}$ at 14 GHz, for 21 GHz it is lower by approximately the same factor. Reasons for this could be manifold and have to be further investigated in the future.

Frequency [GHz]	Backend	Mean SNR	Median SNR
14	SPECPOL	73	63
14	OPTOCBE	44	36
17	SPECPOL	45	42
17	OPTOCBE	44	33
19	SPECPOL	42	35
19	OPTOCBE	37	28
21	SPECPOL	29	23
21	OPTOCBE	43	35
36	SPECPOL	30	25
36	OPTOCBE	25	20
39	SPECPOL	21	17
39	OPTOCBE	23	19

Table 4.3: Mean and median values of the SNR distributions for all frequencies and both backends.

Nevertheless, overall it can be said that, while there are some minor differences between the backends, the general results agree well in the vast majority of all cases. Since their SNRs are comparable, this also means that the relative errors for the measurements are nearly the same. This is a very important finding as it suggests that both backends, regardless if the second horn is subtracted or not, yield comparable results. Here it has to be stressed that this outcome is probably highly dependent on the fact that TELAMON observations are generally conducted under „good“ weather conditions where the subtraction of the weather effects does not have a significant impact, as shown in this section. A statistical study of this effect should be performed once more „bad weather data“ are available.

All in all, it is therefore possible to interchange the derived flux densities of the two backends and use the value from the other backend in cases where one of the two did not detect a source.

4.2 Polarization Data

After the SPECPOL flux densities were juxtaposed with the OPTOCBE values and a generally good agreement was found, it is now time to investigate the derived polarization data. This is done for all epochs indicated by a „Y“ in the second column of Table 3.2 and for all possible frequencies. Here it is very important to note that technical problems have so far prevented the measurement of meaningful polarization data with the 14 mm receiver. The exact problem is not known, but it could potentially be due to erroneous phase referencing in the receiver so that the measured Stokes Q and U values are not what they should be². In the previous section the 14 mm values could be used, because the Stokes I flux does not suffer from this problem. Also, the other two receivers are not affected by this problem, so the analysis of the polarization data is limited to the 20 mm and 7 mm receivers at 14 GHz and 17 GHz as well as 36 GHz and 39 GHz, respectively.

4.2.1 General Results

Before diving into the polarization data, like the distribution of linear polarization or EVPAs, the properties of the Müller matrix elements and the derived instrumental effects are further investigated.

4.2.1.1 Müller Matrix and Instrumental Properties

For an ideal instrument, the Müller matrix introduced in Eq. 2.49 would be the identity matrix, as the polarization characteristics of the wave are not altered by it. Realistic measurement conditions, however, do not follow this simple case. Rather, all off-diagonal elements take some other values than 0 and even the diagonal elements are not equal to 1. Changing weather conditions or changes to the backend itself can cause the matrix elements to be different for distinct observations. Nevertheless, they should still be in a realistic realm of values. For this work, a Müller matrix was accepted if the absolute values of its individual elements were $\lesssim 10$, although this constrained is tightened for some elements. Also, the associated errors were checked and matrices with epochs with unrealistic errors were excluded from the analysis.

The evolution of the Müller matrix elements is exemplary shown in Fig. 4.10 for the 14 GHz data. The development of the other three frequencies is shown in Appendix B. Overall, the elements appear to be stable, with a few outliers that do not necessarily belong to the same epoch. Using the shown elements, it is possible to calculate an average Müller matrix that describes the behavior of the used 14 GHz receiver. This matrix is found to be

$$\mathcal{M}_{14\text{GHz}} = \begin{pmatrix} 2.5656 \pm 0.0060 & 0.17 \pm 0.10 & 0.63 \pm 0.20 \\ 0.00331 \pm 0.00033 & -0.8887 \pm 0.0057 & 3.736 \pm 0.017 \\ 0.00136 \pm 0.00036 & -4.509 \pm 0.011 & 0.453 \pm 0.026 \end{pmatrix}.$$

Again, the average Müller matrices from the other frequencies are given in Appendix B. These matrices are an important by-product of the analysis, as they can, in theory, be applied to observational data with „bad“ Müller matrices or epochs in which not enough calibrators were observed, to still recover polarimetric data of the observed sources. However, this was not done in this thesis, as the method has to be validated first by applying the average matrices to „good“ data and then checking if the results are in an acceptable range around the original results.

²Alex Kraus, priv. comm.

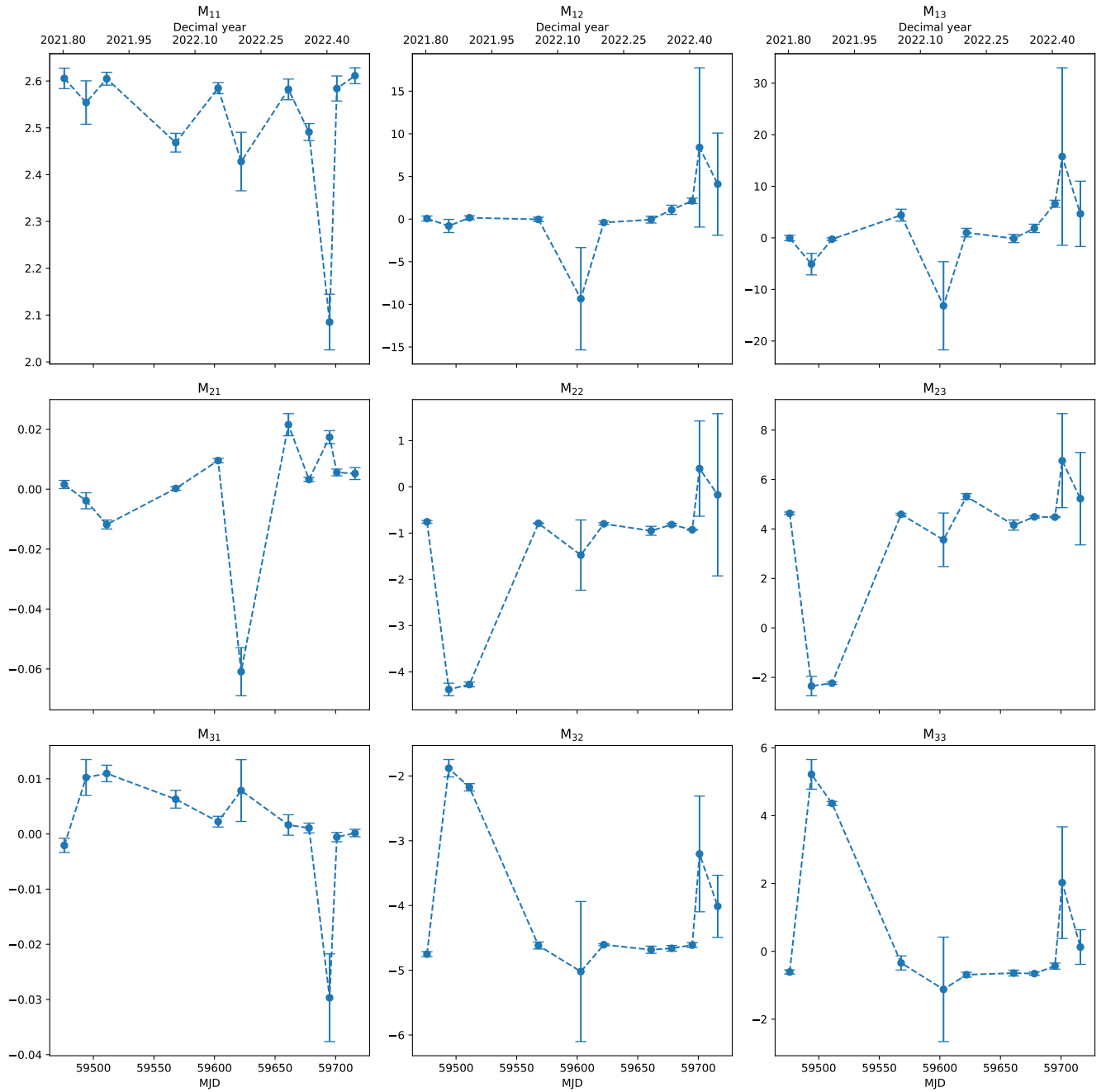


Figure 4.10: Evolution of the 14 GHz Müller matrix elements throughout all observations carried out in the framework of this thesis that are marked with „Y“ in Table 3.2.

From Fig. 4.10 and the average Müller matrix, the relatively large variation in the elements M_{12} and M_{13} stands out, leading to a depolarization as defined in Eq. 2.52. Although the polarized flux should not have a huge influence on the total intensity due to its relative weakness, for a large depolarization the effect becomes noticeable. Figure 4.11 shows the evolution of the depolarization across all used observations and frequencies. Here it becomes clear why it is

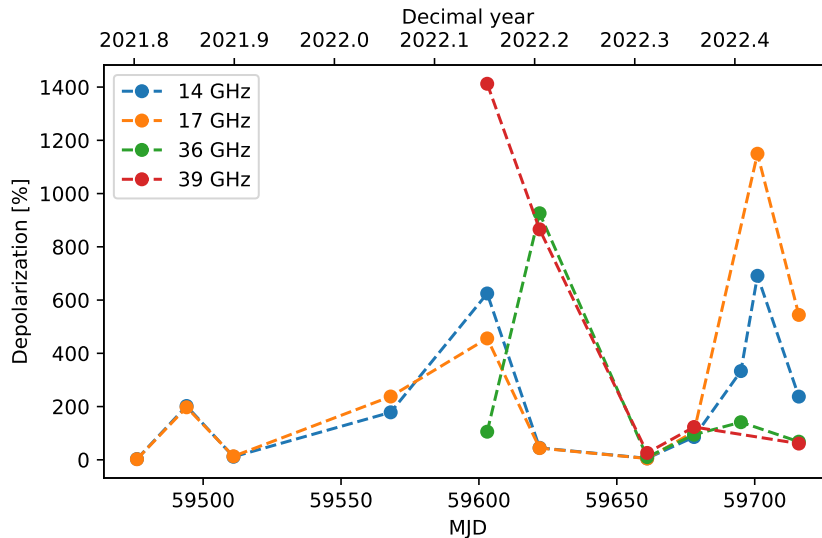


Figure 4.11: Evolution of the depolarization of the frequencies, defined via Eq. 2.52.

reasonable to not perform the Stokes I correction, as explained in Sect. 3.4.

On the other hand, the instrumental polarization (Eq. 2.51) has to be low in order for the data to make sense, since the overflow of total to polarized intensity is way more significant. For the used data it was made sure that the instrumental polarization is low, i.e., $\lesssim 1\%$, for all epochs, although outliers that are not too far from this value and show an overall sensible Müller matrix are permitted as well. As can be seen in Fig. 4.12, this is in fact the case, with most values being below 1%. One exception is formed by the 17 GHz data that exhibits an instrumental polarization of $\sim 1.5\%$, however, since it is nearly constant, this does not appear to be a problem. The increase of the instrumental polarization in the one epoch in February seems odd, however, upon further investigation of the Müller matrices, no major outliers could be identified and therefore the epoch was not excluded. The position angle of the spurious linear polarization introduced by the instrument is given by Eq. 2.53 and evolves as shown in Fig. 4.13. It changes, in the most extreme case, by up to 80° between two epochs and generally is not as stable as the instrumental polarization. For unpolarized sources, this angle is, together with a time-dependent rotation, inscribed into their EVPAs, as their intrinsic position angle is 0° .

4.2.1.2 Polarization Distribution

The data reduction procedure introduced in Sect. 2.5 and Sect. 3.4 was applied to all available scans for all dates where polarization data was taken (see Table 3.2). In the following, only sources are analyzed that are considered to be significantly polarized, where „significant polarization“ is defined to mean $p_{\text{lin}} > 2\sigma_{p_{\text{lin}}}$.

Out of a total of 87 observed sample sources at 20 mm and 7 mm, 46 were found to be significantly polarized at least once at one frequency. These sources can be found in Table A.1 in

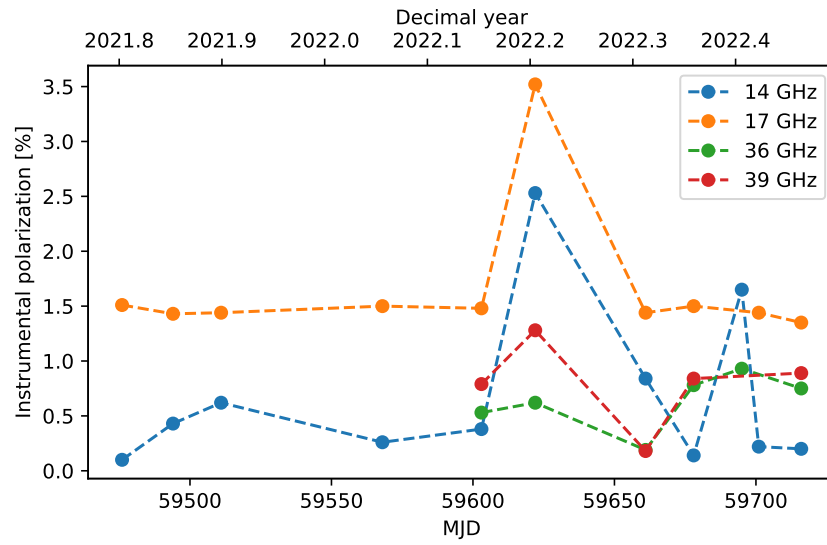


Figure 4.12: Evolution of the instrumental polarization (Eq. 2.51) for all used epochs and frequencies.

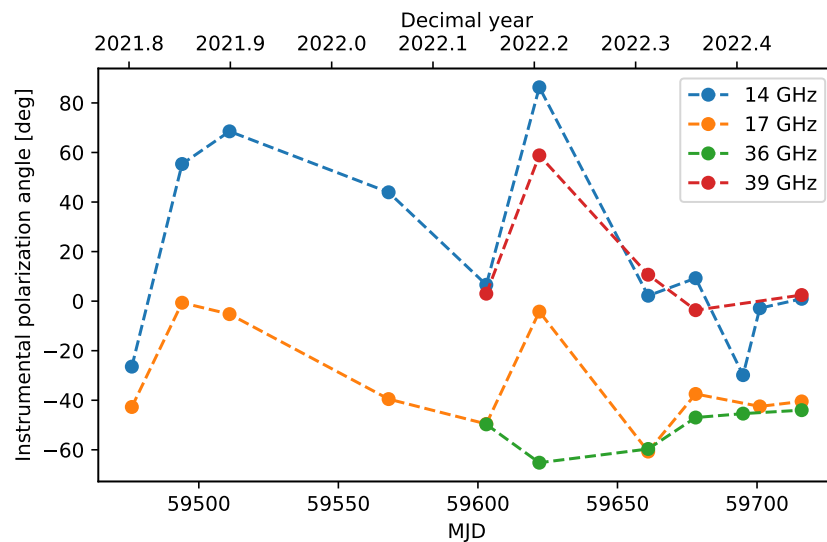


Figure 4.13: Evolution of the instrumental polarization angle, given by Eq. 2.53, throughout all used epochs and frequencies.

Appendix A, where the names of the sources and their detection status for Stokes I and polarization are given. For sources that were detected to be polarized more than once, in this section, their weighted mean is used. Here, an overview of all frequencies is given. In Appendix C, the individual frequency distributions of all presented plots are shown.

Figure 4.14 shows the distribution of the polarized fluxes in the sample, as defined by Eq. 2.40. At 14 GHz and 17 GHz, the largest amount of sources do exhibit a linearly polarized flux den-

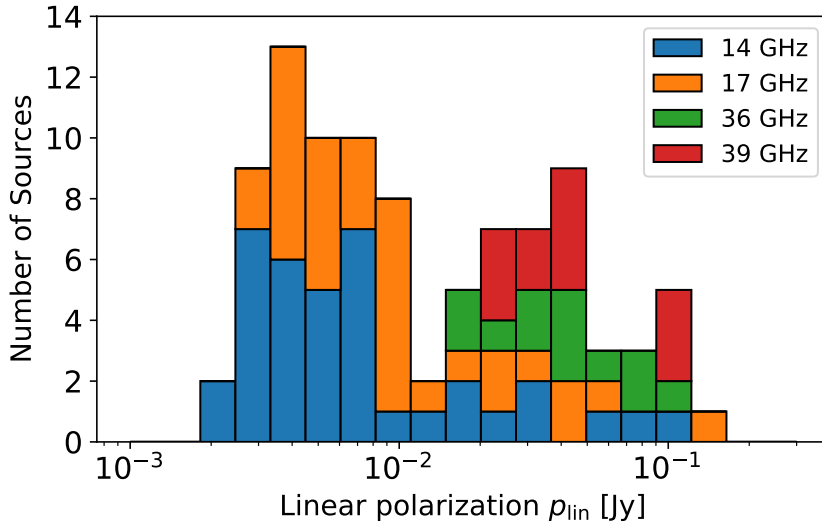


Figure 4.14: Distribution of the linearly polarized flux p_{lin} for all frequencies and all sources considered to be polarized in at least one epoch. Note the logarithmic scaling of the x-axis.

sity $0.002 \text{ Jy} \lesssim p_{\text{lin}} \lesssim 0.01 \text{ Jy}$, while at 36 GHz and 39 GHz a higher polarized flux density is observed with $0.02 \text{ Jy} \lesssim p_{\text{lin}} \lesssim 0.1 \text{ Jy}$. While this seems like a clear dichotomy, it has to be noted that the sources observed at the two wavelengths are not necessarily the same. Actually, there are only 6 sources in the sample that are polarized at more than two frequencies, i.e., at 20 mm as well as at 7 mm. These sources are, with one exception, neutrino-candidate blazars that were included in TELAMON to monitor their flux density evolution around the detection of the neutrino. Typically, sources that are well-detected at 7 mm are not observed at 20 mm in the „regular“ TeV-sample of TELAMON, but these sources make a comparison between the two wavelength bands possible.

To compare, the distribution of Stokes I flux is given in Fig. 4.15. From the figure it is clearly visible that most sources are weaker than 0.3 Jy at the 20 mm frequencies. Assuming a high fractional polarization of 10%, the linear polarization p_{lin} for these sources is lower than 0.03 Jy , which is exactly what Fig. 4.14 suggests.

Using the total intensity I and the linear polarization p_{lin} of a source, the fractional polarization m_l , as defined in Eq. 2.41, can be calculated. The histogram plot of this distribution is presented in Fig. 4.16. Here, the majority of all sources shows a fractional polarization of less than 5%, matching with the expectation of rather low polarizations in these sources (e.g., Tabara & Inoue, 1980). Both at 20 mm and 7 mm, some sources are clearly above this value, with the most extreme case exceeding 10% polarization. Additionally, a higher polarization for the higher frequencies seems to be apparent. As argued by Agudo et al. (2014), this could be explained by a better ordering of the magnetic field closer to the SMBH, where the high frequency emission is expected to be coming from.

As an artifact of the applied Müller formalism (Eq. 3.19), intrinsically unpolarized sources can

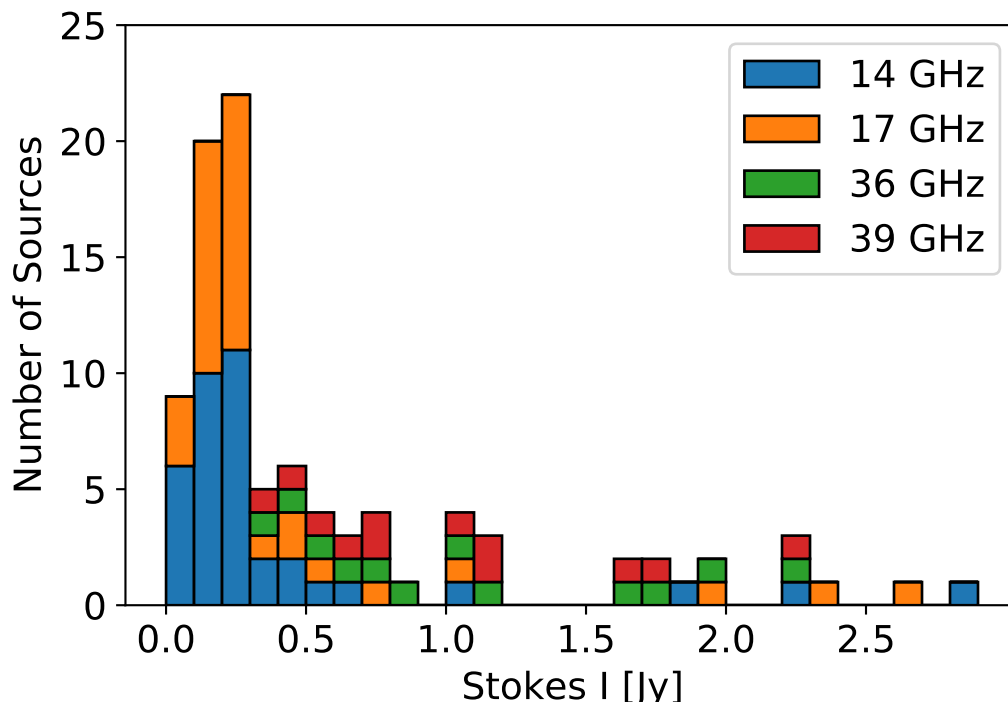


Figure 4.15: Distribution of the total intensity I for all frequencies and all sources considered to be polarized in at least one epoch.

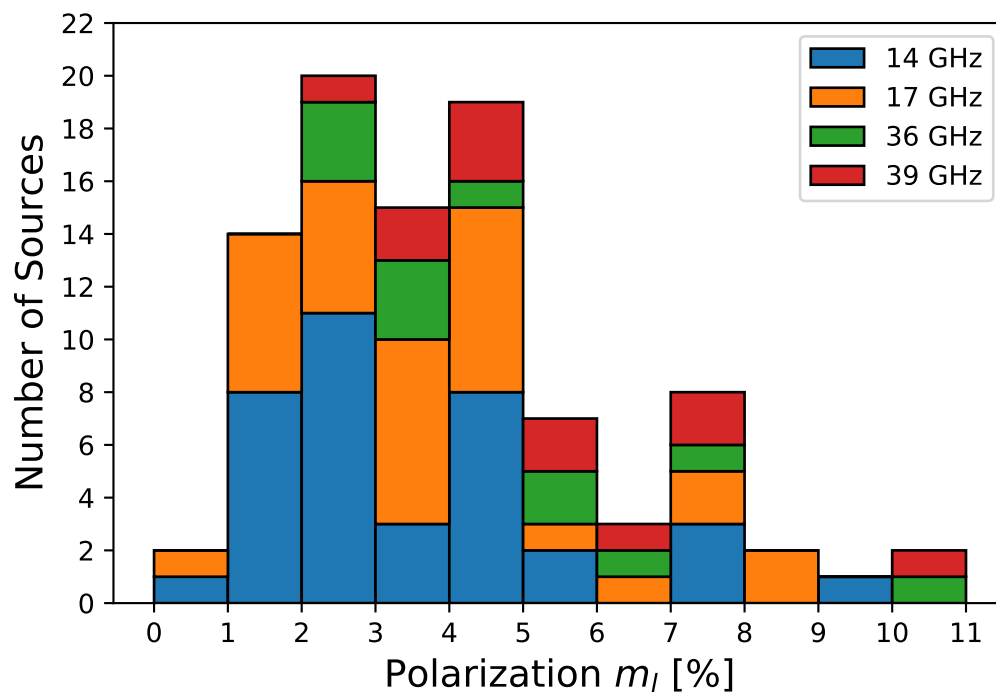


Figure 4.16: Distribution of the fractional polarization m_l for all frequencies and all sources considered to be polarized in at least one epoch.

appear to be polarized in some cases, especially for bright sources. A prime example for this is the ~ 5 Jy bright source NGC 7027 that is assumed to not be polarized. However, in reality, the source is found to have a spurious polarization degree of $m_l \sim 0.2\%$ in several epochs that would be considered significant, as by the definition state in the beginning of the section. Since there are only 2 data points in the $0-1\%$ m_l -bin and NGC 7027 is the brightest source analyzed in this thesis, it can be assumed that the spurious polarization for all other sources is way lower. In such cases, the polarization detection would most likely not be significant anymore.

The electric vector position angles χ (Eq. 2.42) associated with the polarized signal are best displayed in a polar plot. This is done in Fig. 4.17, where the different radii of the frequencies have no physical meaning, but are rather to make the plot clearer. All EVPAs are distributed in a $\sim 180^\circ$ range, showing the $n\pi$ ambiguity of the EVPA. Some values were manually rotated in order to minimize EVPA jumps between epochs.

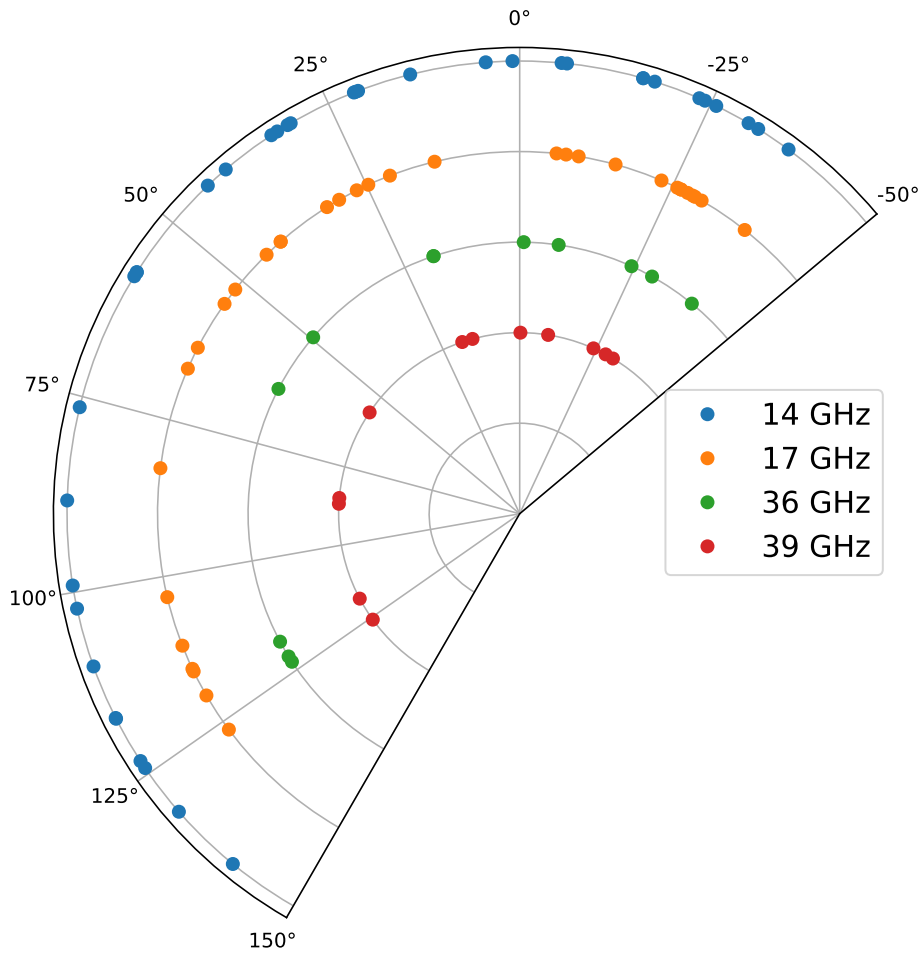


Figure 4.17: Polar plot of the distribution of EVPAs χ for all frequencies and all sources considered to be polarized in at least one epoch. The 180° ambiguity of the EVPA is clearly identifiable. Some EVPA values were manually rotated in order to decrease jumps between epochs. The different radii of the frequencies are purely cosmetic, to make the identification easier.

4.2.2 Some Selected Results

In this section, some sources of special interest are further investigated. To do this, special overview-plots were created, showing the Stokes I and linearly polarized flux p_{lin} , the fractional polarization m_l and the EVPA χ all at once. The sources are named according to their common name, while in parenthesis their J2000 name is given (see also Table A.1). Since it was shown in Sect. 4.1 that the results of OPTOCBE and SPECPOL backends are very similar, OPTOCBE total flux densities are plotted wherever available. In epochs or frequencies where the OPTOCBE did not detect a source, the SPECPOL flux densities are plotted instead to fill in the gaps. This has the huge advantage that the total intensity evolution can be characterized better, as way more epochs are available where the no polarization data were taken (see Table 3.2 column 2). To keep the consistency and also the clarity, only frequencies where the source was detected to be polarized at least once are plotted.

While only a few overview-plots are displayed here in this section, the overview-plots for all other sources are shown in Appendix D. The averaged polarization quantities of all sources and frequencies shown in the overview-plots are given in Table D.1 in the same appendix.

4.2.2.1 TXS 0215+015

TXS 0215+015 is a known γ -ray source in the 4FGL-DR3 catalog (Abdollahi et al., 2022) that was in an elevated γ -ray state with a flux seven times higher than its average flux at the time of the IceCube event IC220225A, as reported by Garrappa et al. (2022). Triggered by this, several observations at different wavelengths in the radio (Kadler et al., 2022; Plavin et al., 2022) and the optical (Nesci, 2022) were conducted on this source, all revealing a major flare. Two days after the neutrino event, TELAMON observations³ revealed an intriguing spectrum that could be interpreted in the shock-in-jet model (Marscher & Gear, 1985), where the shock had already moved outward of the 7 mm emission region but still dominated at the lower frequencies.

In Fig. 4.18, the source properties at the initial and all further observations are shown. The vertical black dashed line indicates the time of the neutrino event. Since then, its total flux density has been decreasing more or less continuously by ~ 1 Jy at all frequencies. During the third observation of the source, its polarization state seemed to be elevated at all frequencies, then it decreased by a factor of ~ 3 in the next epoch. Sadly, the two observations before this polarization flare did not take meaningful polarization data, therefore the flare cannot be confirmed as of now. In the future, when the average Müller matrix method of recovering polarization data for epochs with „bad“ Müller matrices or not enough calibrators is cross-checked and usable, the two earlier epochs can be investigated and the polarization state can be derived.

If the flare is found to be real and longer than one epoch, this would be an interesting case, as other studies, such as MOJAVE (Lister et al., 2018), that have been monitoring this source for a long time, have not found such a large polarization flare. At 15 GHz, MOJAVE find a historically maximal linear polarization of $p_{\text{lin}} \sim 0.09$ Jy with a maximum fractional polarization of $m_l = 4\%$ for TXS 0215+015⁴. TELAMON data near this frequency, on the other hand, show a linear polarization of $p_{\text{lin}} \sim 0.2$ Jy with $m_l \sim 6\%$. Of course, it has to be noted that MOJAVE observations are performed using Very Long Baseline Interferometry (VLBI), i.e., an imaging technique using multiple telescopes that act as one large telescope. Therefore, the beam of this telescope is different from the one of a single-dish telescope such as Effelsberg and different

³<http://telamon.astro.uni-wuerzburg.de/sources/0217-0144>

⁴<https://www.physics.purdue.edu/astro/MOJAVE/sourcepages/0215+015.shtml>

length-scales are probed, potentially leading to depolarization or Faraday-rotation, as explained in Sect. 2.4. A routine MOJAVE observation on this source was performed in early January, shortly before the IceCube event, showing a high flux state slightly below the TELAMON flux state, yet no signs of a polarization flare but rather a historical low state. Interestingly, both MOJAVE and TELAMON find the same EVPA⁵ of -30° . Another observation was performed in early April shortly after the neutrino event, but the results have not been published as of June 2022.

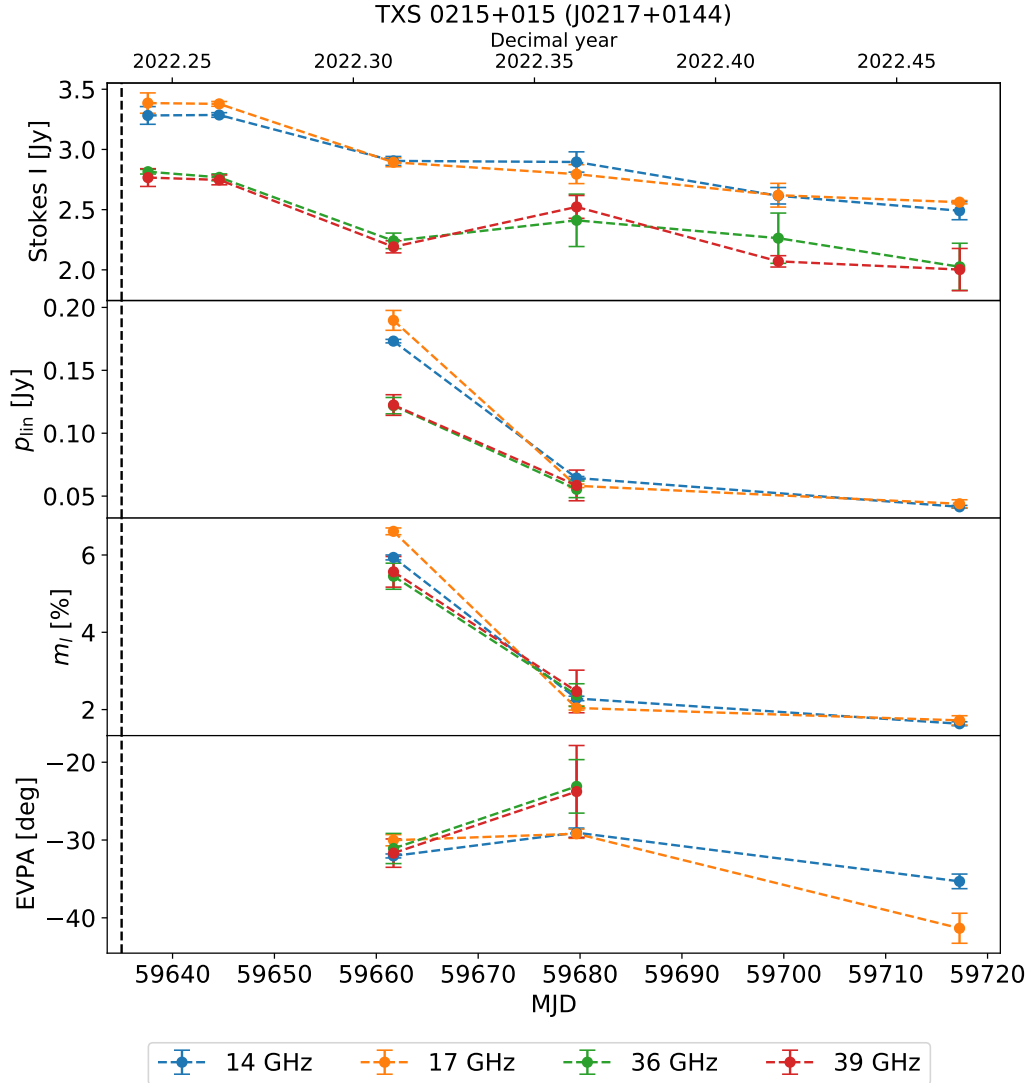


Figure 4.18: Overview-plot of TXS 0215+015 (J0217+0144). Shown are the total Stokes I flux density (top), the linear polarization p_{lin} (second from the top), the fractional polarization m_l (third from the top) and the EVPA χ (bottom) TELAMON lightcurves of the source. The vertical black dashed line marks the time of the neutrino event. Since the beginning of the TELAMON observations, the source decreased by ~ 1 Jy in total flux density. In the third epoch, signs of a potential polarization flare can be seen.

⁵MOJAVE states the EVPA as 150° , but due to the $n\pi$ ambiguity, this can be rotated to be -30° .

4.2.2.2 PG 1553+113

This HBL object shows quasi-periodic γ -ray emission with a period of ~ 2.2 yr (Ackermann et al., 2015). Lico et al. (2020) found that this periodicity can, in parts, be explained by a wobbling of the jet. They observed PG 1553+113 roughly every two months over two years between 2015 and 2017 with the Very Long Baseline Array, extracting total and linearly polarized intensity values. At 15 GHz, they find the total intensity flux to vary between 120 – 200 mJy, while single-dish observations supplied by the Owens Valley Radio Observatory monitoring program show higher fluxes between 200 – 300 mJy in the same time period. At the same frequency, they find average polarization values of $p_{\text{lin}} = 2.6$ mJy and an average fractional polarization of 1.7%. The latter is approximately consistent with the results found in this work, as Lico et al. (2020) state that the fractional polarization varies between 0.7 – 3.1%, which is also seen in Fig. 4.19. However, TELAMON data reveal a higher Stokes I and polarized flux density than found by Lico et al. (2020). Nevertheless, both studies show signs of EVPA variability over the duration of the monitoring. As the position angle of the jet axis in this source is $\sim 50^\circ$ (Lico et al., 2020), both studies find EVPAs that are roughly transverse and parallel to this axis. In the TELAMON data, this change happened in ~ 3 months. Here, the total and polarized intensity also show signs of achromatic variability.

As was shown by Blinov et al. (2015) and Blinov et al. (2016), this source can exhibit EVPA changes of more than 100° in time-scales of ~ 100 days at optical wavelengths.

PG 1553+113 was also observed five times in the framework of Myserlis (2015) with the Effelsberg 100 m telescope at slightly lower frequencies than in TELAMON, where it was not found to be polarized, but also showed a lower total intensity flux density. It has to be noted that the criteria for significant polarization are defined more strictly in the work of Myserlis (2015).

This source is a promising candidate for long-term monitoring to see if the radio emission follows the periodicity of the γ -emission and how the polarization behaves during the flux evolution.

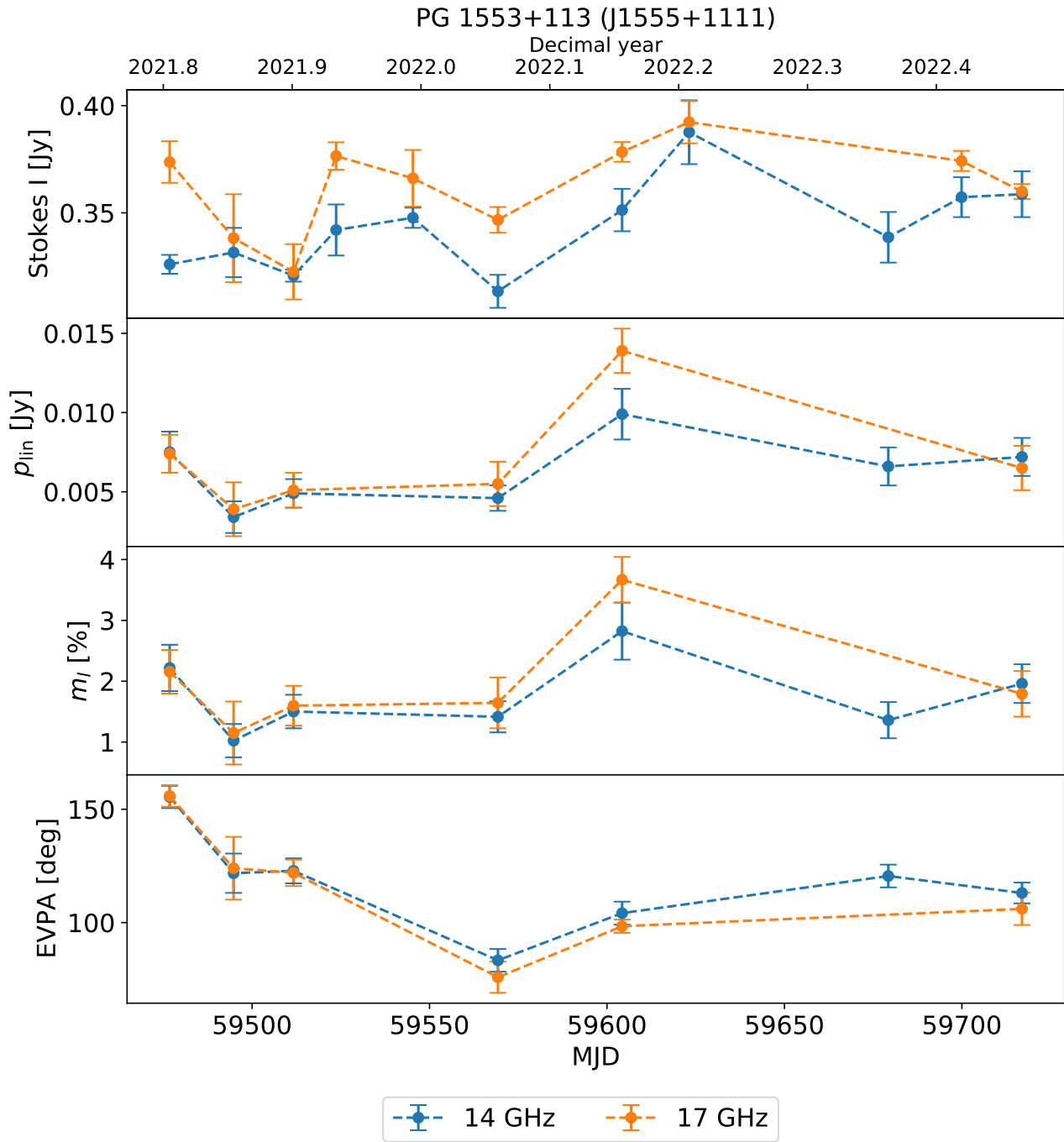


Figure 4.19: Overview-plot of PG 1553+113 (J1555+1111). Shown are the total Stokes I flux density (top), the linear polarization p_{lin} (second from the top), the fractional polarization m_l (third from the top) and the EVPA χ (bottom) TELAMON lightcurves of the source.

4.2.2.3 PKS 0735+17

This γ -ray bright source is one of the brightest blazars in the radio sky in the 5th Roma-BZCat catalog (Massaro et al., 2015). Recently, in December 2021, the source was found to be in spatial coincidence with four different neutrino detections by the IceCube, KM3NeT, Baikal and Baksan neutrino detectors. Sahakyan et al. (2022) collected all available near-simultaneous data of the largest flare of the source since at least 2008⁶. According to Sahakyan et al. (2022), PKS 0735+17 is a very promising neutrino source candidate, as it has very similar properties as other likely neutrino sources candidates such as the famous TXS 0506+056 (Padovani et al., 2018). For more information, it is referred to the original paper by Sahakyan et al. (2022). TELAMON first observed the source on the day of the IceCube neutrino alert and a few times after that⁷. The overview-plot of PKS 0735+17 is shown in Fig. 4.20. Its Stokes I flux density

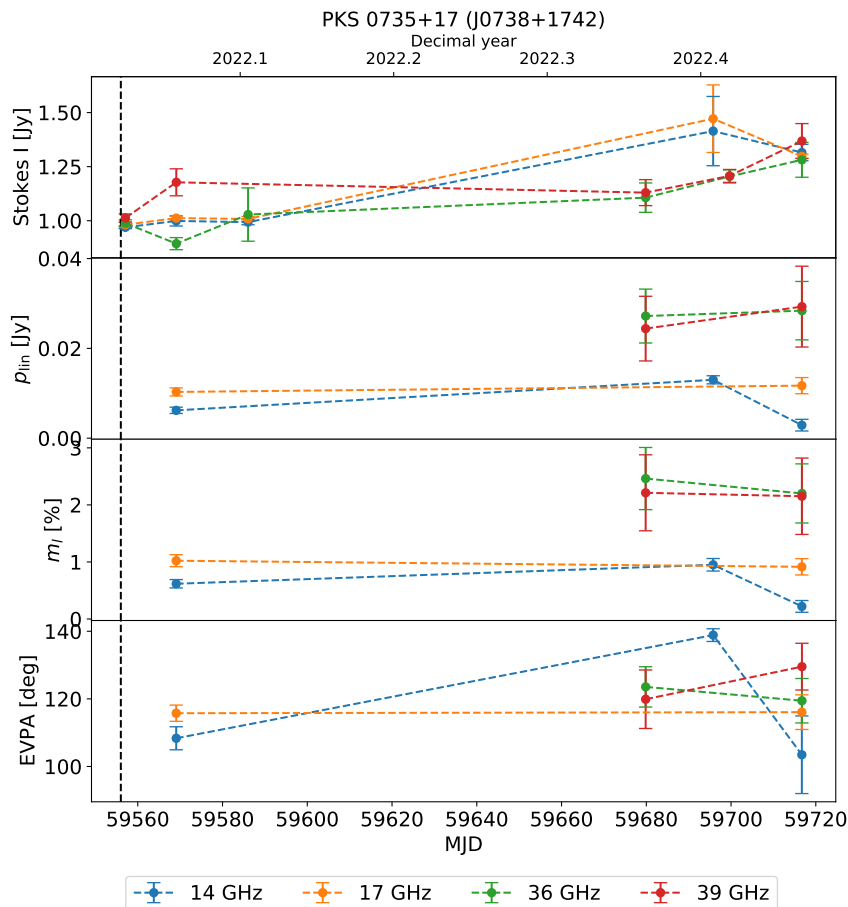


Figure 4.20: Overview-plot of PKS 0738+17 (J0738+1742). Shown are the total Stokes I flux density (top), the linear polarization p_{lin} (second from the top), the fractional polarization m_l (third from the top) and the EVPA χ (bottom) TELAMON lightcurves of the source. The vertical black dashed line indicates the time of the neutrino event IC211208A that this source is associated with.

increases by ~ 0.25 Jy after the initial observation at all four frequencies, while the polarized flux density only increases marginally. With that, the fractional polarization stays approximately

⁶In 2008, the *Fermi*-satellite was launched and they only consider data taken after this point.

⁷See <http://telamon.astro.uni-wuerzburg.de/sources/0738-1742>

constant with values of $m_l \sim 1\%$ at 20 mm and $m_l \sim 2\%$ at 7 mm. Especially in the 20 mm band, this is one of the lowest fractional polarizations in the sample.

4.2.2.4 PKS 1725+123

This source is associated with the IceCube event IC 201021A⁸ and was in an enhanced state shortly after the neutrino detection, as shown by Nanci et al. (2022), making it yet another promising neutrino source candidate. As it was originally included into the TELAMON sample in July 2021⁹, two observations were conducted on the source before the beginning of the data taking process of this thesis. Since then, its fractional polarization increased continuously from $m_l \sim 7\%$ to $m_l \sim 10\%$ in the 20 mm band, see Fig. 4.21. At 36 GHz, the situation seems to be reversed, as the fractional polarization decreases from $m_l \sim 9\%$ to $m_l \sim 6\%$ over a shorter period of time. Simultaneously, its Stokes I flux decreases steadily, while its polarized flux density p_{lin} stays relatively constant at 20 mm and slightly decreases at 36 GHz, leading to the observed m_l evolution.

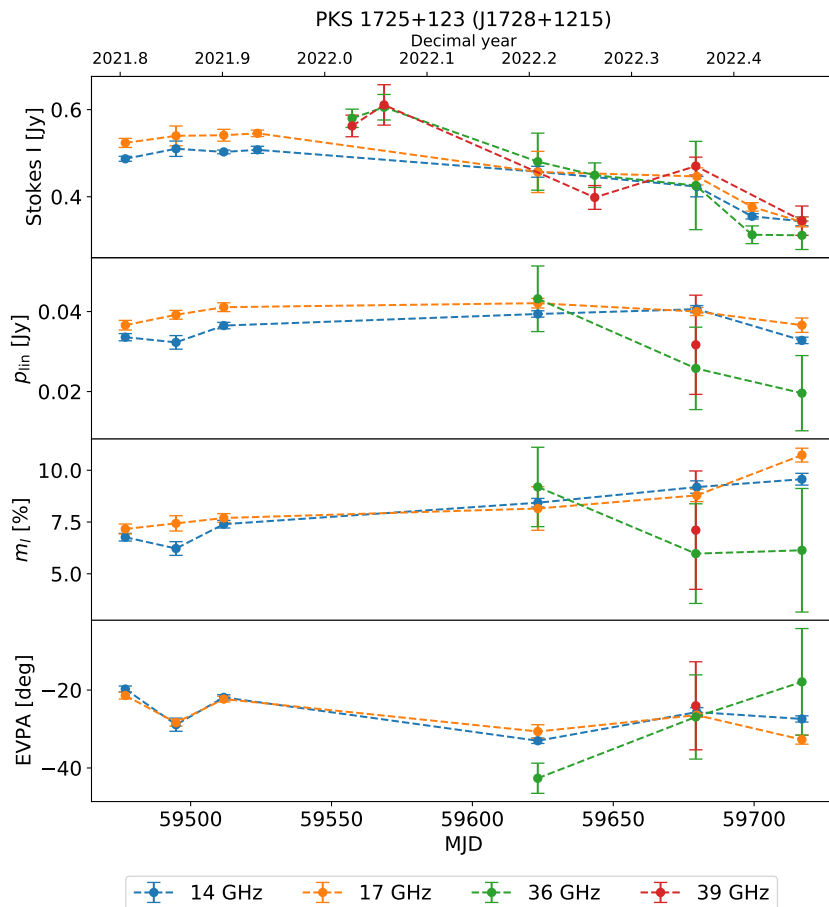


Figure 4.21: Overview-plot of PKS 1725+123 (J1728+1215). Shown are the total Stokes I flux density (top), the linear polarization p_{lin} (second from the top), the fractional polarization m_l (third from the top) and the EVPA χ (bottom) TELAMON lightcurves of the source. The time of the neutrino event is not shown in the figure, as it happened roughly one year before the first data point in the plot.

⁸<https://gcn.gsfc.nasa.gov/gcn/gcn3/28715.gcn3>

⁹<http://telamon.astro.uni-wuerzburg.de/sources/1728-1215>

In this chapter, the results presented in Chapter 4 are put into context by comparing them with two other studies of partly overlapping sources, namely Myserlis (2015) as part of the F-GAMMA project and MOJAVE (Lister et al., 2018). On top of that, some preliminary rotation measures (Eq. 2.44), derived from the observed EVPAs, are investigated.

5.1 Comparison With Other Studies

5.1.1 MOJAVE Polarization Study

In contrast to the single-dish program TELAMON, MOJAVE uses the Very Long Baseline Array (VLBA) to study AGN jets, reaching a resolution of better than 1 milliarcsecond. As was already introduced in Sect. 2.4, the observed polarization can vary depending on the resolution, i.e., on the probed length scale. A total of 30 sources are in the overlapping source sample of both monitoring programs¹. However, as MOJAVE mostly observes at 15 GHz, not all of the sources were observed at the same frequencies, making a comparison harder. Nevertheless, to see how strong the depolarization effect is in the coincident sources, Table 5.1 gives the maximal fractional polarization measured by the two programs throughout their existence. Since MOJAVE has been running way longer than TELAMON, simply averaging over all fractional polarizations could be influenced by potential flares or low-states at the time of the TELAMON observations. Therefore, the maximally reached m_l values are compared, to see if any of the two are significantly higher or lower than the other. Looking at Table 5.1 it is discernible that in most cases, the historical maximum MOJAVE fractional polarization is higher than the maximal value observed during the 6 months of TELAMON. This makes sense, as the depolarization effect diminishes the observed m_l for single-dish telescopes, while for VLBI measurements, the misaligned EVPAs can still be added up to result in an overall higher value. Although the fractional polarizations found by MOJAVE appear to be higher, the values are still very comparable with the TELAMON values, especially keeping in mind the different observing frequencies, with only a few exceptions.

One such exception is the case of J1145+1936 (3C 264), where the TELAMON polarization is higher than the one given by MOJAVE. This could potentially be explained by a flare of the source. However, as the Stokes I TELAMON data² does not show any signs of a flare and MOJAVE did not detect such a flare in four years of monitoring the source, this possibility seems unlikely. A different explanation could be the fact that the VLBA beam missed some of the polarization that the Effelsberg beam detected. This missing polarization could either be

¹See <https://www.physics.purdue.edu/astro/MOJAVE/allsources.html> for the full MOJAVE target list.

²<http://telamon.astro.uni-wuerzburg.de/sources/1145-1936>

Table 5.1: Comparison of the maximal fractional polarization m_l ever observed by TELAMON and MOJAVE. When two sources were not observed at the same frequency, the nearest TELAMON frequency value is given. The TELAMON values are rounded to have the same significant digits as the MOJAVE values.

Name (J2000)	TELAMON frequency [GHz]	TELAMON m_l [%]	MOJAVE m_l [%] at 15 GHz
0112+2244	36	7.3	8.0
0214+5144	14	1.8	4.5
0222+4302	36	6.3	9.0
0303-2407	14	1.7	2.7
0316+4119	14	—	4.1
0509+0541	36	—	4.7
0521+2112	36	—	6.2
0738+1742	14	1.0	4.9
0809+5219	14	3.4	5.6
1015+4926	14	2.6	8.5
1104+3812	39	4.3	3.7
1136+7009	14	5.3	4.2
1145+1936	14	4.9	1.8
1217+3007	36	—	3.1
1221+2813	36	3.9	5.4
1230+2518	36	—	9.6
1415+1320	36	—	0.4
1422+3223	36	2.8	4.3
1427+2348	36	—	4.5
1443+2501	14	7.3	10.9
1518-2731	14	2.7	2.4
1555+1111	14	2.8	3.5
1653+3945	36	2.1	4.4
1728+1215	14	9.6	11.0
1728+5013	14	2.9	6.1
1743+1935	14	2.0	4.3
1751+0938	14	6.2	11.3
1959+6508	14	4.4	4.6
2243+2021	14	2.5	—
2347+5142	14	3.0	4.5

source intrinsic at a larger distance from the VLBI core or due to other sources in the vicinity of the target source or near the line-of-sight.

Another interesting example is the case of TXS 0506+056 (J0509+0541), where no polarization was detected by TELAMON in five different epochs with usable polarization data. MOJAVE, on the other hand, states a historical maximum value of $m_l = 4.7\%$. In an observation in close proximity to a TELAMON observation on 24.02.2022³, MOJAVE find $m_l = 1.1\%$. While the TELAMON observation was conducted at higher frequencies, the polarization image provided by MOJAVE, shown in Fig. 5.1, still presents a good reason why no polarization was detected by TELAMON, since parts of the individual EVPAs are perpendicular to other parts. Vectorially adding them together results in the explained depolarization for single-dish observations.

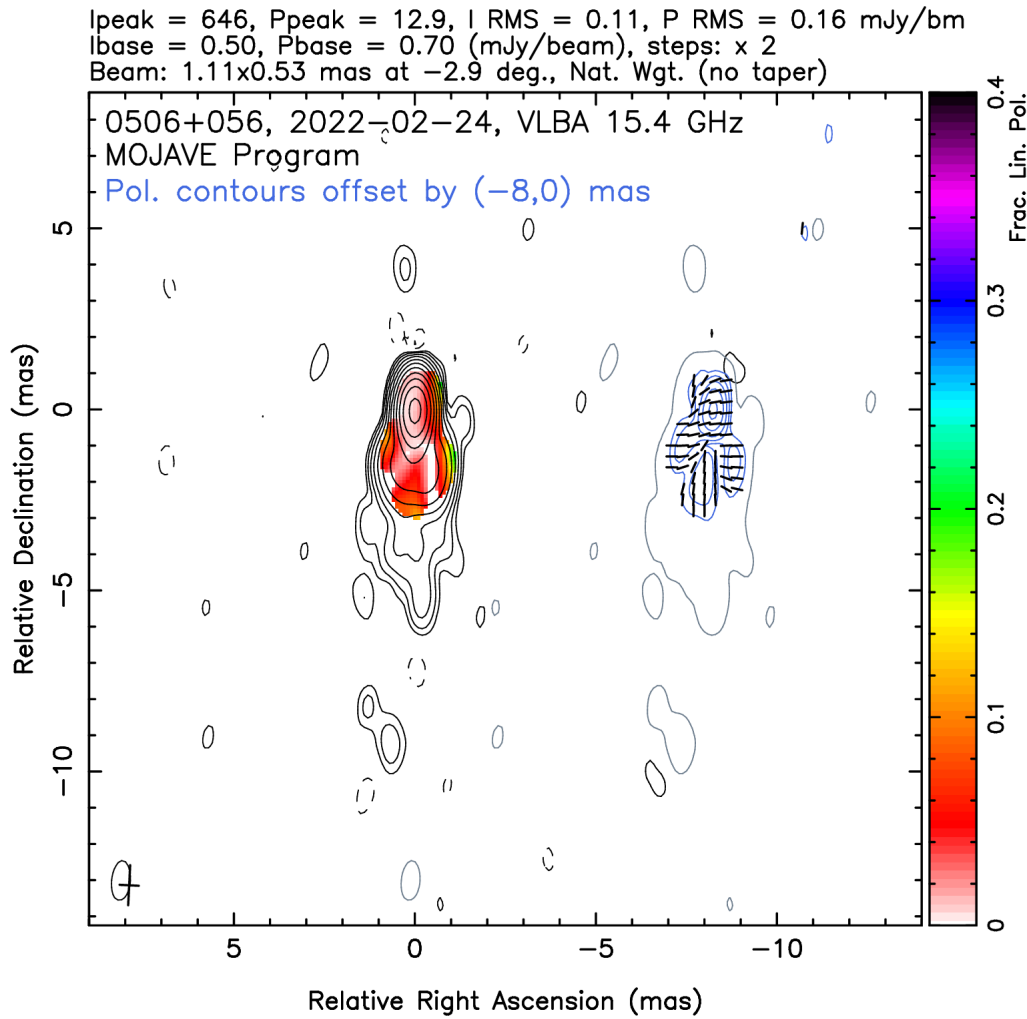


Figure 5.1: MOJAVE polarization image of TXS 0506+056 (J0509+0541) from 24.02.2022³, showing misaligned EVPAs that, when added up vectorially, result in a lower net-EVPA.

These examples show why it is important to keep both of these effects in mind when observing polarization with either a single-dish or VLBI telescope. The best case scenario would be to observe the target source with both methods simultaneously, making the estimation of the

³<https://www.physics.purdue.edu/astro/MOJAVE/sourcepages/0506+056.shtml>

depolarization possible.

5.1.2 F-GAMMA Polarization Study

In contrast to the MOJAVE program, F-GAMMA (Angelakis et al., 2019) uses the same instrument as TELAMON, i.e., the Effelsberg 100 m telescope. Their sample is made up of *Fermi* GeV-blazars with most of the sources being FSRQs. However, there are still 15 sources coincident in the F-GAMMA and the TELAMON sample. Myserlis (2015) presents the polarization characteristics of the F-GAMMA sources at 2.64 GHz, 4.85 GHz, 8.35 GHz and 10.45 GHz. These are slightly lower than the lowest TELAMON frequency, but the results should still be comparable. Actually, as argued by Agudo et al. (2014), the sources are expected to be increasingly polarized with increasing frequency due to the better ordering of the magnetic field closer to the SMBH. To check this assumption, a comparison between the two studies is drawn in Table 5.2, where the highest still significantly polarized F-GAMMA frequency and the lowest significantly polarized TELAMON frequency is given for the overlapping sources. In eight out

Table 5.2: Comparison of the fractional polarizations m_l of the coincident sources between the F-GAMMA and TELAMON sample. For the F-GAMMA data the highest frequency where a significant polarization was detected is shown, while for the TELAMON data the lowest such frequency is given. F-GAMMA data taken from Myserlis (2015).

Name (J2000)	TELAMON frequency [GHz]	TELAMON m_l [%]	F-GAMMA frequency [GHz]	F-GAMMA m_l [%]
0217+0144	14	3.0	10.45	2.9
0221+3556	36	10.2	10.45	7.4
0222+4302	36	6.3	10.45	2.1
0738+1742	14	0.6	10.45	2.0
1104+3812	39	4.3	10.45	3.2
1136+7009	14	4.4	8.35	3.8
1217+3007	—	—	8.35	3.3
1221+2813	36	3.9	8.35	2.9
1542+6129	14	2.5	—	—
1555+1111	14	1.6	—	—
1653+3945	36	2.1	10.45	1.6
1751+0939	14	6.0	10.45	3.3
1959+6508	14	3.3	—	—
2158-3013	—	—	2.64	3.0
2347+5142	14	2.1	—	—

of the 15 cases, the TELAMON data does indeed show a higher fractional polarization. This number does not sound convincing, but it has to be noted that in six cases, either of the two studies did not detect a significant polarization at all. In cases where no F-GAMMA polarization was detected, this can be explained by the argument of increasing polarization with increasing frequency. There is also an example, namely 1217+3007, where this seems to be the

other way around. Myserlis (2015) reports a fractional polarization $m_l = 5.4\%$ at 2.64 GHz with a decreasing percentage at 4.85 GHz and 8.35 GHz. At 10.45 GHz, the source was not found to be significantly polarized in 21 distinct scans. Assuming this trend to continue, it explains why in TELAMON, no polarization was observed.

Of course, this comparison can be drawn for the other polarization parameters, i.e., the linear polarization p_{lin} and the EVPA, as well. Here, the comparison of only one property is sufficient to get an overview of potential similarities or differences. Overall, the results of the two studies agree well, meaning that the Effelsberg 100 m telescope likely produces meaningful polarization data even for high radio frequencies.

5.2 Rotation Measures

In Sect. 2.4, Faraday rotation was introduced as an effect that results in the rotation of the EVPA. Since this rotation is wavelength-dependent (Eq. 2.43), assuming there to be no systematic errors, the difference between the EVPAs at 14 GHz and 17 GHz (as well as between 36 GHz and 39 GHz) can be attributed solely to Faraday rotation and is characterized by the rotation measure RM. Following Taylor et al. (2009), the observed RM is calculated as

$$\text{RM} \propto \frac{\Delta\chi}{\lambda_2^2 - \lambda_1^2}, \quad (5.1)$$

where $\Delta\chi$ is the EVPA difference between the two frequencies and λ_1 and λ_2 are the center wavelengths of the two frequency bands. The resulting RM lightcurves are shown in Appendix E and one example is presented in Fig. 5.2. This source shows hints of RM variability with chang-

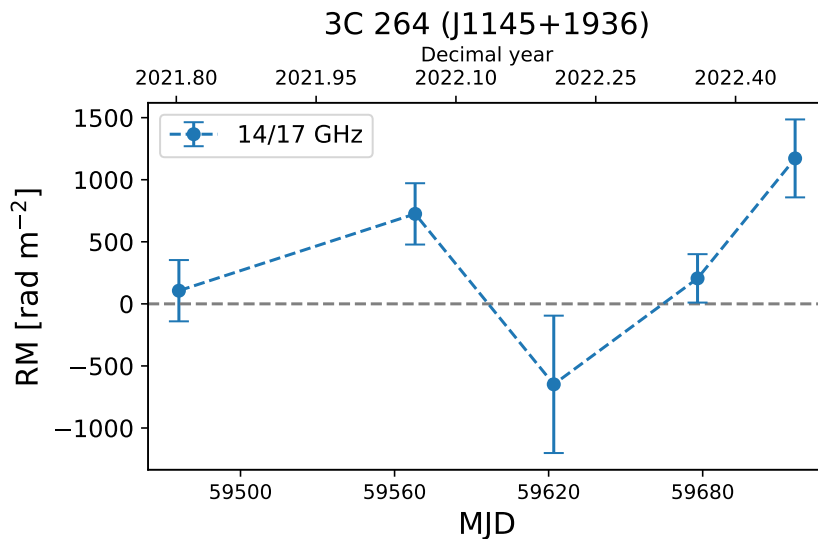


Figure 5.2: Rotation measures of 3C 264 (J1145+1936), calculated using Eq. 5.1 for the two frequencies 14 GHz and 17 GHz.

ing signs and significant non-zero RMs.

The overall RM distribution in the sample is plotted in Fig. 5.3 for the 20 mm frequencies and in Fig. 5.4 for the 7 mm frequencies. As can be seen, the rotation measures mostly cluster around 0, indicating no Faraday rotation between the two frequencies. This is also visible in the individual source RM lightcurves in Appendix E, where most RM values are in agreement

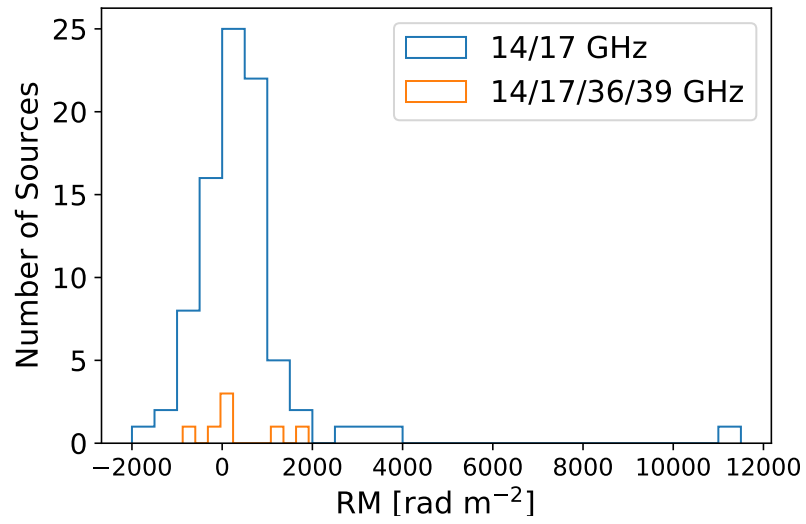


Figure 5.3: Distribution of the RMs between 14 GHz and 17 GHz derived via Eq. 5.1. Also, the RMs estimated by fitting a linear function to all four frequencies are shown.

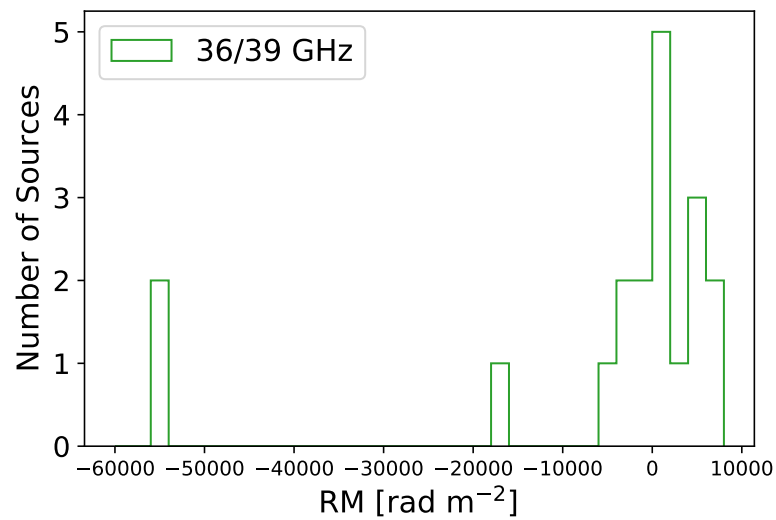


Figure 5.4: Distribution of the RMs between 36 GHz and 39 GHz derived via Eq. 5.1.

with 0 with respect to their errors. Some sources do show signs of non-zero RMs, but these are typically in only a few epochs. Generally it has to be said that the error bars for the 7 mm RMs are very large, of the order of $\sim 10\,000 \text{ rad m}^{-2}$, which seems to be quite large compared to the ones at 20 mm that are approximately one order of magnitude smaller. The large errors can be explained by the typically larger errors of the EVPAs at the higher frequencies that, through Gaussian error propagation, influence the error of the RMs. When there are more than two frequencies available, the RM can be derived as the slope of a linear fit to the data in a EVPA versus λ^2 plot. This was done for the five sample sources that had significant EVPA detections at all four frequencies. The resulting rotation measures are plotted in Fig. 5.3. They seem to agree with the overall trend of $-2000 \text{ rad m}^{-2} < \text{RM} < 2000 \text{ rad m}^{-2}$, but this is not highly significant, as only seven distinct detections could be analyzed in this way.

Compared to other studies such as Taylor et al. (2009) and Myserlis (2015), the RMs derived in this work are slightly higher. Taylor et al. (2009) find RMs of $|\text{RM}| \lesssim 200 \text{ rad m}^{-2}$ at $\sim 1.4 \text{ GHz}$, while Myserlis (2015) finds $|\text{RM}| \lesssim 100 \text{ rad m}^{-2}$ for frequencies between 2.64 GHz and 10.45 GHz. In this work, the resulting arithmetic mean of the rotation measures at 20 mm and 7 mm are $\text{RM} \approx 470 \text{ rad m}^{-2}$ and $\text{RM} \approx -5400 \text{ rad m}^{-2}$, respectively. However, the standard deviations of the distributions are also quite large, being $\sim 1500 \text{ rad m}^{-2}$ and $\sim 20\,000 \text{ rad m}^{-2}$ for the low and high frequencies. Actually, Goddi et al. (2021) find RM uncertainties of $(1-3) \times 10^4 \text{ rad m}^{-2}$ and $(0.06-1.0) \times 10^4 \text{ rad m}^{-2}$ at 3 mm and 1.3 mm, respectively, for a dozen RL AGN, using ALMA. The RM values derived for TELAMON sources and frequencies are therefore located in-between the three other studies.

By using the fitting method, another property, the intrinsic EVPA χ_0 , can be extracted as the EVPA-axis intersect of the plot, similar to Eq. 2.45. Doing this for the 20 mm data, the difference $\chi_{\text{obs}} - \chi_0$ can be calculated, using the observed 14 GHz EVPA as χ_{obs} . The resulting distribution of this difference is shown in Fig. 5.5. Here, the vast majority of differences lie

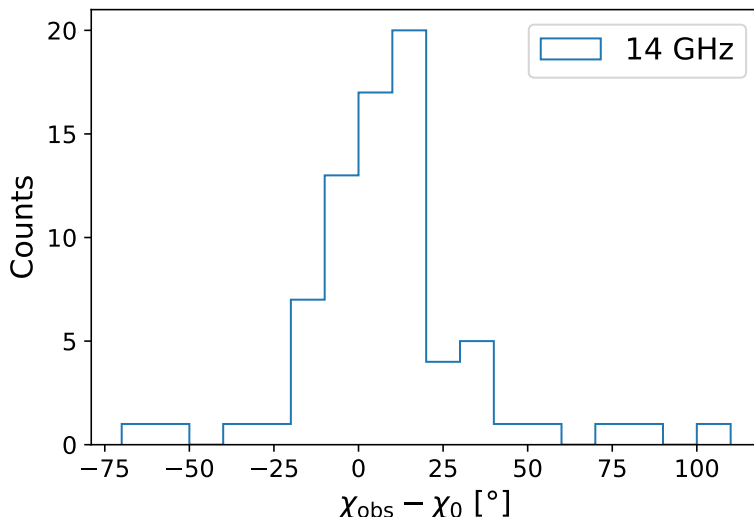


Figure 5.5: Histogram of the difference $\chi_{\text{obs}} - \chi_0$ between the observed EVPA χ_{obs} at 14 GHz and the intrinsic EVPA χ_0 .

between $\pm 25^\circ$, although there are some outliers with double or triple that value.

It has to be noted that fitting a line through only two data points is generally not a good practice, as minor fluctuations of the data heavily influence the fit, possibly leading to vastly

different results. Including more frequencies, and therefore more data points, into the fitting process would increase the significance of the results. However, for the TELAMON data, as already mentioned before, only five sources were detected in the two usable wavelength bands so that the statistical value of the results would not be very high. This also means that the distribution shown in Fig. 5.5 has to be taken with a grain of salt.

[Taylor et al. \(2009\)](#) showed that rotation measures of the order of $|\text{RM}| \sim 200 \text{ rad m}^{-2}$ can be explained as the Faraday rotation happening in our Galaxy. Since the derived RMs in this thesis are higher, they cannot fully be explained by Galactic Faraday rotation. Different possible scenarios for the origin of Faraday rotation in AGN are discussed in [Martí-Vidal & Goddi \(2021\)](#). Without further information, however, they cannot be investigated in more detail.

In this thesis, TELAMON data, obtained by the Effelsberg 100 m telescope at high radio frequencies, was analyzed using two different receiver backends. While the OPTOCBE backend is only sensitive to Stokes I , i.e., the total intensity of the radiation, the SPECPOL backend additionally detects Stokes Q and U , making it possible to derive the polarization characteristics of the wave. After the necessary data reduction steps, the obtained Stokes I flux densities of the two backends were compared to see if there are any significant differences between them. Overall, they agree well within their measured flux densities, their detection statistics and their signal-to-noise ratios.

The polarization analysis is performed using the Müller formalism that uses sources of known flux density and polarization to correct the measured Stokes parameters for instrumental effects. These effects are encoded in a matrix that is then inverted and applied to the measured data, yielding the true Stokes parameter of the signal. From them, the linear polarization p_{lin} , the fractional polarization m_l and the EVPA χ can be calculated. In this work, a source was defined to be significantly polarized when it fulfills $p_{\text{lin}} > 2\sigma_{p_{\text{lin}}}$. As expected, most of the sources are polarized at a level $m_l < 5\%$. Some of the sources exhibit particularly interesting properties, e.g., TXS 0215+015 that shows signs of a polarization flare higher than historical MOJAVE data.

Comparing the results of this thesis with the results of MOJAVE for the same sources indicates differences between the polarization values. However, in the most cases, these differences can be explained by Faraday rotation of the EVPAs, leading to misaligned local EVPAs that, when added vectorially, result in a lower net-EVPA. This can also explain why some sources were not detected to be polarized by TELAMON, but by MOJAVE.

[Myserlis \(2015\)](#) presents polarization data of sources observed in the framework of F-GAMMA, who also used the Effelsberg 100 m telescope, albeit at slightly lower frequencies. In a majority of all cases, sources that were observed in both monitoring programs are higher polarized in TELAMON. This is in agreement with the expectation that at higher frequencies the magnetic fields near the centers of AGN are better ordered, leading to a higher polarization ([Agudo et al., 2014](#)).

To characterize the amount of Faraday rotation present in the line-of-sight to the source, the rotation measure is calculated as the ratio of EVPA change between two (or more) frequencies and the square of the observing wavelength. Most derived rotation measures are in agreement with no Faraday rotation occurring and cluster around $|\text{RM}| = 2000 \text{ rad m}^{-2}$ at 20 mm, with 7 mm values being higher by approximately one order of magnitude. Compared to other studies such as [Taylor et al. \(2009\)](#) and [Myserlis \(2015\)](#), the RMs derived in this work are higher by a factor of 2 – 4, potentially indicating that the rotation is not solely of Galactic origin.

This thesis was started with the intention to test whether meaningful polarization data could be derived for TELAMON sources at high radio frequencies. Therefore, only first order data products are presented here. Future works will undoubtedly give deeper insight into the polarization of TELAMON sources. The variability of the polarized flux can be characterized, its correlation to the total flux can be analyzed and much more.

Assuming the SPECPOL at 14mm to get fixed at a future time, there are more data to be analyzed. This would also improve the ability to find the intrinsic EVPA by applying a linear fit to the plot of EVPA versus the square of the observing wavelengths. Having four instead of two data points in this plot heavily increases the significance of the resulting fit values. Also, in the next years, a new EDD receiver version will be available, hopefully increasing the data quality even more.

A revision of the data analysis process is also imaginable. Myserlis (2015) showed that it is possible to get higher quality results by removing artifacts from the Stokes Q and U scans and using an Airy disk pattern instead of a Gaussian approximation of the antenna pattern. With this, a Stokes V study on TELAMON data could be possible as well.

The error budget of the polarization data is currently assumed to be dominated by the error introduced on the calibration process. While the Müller matrix elements are calculated with a respective error, this error is not used, as the inversion of this „error-matrix“ is highly non-trivial. A possible way of calculating the error of polarization measurements is given by Thiel (1976). Lastly, alternatives to the Müller matrix method can be explored. The method presented by Myserlis (2015) and Myserlis et al. (2018), for example, performs better for low polarized sources.

Bibliography

- Abdollahi S., et al., 2022, *The Astrophysical Journal Supplement*, in press, arXiv:2201.11184
- Ackermann M., et al., 2015, *The Astrophysical Journal Letters*, 813, L41
- Agudo I., Thum C., Gómez J., Wiesemeyer H., 2014, *Astronomy & Astrophysics*, 566, A59
- Agudo I., et al., 2018, *Monthly Notices of the Royal Astronomical Society*, 474, 1427
- Albert J., et al., 2007, *The Astrophysical Journal*, 669, 862
- Aller M. F., Aller H. D., Hughes P. A., 1996, in Miller H. R., Webb J. R., Noble J. C., eds, *Astronomical Society of the Pacific Conference Series Vol. 110, Blazar Continuum Variability*. p. 193
- Angelakis E., et al., 2019, *Astronomy & Astrophysics*, 626, A60
- Antonucci R., 1993, *Annual Review of Astronomy and Astrophysics*, 31, 473
- Bach U., Kraus A., 2020, *Effelsberg Radio Observatory 2017-2018 Biennial Report, International VLBI Service for Geodesy and Astrometry 2017+2018 Biennial Report*, edited by K. L. Armstrong, K. D. Baver, and D. Behrend, NASA/TP-2020-219041
- Bach U., Kraus A., Fürst E., Polatidis A., 2007, *First report about the commissioning of the new Effelsberg sub-reflector. Effelsberg memo series*
- Beckmann V., Shrader C. R., 2012, *Active Galactic Nuclei*. Wiley-VCH, Berlin
- Bell A., 1978, *Monthly Notices of the Royal Astronomical Society*, 182, 147
- Beuchert T., 2013, M.Sc. thesis, *Of Radio-loud and Radio-quiet AGN, Single Dish Radio Polarimetry and X-ray Variability Study of Polar Scattered Seyfert I Galaxies*. Friedrich-Alexander Universität Erlangen-Nürnberg, Erlangen
- Biteau J., et al., 2020, *Nature Astronomy*, 4, 124–131
- Blandford R., Eichler D., 1987, *Physics Reports*, 154, 1
- Blandford R., Meier D., Readhead A., 2019, *Annual Review of Astronomy and Astrophysics*, 57, 467
- Blinov D., et al., 2015, *Monthly Notices of the Royal Astronomical Society*, 453, 1669

- Blinov D., et al., 2016, *Monthly Notices of the Royal Astronomical Society*, 457, 2252
- Burke B. F., Graham-Smith F., Wilkinson P. N., 2019, *An introduction to radio astronomy*. Cambridge University Press, Cambridge
- Donato D., Ghisellini G., Tagliaferri G., Fossati G., 2001, *Astronomy & Astrophysics*, 375, 739
- Eppel F., 2021, M.Sc. thesis, *Variability Study of High-Peaked BL Lac Objects at Millimeter Wavelengths*. Julius-Maximilians Universität Würzburg, Würzburg
- Fanaroff B. L., Riley J. M., 1974, *Monthly Notices of the Royal Astronomical Society*, 167, 31P
- Fermi E., 1949, *Physical review*, 75, 1169
- Fossati G., Maraschi L., Celotti A., Comastri A., Ghisellini G., 1998, *Monthly Notices of the Royal Astronomical Society*, 299, 433
- Gammie C. F., 1999, *The Astrophysical Journal*, 522, L57
- Garrappa S., Buson S., Cheung C. C., Sinapius J., 2022, *The Astronomer's Telegram*, 15243, 1
- Ghisellini G., Tavecchio F., 2009, *Monthly Notices of the Royal Astronomical Society*, 397, 985
- Ghisellini G., Righi C., Costamante L., Tavecchio F., 2017, *Monthly Notices of the Royal Astronomical Society*, 469, 255
- Giommi P., Padovani P., 2021, *MDPI Universe*, 7, 492
- Goddi C., et al., 2021, *The Astrophysical Journal Letters*, 910, L14
- Heßdörfer J., 2021, B.Sc. thesis, *Flux density measurements of TeV blazars with the Effelsberg 100 m telescope*. Julius-Maximilians Universität Würzburg, Würzburg
- Hiriart D., Benítez E., Heidt J., López J. M., Mújica R., 2019, in Belluzzi L., Casini R., Romoli M., Trujillo Bueno J., eds, *Astronomical Society of the Pacific Conference Series Vol. 526, Solar Polarisation Workshop 8*. p. 279
- Hönig S. F., 2019, *The Astrophysical Journal*, 884, 171
- Jansky K. G., 1935, *Proceedings of the Institute of Radio Engineers*, 23, 1158
- Kadler M., et al., 2021, *PoS, ICRC2021*, 974
- Kadler M., Stevens J., Ojha R., Edwards P. G., 2022, *The Astronomer's Telegram*, 15245, 1
- Kellermann K., 2014, *Journal of Astronomical History and Heritage*, 17, 267
- Kellermann K., Sheets B., 1984, *Proceedings of a Workshop held at the National Radio Astronomy Observatory*
- Kellermann K., Sramek R., Schmidt M., Shaffer D., Green R., 1989, *The Astronomical Journal*, 98, 1195
- Kraus J., 1966, *Radio Astronomy*. McGraw-Hill Book Company, New York

- Kraus A., 1997, Kurzzzeitvariabilität aktiver Galaxienkerne in totaler und polarisierter Flußdichte. Rheinische Friedrich-Wilhelms-Universität zu Bonn, Bonn
- Lico R., et al., 2020, *Astronomy & Astrophysics*, 634, A87
- Lister M., et al., 2018, *The Astrophysical Journal Supplement Series*, 234, 12
- Longair M. S., 2010, *High Energy Astrophysics*. Cambridge university press, Cambridge
- Mannheim K., 1993, *Astronomy and Astrophysics*, 269, 67
- Marconi A., et al., 2004, *Monthly Notices of the Royal Astronomical Society*, 351, 169
- Marscher A. P., Gear W. K., 1985, *The Astrophysical Journal*, 298, 114
- Martí-Vidal I., Goddi C., 2021, *MDPI Galaxies*, 9, 51
- Martini P., Weinberg D. H., 2001, *The Astrophysical Journal*, 547, 12
- Massaro E., et al., 2015, *Astrophysics and Space Science*, 357, 1
- Massey Jr F. J., 1951, *Journal of the American statistical Association*, 46, 68
- Myserlis I., 2015, PhD thesis, A framework for the study of physical conditions in astrophysical plasmas through radio and optical polarization: Application to extragalactic jets. Universität zu Köln, Köln
- Myserlis I., et al., 2018, *Astronomy & Astrophysics*, 609, A68
- Nanci C., et al., 2022, *Astronomy & Astrophysics*, in press, arXiv:2203.13268
- Nenkova M., Sirocky M. M., Nikutta R., Ivezić Ž., Elitzur M., 2008, *The Astrophysical Journal*, 685, 160
- Nesci R., 2022, *The Astronomer's Telegram*, 15248, 1
- Padovani P., 2011, *Monthly Notices of the Royal Astronomical Society*, 411, 1547
- Padovani P., Giommi P., 1995, *ApJ*, 444, 567
- Padovani P., et al., 2017, *The Astronomy and Astrophysics Review*, 25, 2
- Padovani P., et al., 2018, *Monthly Notices of the Royal Astronomical Society*, 480, 192
- Perley R., Butler B., 2013, *The Astrophysical Journal Supplement Series*, 206, 16
- Perley R. A., Butler B. J., 2017, *The Astrophysical Journal Supplement Series*, 230, 7
- Plavin A., et al., 2022, *The Astronomer's Telegram*, 15247, 1
- Rohlfs K., Wilson T. L., 2013, *Tools of radio astronomy*. Springer Berlin, Heidelberg
- Ruze J., 1966, *Proceedings of the IEEE*, 54, 633
- Rybicki G. B., Lightman A. P., 1979, *Radiative processes in astrophysics*. Wiley-VCH, Weinheim

- Sahakyan N., et al., 2022, *Monthly Notices of the Royal Astronomical Society*, in press, arXiv:2204.05060
- Saikia D., Salter C., 1988, *Annual Review of Astronomy and Astrophysics*, 26, 93
- Schmidt M., 1963, *Nature*, 197, 1040
- Seyfert C. K., 1943, *The Astrophysical Journal*, 97, 28
- Shakura N. I., Sunyaev R. A., 1973, *Astronomy & Astrophysics*, 24, 337
- Shapiro S. S., Wilk M. B., 1965, *Biometrika*, 52, 591
- Shastri P., Wilkes B. J., Elvis M., McDowell J., 1993, *The Astrophysical Journal*, 410, 29
- Shields G. A., 1999, *Publications of the Astronomical Society of the Pacific*, 111, 661
- Tabara H., Inoue M., 1980, *Astronomy and Astrophysics Supplement Series*, 39, 379
- Taylor J., 1997, *Introduction to error analysis, the study of uncertainties in physical measurements*. University Science Books, Sausalito
- Taylor A., Stil J., Sunstrum C., 2009, *The Astrophysical Journal*, 702, 1230
- Thiel M. A., 1976, *Journal of the Optical Society of America*, 66, 65
- Turlo Z., Forkert T., Sieber W., Wilson W., 1985, *Astronomy and Astrophysics*, 142, 181
- Urry C. M., Padovani P., 1995, *Publications of the Astronomical Society of the Pacific*, 107, 803
- Woo J.-H., Urry C. M., 2002, *The Astrophysical Journal*, 579, 530
- Zhang L., Fan J., Zhu J., 2021, *Publications of the Astronomical Society of Japan*, 73, 313
- Zijlstra A. A., Van Hoof P., Perley R., 2008, *The Astrophysical Journal*, 681, 1296

A | List of All Observed Sources

Table A.1: All sources observed in the framework of this thesis, given with their J2000 names and their alternative names. „Y“ and „N“ correspond to significant detections and non-detections, respectively.

Name (J2000)	Alt. name	Detected Stokes I?	Significant polarization?
0035+5950	1ES 0033+595	Y	N
0112+2244	S2 0109+22	Y	Y
0152+0146	RGB J0152+017	N	N
0214+5144	TXS 0210+515	Y	Y
0217+0144	TXS 0215+014	Y	Y
0221+3556	S3 0218+35	Y	Y
0222+4302	3C 66A	Y	Y
0232+2017	1ES 0229+200	Y	N
0242+1101	PKS 0239+108	Y	N
0245+2405	B2 0242+23	Y	N
0258+2030	NVSS J025807+203001	Y	Y
0303-2407	PKS 0301-243	Y	Y
0308+0406	NGC 1218	N	N
0313+0228	TXS 0310+022	Y	Y
0316+4119	IC 310	Y	N
0319+1845	[HB89] 0317+185	Y	N
0416+0105	1ES 0414+09	Y	N
0507+6737	1ES 0502+675	Y	N
0509+0541	TXS 0506+056	Y	N
0521+2112	RGB J0521+212	Y	N
0650+2502	1ES 0647+250	Y	N
0658+0637	NVSS J065844+063711	Y	N
0710+5909	RGB J0710+591	Y	N
0726+0636	WISEA J072636.35+063643.0	Y	N
0733+0456	WISEA J073357.44+045614.6	Y	N

Name (J2000)	Alt. name	Detected Stokes I?	Significant polarization?
0738+1742	PKS 0735+17	Y	Y
0809+5219	1ES 0806+524	Y	Y
0812+0237	1RXS J081201.8+023735	Y	N
0836+71	0836+71	Y	Y
0855-0021	WISEA J085554.47-002146.3	Y	N
0901-0037	WISEA J090125.79-003703.4	Y	N
0913-2103	MRC 0910-208	Y	N
1015+4926	1ES 1011+496	Y	Y
1025+1253	NVSS J102556+12534	Y	Y
1058+2817	GB6 J1058+2817	Y	Y
1104+3812	MRK 421	Y	Y
1136+7009	MRK 180	Y	Y
1145+1936	3C 264	Y	Y
1217+3007	ON 325	Y	N
1221+2813	W Comae	Y	Y
1221+3010	1ES 1218+304	Y	N
1230+2518	ON 246	Y	N
1415+1320	PKS 1413+135	Y	N
1417+2543	[HB89] 1415+259	Y	N
1422+3223	OQ 334	Y	Y
1427+2348	OQ 240	Y	N
1428+4240	1ES 1426+428	N	N
1443+1200	WISE J144248.24+120040.3	N	N
1443+2501	1ES 1440+122	Y	Y
1451-0127	[HB89] 1449-012	Y	Y
1458-0037	NVSS J145859-003750	Y	Y
1510+5702	TXS 1508+572	Y	Y
1518-2731	TXS 1515-273	Y	Y
1542+6129	GB6 J1542+6129	Y	Y
1555+1111	PG 1553+113	Y	Y
1653+3945	MRK 501	Y	Y
1725+1152	WISE J172504.34+115215.5	Y	N
1728+1215	PKS 1725+123	Y	Y
1728+5013	I Zw 187	Y	Y
1743+1935	1ES 1741+196	Y	Y
1746+1127	CRATES J174656.86+112718.2	Y	Y
1751+0939	OT 081	N	N
1752-1011	TXS 1749-101	Y	Y

Name (J2000)	Alt. name	Detected Stokes I?	Significant polarization?
1758-1203	TXS 1755-120	Y	Y
1803+2521	TXS 1801+253	Y	Y
1813+3144	B2 1811+31	Y	Y
1943+2118	HESS J1943+213	Y	N
1958-3011	1RXS J195815.6-301119	Y	N
1959+6508	1ES 1959+650	Y	Y
2001+4352	MAGIC J2001+435	Y	Y
2018+3851	TXS 2016+386	Y	Y
2049+1822	TXS 2047+181	Y	Y
2108+1430	4C +14.77	Y	Y
2121+3015	B2 2119+30	Y	N
2123+3012	B2 2121+29B	Y	Y
2126+2904	B2 2124+28	Y	Y
2158-3013	PKS 2155-304	Y	N
2212+0646	TXS 2210+065	Y	Y
2215+0544	WISEA J221513.47+054454.5	N	N
2224+0354	WISE J222424.97+035458.2	N	N
2243+2021	RGB J2243+203	Y	Y
2306+0837	WISEA J230601.26+083715.2	Y	N
2306+0939	WISEA J230625.14+093912.2	Y	N
2343+2614	WISEA J234327.80+261411.6	Y	N
2344+2559	B2 2342+25	Y	N
2347+5142	1ES 2344+514	Y	Y
2348+2448	B2 2345+24A	Y	N

B Evolution of the Müller Matrix Elements and Average Müller Matrices

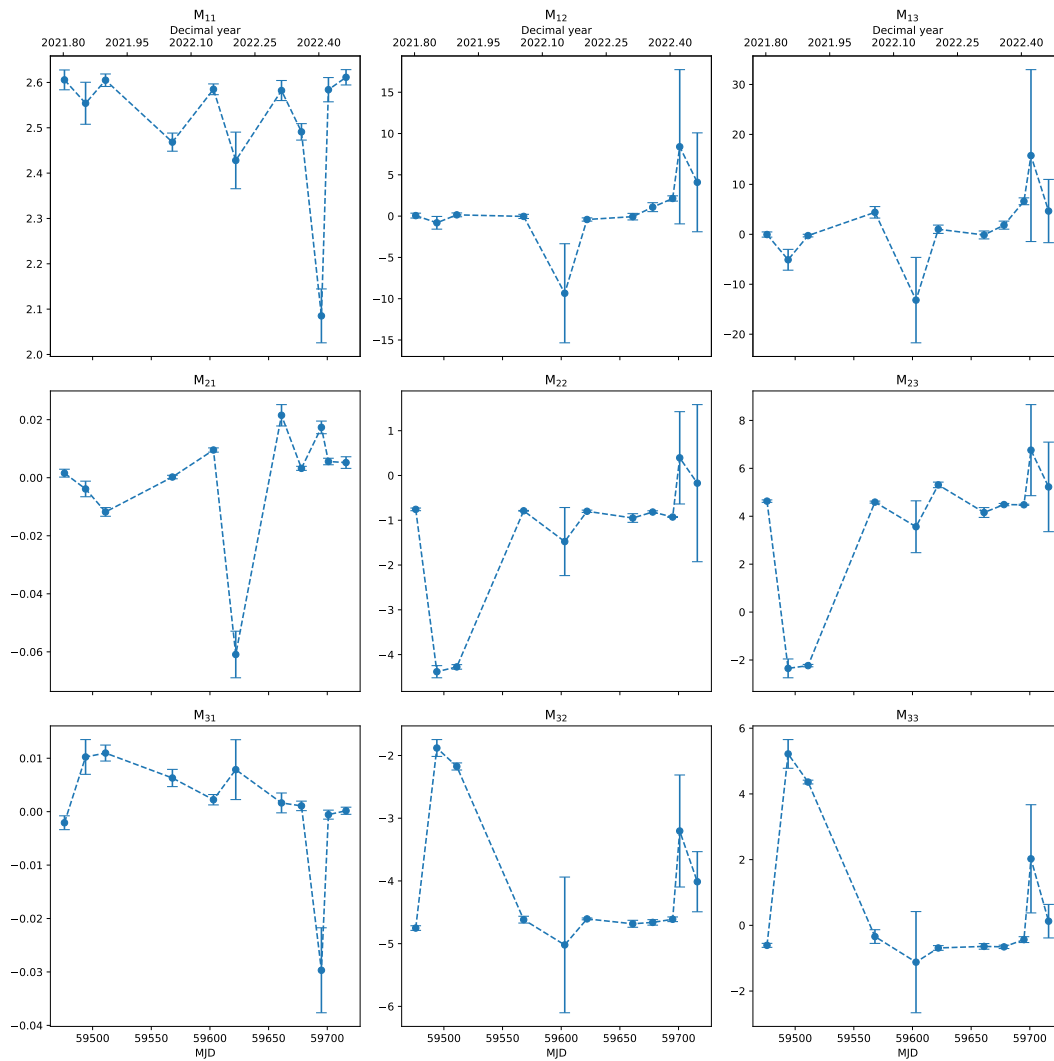


Figure B.1: Evolution of the 14 GHz Müller matrix elements throughout all observations carried out in the framework of this thesis that are marked with „Y“ in Table 3.2.

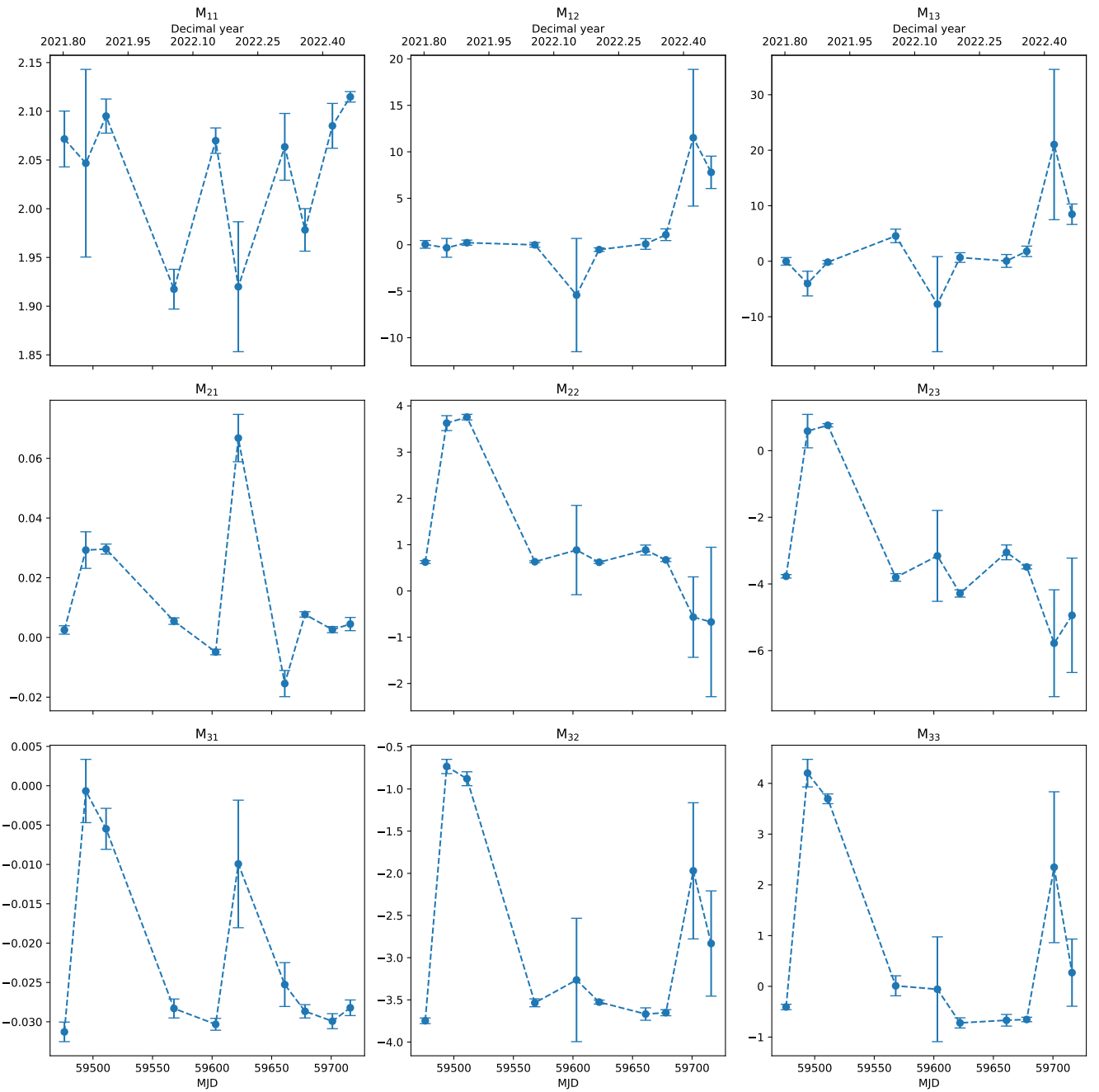


Figure B.2: Evolution of the 14 GHz Müller matrix elements throughout all observations carried out in the framework of this thesis that are marked with „Y“ in Table 3.2.

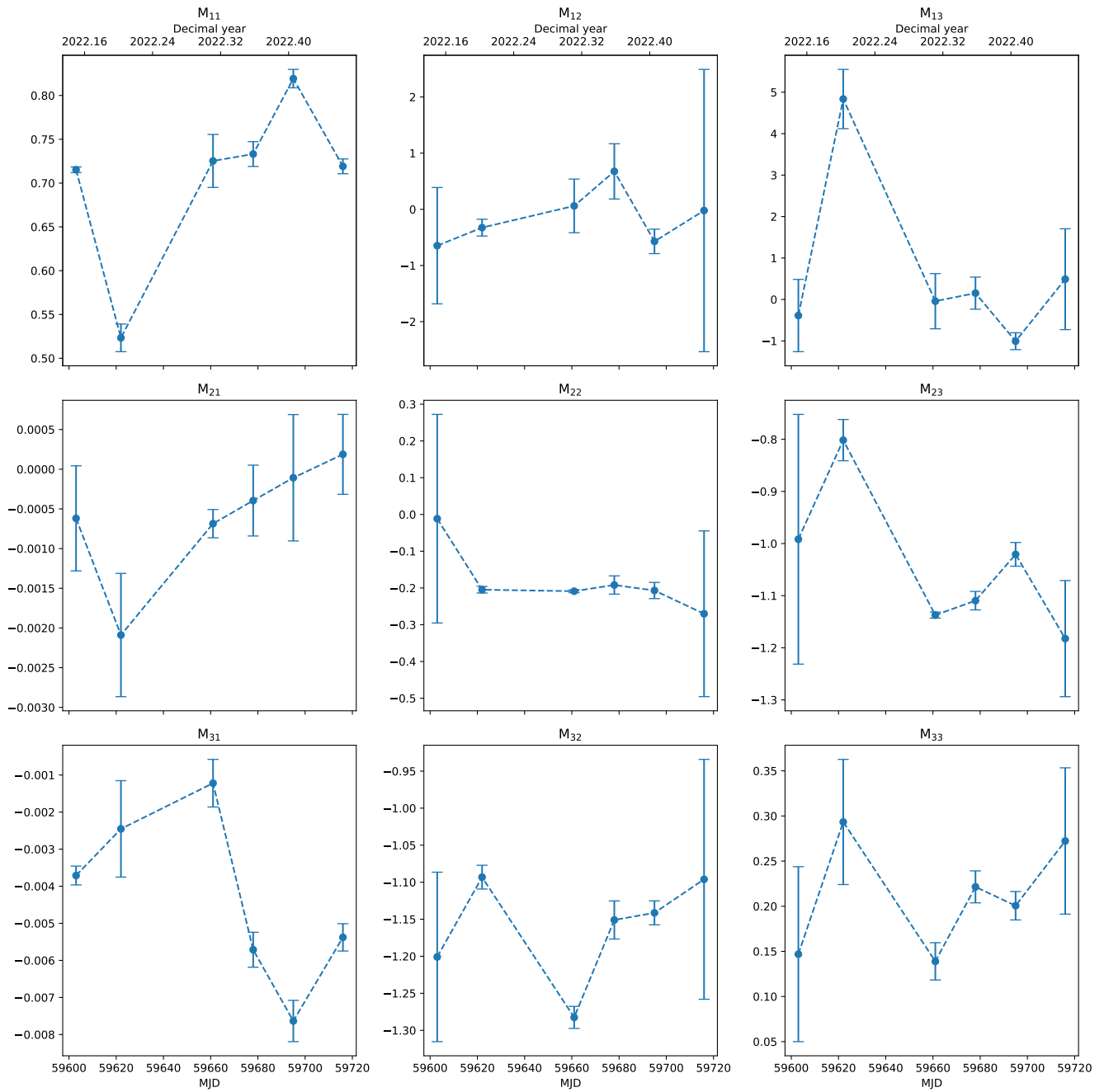


Figure B.3: Evolution of the 14 GHz Müller matrix elements throughout all observations carried out in the framework of this thesis that are marked with „Y“ in Table 3.2.

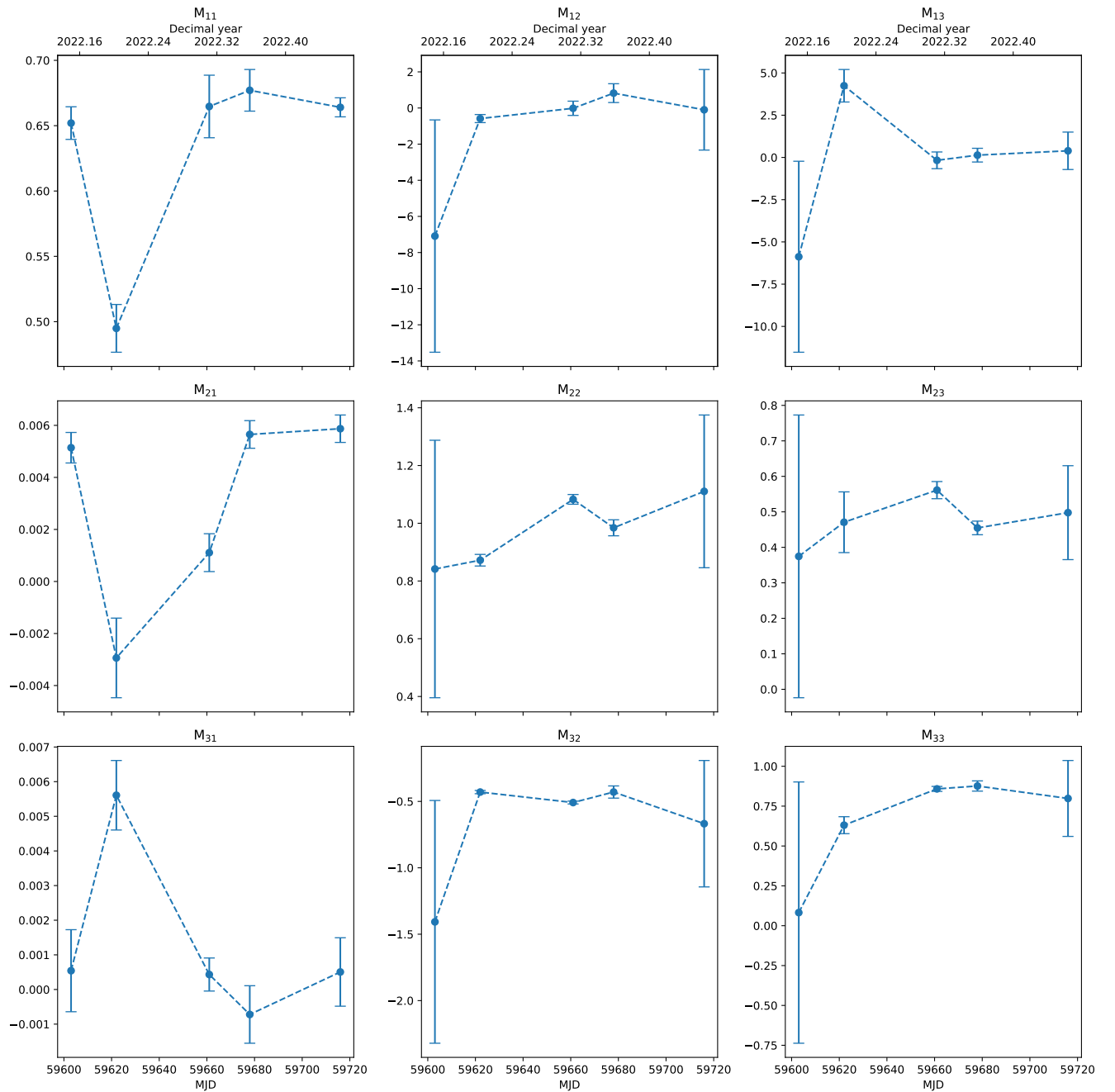


Figure B.4: Evolution of the 14 GHz Müller matrix elements throughout all observations carried out in the framework of this thesis that are marked with „Y“ in Table 3.2.

The averaged Müller matrix elements for all observations shown in the figures above are:

$$\mathcal{M}_{14\text{ GHz}} = \begin{pmatrix} 2.5656 \pm 0.0060 & 0.17 \pm 0.10 & 0.63 \pm 0.20 \\ 0.00331 \pm 0.00033 & -0.8887 \pm 0.0057 & 3.736 \pm 0.017 \\ 0.00136 \pm 0.00036 & -4.509 \pm 0.011 & 0.453 \pm 0.026 \end{pmatrix}$$

$$\mathcal{M}_{17\text{ GHz}} = \begin{pmatrix} 2.0901 \pm 0.0044 & -0.09 \pm 0.12 & 0.36 \pm 0.25 \\ 0.00451 \pm 0.00043 & 0.796 \pm 0.013 & -2.186 \pm 0.028 \\ -0.02858 \pm 0.00038 & -3.423 \pm 0.015 & -0.122 \pm 0.029 \end{pmatrix}$$

$$\mathcal{M}_{36\text{ GHz}} = \begin{pmatrix} 0.7178 \pm 0.0028 & -0.32 \pm 0.12 & -0.38 \pm 0.16 \\ -0.00061 \pm 0.00015 & -0.2077 \pm 0.0036 & -1.1224 \pm 0.0053 \\ -0.00452 \pm 0.00017 & -1.1753 \pm 0.0085 & 0.195 \pm 0.010 \end{pmatrix}$$

$$\mathcal{M}_{39\text{ GHz}} = \begin{pmatrix} 0.6484 \pm 0.0054 & -0.30 \pm 0.18 & 0.40 \pm 0.29 \\ 0.00460 \pm 0.00028 & 0.994 \pm 0.012 & 0.495 \pm 0.015 \\ 0.00085 \pm 0.00034 & -0.4731 \pm 0.0080 & 0.846 \pm 0.013 \end{pmatrix}$$

C | Polarization Properties Distributions

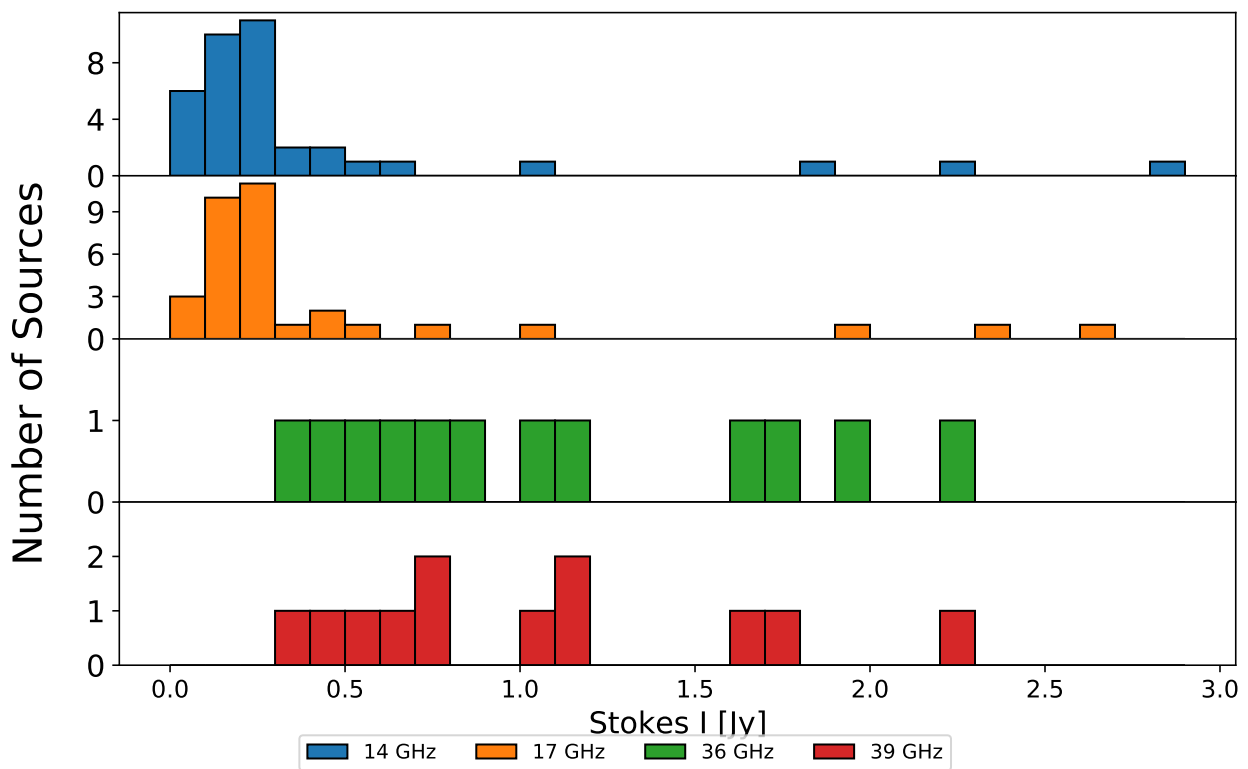


Figure C.1: Distribution of the total intensity Stokes I flux for all sources considered to be polarized in at least one epoch for each individual frequency.

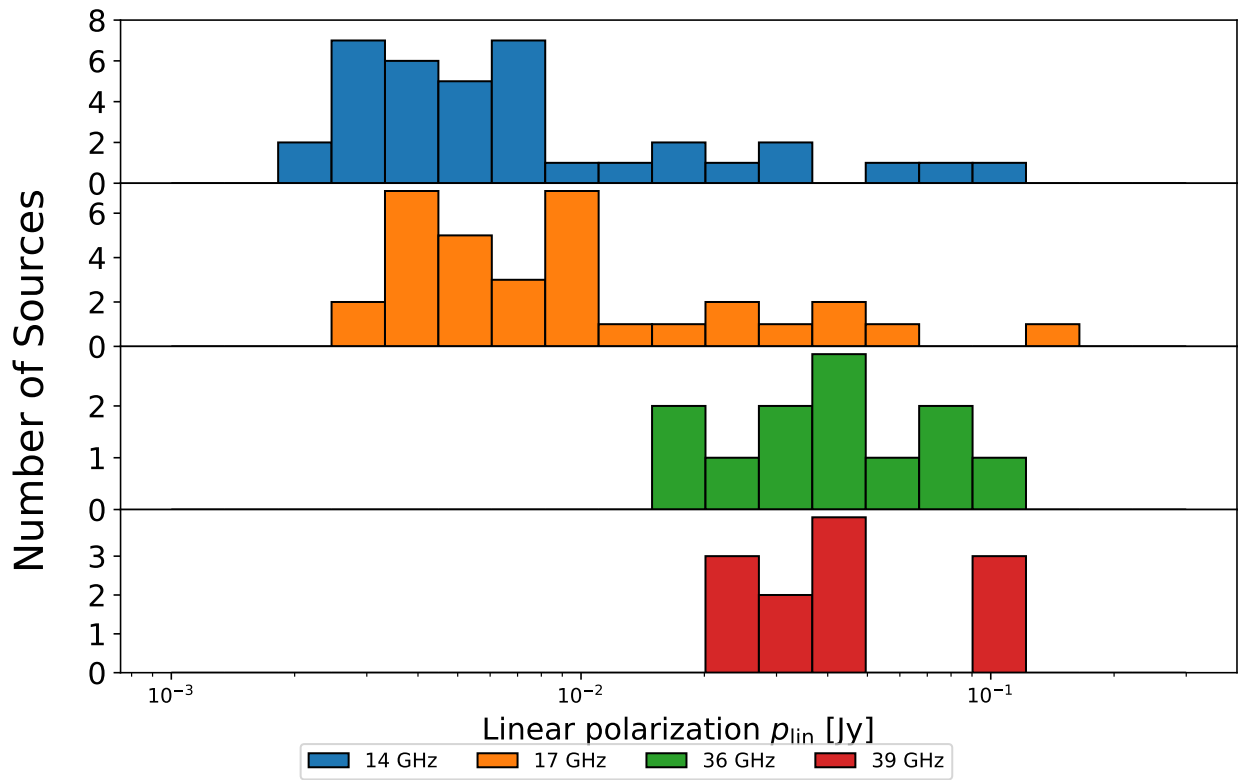


Figure C.2: Distribution of the linearly polarized flux p_{lin} for all sources considered to be polarized in at least one epoch for each individual frequency.

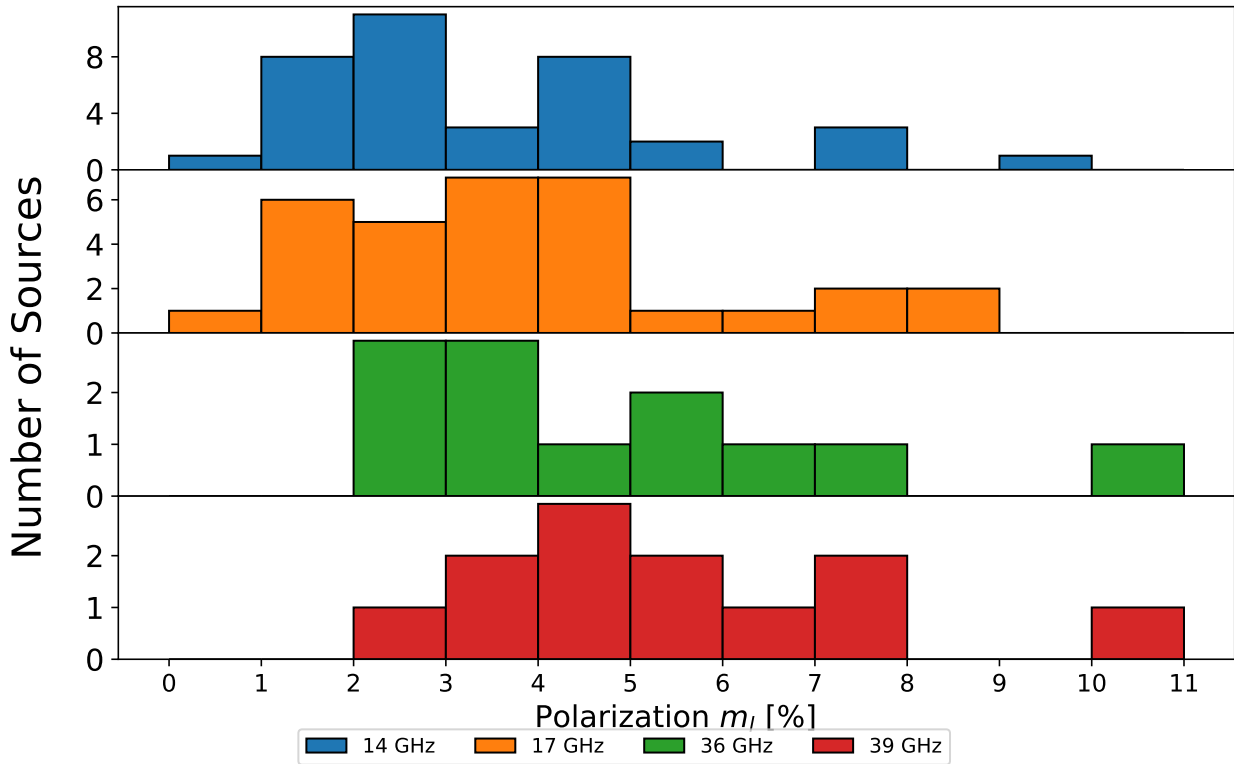


Figure C.3: Distribution of the fractional polarization m_l for all sources considered to be polarized in at least one epoch for each individual frequency.

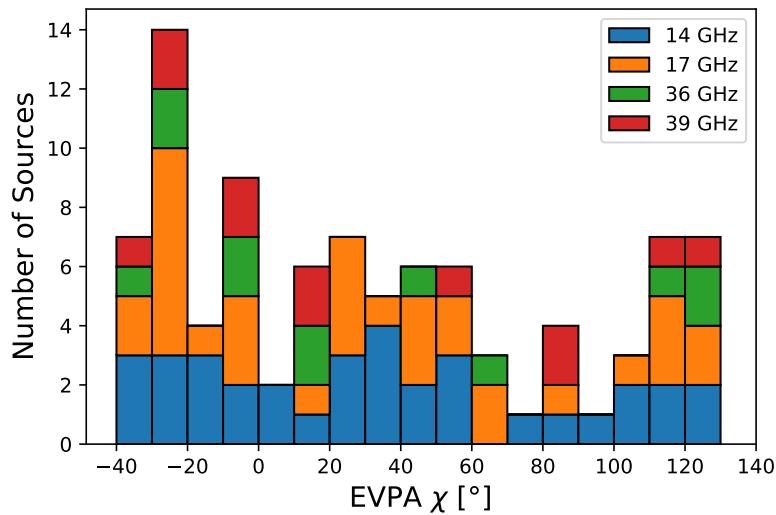


Figure C.4: Distribution of the EVPA χ for all frequencies and sources considered to be polarized in at least one epoch.

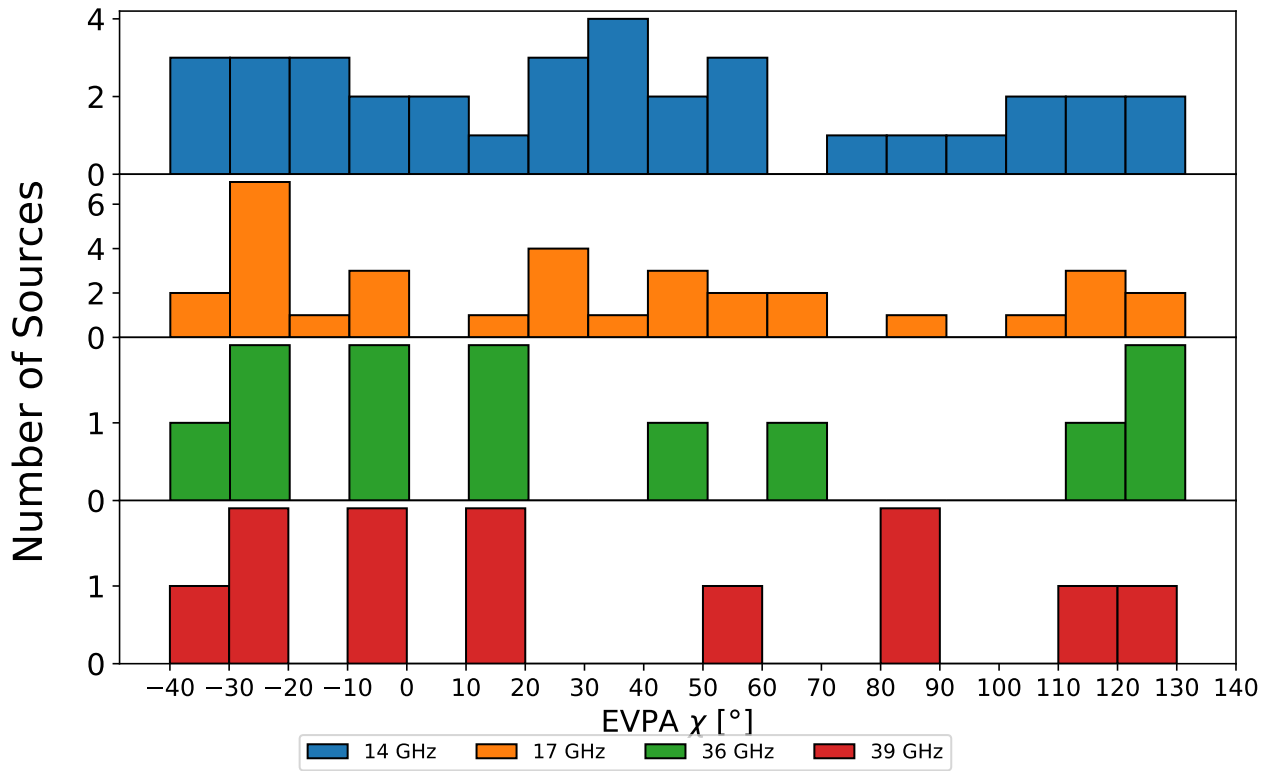


Figure C.5: Distribution of the EVPA χ for all sources considered to be polarized in at least one epoch for each individual frequency.

D | Overview-Plots and Overview-Table of All Sources

Table D.1: Averaged polarization data of all sources and all frequencies where polarization was significantly detected at least once, as presented in the overview-plots in this appendix. The common names of these sources can be found in Table A.1.

Name (J2000)	Frequency	Quantity	Mean	Error
0112+2244	36	Stokes I [Jy]	1.326	0.011
		p_{lin} [Jy]	0.0868	0.0035
		m_l [%]	5.67	0.18
		EVPA [°]	118.09	0.79
	39	Stokes I [Jy]	1.593	0.016
		p_{lin} [Jy]	0.098	0.0051
		m_l [%]	5.7	0.29
		EVPA [°]	118.0	1.1
0214+5144	14	Stokes I [Jy]	0.1667	0.0017
		p_{lin} [Jy]	0.002 71	0.000 46
		m_l [%]	1.58	0.27
		EVPA [°]	40.5	5.1
0217+0144	14	Stokes I [Jy]	3.138	0.016
		p_{lin} [Jy]	0.0824	0.0007
		m_l [%]	2.993	0.033
		EVPA [°]	-31.8	0.23
	17	Stokes I [Jy]	2.837	0.011
		p_{lin} [Jy]	0.0593	0.0013
		m_l [%]	3.114	0.043
		EVPA [°]	-30.15	0.44
	36	Stokes I [Jy]	2.759	0.015
		p_{lin} [Jy]	0.0892	0.0046

Name (J2000)	Frequency	Quantity	Mean	Error
		m_l [%]	3.7	0.22
		EVPA [°]	-29.2	1.7
	39	Stokes I [Jy]	2.425	0.024
		p_{lin} [Jy]	0.1025	0.0068
		m_l [%]	4.51	0.32
		EVPA [°]	-31.0	1.7
0221+3556	36	Stokes I [Jy]	0.4675	0.0078
		p_{lin} [Jy]	0.045	0.004
		m_l [%]	10.2	1.1
		EVPA [°]	49.5	2.1
	39	Stokes I [Jy]	0.4504	0.0098
		p_{lin} [Jy]	0.0396	0.0065
		m_l [%]	10.4	1.8
		EVPA [°]	56.0	4.0
0222+4302	36	Stokes I [Jy]	0.84	0.01
		p_{lin} [Jy]	0.0412	0.0049
		m_l [%]	6.28	0.78
		EVPA [°]	-8.2	4.1
	39	Stokes I [Jy]	0.783	0.011
		p_{lin} [Jy]	0.0454	0.0072
		m_l [%]	7.2	1.2
		EVPA [°]	-9.0	4.8
0258+2030	14	Stokes I [Jy]	0.079	0.0007
		p_{lin} [Jy]	0.0025	0.0011
		m_l [%]	3.2	1.4
		EVPA [°]	99.12	12.0
0303-2407	14	Stokes I [Jy]	0.2108	0.0018
		p_{lin} [Jy]	0.00357	0.00091
		m_l [%]	1.7	0.42
		EVPA [°]	116.9	7.1
0313+0228	14	Stokes I [Jy]	0.2214	0.0024
		p_{lin} [Jy]	0.0054	0.0008
		m_l [%]	2.37	0.35
		EVPA [°]	-5.3	4.8
	17	Stokes I [Jy]	0.2402	0.0031
		p_{lin} [Jy]	0.01	0.001
		m_l [%]	4.02	0.43

Name (J2000)	Frequency	Quantity	Mean	Error	
0738+1742	14	EVPA [°]	-7.4	3.6	
		Stokes I [Jy]	0.9825	0.0053	
		p_{lin} [Jy]	0.00787	0.00051	
	17	m_l [%]	0.591	0.052	
		EVPA [°]	131.2	1.6	
		Stokes I [Jy]	1.0814	0.0052	
		p_{lin} [Jy]	0.0106	0.0008	
		m_l [%]	0.984	0.085	
		EVPA [°]	115.8	2.2	
	36	Stokes I [Jy]	1.016	0.012	
		p_{lin} [Jy]	0.0278	0.0044	
		m_l [%]	2.32	0.38	
EVPA [°]		121.7	4.4		
39		Stokes I [Jy]	1.087	0.015	
		p_{lin} [Jy]	0.0263	0.0056	
	m_l [%]	2.18	0.47		
0809+5219	14	EVPA [°]	125.8	5.4	
		Stokes I [Jy]	0.1256	0.0015	
		p_{lin} [Jy]	0.00321	0.00094	
		m_l [%]	2.34	0.69	
	17	EVPA [°]	140.7	8.1	
		Stokes I [Jy]	0.1202	0.0017	
		p_{lin} [Jy]	0.004	0.0014	
		m_l [%]	3.3	1.1	
	0836+71	14	EVPA [°]	126.6	9.4
			Stokes I [Jy]	2.223	0.054
			p_{lin} [Jy]	0.0648	0.0038
			m_l [%]	2.91	0.19
17		EVPA [°]	109.71	0.81	
		Stokes I [Jy]	2.353	0.045	
		p_{lin} [Jy]	0.0368	0.0055	
		m_l [%]	1.55	0.25	
36		EVPA [°]	115.4	3.5	
		Stokes I [Jy]	1.87	0.11	
		p_{lin} [Jy]	0.0655	0.0099	
		m_l [%]	3.41	0.54	
		EVPA [°]	123.0	4.0	

Name (J2000)	Frequency	Quantity	Mean	Error
1015+4926	14	Stokes I [Jy]	0.2331	0.0024
		p_{lin} [Jy]	0.006 04	0.000 43
		m_l [%]	2.41	0.18
		EVPA [°]	−6.0	2.3
	17	Stokes I [Jy]	0.2379	0.0021
		p_{lin} [Jy]	0.005 47	0.000 62
		m_l [%]	2.34	0.27
		EVPA [°]	−9.4	3.3
1025+1253	14	Stokes I [Jy]	0.6095	0.0068
		p_{lin} [Jy]	0.0113	0.0004
		m_l [%]	1.71	0.07
		EVPA [°]	57.8	1.0
	17	Stokes I [Jy]	0.7662	0.0048
		p_{lin} [Jy]	0.011 04	0.000 69
		m_l [%]	1.5	0.092
		EVPA [°]	44.3	2.2
	36	Stokes I [Jy]	1.074	0.021
		p_{lin} [Jy]	0.042	0.004
		m_l [%]	4.02	0.39
		EVPA [°]	18.5	2.7
39	Stokes I [Jy]	1.12	0.02	
	p_{lin} [Jy]	0.046	0.005	
	m_l [%]	4.27	0.47	
	EVPA [°]	18.5	3.0	
1058+2817	14	Stokes I [Jy]	0.089 93	0.000 68
		p_{lin} [Jy]	0.004 67	0.000 58
		m_l [%]	5.04	0.64
		EVPA [°]	20.9	3.7
	17	Stokes I [Jy]	0.1041	0.0019
		p_{lin} [Jy]	0.004 51	0.000 85
		m_l [%]	4.98	0.98
		EVPA [°]	21.0	5.8
1104+3812	39	Stokes I [Jy]	0.444	0.018
		p_{lin} [Jy]	0.025	0.008
		m_l [%]	4.3	1.6
		EVPA [°]	86.84	35.0
1136+7009	14	Stokes I [Jy]	0.162	0.0016

Name (J2000)	Frequency	Quantity	Mean	Error
		p_{lin} [Jy]	0.007 37	0.000 37
		m_l [%]	4.42	0.23
		EVPA [°]	-15.8	1.7
	17	Stokes I [Jy]	0.161	0.0016
		p_{lin} [Jy]	0.008 22	0.000 51
		m_l [%]	4.93	0.33
		EVPA [°]	-23.1	2.6
1145+1936	14	Stokes I [Jy]	0.5421	0.0035
		p_{lin} [Jy]	0.022 85	0.000 35
		m_l [%]	4.223	0.069
		EVPA [°]	124.2	0.5
	17	Stokes I [Jy]	0.4269	0.0021
		p_{lin} [Jy]	0.018 82	0.000 56
		m_l [%]	4.28	0.13
		EVPA [°]	120.12	0.83
1221+2813	36	Stokes I [Jy]	0.4955	0.0076
		p_{lin} [Jy]	0.0207	0.0083
		m_l [%]	3.9	1.6
		EVPA [°]	18.53	12.0
	39	Stokes I [Jy]	0.494	0.012
		p_{lin} [Jy]	0.037	0.017
		m_l [%]	5.0	2.4
		EVPA [°]	15.11	21.0
1422+3223	36	Stokes I [Jy]	0.744	0.0071
		p_{lin} [Jy]	0.0201	0.0054
		m_l [%]	2.83	0.77
		EVPA [°]	62.6	7.2
	39	Stokes I [Jy]	0.828	0.011
		p_{lin} [Jy]	0.0254	0.0082
		m_l [%]	3.8	1.3
		EVPA [°]	85.01	30.0
1443+2501	14	Stokes I [Jy]	0.2354	0.0011
		p_{lin} [Jy]	0.011	0.000 26
		m_l [%]	4.81	0.12
		EVPA [°]	-30.37	0.68
	17	Stokes I [Jy]	0.2125	0.0012
		p_{lin} [Jy]	0.010 66	0.000 37

Name (J2000)	Frequency	Quantity	Mean	Error
		m_l [%]	4.95	0.17
		EVPA [°]	-28.96	0.95
1451-0127	14	Stokes I [Jy]	0.1634	0.0049
		p_{lin} [Jy]	0.0077	0.0009
		m_l [%]	4.7	0.57
		EVPA [°]	-23.4	3.5
	17	Stokes I [Jy]	0.156	0.011
		p_{lin} [Jy]	0.0087	0.0018
		m_l [%]	5.7	1.2
		EVPA [°]	-27.6	7.1
1458-0037	14	Stokes I [Jy]	0.0805	0.0035
		p_{lin} [Jy]	0.0033	0.0014
		m_l [%]	4.1	1.8
		EVPA [°]	102.1	10.0
1510+5702	14	Stokes I [Jy]	0.2421	0.0029
		p_{lin} [Jy]	0.0042	0.0011
		m_l [%]	1.49	0.39
		EVPA [°]	-15.8	7.4
	17	Stokes I [Jy]	0.222	0.0041
		p_{lin} [Jy]	0.0043	0.0015
		m_l [%]	1.56	0.53
		EVPA [°]	-15.35	10.0
1518-2731	14	Stokes I [Jy]	0.204	0.0031
		p_{lin} [Jy]	0.005	0.0012
		m_l [%]	2.46	0.58
		EVPA [°]	21.5	6.5
1542+6129	14	Stokes I [Jy]	0.1021	0.0012
		p_{lin} [Jy]	0.0024	0.0011
		m_l [%]	2.5	1.1
		EVPA [°]	-17.36	12.0
1555+1111	14	Stokes I [Jy]	0.3311	0.0018
		p_{lin} [Jy]	0.0056	0.0004
		m_l [%]	1.58	0.12
		EVPA [°]	116.8	2.0
	17	Stokes I [Jy]	0.367	0.002
		p_{lin} [Jy]	0.00704	0.00054
		m_l [%]	2.06	0.16

Name (J2000)	Frequency	Quantity	Mean	Error	
1653+3945	36	EVPA [°]	111.4	2.1	
		Stokes I [Jy]	0.901	0.014	
		p_{lin} [Jy]	0.0198	0.0081	
	39	m_l [%]	2.06	0.85	
		EVPA [°]	-0.85	13.0	
		Stokes I [Jy]	1.005	0.024	
		p_{lin} [Jy]	0.0398	0.0061	
		m_l [%]	3.8	0.65	
		EVPA [°]	-0.2	9.6	
1728+1215	14	Stokes I [Jy]	0.4617	0.0026	
		p_{lin} [Jy]	0.036 34	0.000 37	
		m_l [%]	7.757	0.093	
	17	EVPA [°]	-25.74	0.34	
		Stokes I [Jy]	0.4756	0.0042	
		p_{lin} [Jy]	0.039 61	0.000 48	
	36	m_l [%]	8.12	0.12	
		EVPA [°]	-25.8	0.35	
		Stokes I [Jy]	0.452	0.011	
	39	p_{lin} [Jy]	0.0311	0.0053	
		m_l [%]	7.6	1.3	
		EVPA [°]	-39.3	3.5	
	1728+5013	14	Stokes I [Jy]	0.471	0.012
			p_{lin} [Jy]	0.032	0.012
			m_l [%]	7.1	2.9
17		EVPA [°]	-24.04	11.0	
		Stokes I [Jy]	0.128 88	0.000 75	
		p_{lin} [Jy]	0.003 31	0.000 35	
36		m_l [%]	2.56	0.28	
		EVPA [°]	58.4	3.0	
		Stokes I [Jy]	0.1255	0.0018	
39	p_{lin} [Jy]	0.0037	0.000 66		
	m_l [%]	3.1	0.6		
	EVPA [°]	62.7	5.2		
1743+1935	14	Stokes I [Jy]	0.2205	0.0014	
		p_{lin} [Jy]	0.003 91	0.000 36	
		m_l [%]	1.79	0.16	
		EVPA [°]	57.7	2.8	

Name (J2000)	Frequency	Quantity	Mean	Error
1746+1127	17	Stokes I [Jy]	0.2192	0.0027
		p_{lin} [Jy]	0.004 24	0.000 52
		m_l [%]	1.97	0.24
		EVPA [°]	54.6	4.3
1751+0939	14	Stokes I [Jy]	0.1617	0.0026
		p_{lin} [Jy]	0.0073	0.0008
		m_l [%]	4.56	0.52
		EVPA [°]	21.3	3.6
1752-1011	17	Stokes I [Jy]	0.16	0.01
		p_{lin} [Jy]	0.006	0.0017
		m_l [%]	3.44	0.96
		EVPA [°]	26.7	8.3
1752-1011	14	Stokes I [Jy]	2.344	0.017
		p_{lin} [Jy]	0.1117	0.000 89
		m_l [%]	5.99	0.073
		EVPA [°]	-24.16	0.19
1752-1011	17	Stokes I [Jy]	2.2822	0.0097
		p_{lin} [Jy]	0.147 35	0.000 92
		m_l [%]	7.192	0.092
		EVPA [°]	-26.43	0.24
1752-1011	36	Stokes I [Jy]	1.98	0.015
		p_{lin} [Jy]	0.0976	0.0088
		m_l [%]	5.72	0.57
		EVPA [°]	-24.3	2.5
1752-1011	39	Stokes I [Jy]	2.22	0.019
		p_{lin} [Jy]	0.103	0.011
		m_l [%]	6.18	0.81
		EVPA [°]	-28.3	3.0
1752-1011	14	Stokes I [Jy]	0.2201	0.0044
		p_{lin} [Jy]	0.003 77	0.000 57
		m_l [%]	1.7	0.27
		EVPA [°]	123.1	6.4
1758-1203	17	Stokes I [Jy]	0.2071	0.0023
		p_{lin} [Jy]	0.0061	0.0012
		m_l [%]	2.75	0.52
		EVPA [°]	66.38	48.0
1758-1203	17	Stokes I [Jy]	0.184	0.025

Name (J2000)	Frequency	Quantity	Mean	Error
		p_{lin} [Jy]	0.0111	0.0032
		m_l [%]	6.4	1.9
		EVPA [°]	-26.5	11.0
1803+2521	14	Stokes I [Jy]	0.1653	0.0014
		p_{lin} [Jy]	0.006 93	0.000 67
		m_l [%]	4.02	0.39
		EVPA [°]	32.4	3.2
	17	Stokes I [Jy]	0.1708	0.0015
		p_{lin} [Jy]	0.005 44	0.000 87
		m_l [%]	2.95	0.46
		EVPA [°]	24.7	4.9
1813+3144	14	Stokes I [Jy]	0.1107	0.0011
		p_{lin} [Jy]	0.002 96	0.000 84
		m_l [%]	2.65	0.75
		EVPA [°]	76.4	9.8
	17	Stokes I [Jy]	0.1081	0.0026
		p_{lin} [Jy]	0.004	0.0011
		m_l [%]	3.55	0.98
		EVPA [°]	103.3	7.7
1959+6508	14	Stokes I [Jy]	0.207 61	0.000 89
		p_{lin} [Jy]	0.007 01	0.000 47
		m_l [%]	3.27	0.22
		EVPA [°]	0.9	2.0
	17	Stokes I [Jy]	0.1895	0.0015
		p_{lin} [Jy]	0.007 56	0.000 69
		m_l [%]	3.64	0.33
		EVPA [°]	-5.8	2.6
2001+4352	14	Stokes I [Jy]	0.2563	0.0029
		p_{lin} [Jy]	0.019 13	0.000 65
		m_l [%]	7.4	0.29
		EVPA [°]	88.32	0.74
	17	Stokes I [Jy]	0.2829	0.0025
		p_{lin} [Jy]	0.025 34	0.000 98
		m_l [%]	7.61	0.31
		EVPA [°]	82.77	0.92
2018+3851	14	Stokes I [Jy]	0.4193	0.0035
		p_{lin} [Jy]	0.020 01	0.000 41

Name (J2000)	Frequency	Quantity	Mean	Error
		m_l [%]	4.39	0.089
		EVPA [°]	14.0	0.56
	17	Stokes I [Jy]	0.4401	0.0031
		p_{lin} [Jy]	0.020 45	0.000 52
		m_l [%]	4.29	0.13
		EVPA [°]	13.59	0.74
2049+1822	14	Stokes I [Jy]	0.1952	0.0045
		p_{lin} [Jy]	0.0026	0.0012
		m_l [%]	1.33	0.59
		EVPA [°]	30.85	15.0
	17	Stokes I [Jy]	0.1908	0.0017
		p_{lin} [Jy]	0.0036	0.0009
		m_l [%]	1.92	0.48
		EVPA [°]	41.27	12.0
2108+1430	14	Stokes I [Jy]	0.2268	0.0054
		p_{lin} [Jy]	0.0078	0.0008
		m_l [%]	3.47	0.35
		EVPA [°]	4.3	2.9
	17	Stokes I [Jy]	0.2113	0.0092
		p_{lin} [Jy]	0.0097	0.0009
		m_l [%]	4.54	0.44
		EVPA [°]	-28.5	2.8
2123+3012	14	Stokes I [Jy]	0.3598	0.0077
		p_{lin} [Jy]	0.034 16	0.000 65
		m_l [%]	9.63	0.23
		EVPA [°]	43.5	0.7
	17	Stokes I [Jy]	0.2927	0.0021
		p_{lin} [Jy]	0.033 24	0.000 86
		m_l [%]	11.23	0.32
		EVPA [°]	41.3	1.0
2126+2904	14	Stokes I [Jy]	0.0579	0.0028
		p_{lin} [Jy]	0.0041	0.0009
		m_l [%]	7.2	1.6
		EVPA [°]	30.4	7.5
	17	Stokes I [Jy]	0.0545	0.0022
		p_{lin} [Jy]	0.0047	0.0016
		m_l [%]	8.8	3.1

Name (J2000)	Frequency	Quantity	Mean	Error
2212+0646	17	EVPA [°]	29.9	13.0
		Stokes I [Jy]	0.2376	0.0021
		p_{lin} [Jy]	0.0032	0.0015
		m_l [%]	1.37	0.63
2243+2021	14	EVPA [°]	51.75	22.0
		Stokes I [Jy]	0.095 51	0.000 72
		p_{lin} [Jy]	0.0023	0.0006
		m_l [%]	2.45	0.64
	17	EVPA [°]	33.3	8.2
		Stokes I [Jy]	0.1004	0.0013
		p_{lin} [Jy]	0.003	0.001
		m_l [%]	3.4	1.1
2347+5142	14	EVPA [°]	32.15	10.0
		Stokes I [Jy]	0.1645	0.0011
		p_{lin} [Jy]	0.003 45	0.000 42
		m_l [%]	2.07	0.26
	17	EVPA [°]	-36.4	3.7
		Stokes I [Jy]	0.1626	0.0011
		p_{lin} [Jy]	0.0042	0.000 73
		m_l [%]	2.59	0.44
		EVPA [°]	-38.4	5.5

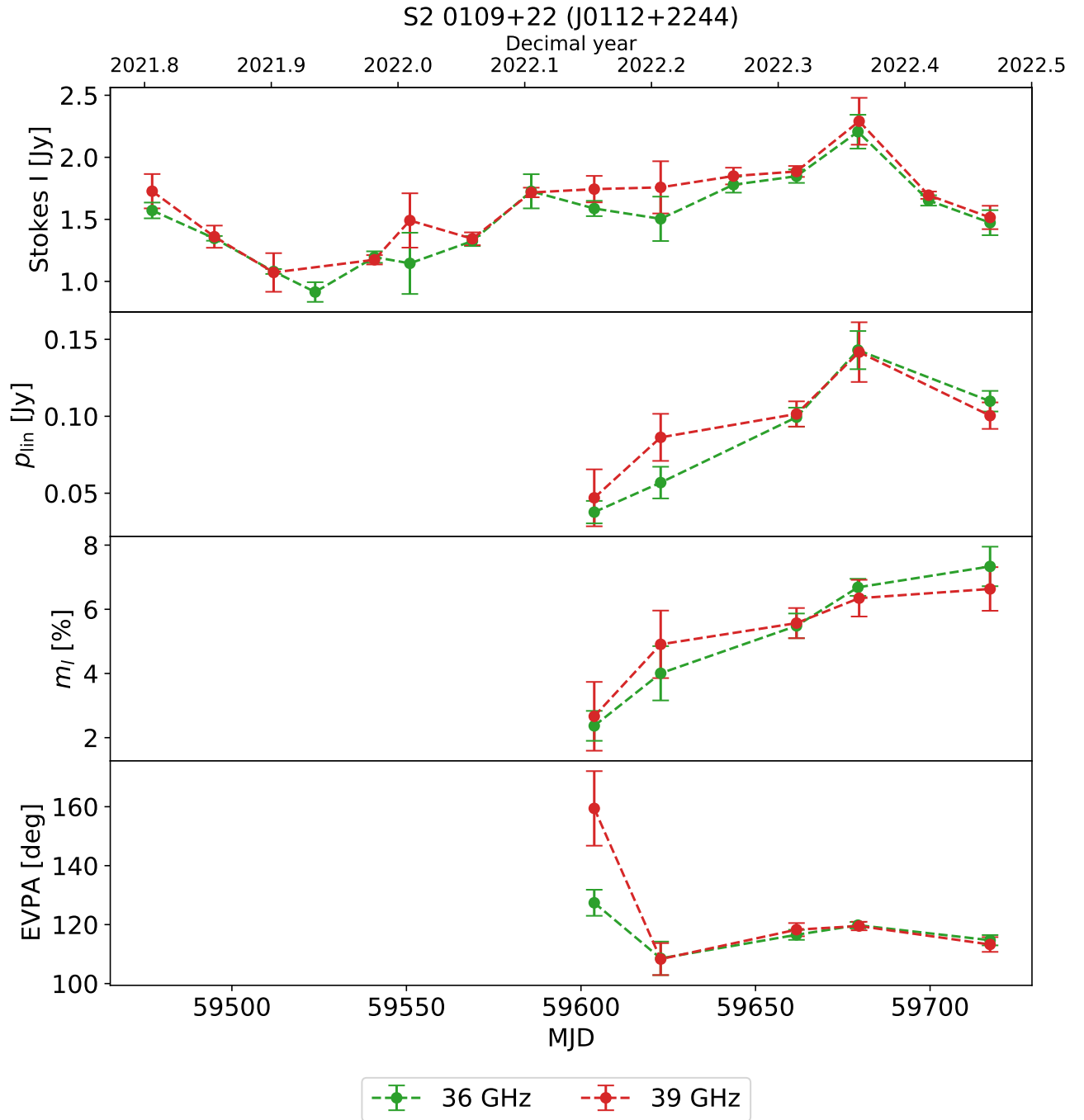


Figure D.1: Overview-plot of S2 0109+22 (J0112+2244).

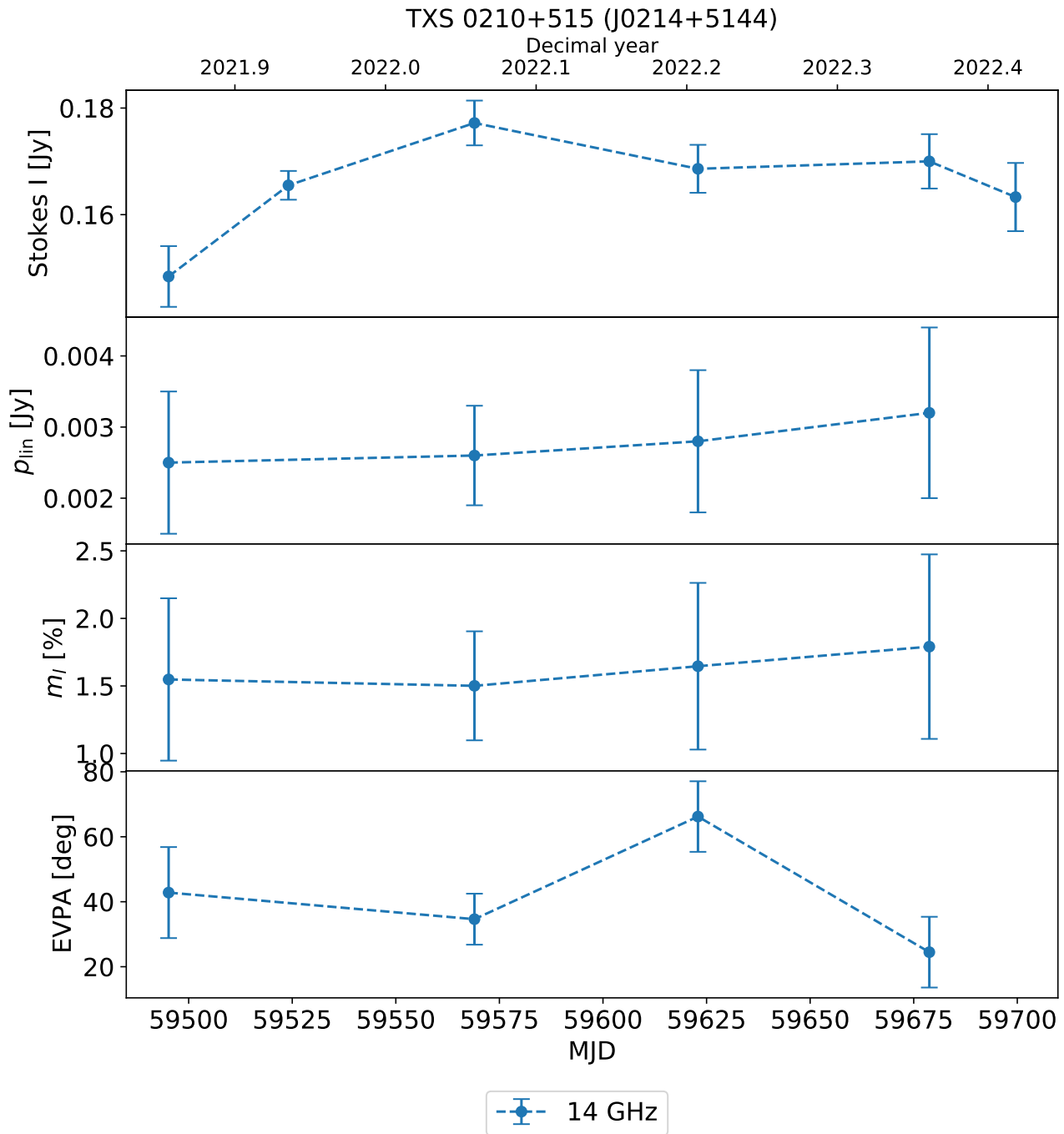


Figure D.2: Overview-plot of TXS 0210+515 (J0214+5144).

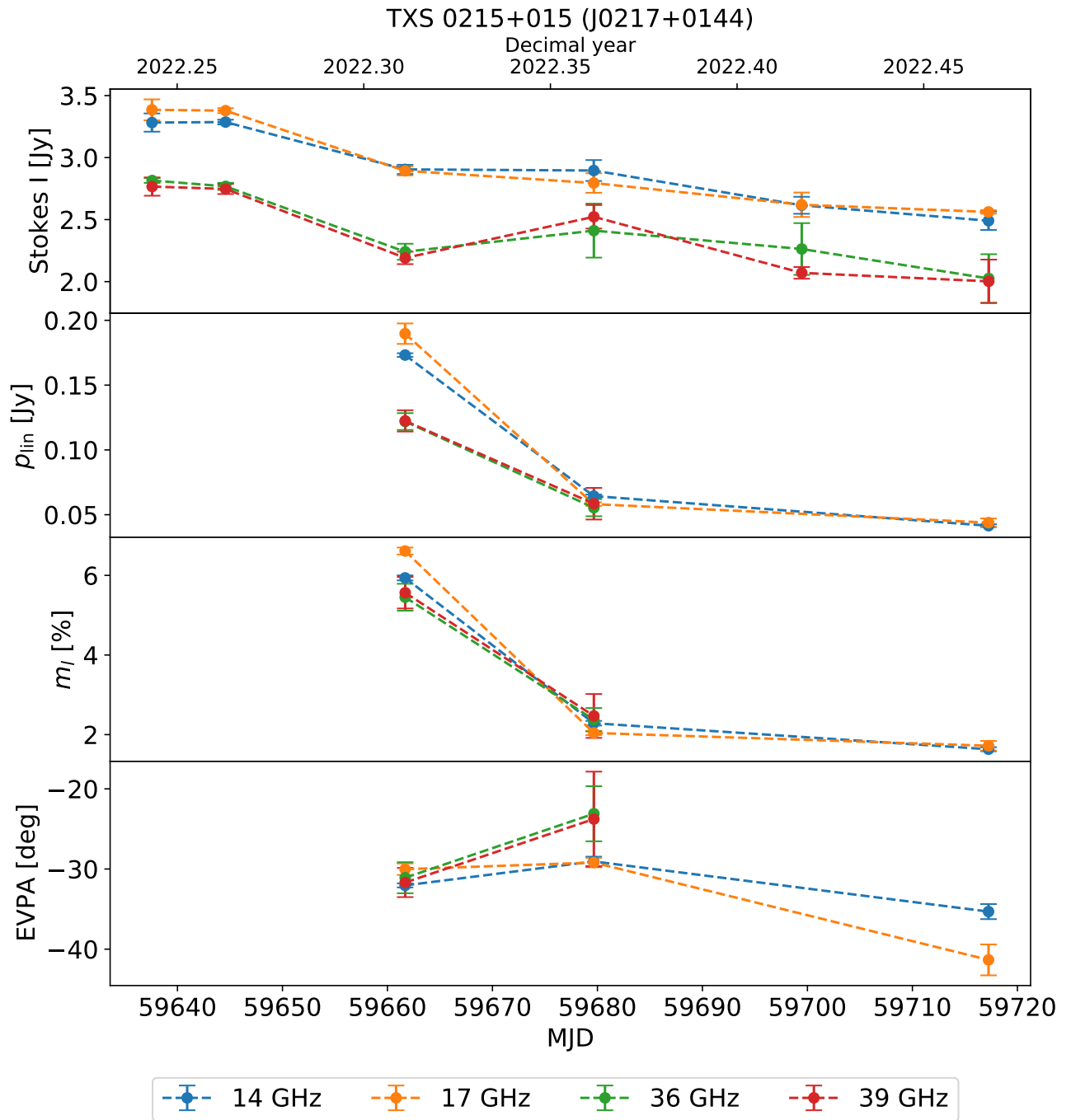


Figure D.3: Overview-plot of TXS 0215+015 (J0217+0144).

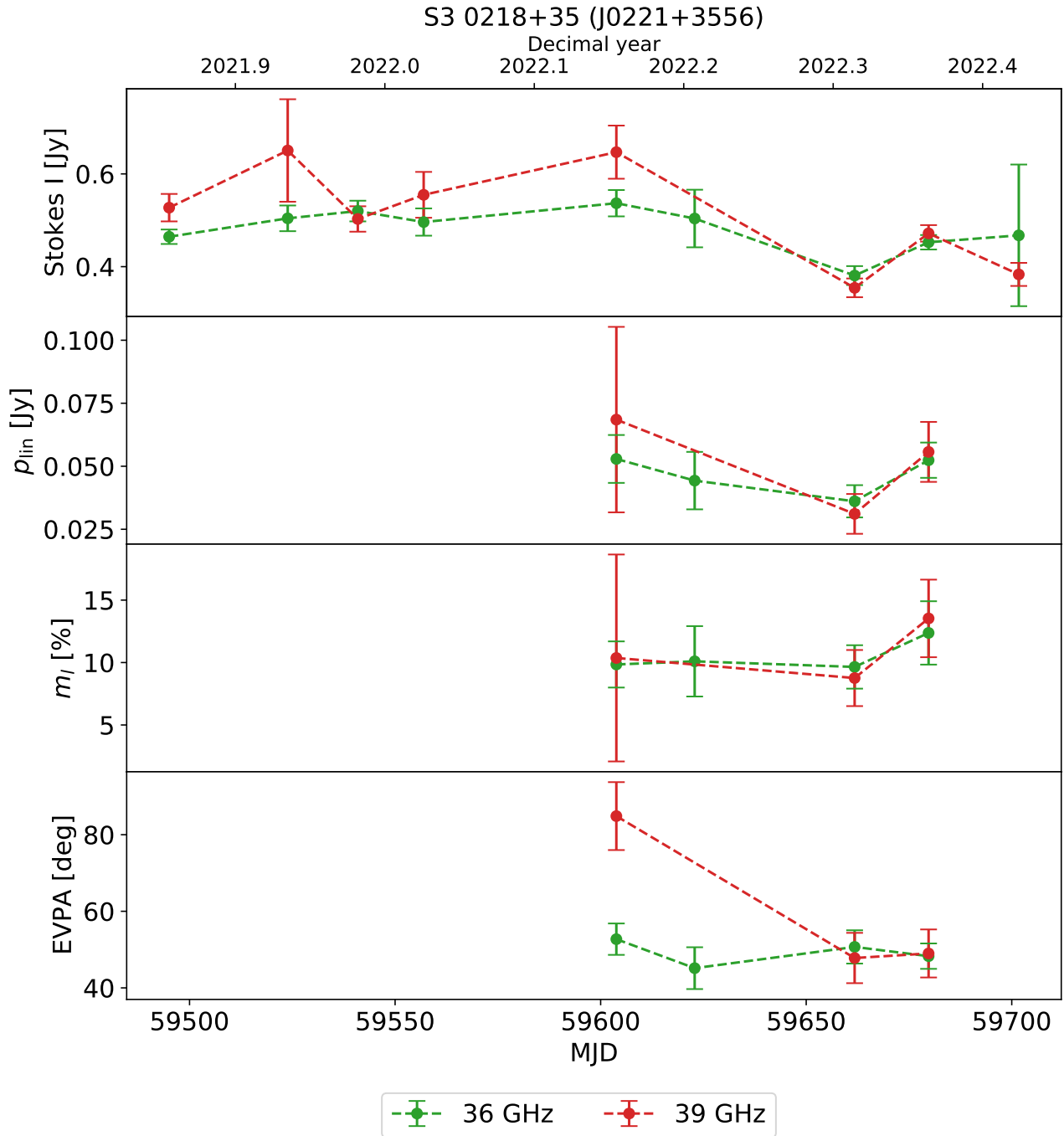


Figure D.4: Overview-plot of S3 0218+35 (J0221+3556).

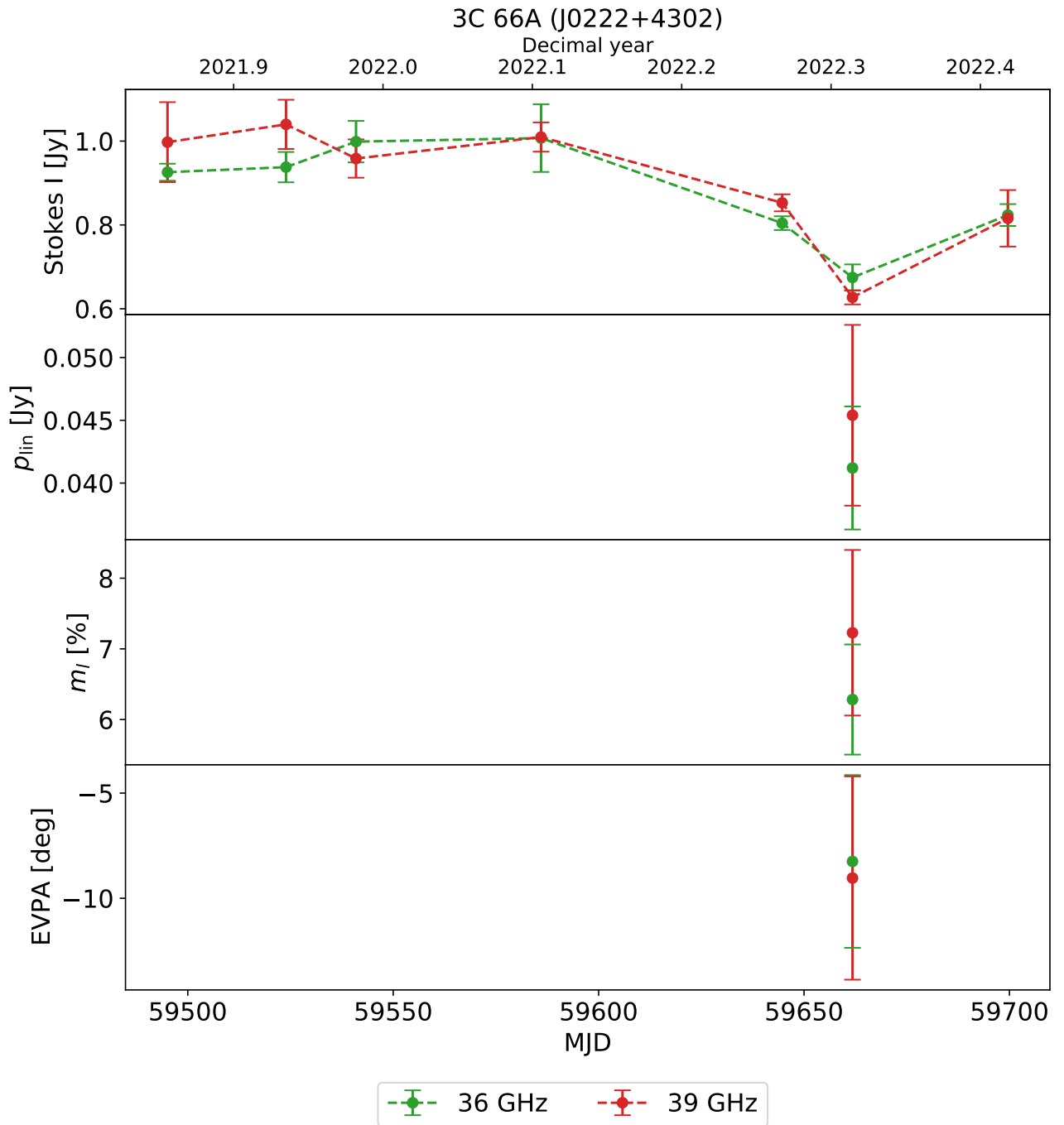


Figure D.5: Overview-plot of 3C 66A (J0222+4302).

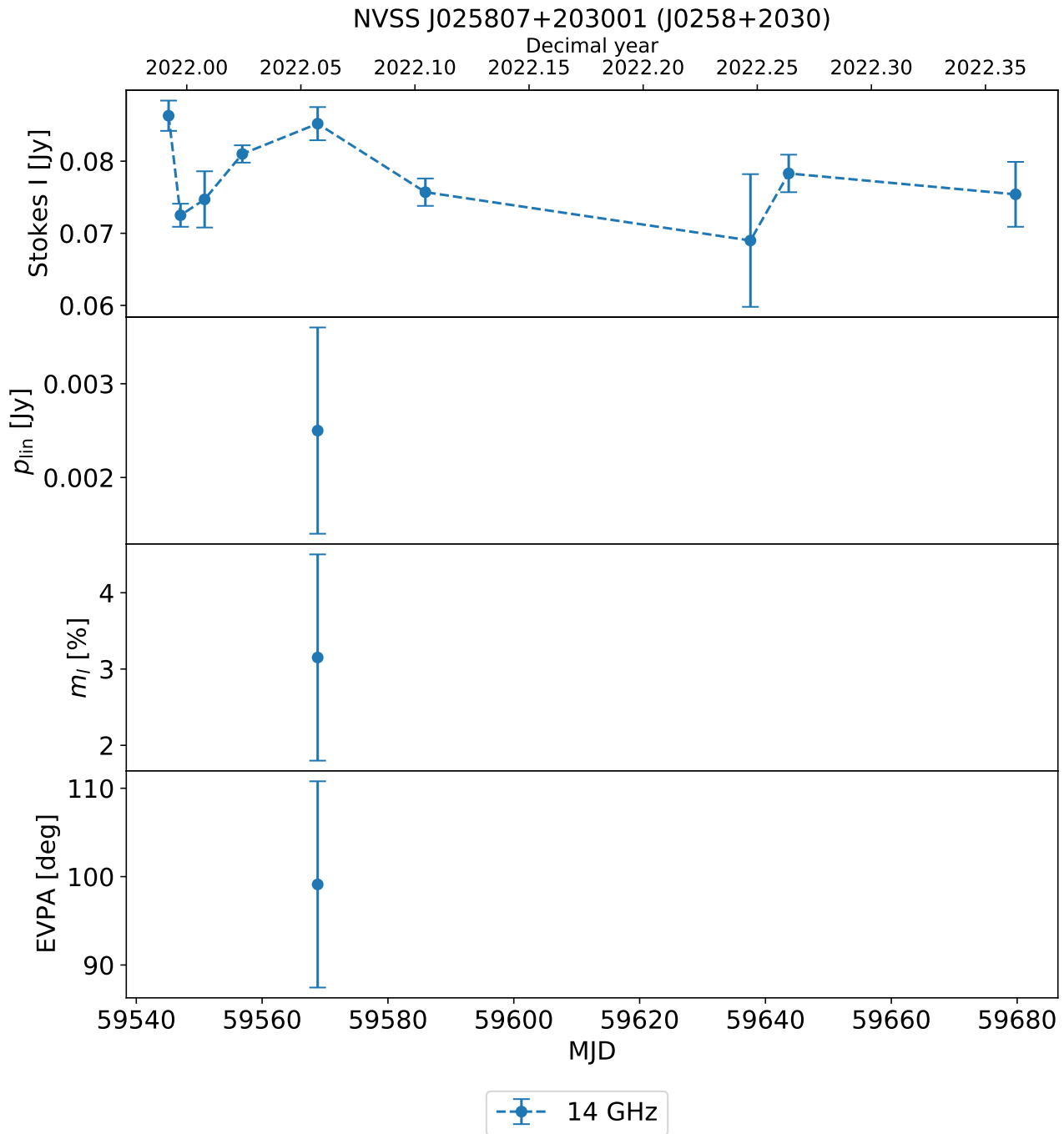


Figure D.6: Overview-plot of NVSS J025807+203001 (J0258+2030).

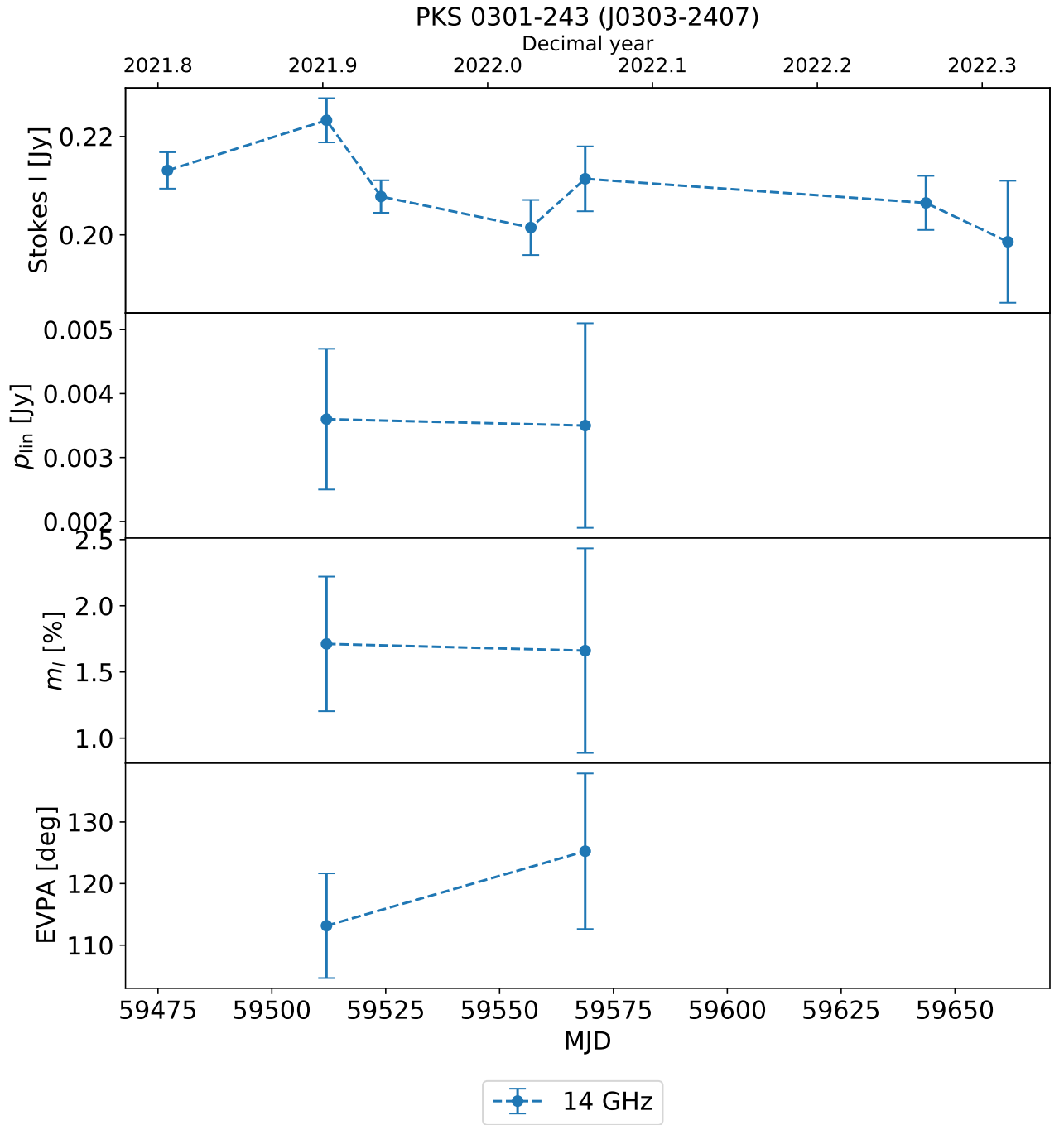


Figure D.7: Overview-plot of PKS 0301-243 (J0303-2407).

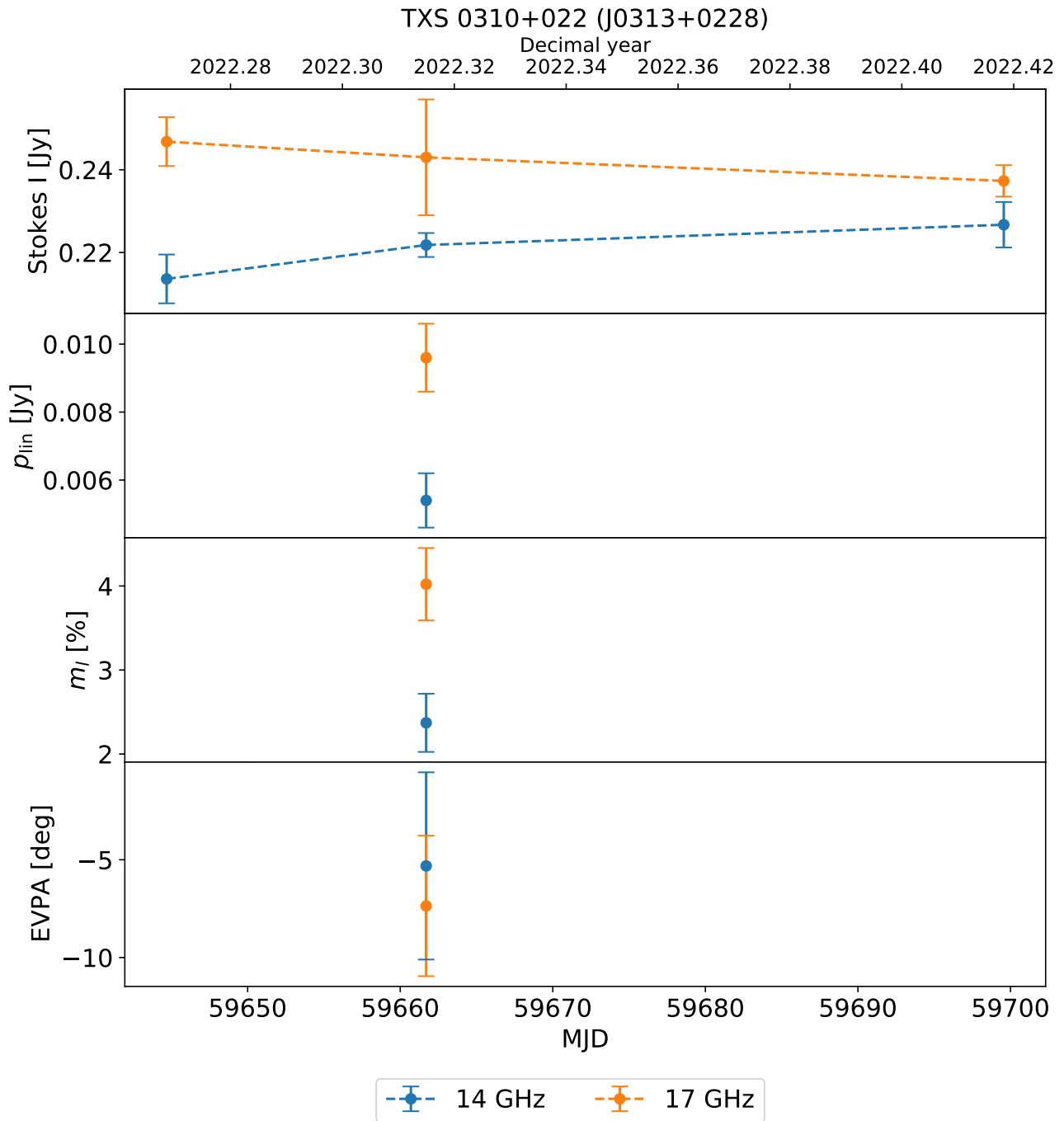


Figure D.8: Overview-plot of TXS 0310+022 (J0313+0228).

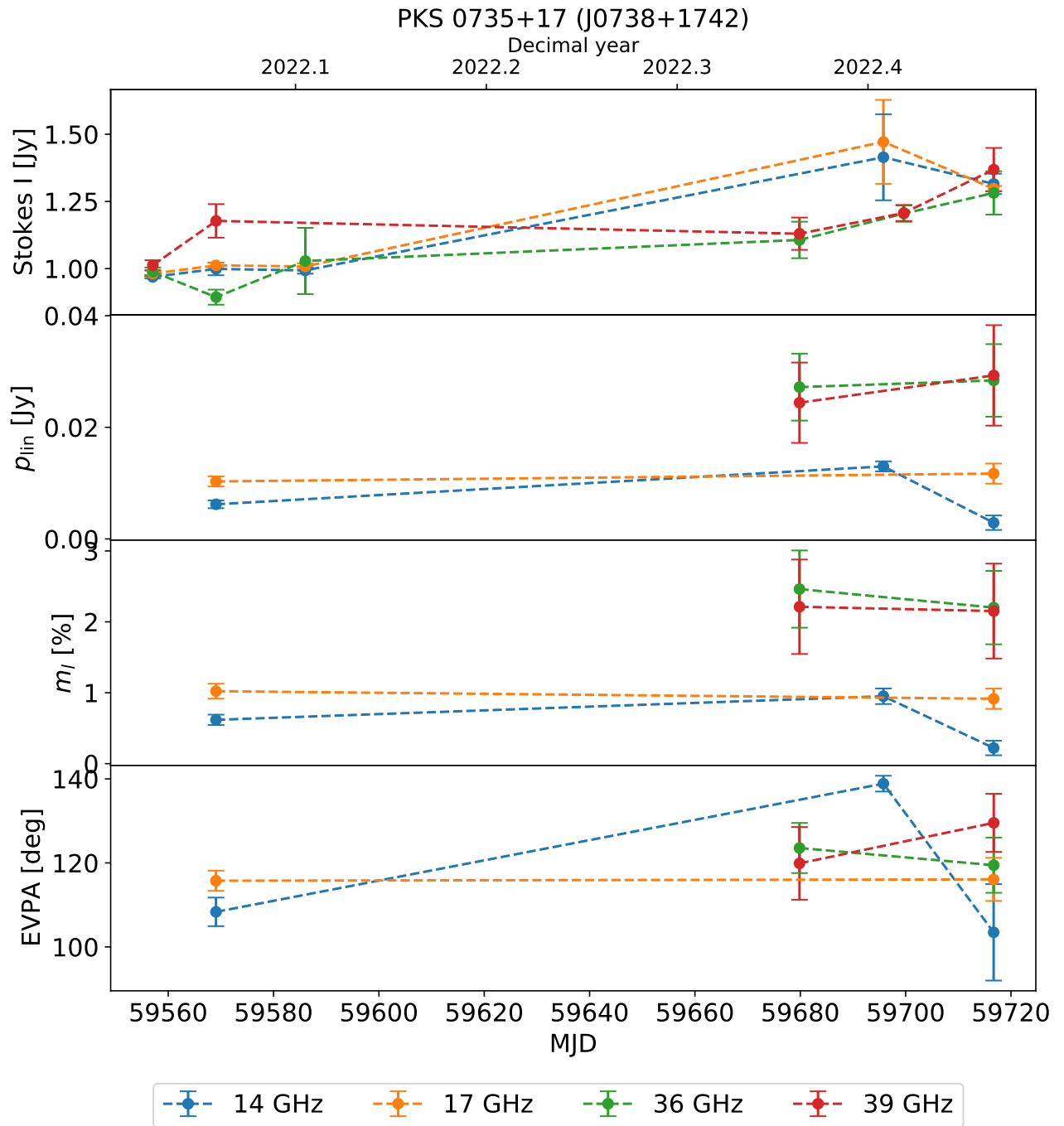


Figure D.9: Overview-plot of PKS 0735+17 (J0738+1742).

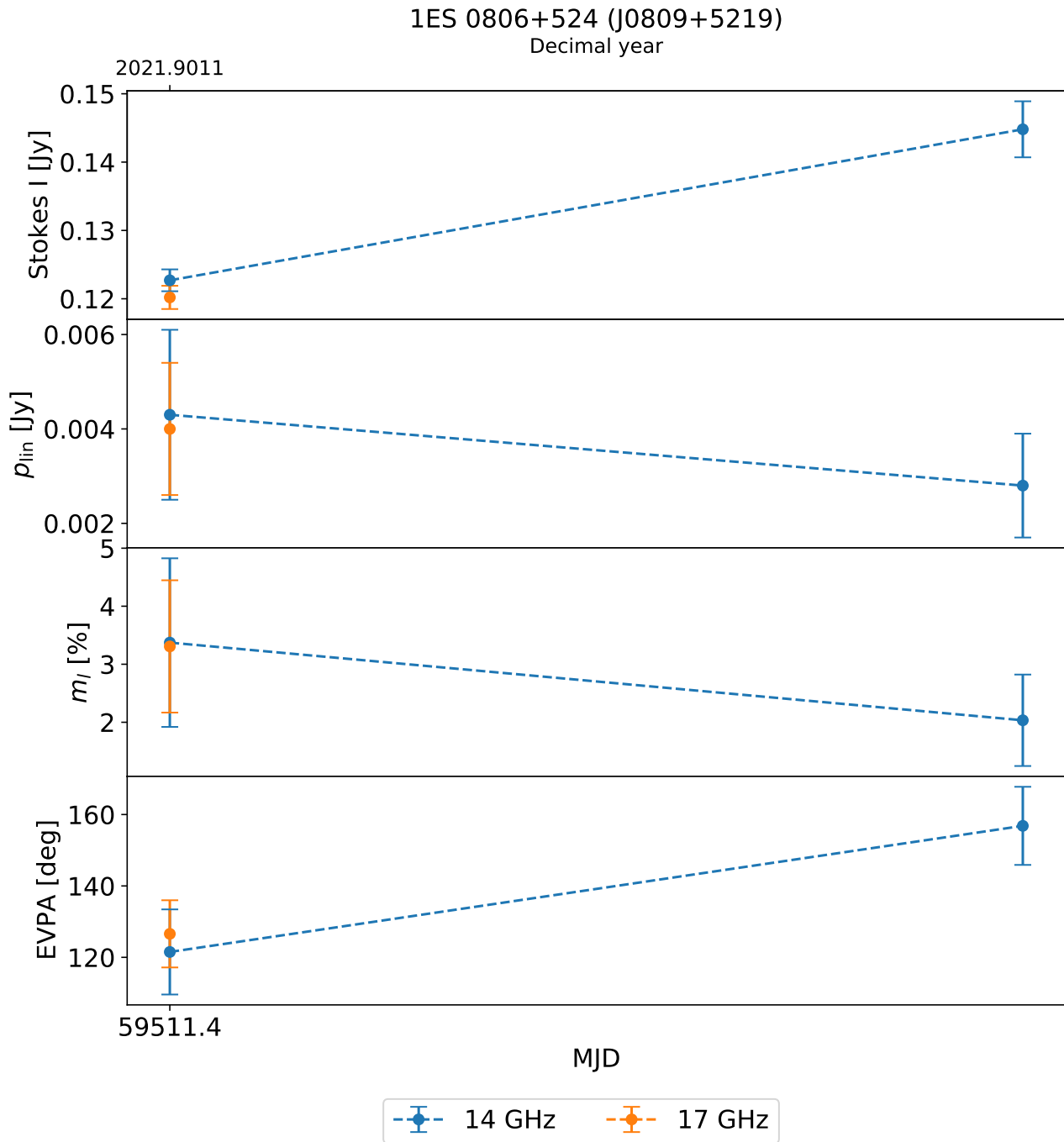


Figure D.10: Overview-plot of 1ES 0806+524 (J0809+5219).

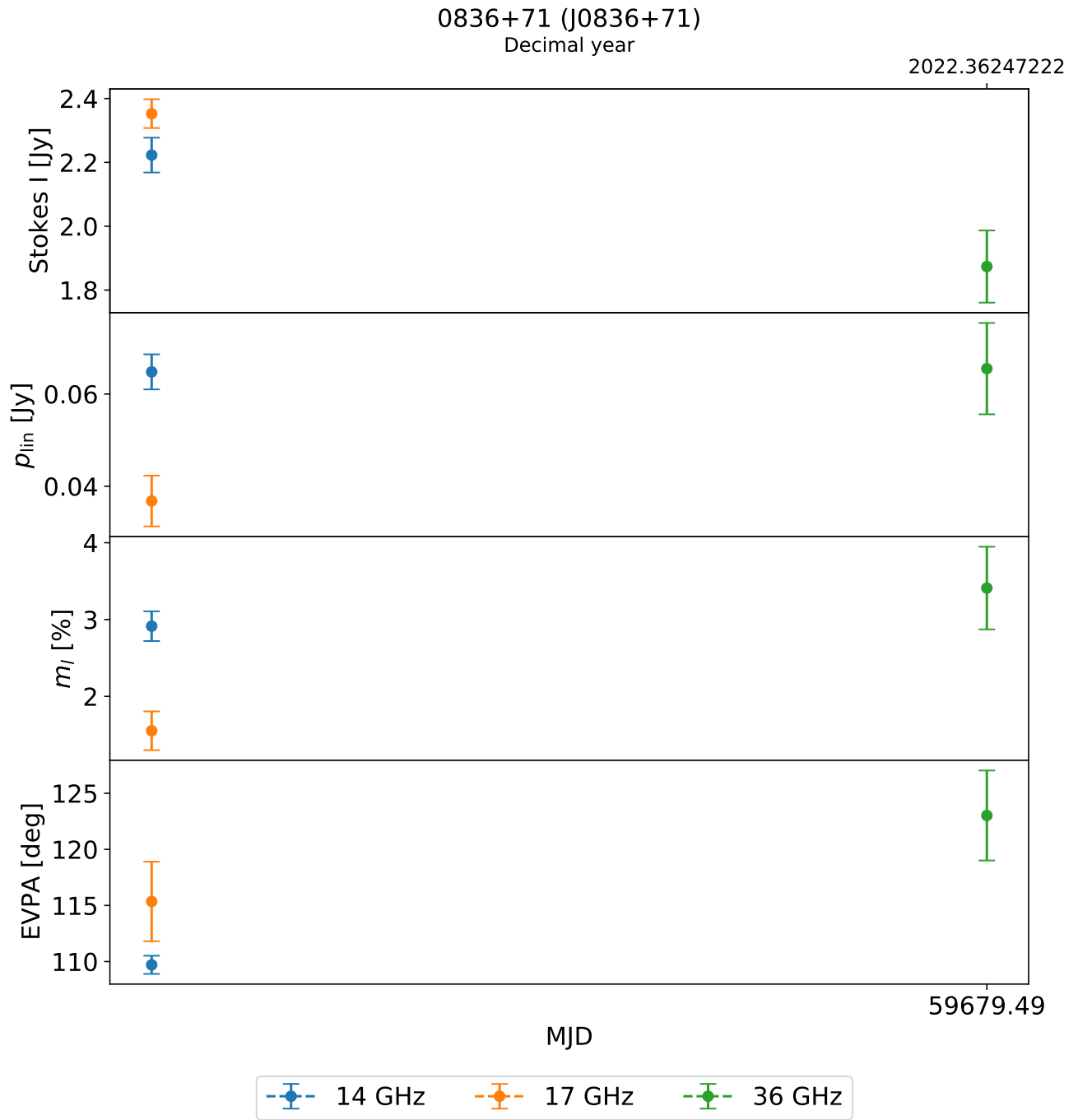


Figure D.11: Overview-plot of 0836+71 (J0836+71).

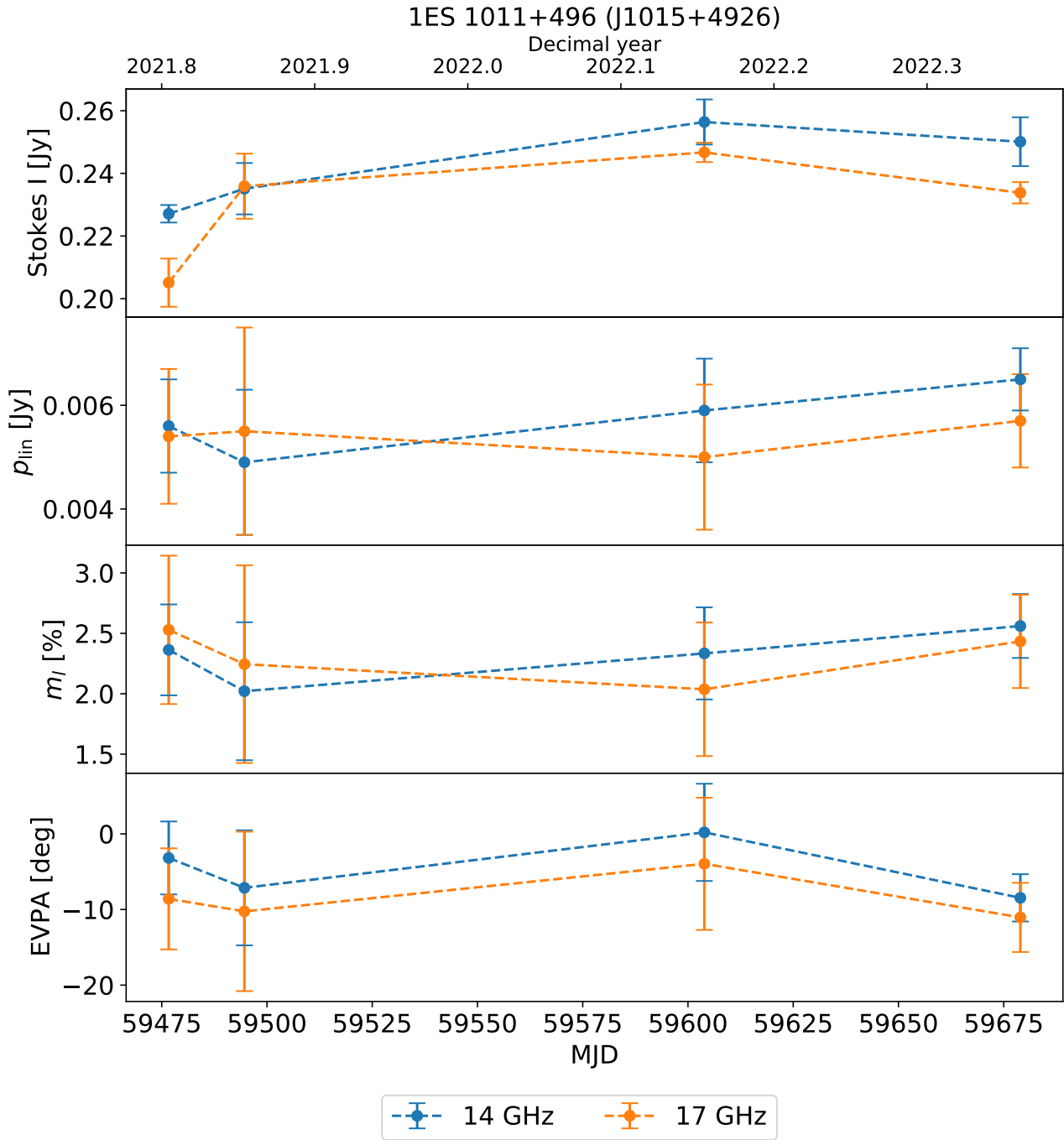


Figure D.12: Overview-plot of 1ES 1011+496 (J1015+4926).

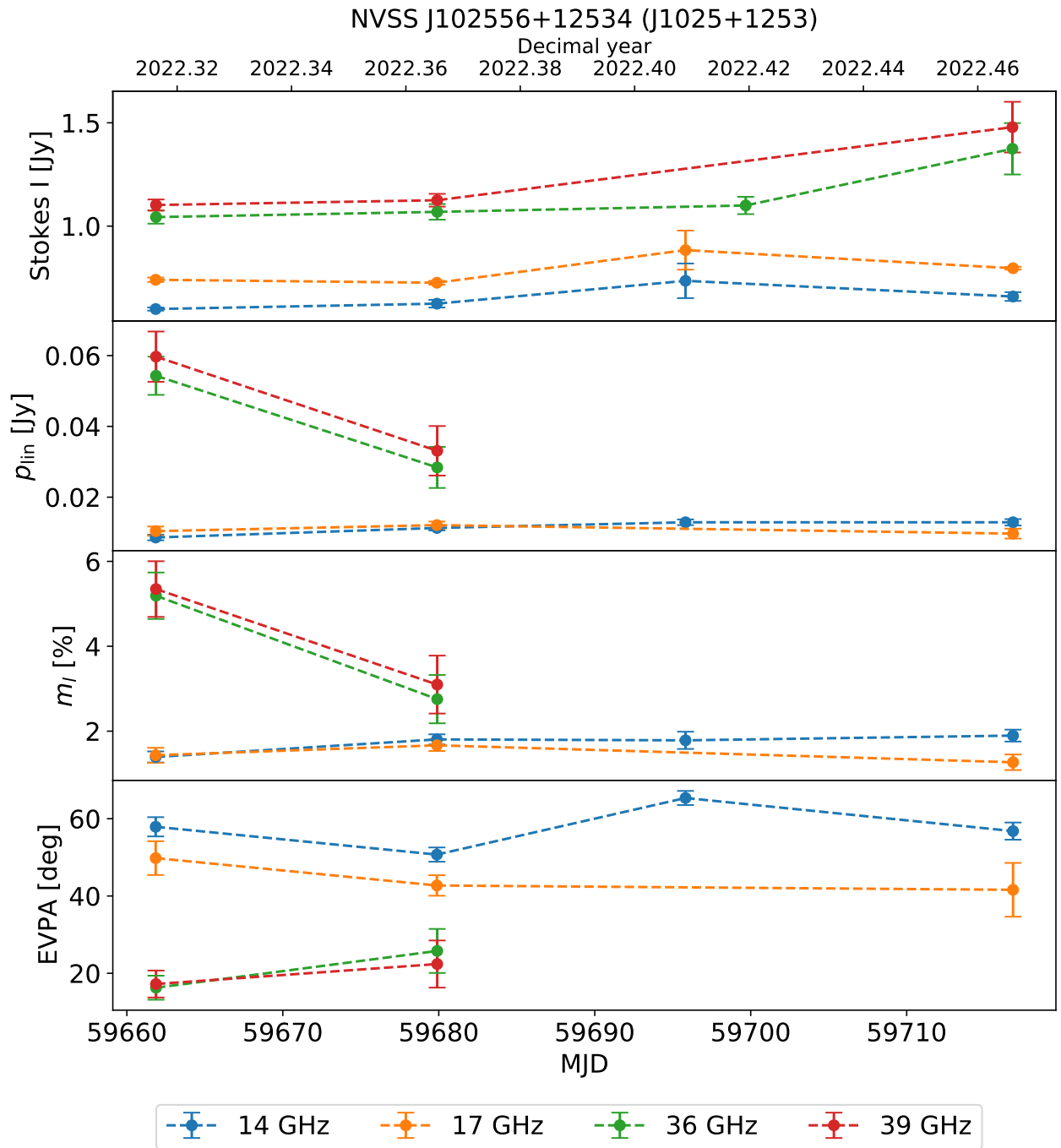


Figure D.13: Overview-plot of NVSS J102556+12534 (J1025+1253).

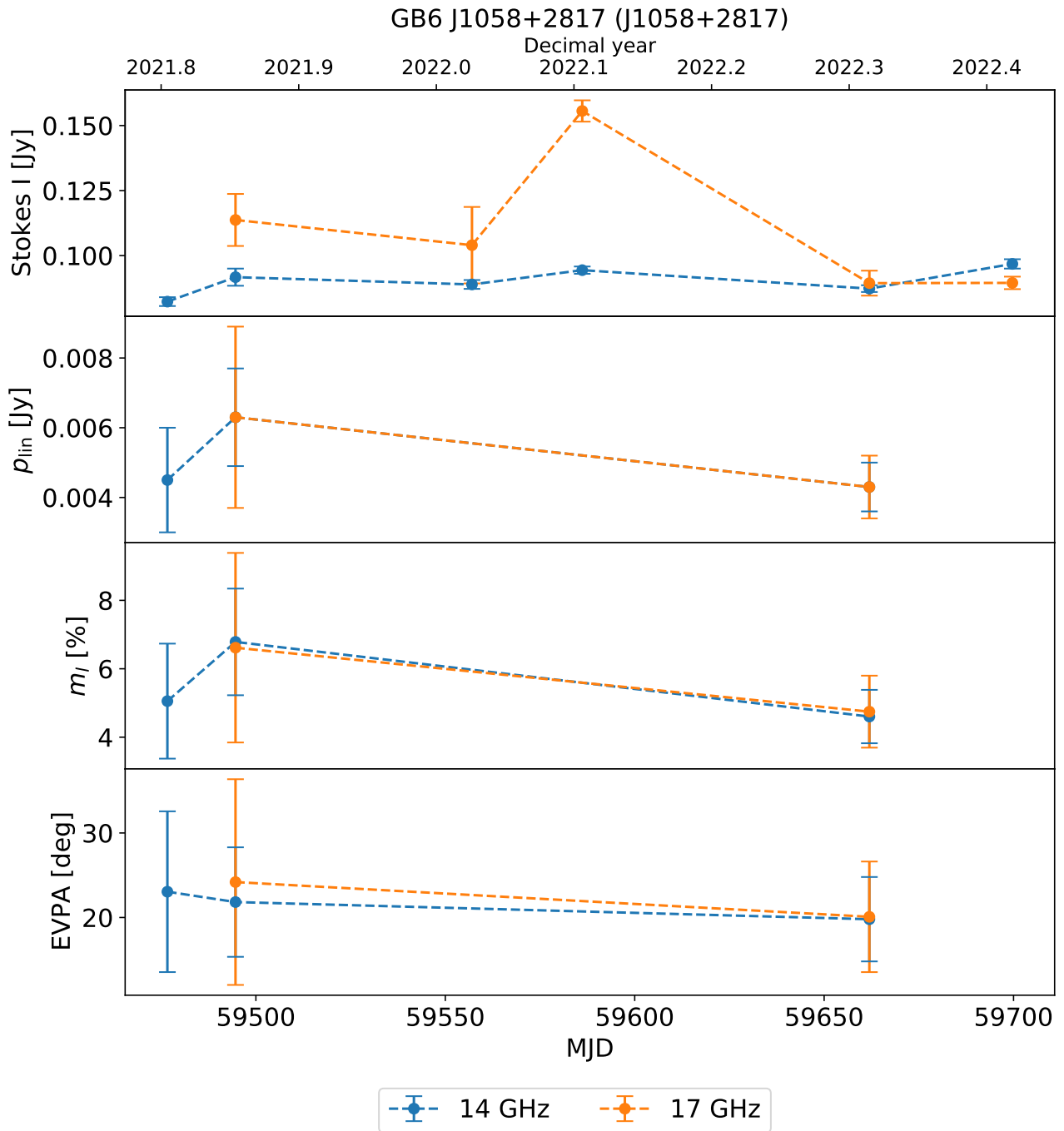


Figure D.14: Overview-plot of GB6 J1058+2817 (J1058+2817).

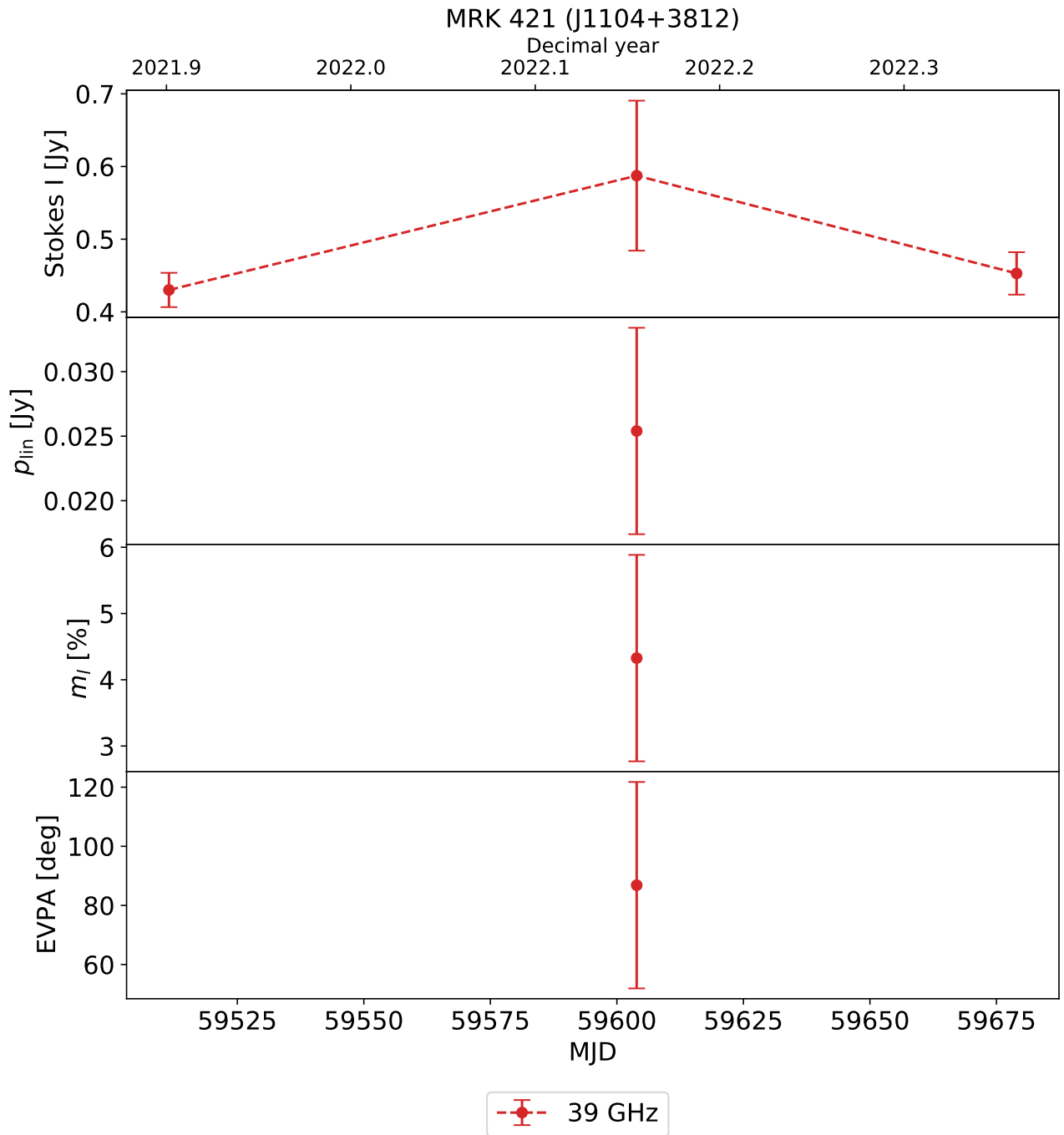


Figure D.15: Overview-plot of MRK 421 (J1104+3812).

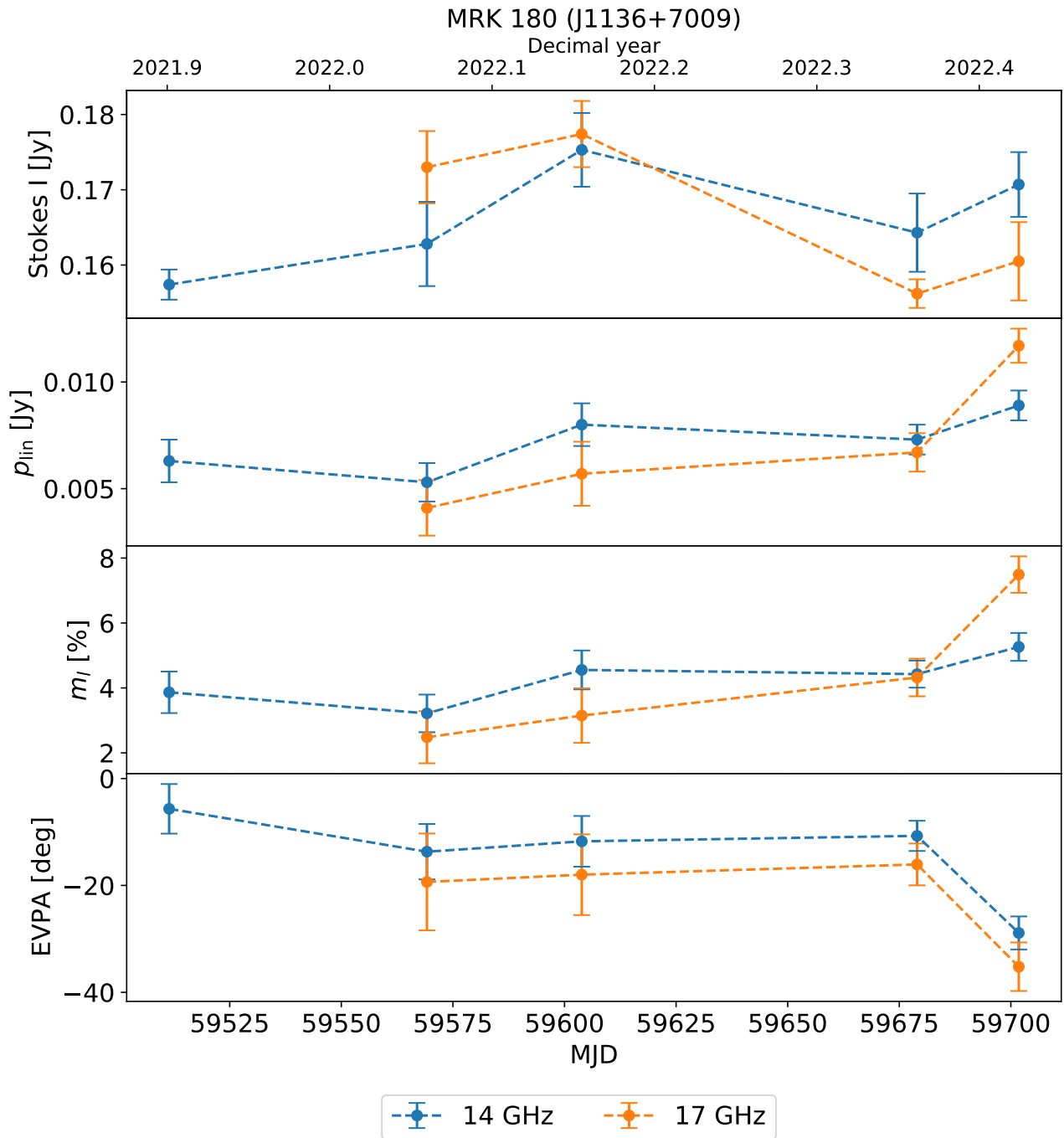


Figure D.16: Overview-plot of MRK 180 (J1136+7009).

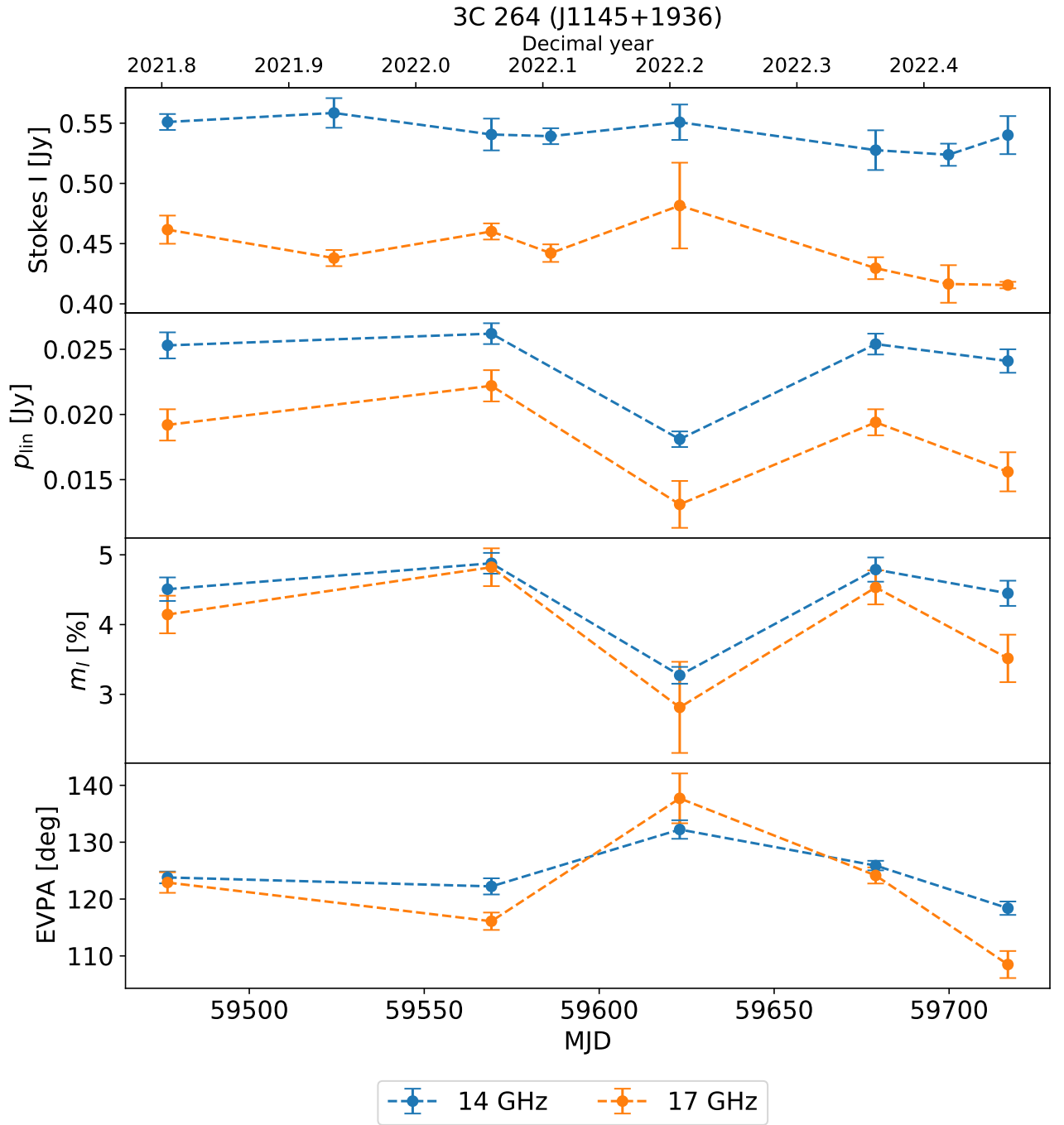


Figure D.17: Overview-plot of 3C 264 (J1145+1936).

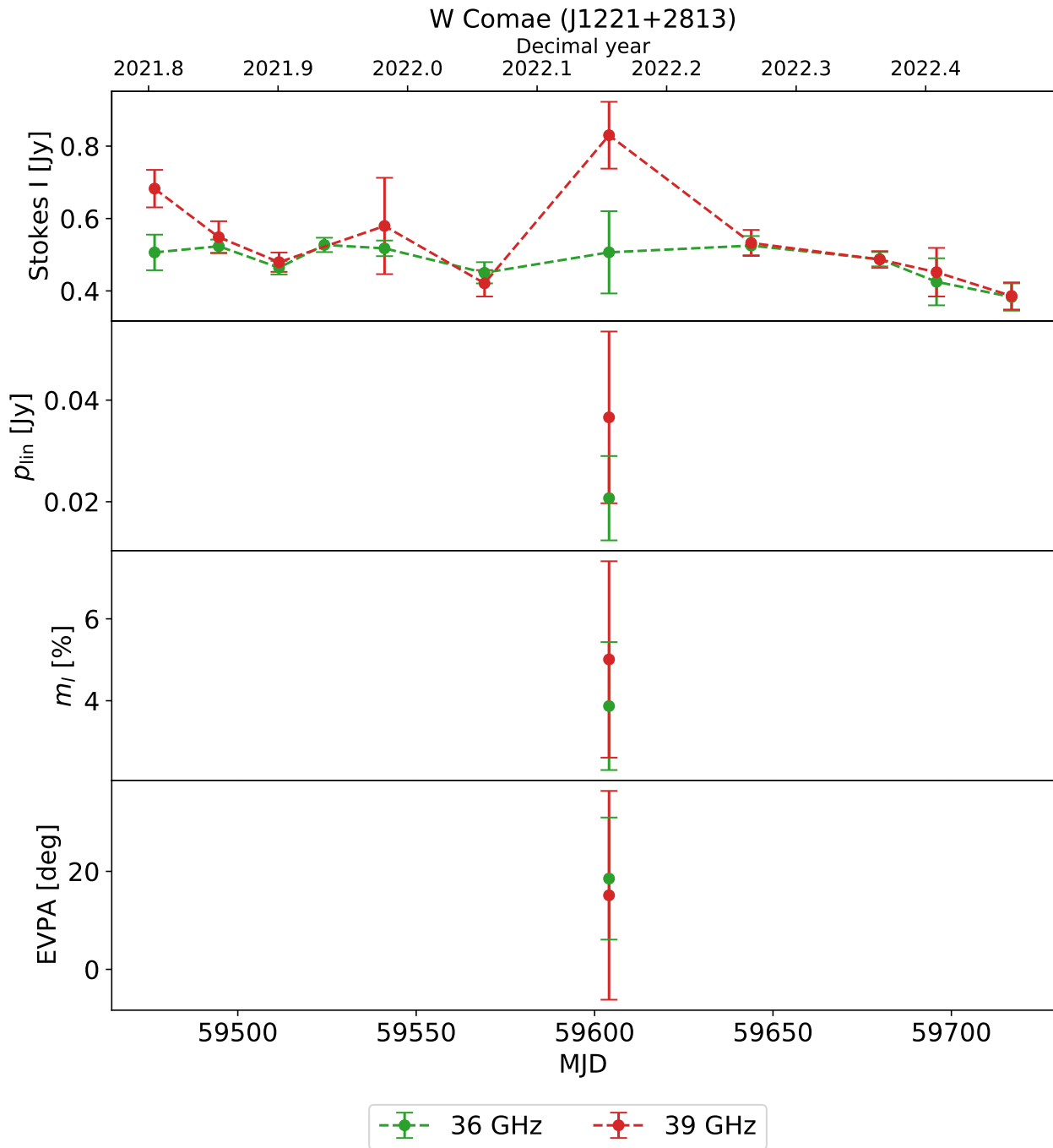


Figure D.18: Overview-plot of W Comae (J1221+2813).

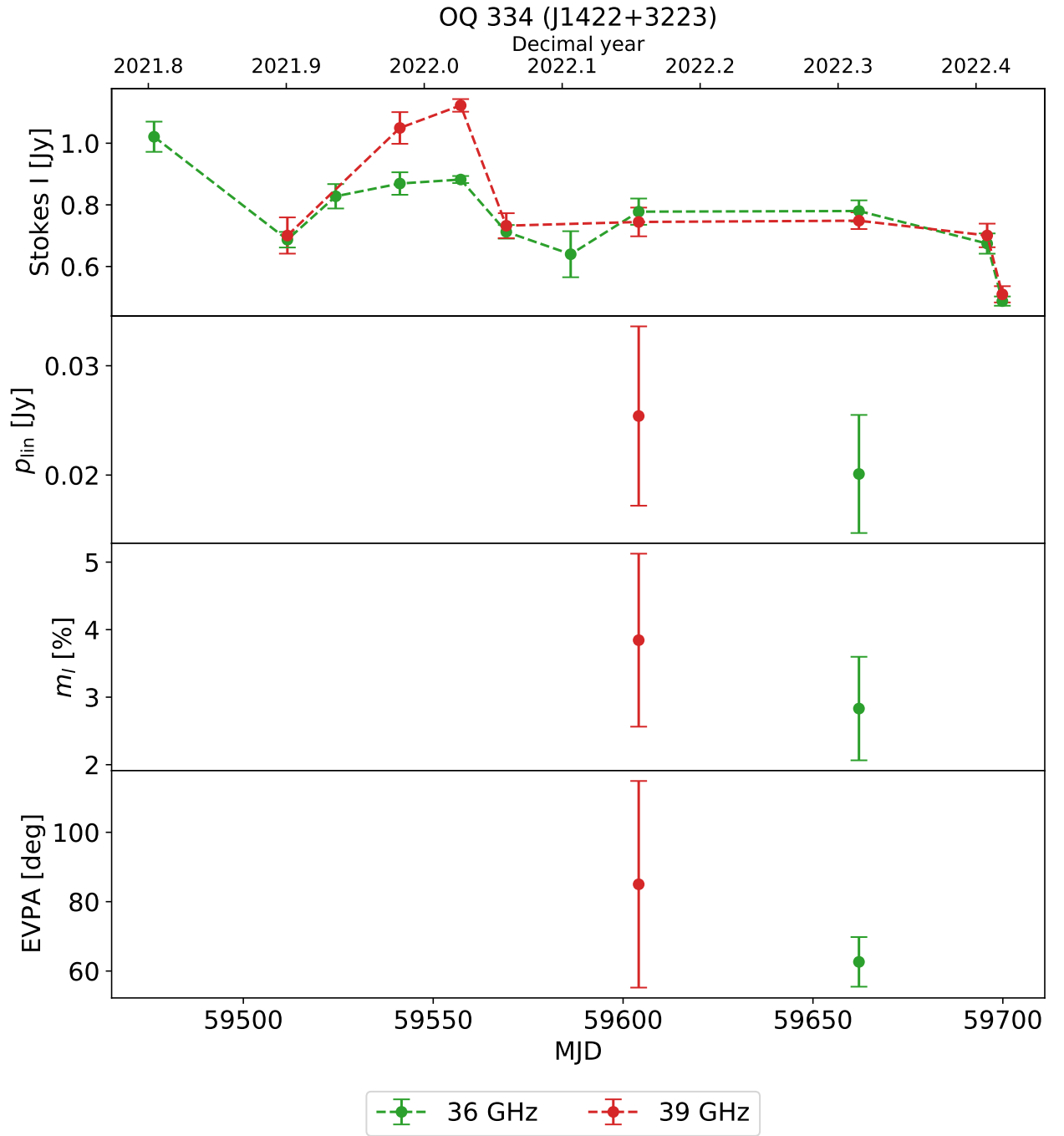


Figure D.19: Overview-plot of OQ 334 (J1422+3223).

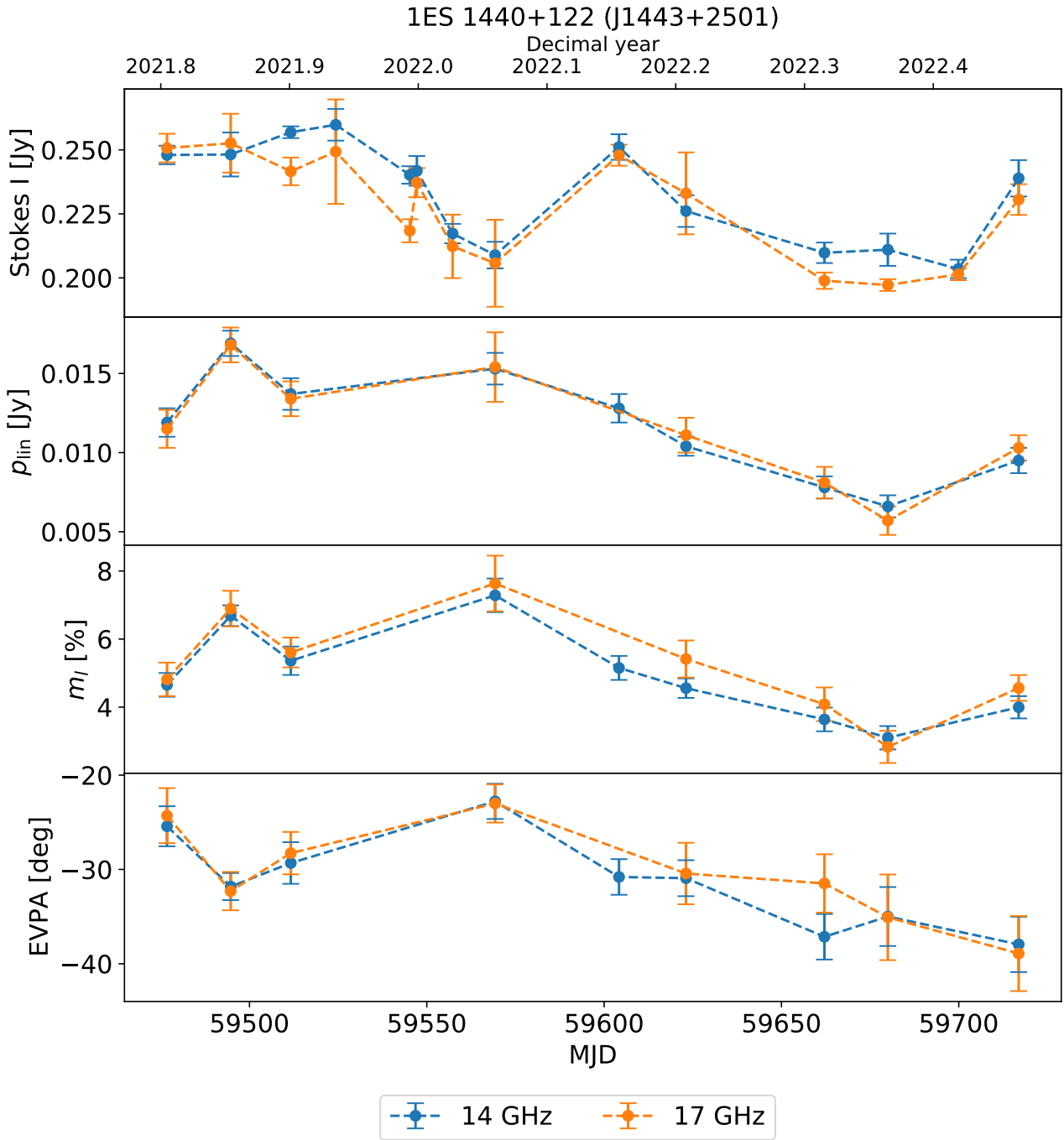


Figure D.20: Overview-plot of 1ES 1440+122 (J1443+2501).

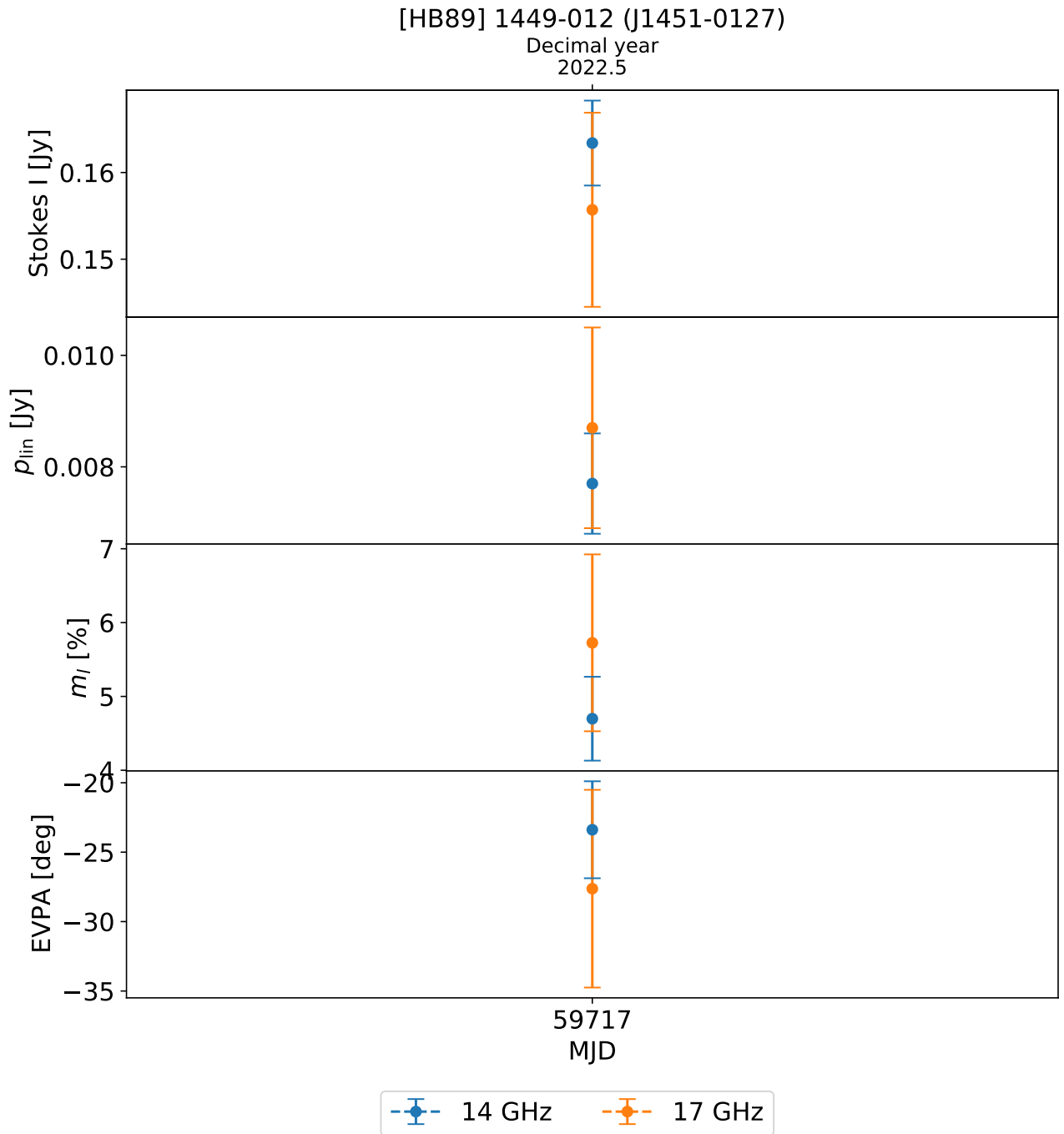


Figure D.21: Overview-plot of [HB89] 1449-012 (J1451-0127).

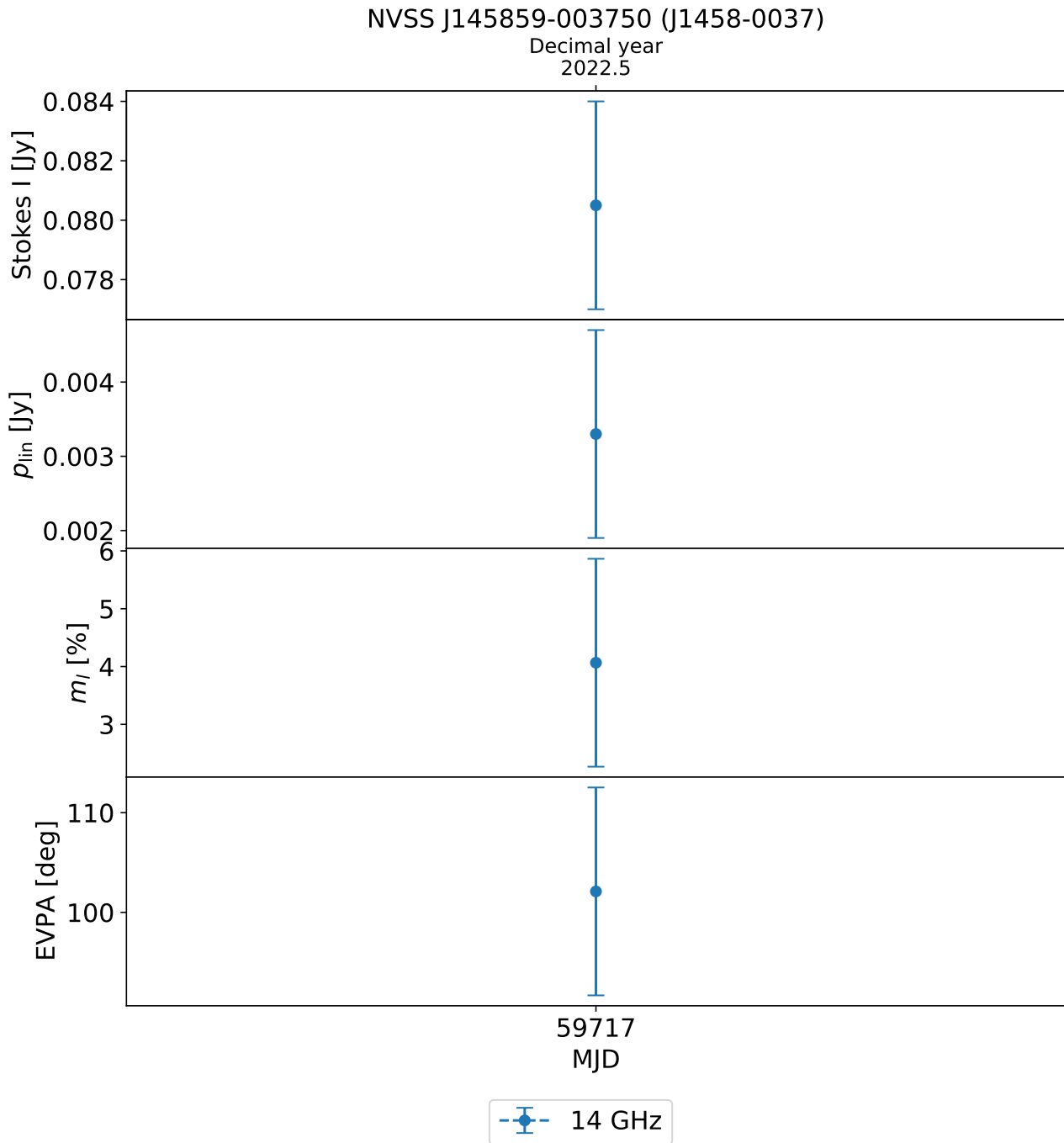


Figure D.22: Overview-plot of NVSS J145859-003750 (J1458-0037).

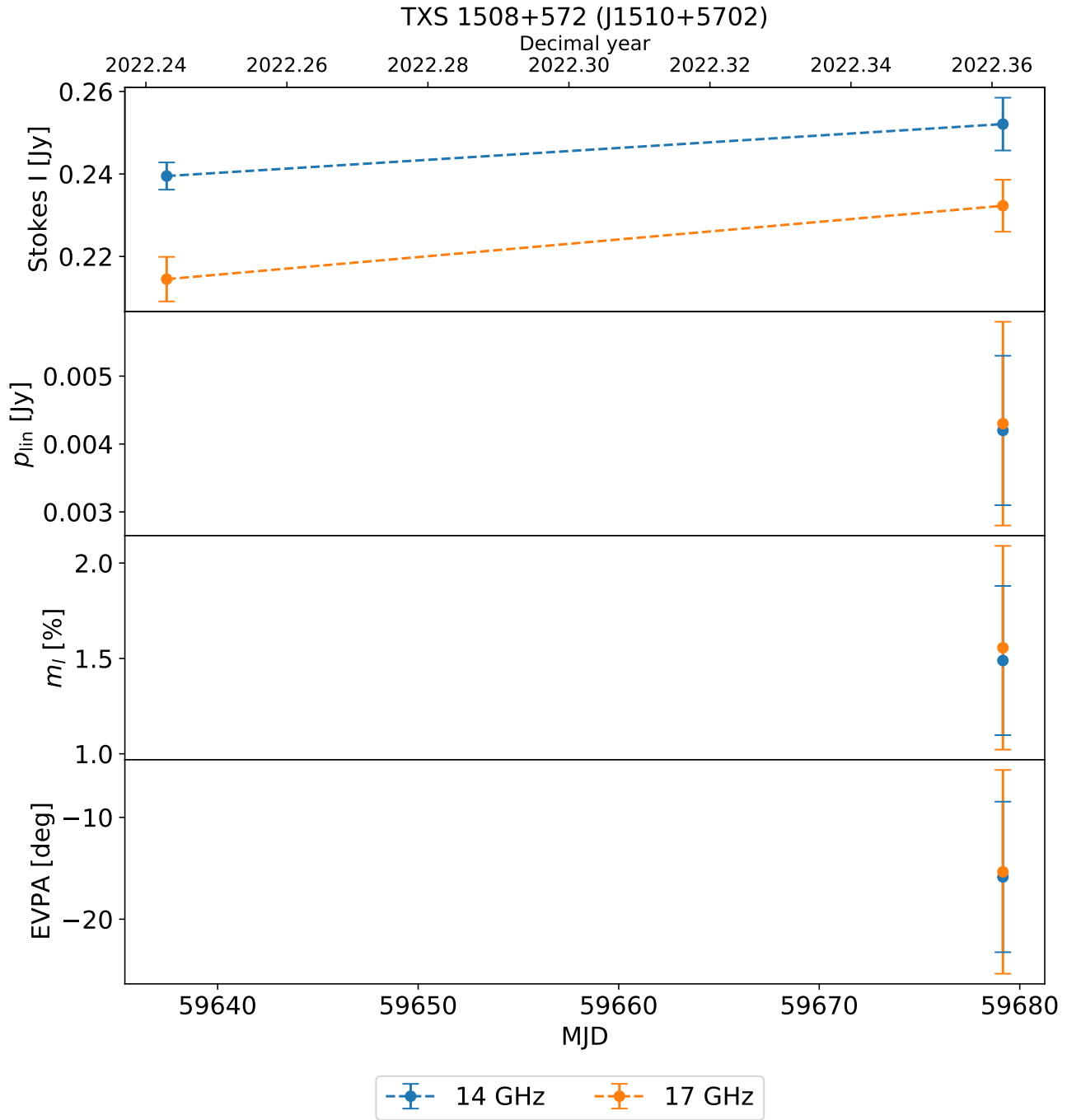


Figure D.23: Overview-plot of TXS 1508+572 (J1510+5702).

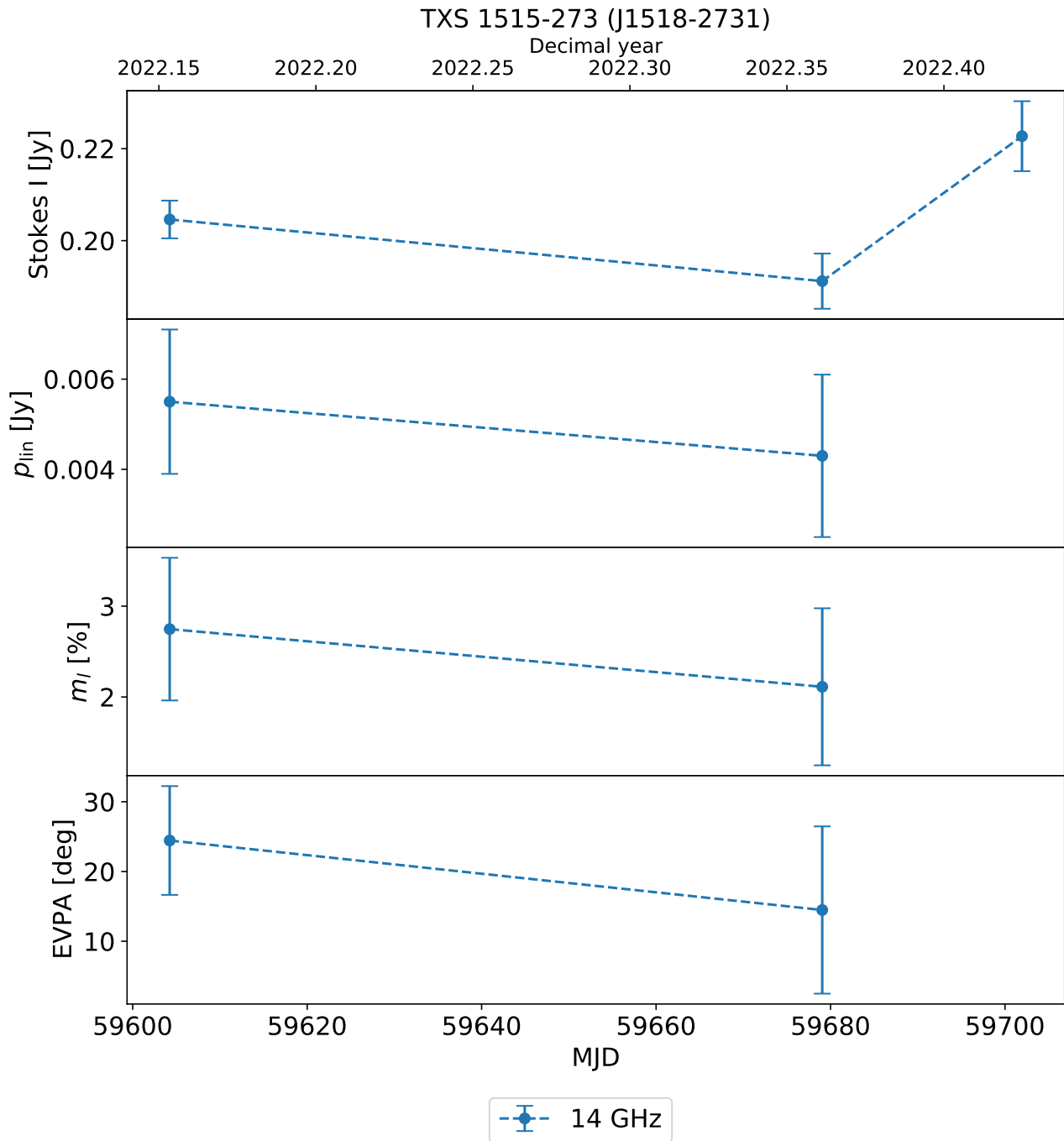


Figure D.24: Overview-plot of TXS 1515-273 (J1518-2731).

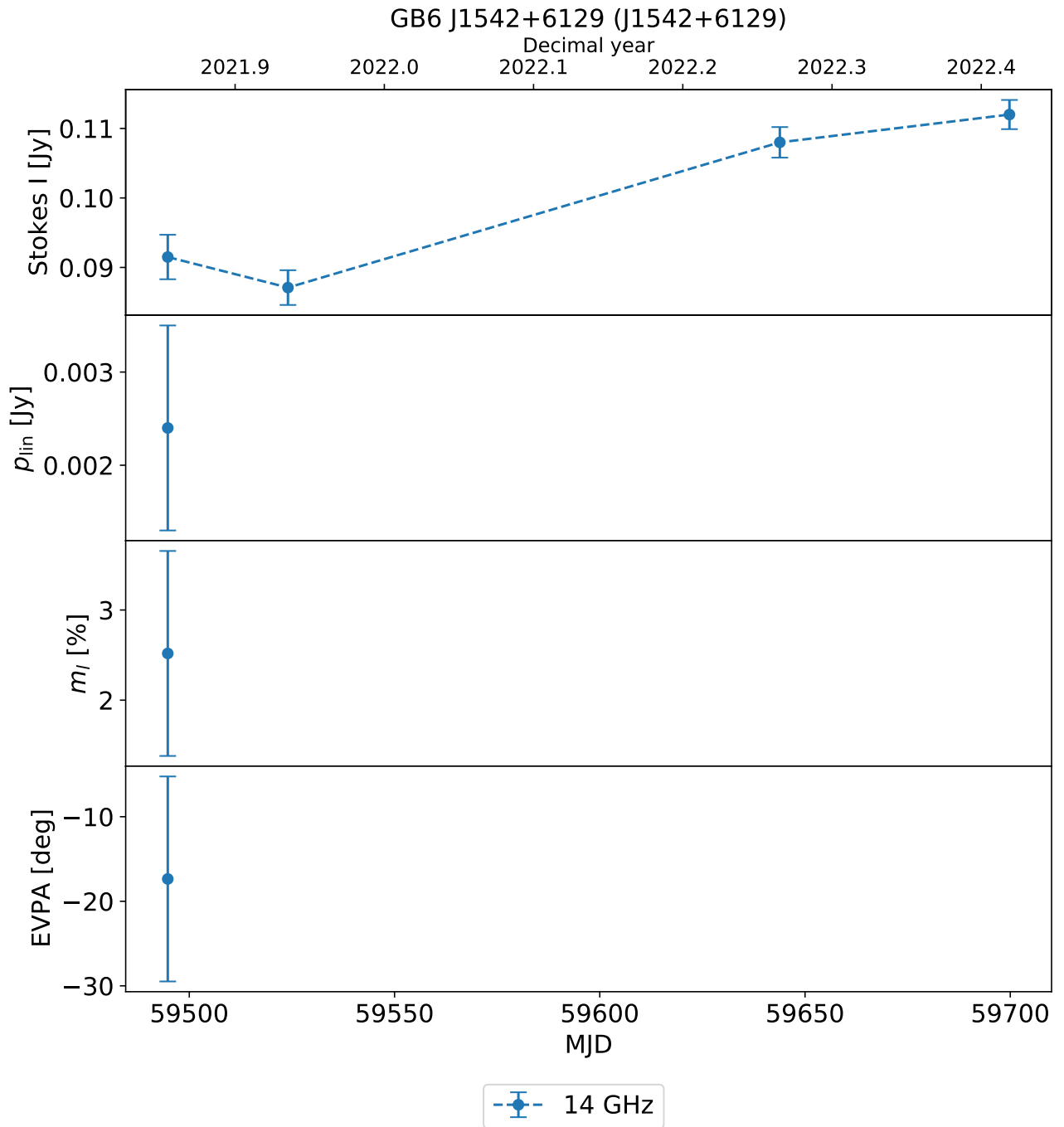


Figure D.25: Overview-plot of GB6 J1542+6129 (J1542+6129).

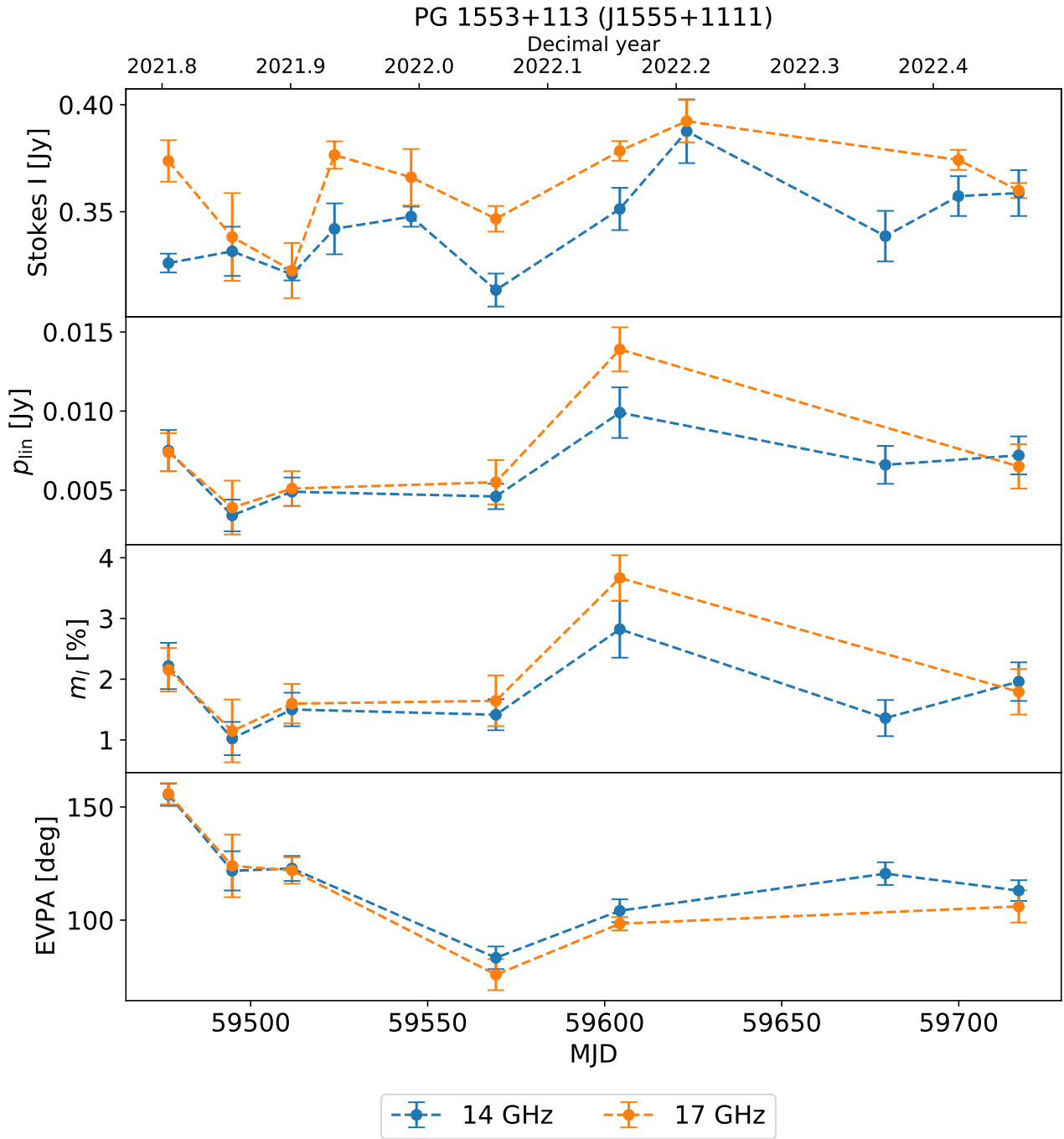


Figure D.26: Overview-plot of PG 1553+113 (J1555+1111).

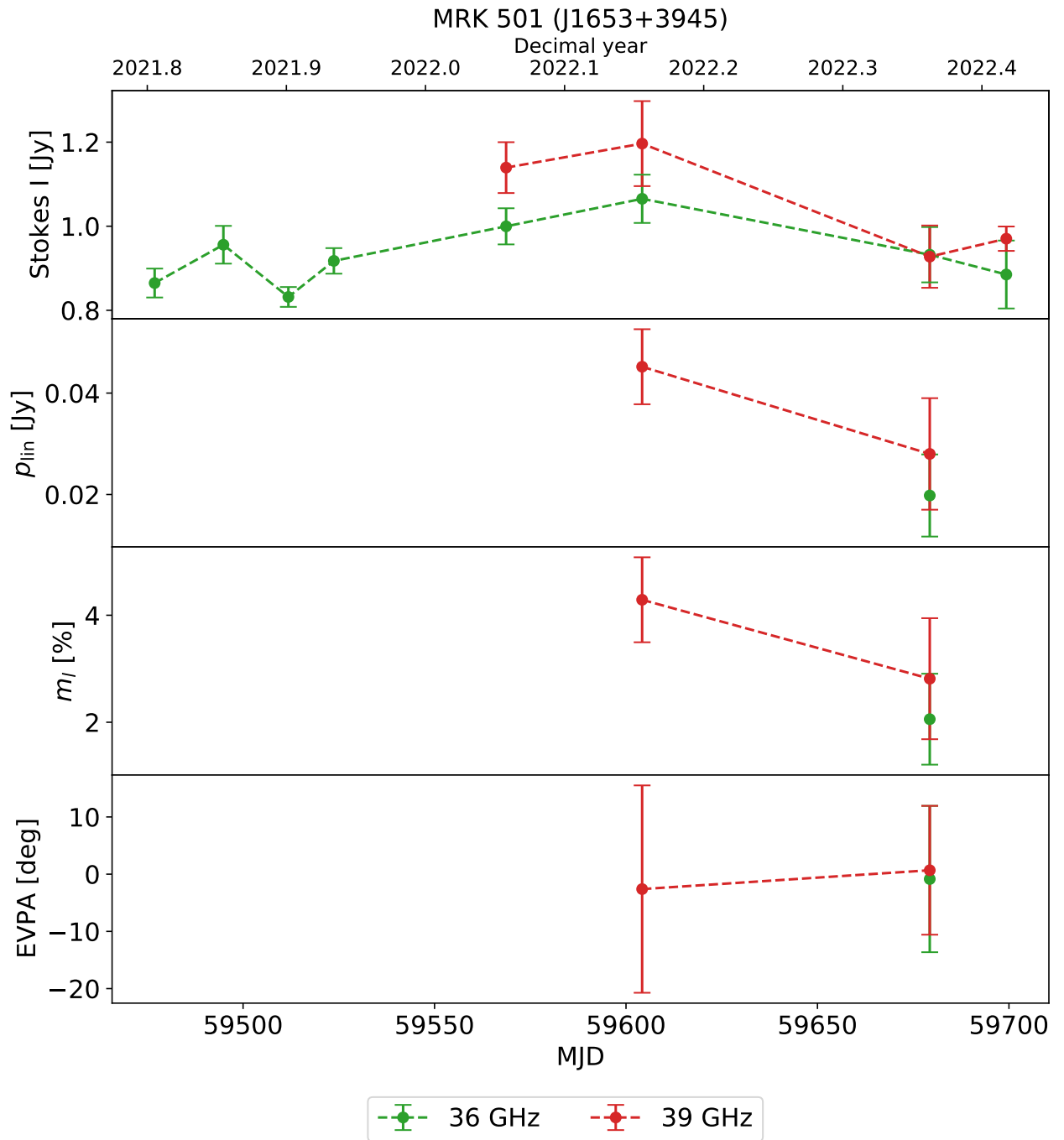


Figure D.27: Overview-plot of MRK 501 (J1653+3945).

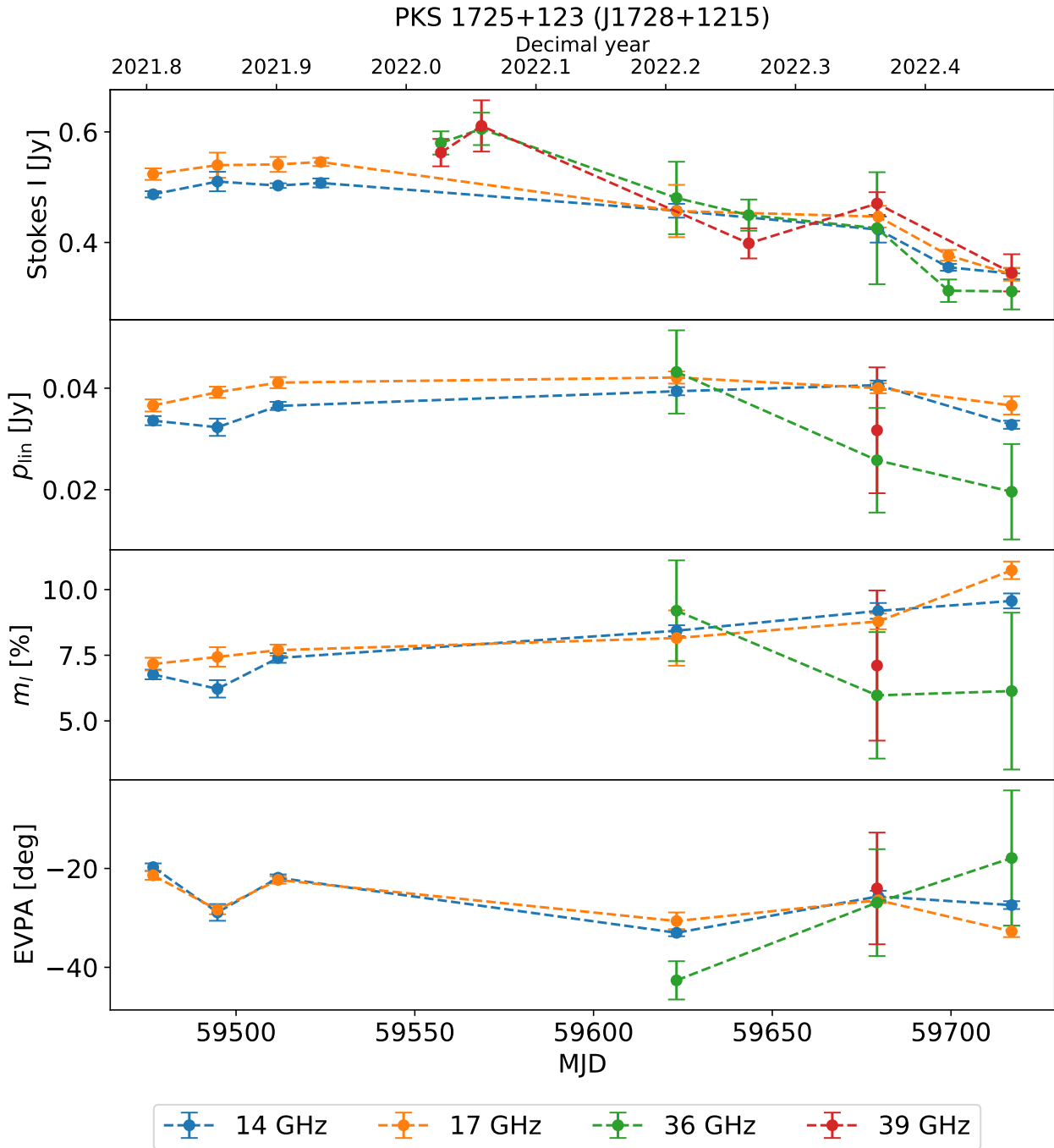


Figure D.28: Overview-plot of PKS 1725+123 (J1728+1215).

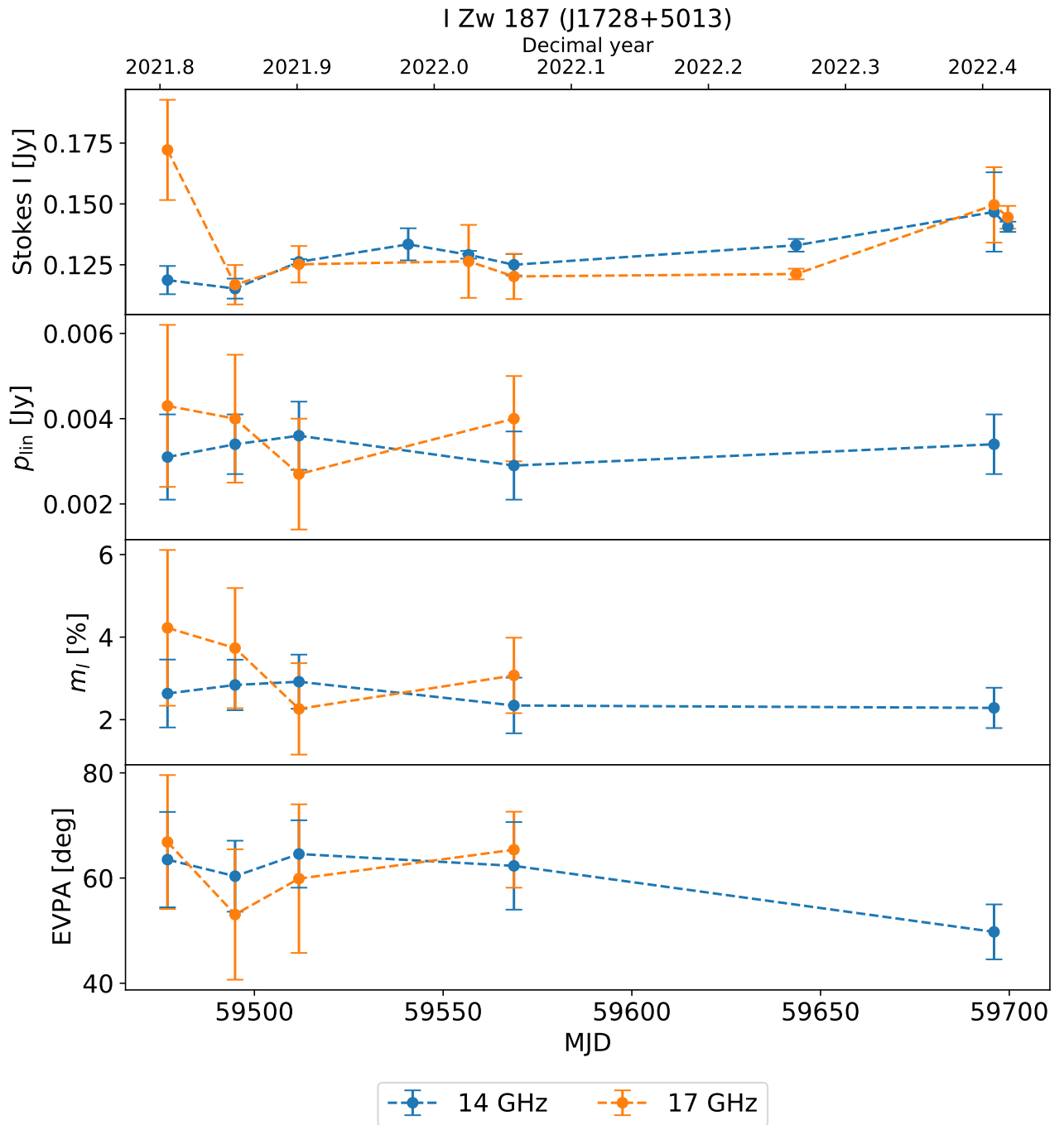


Figure D.29: Overview-plot of I Zw 187 (J1728+5013).

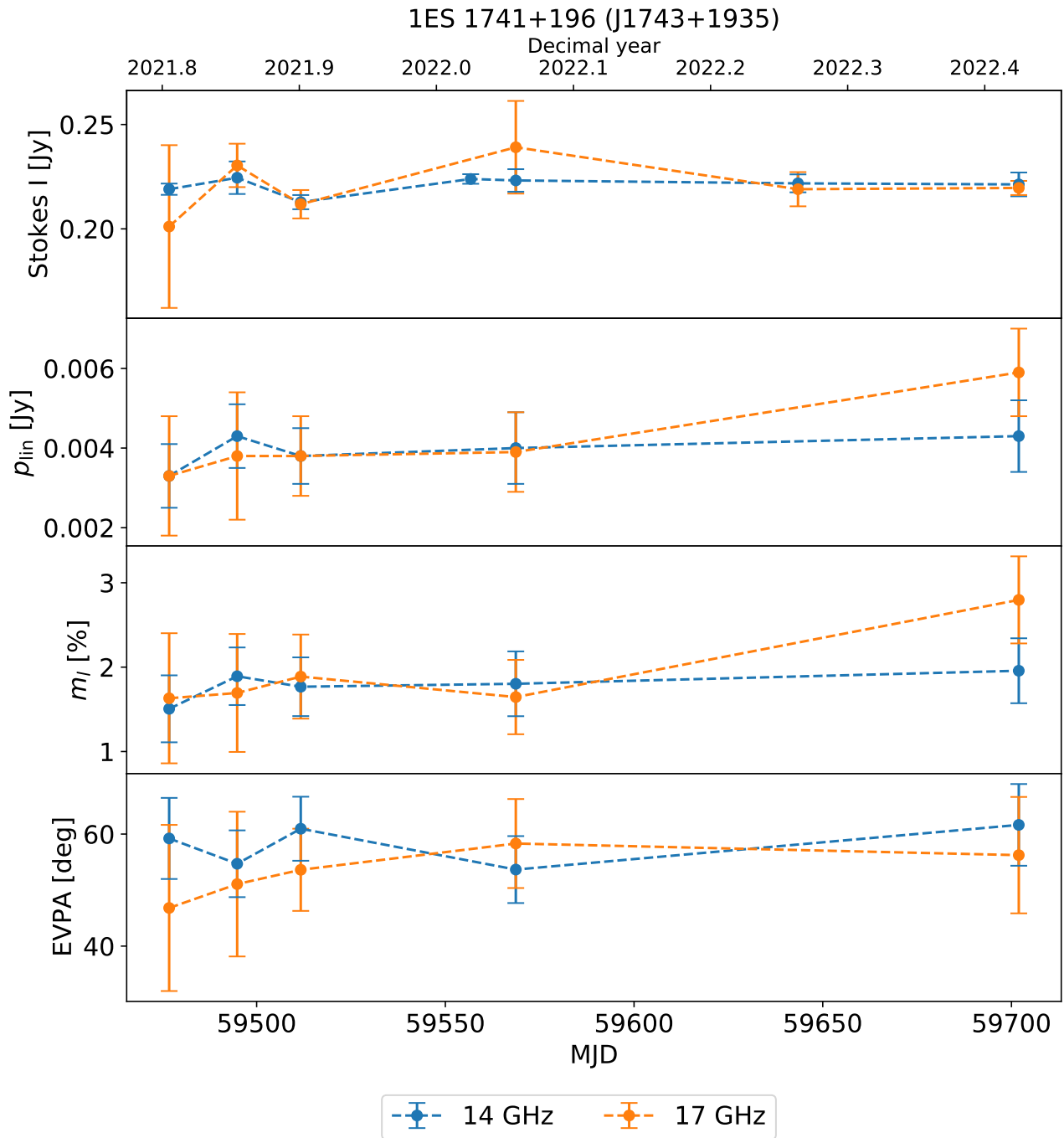


Figure D.30: Overview-plot of 1ES 1741+196 (J1743+1935).

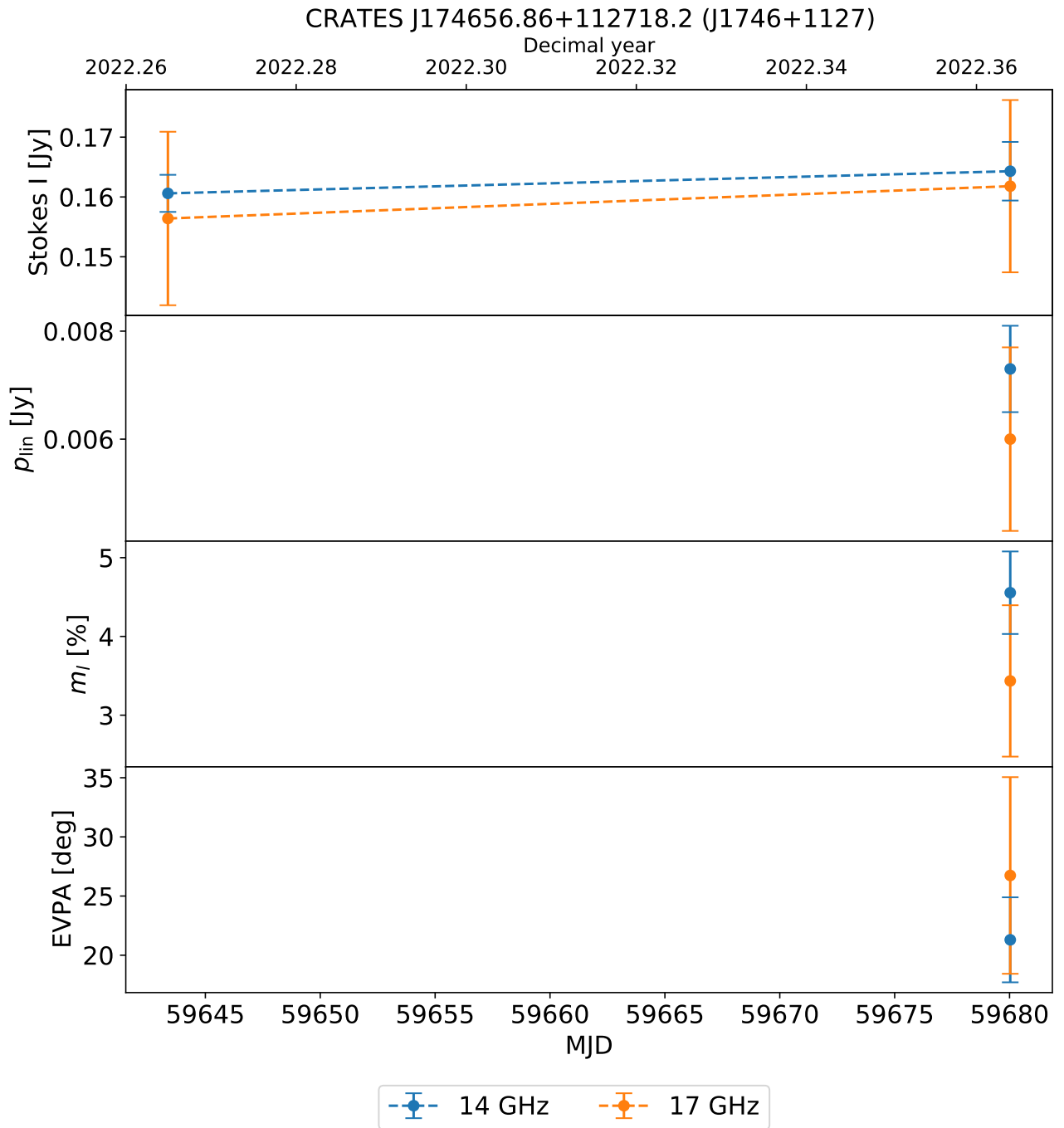


Figure D.31: Overview-plot of CRATES J174656.86+112718.2 (J1746+1127).

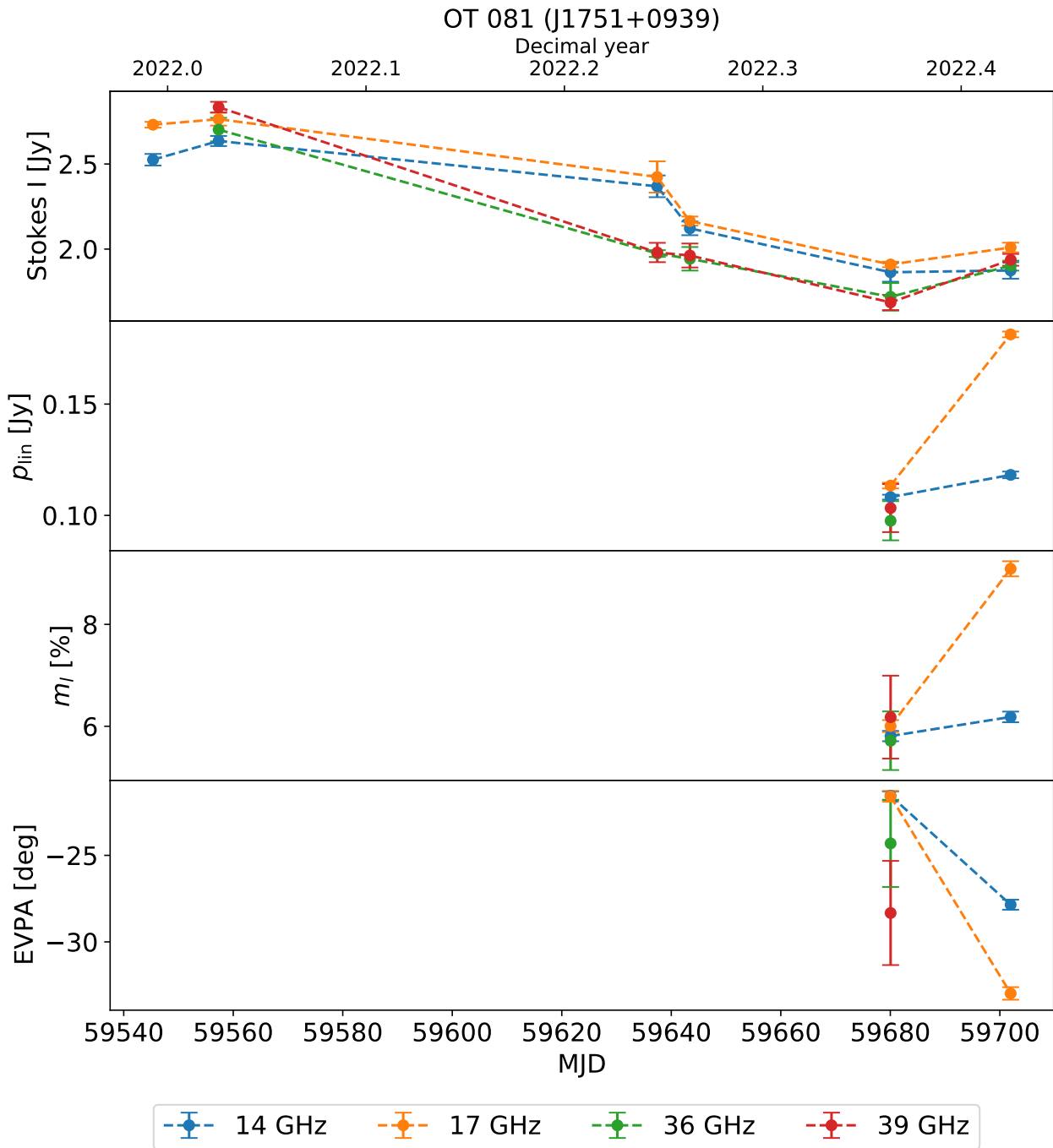


Figure D.32: Overview-plot of OT 081 (J1751+0939).

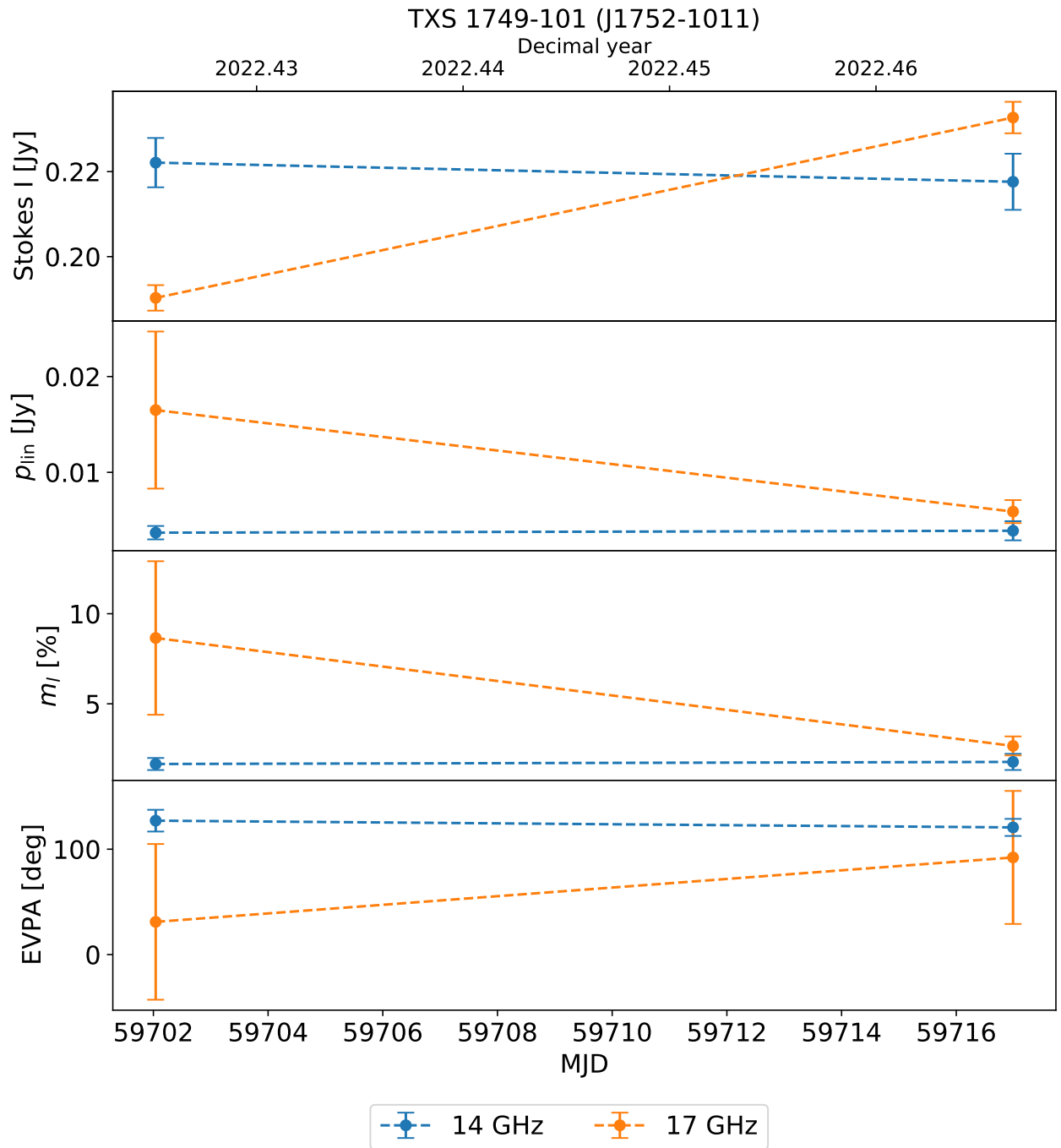


Figure D.33: Overview-plot of TXS 1749-101 (J1752-1011).

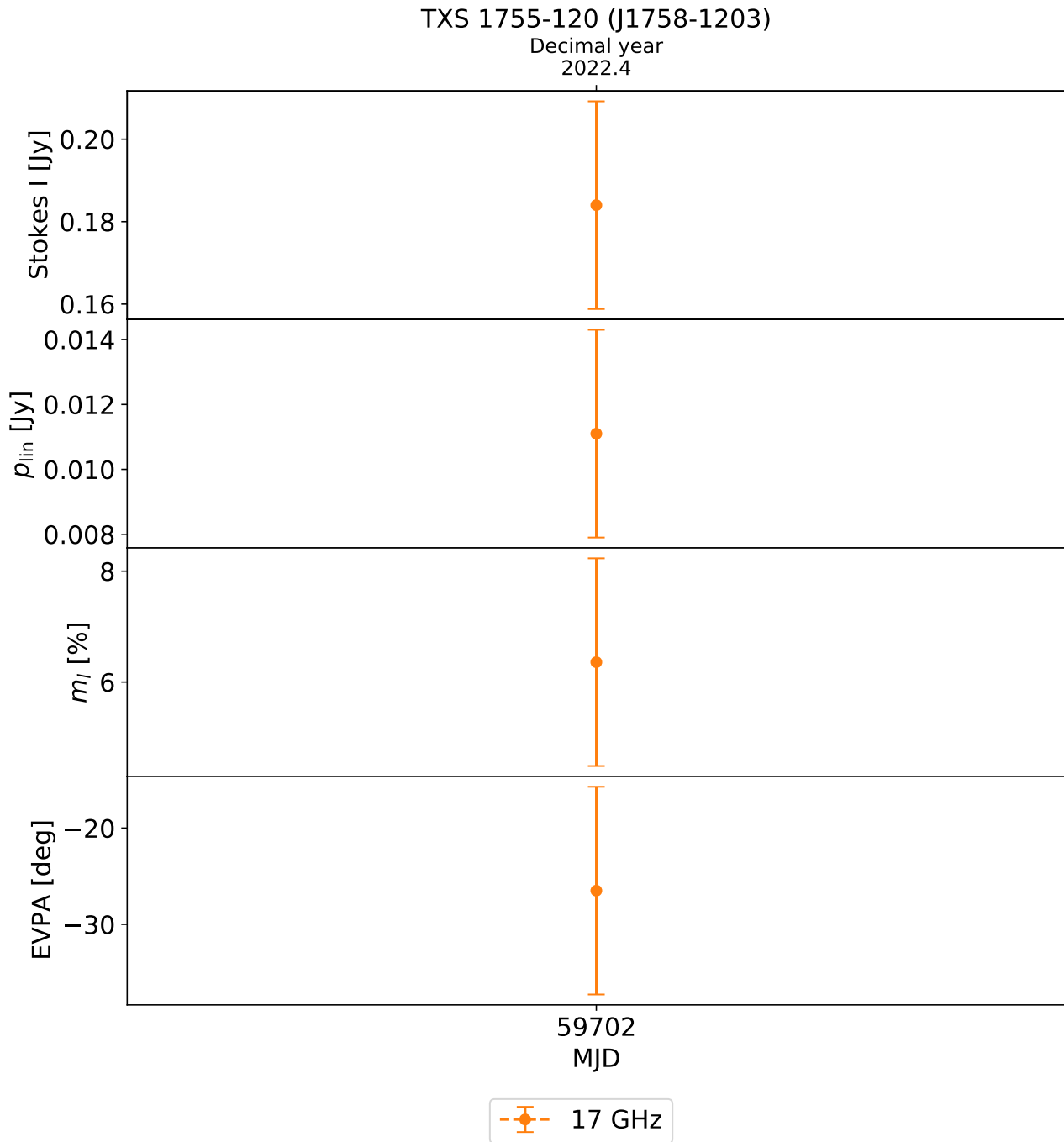


Figure D.34: Overview-plot of TXS 1755-120 (J1758-1203).

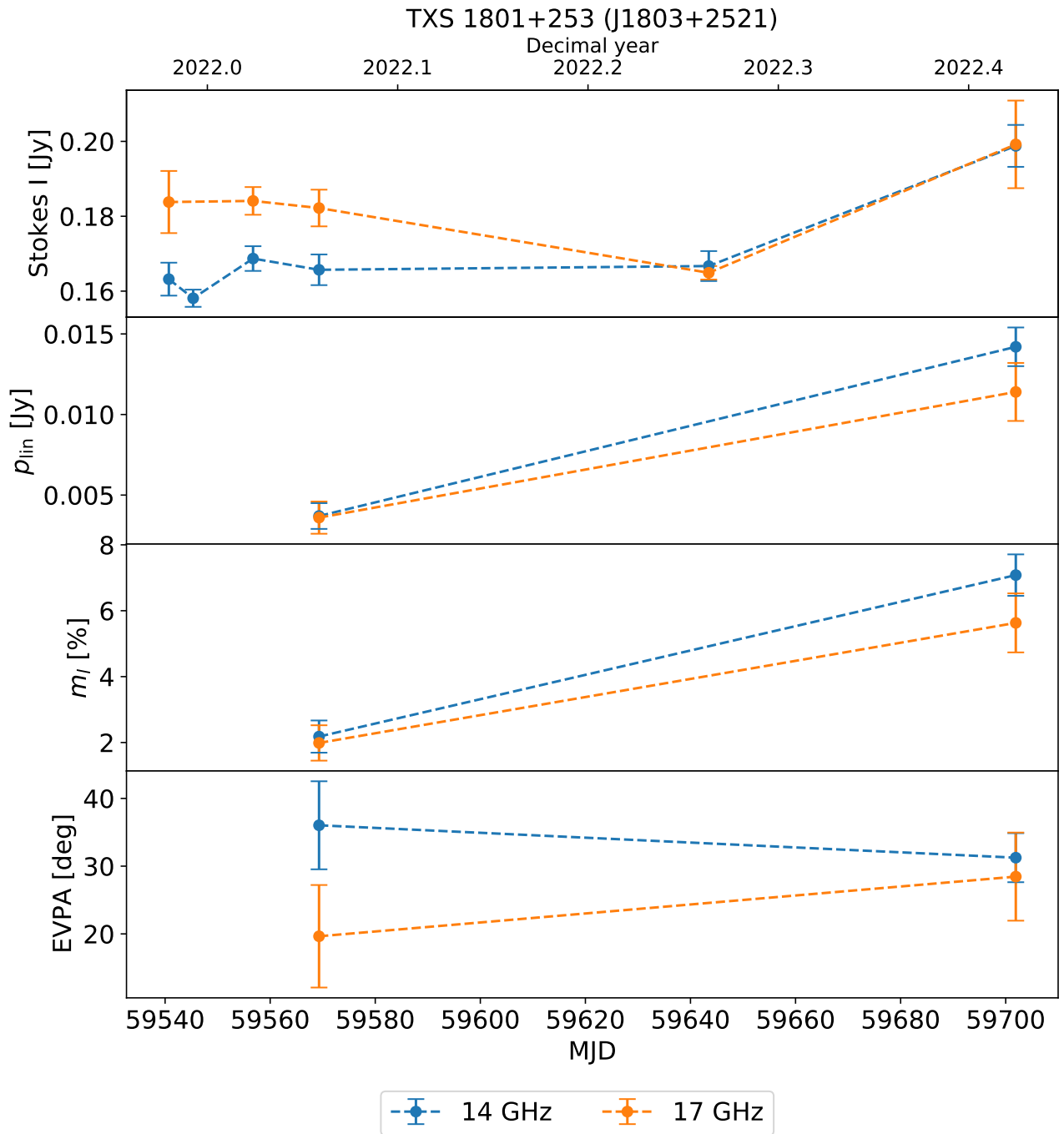


Figure D.35: Overview-plot of TXS 1801+253 (J1803+2521).

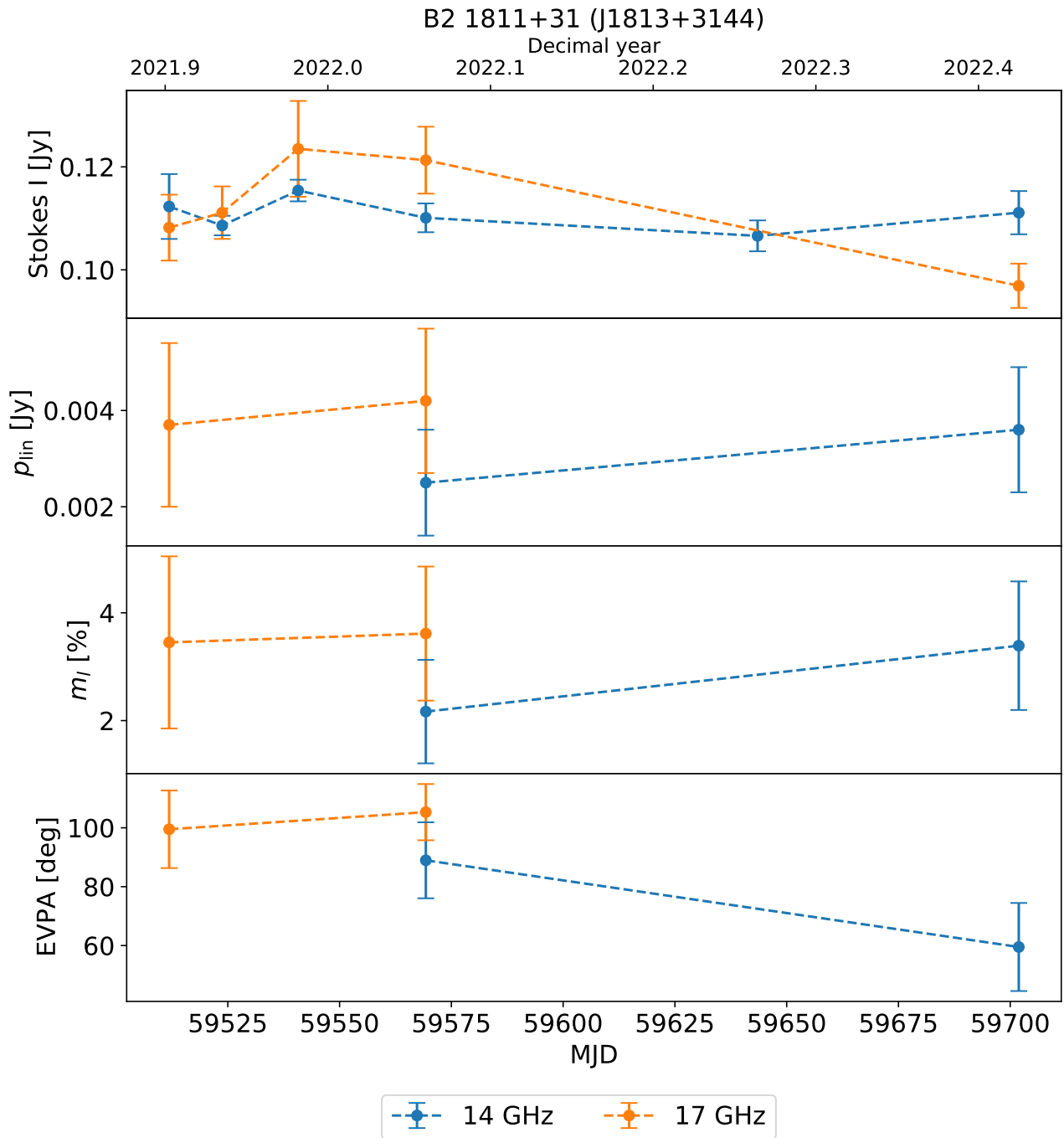


Figure D.36: Overview-plot of B2 1811+31 (J1813+3144).

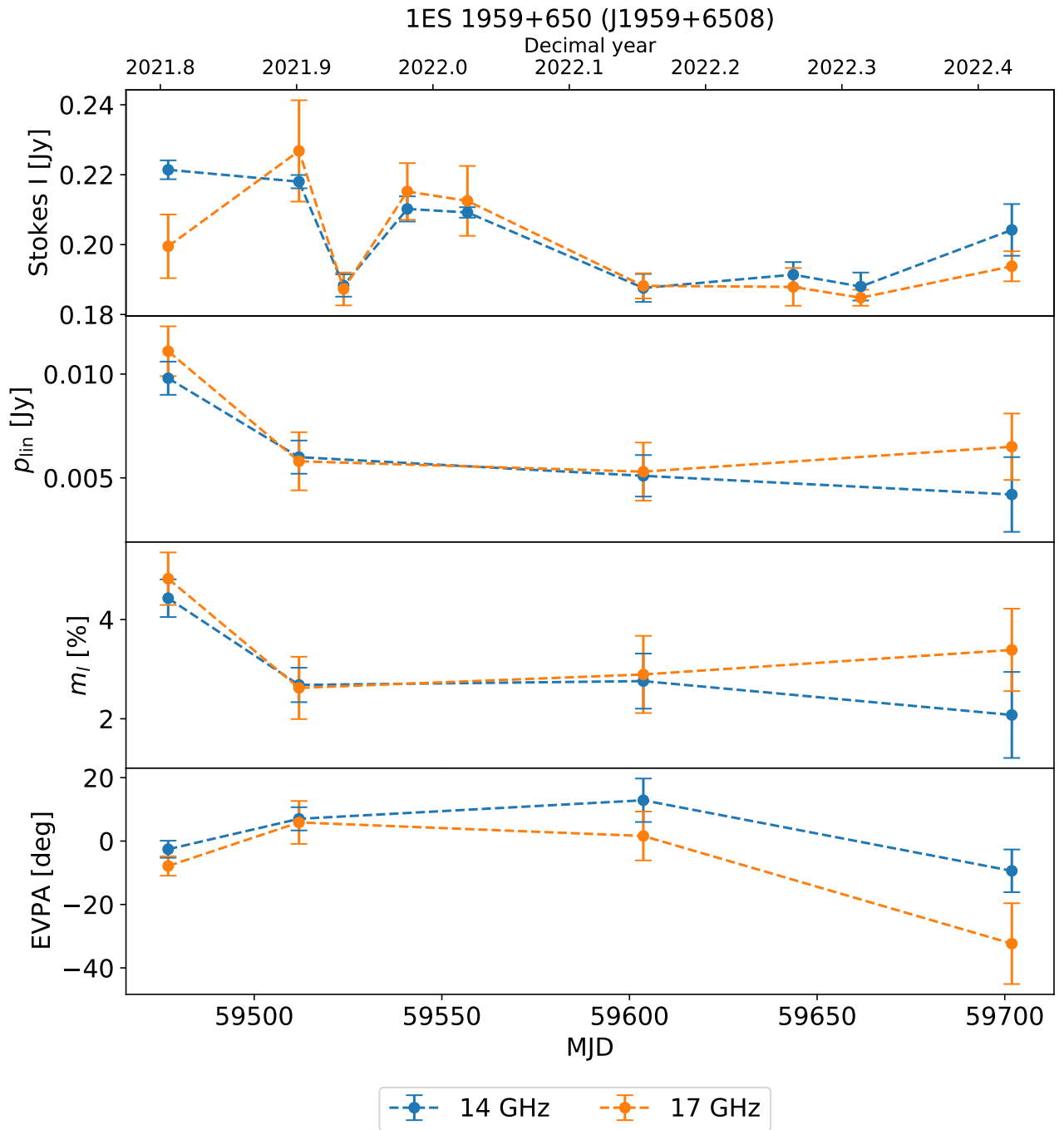


Figure D.37: Overview-plot of 1ES 1959+650 (J1959+6508).

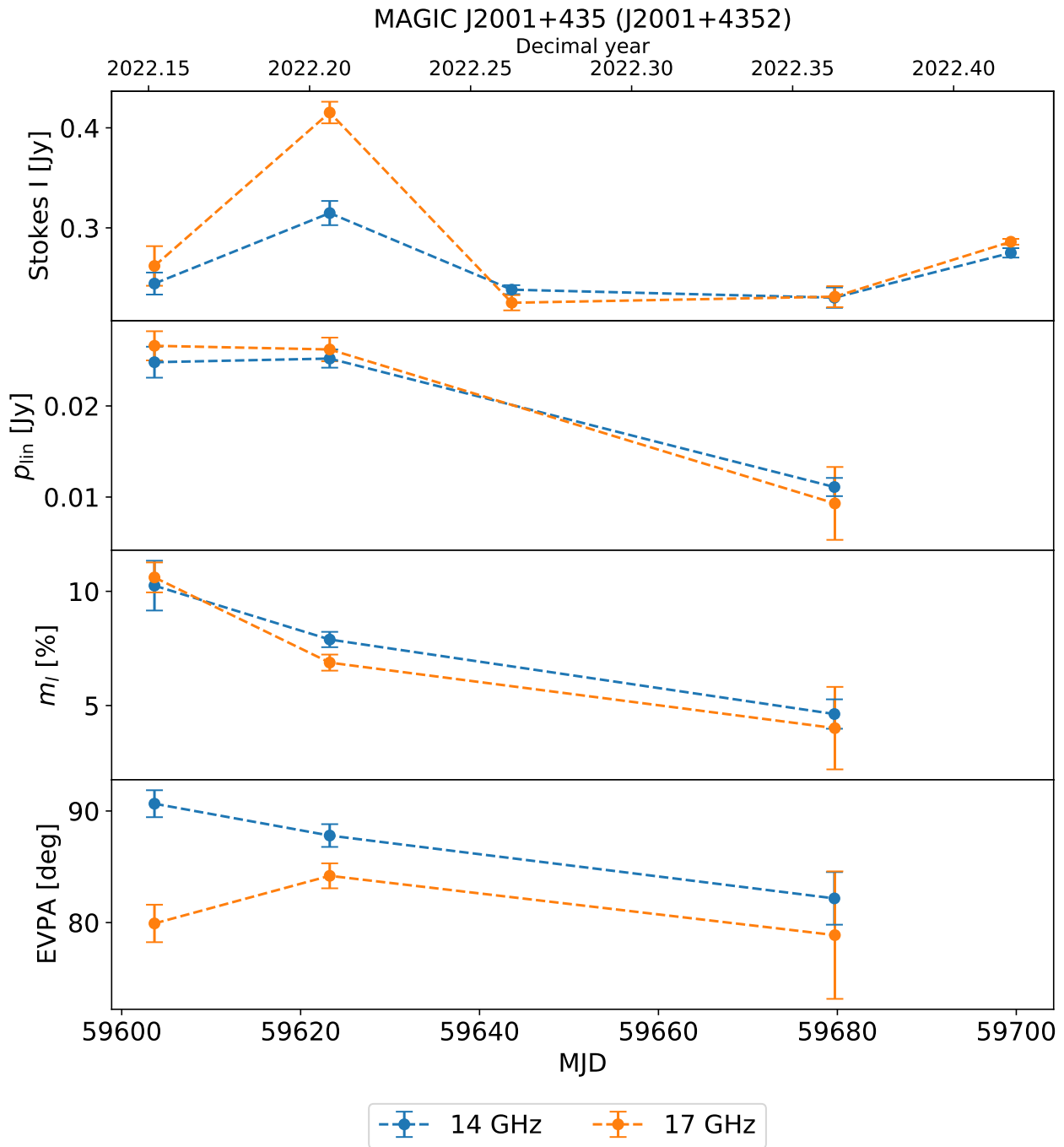


Figure D.38: Overview-plot of MAGIC J2001+435 (J2001+4352).

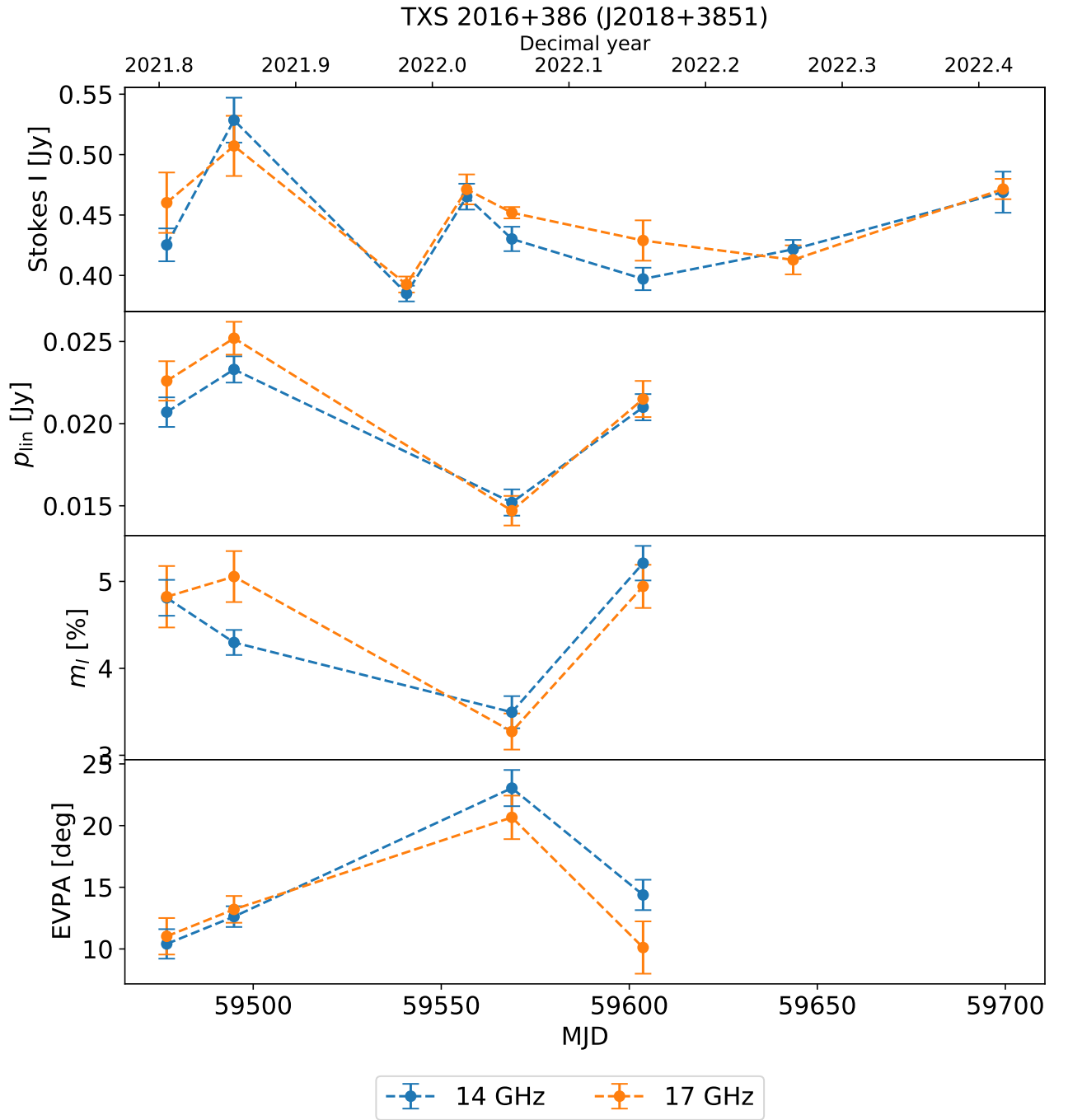


Figure D.39: Overview-plot of TXS 2016+386 (J2018+3851).

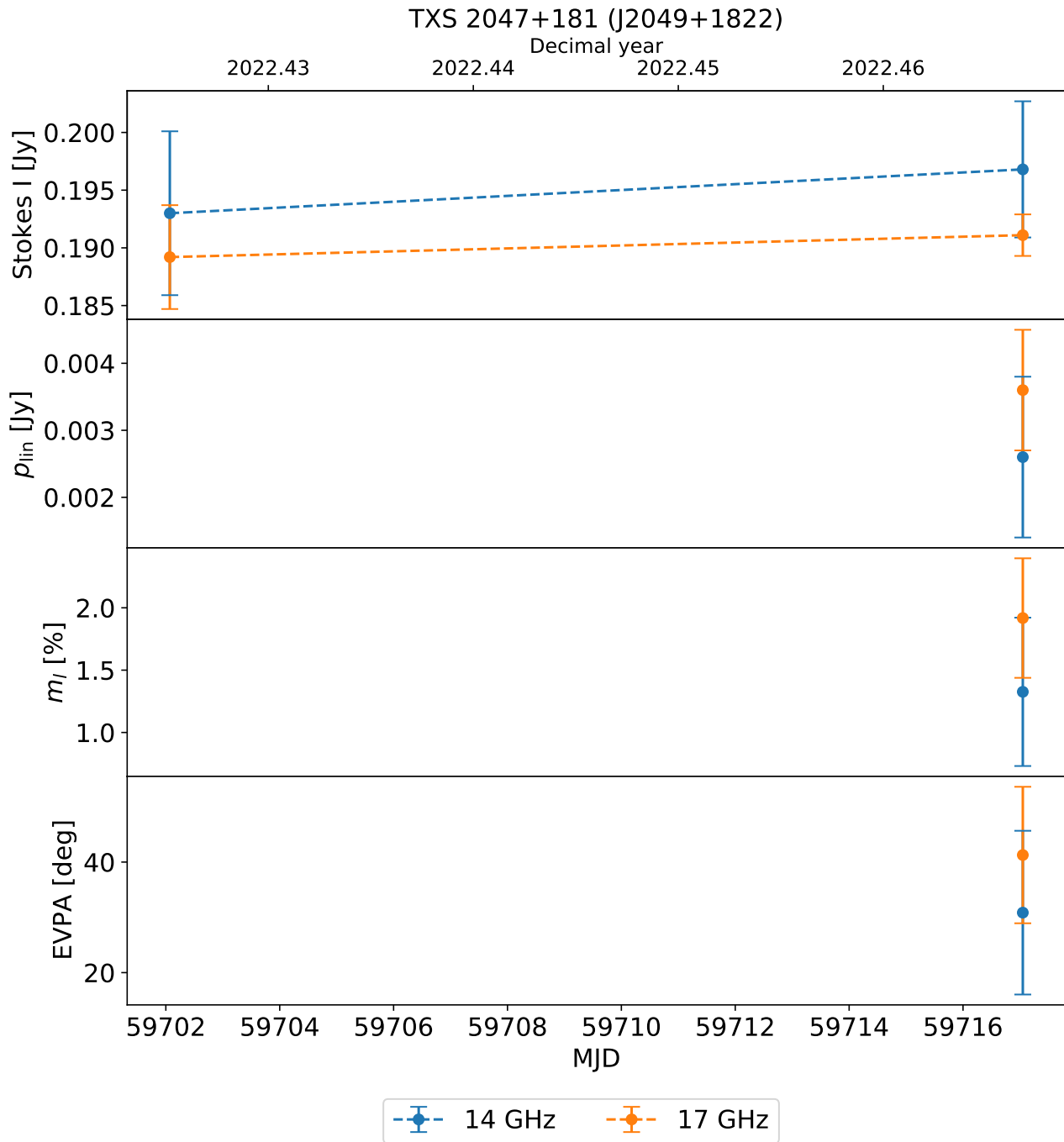


Figure D.40: Overview-plot of TXS 2047+181 (J2049+1822).

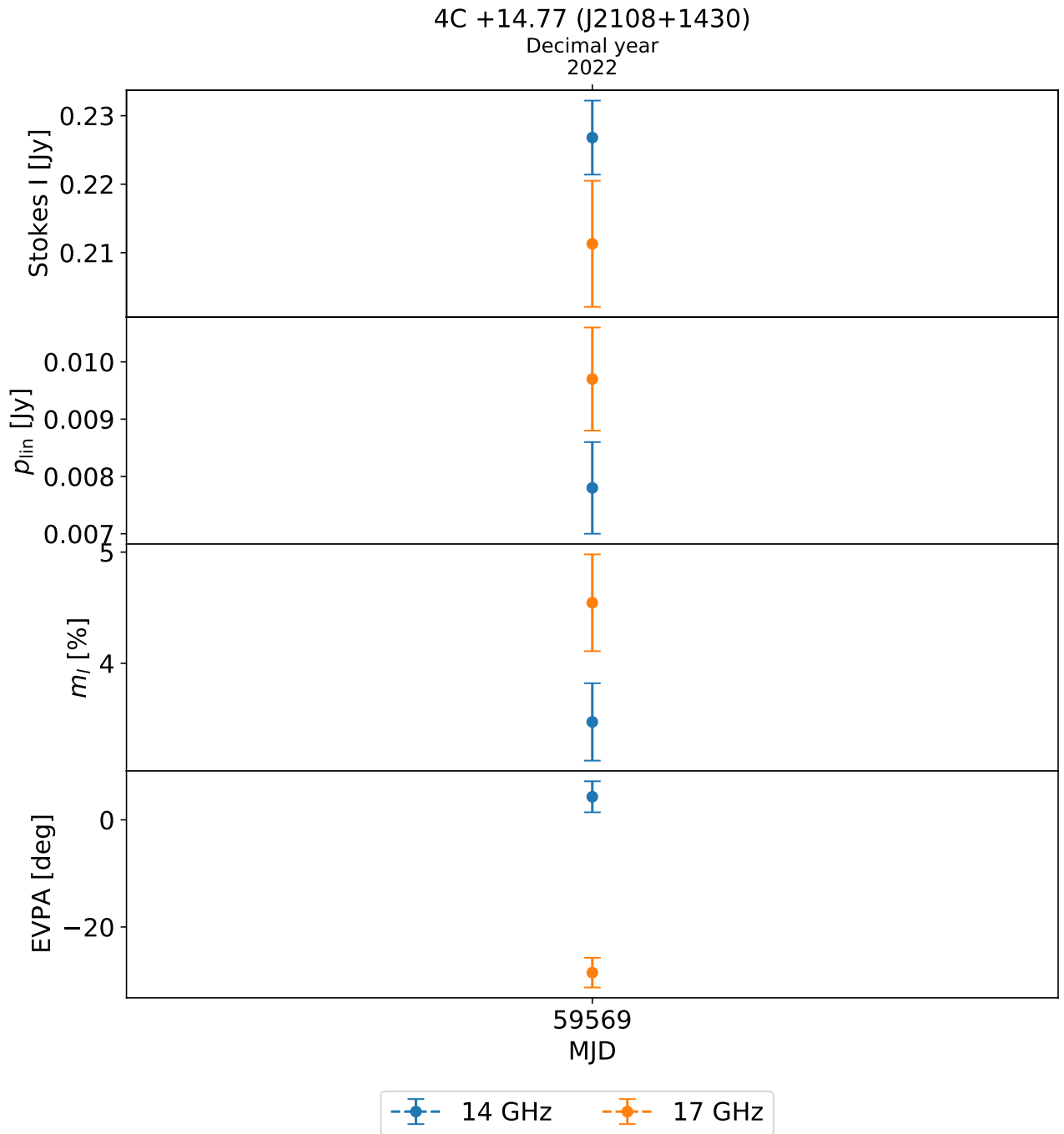


Figure D.41: Overview-plot of 4C +14.77 (J2108+1430).

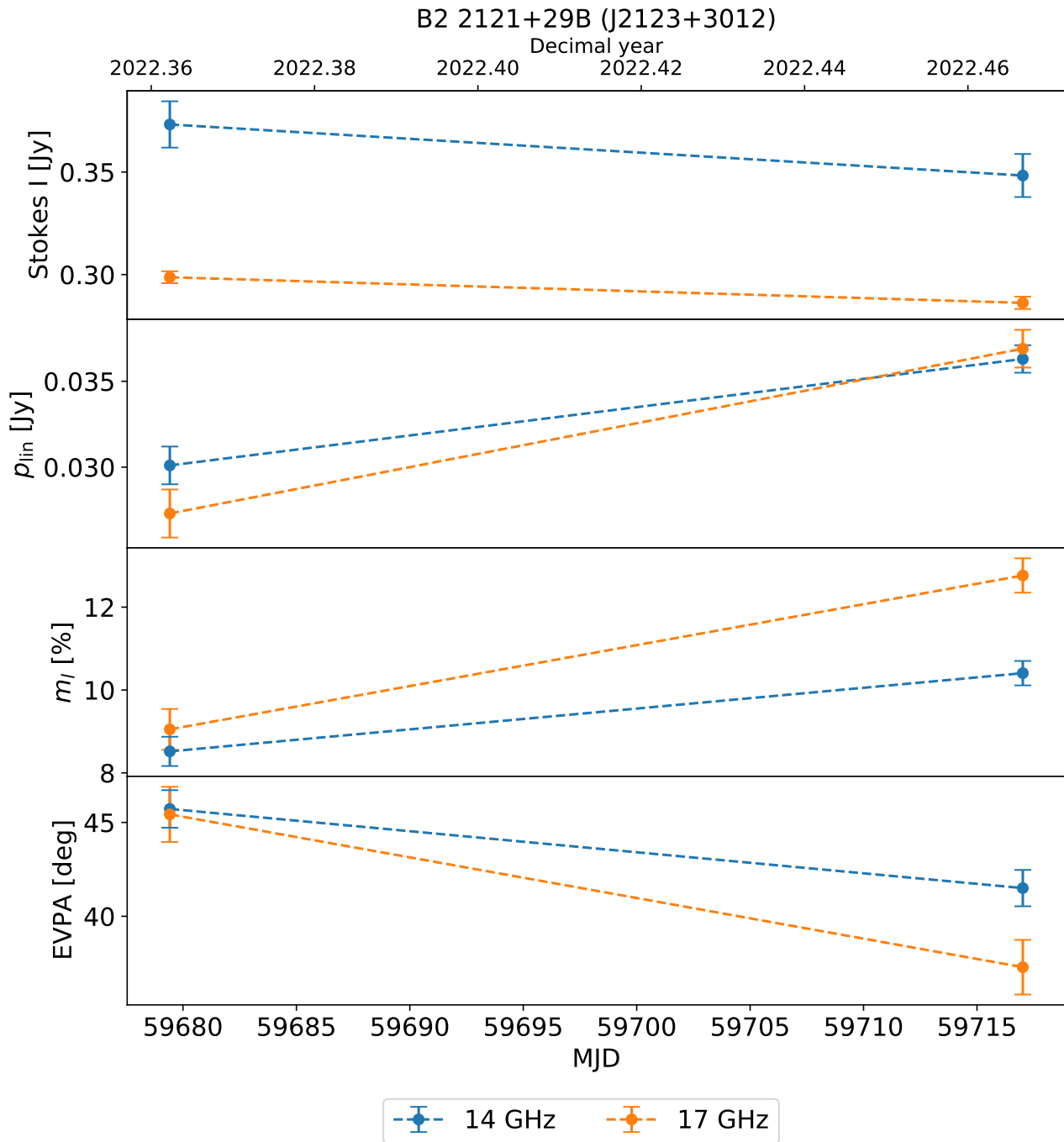


Figure D.42: Overview-plot of B2 2121+29B (J2123+3012).

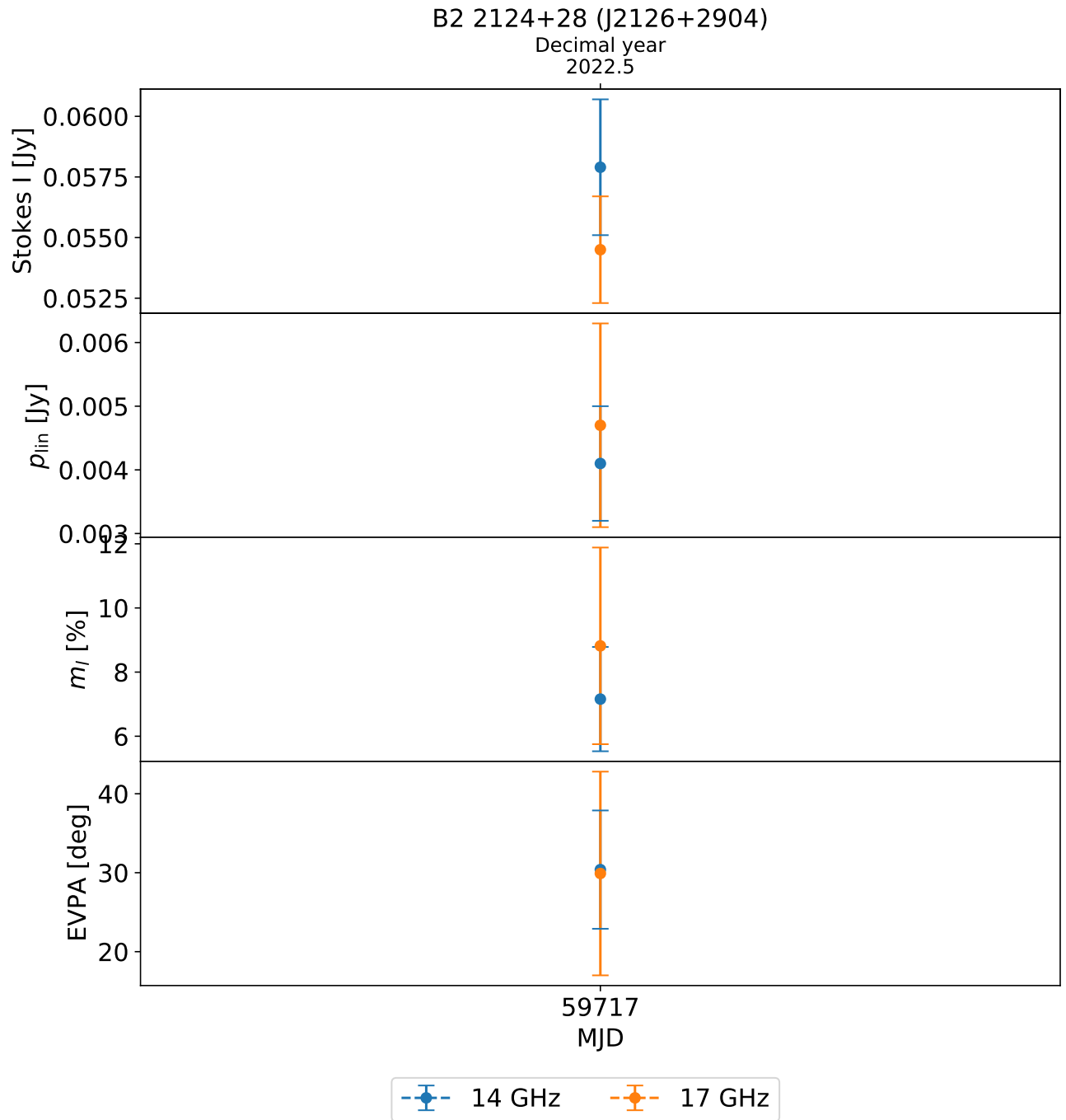


Figure D.43: Overview-plot of B2 2124+28 (J2126+2904).

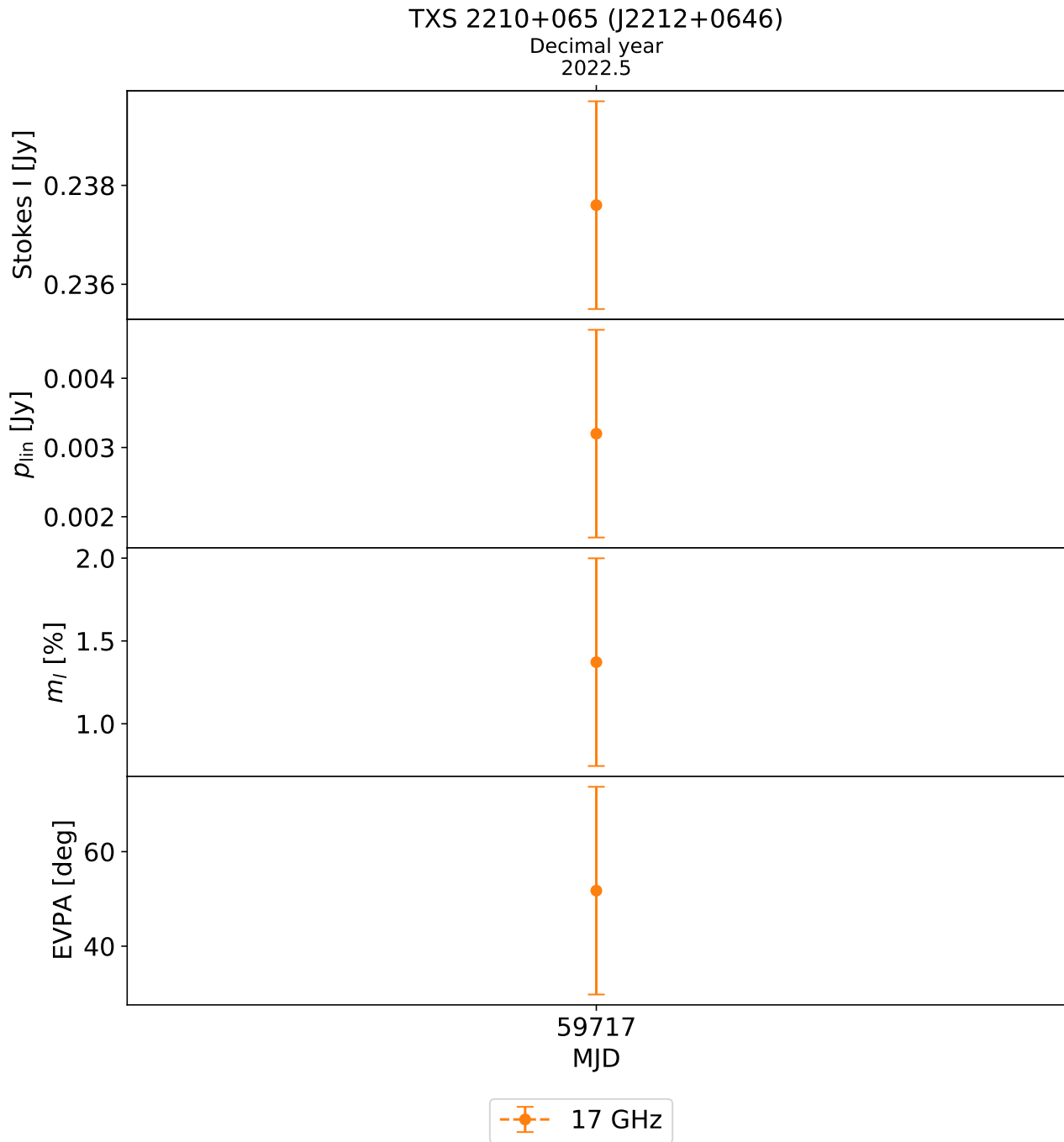


Figure D.44: Overview-plot of TXS 2210+065 (J2212+0646).

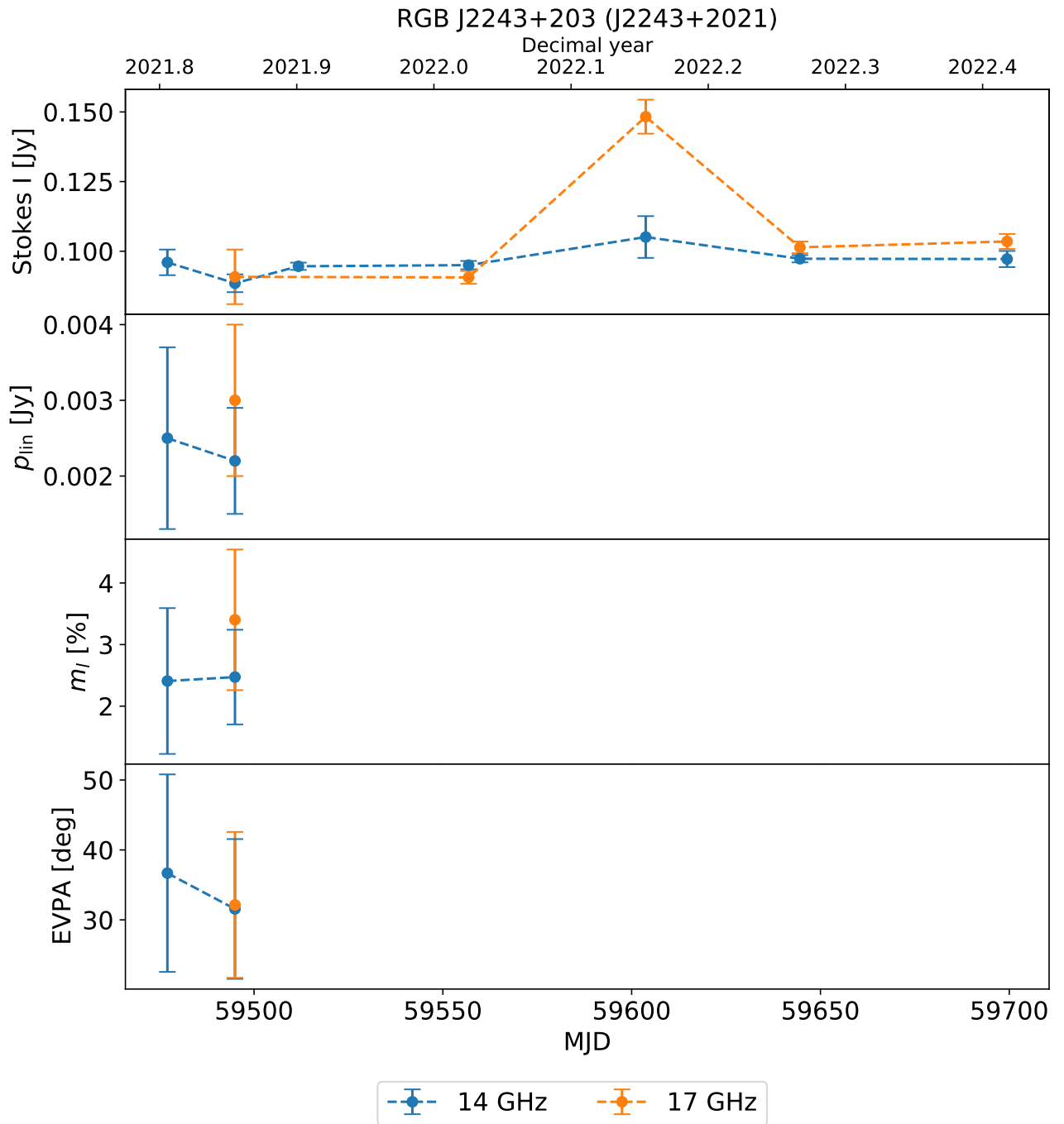


Figure D.45: Overview-plot of RGB J2243+203 (J2243+2021).

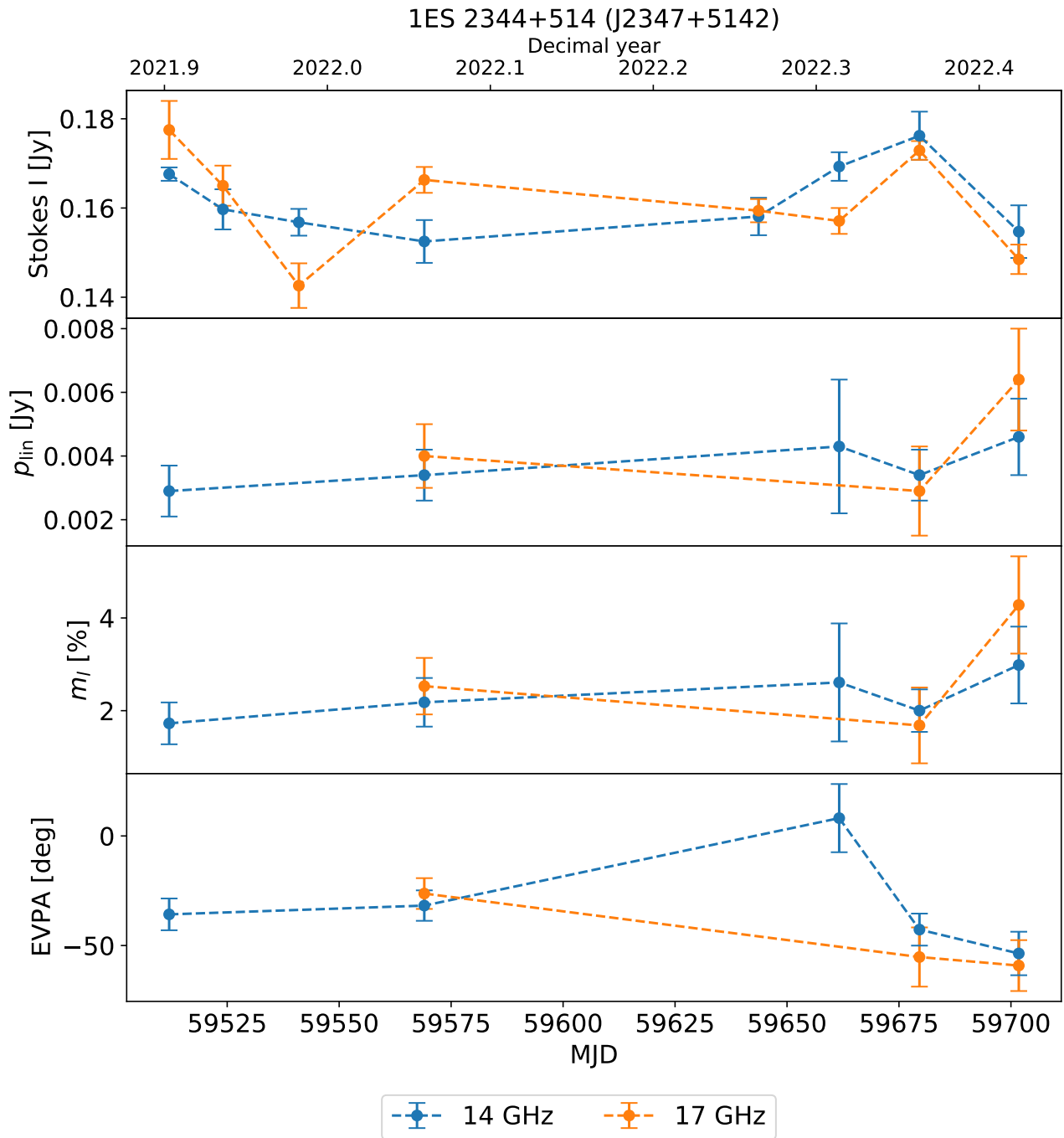


Figure D.46: Overview-plot of ES 2344+514 (J2347+5142).

E | Rotation Measures

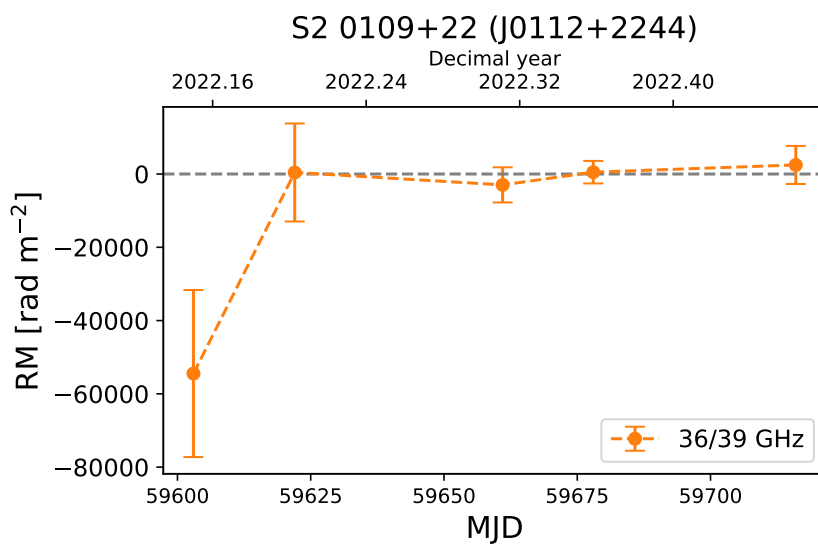


Figure E.1: Rotation measures of S2 0109+22 (J0112+2244).

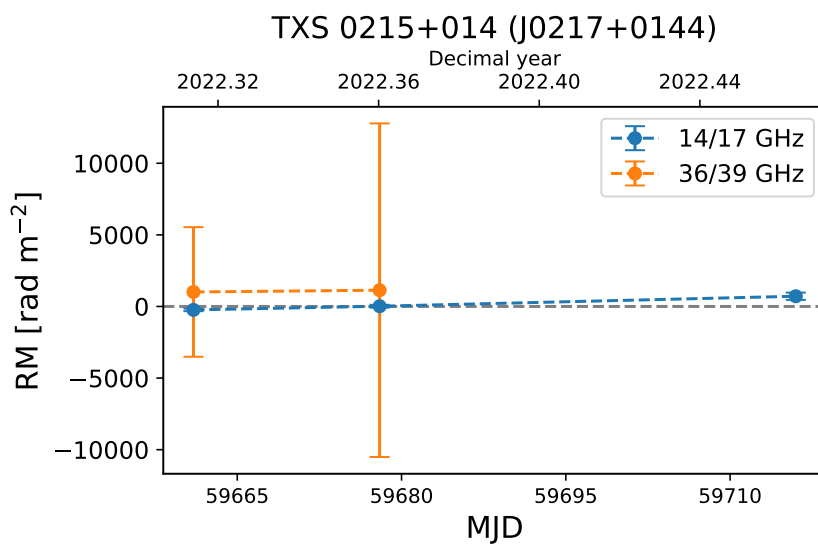


Figure E.2: Rotation measures of TXS 0215+014 (J0217+0144).

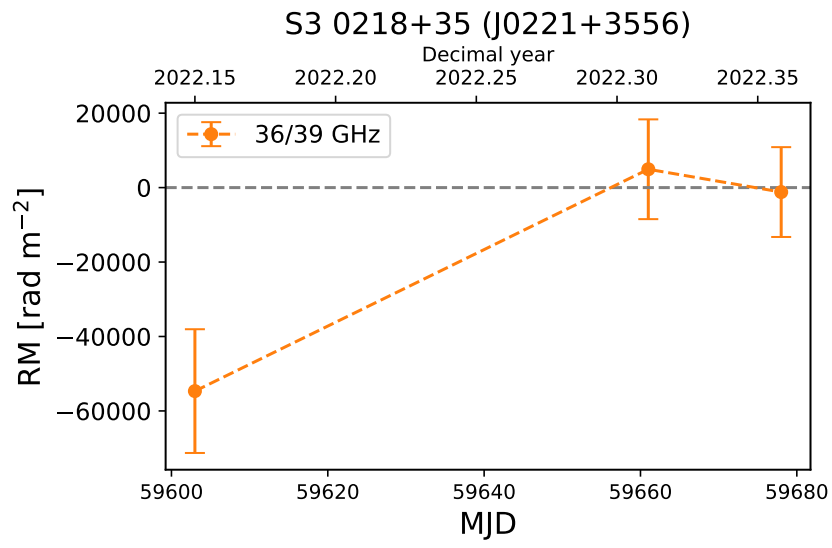


Figure E.3: Rotation measures of S3 0218+35 (J0221+3556).

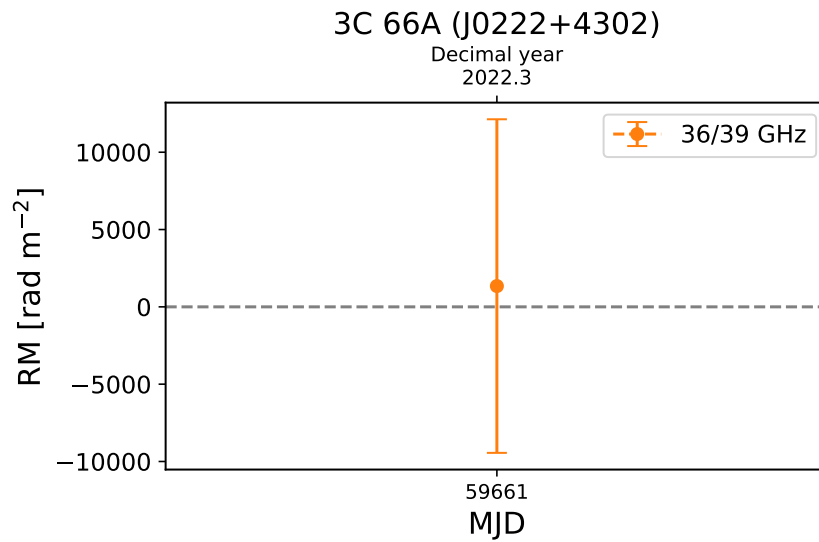


Figure E.4: Rotation measures of 3C 66A (J0222+4302).

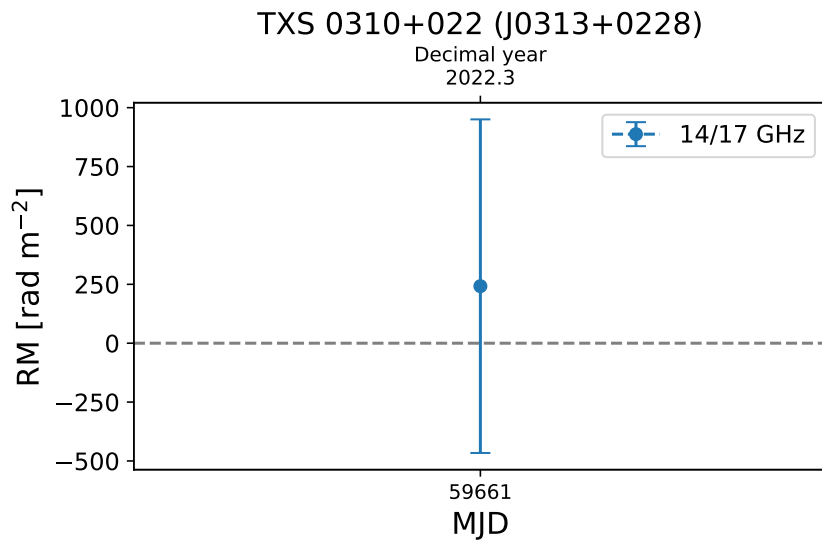


Figure E.5: Rotation measures of TXS 0310+022 (J0313+0228).

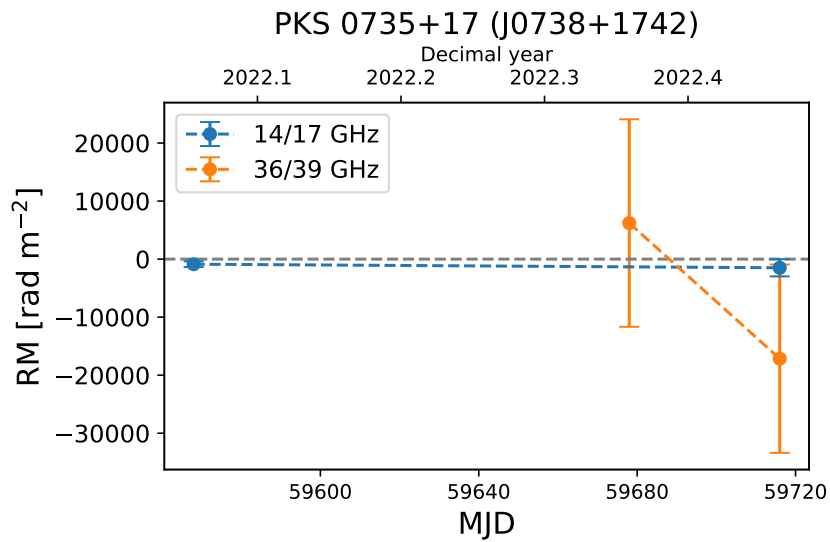


Figure E.6: Rotation measures of PKS 0735+17 (J0738+1742).

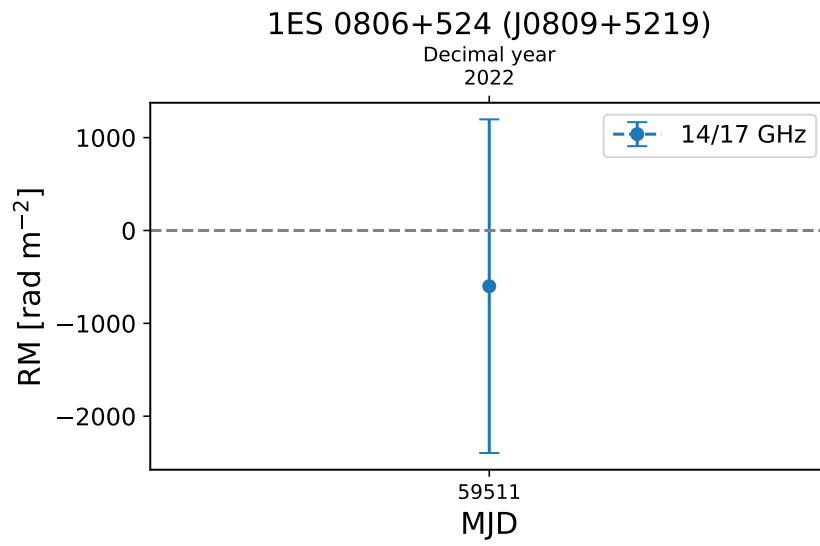


Figure E.7: Rotation measures of 1ES 0806+524 (J0809+5219).

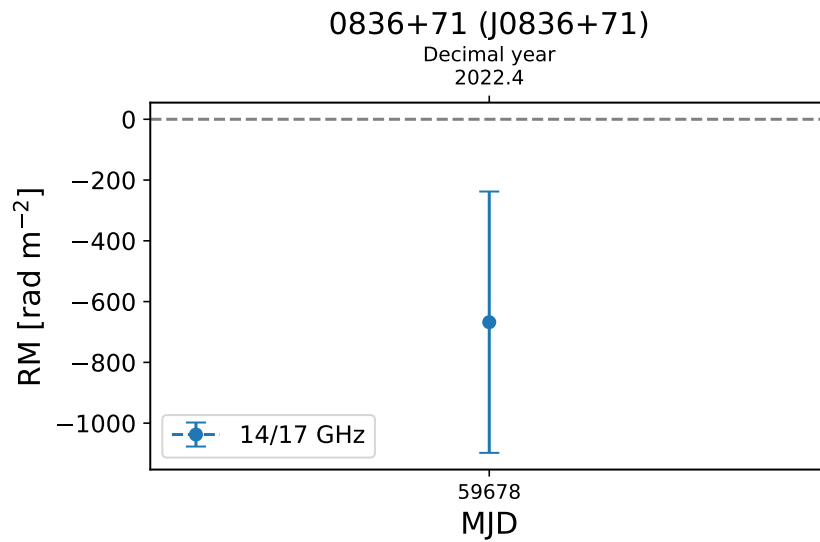


Figure E.8: Rotation measures of 0836+71 (J0836+71).

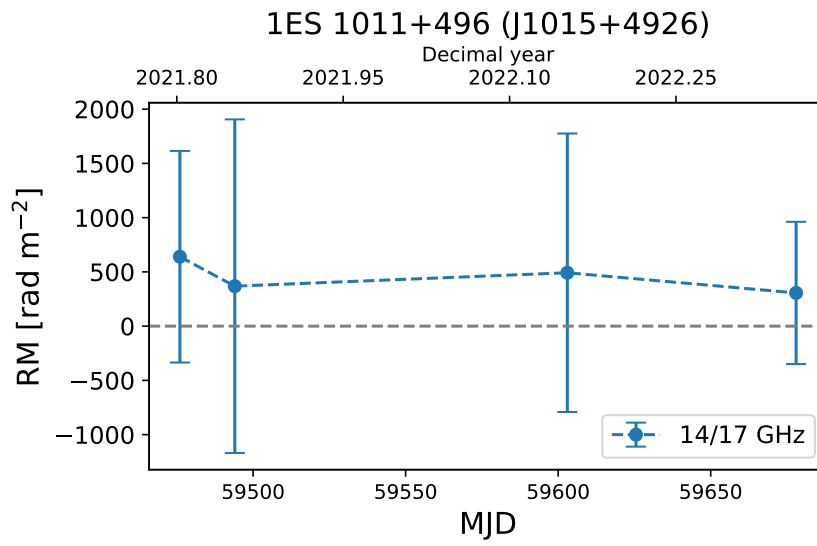


Figure E.9: Rotation measures of 1ES 1011+496 (J1015+4926).

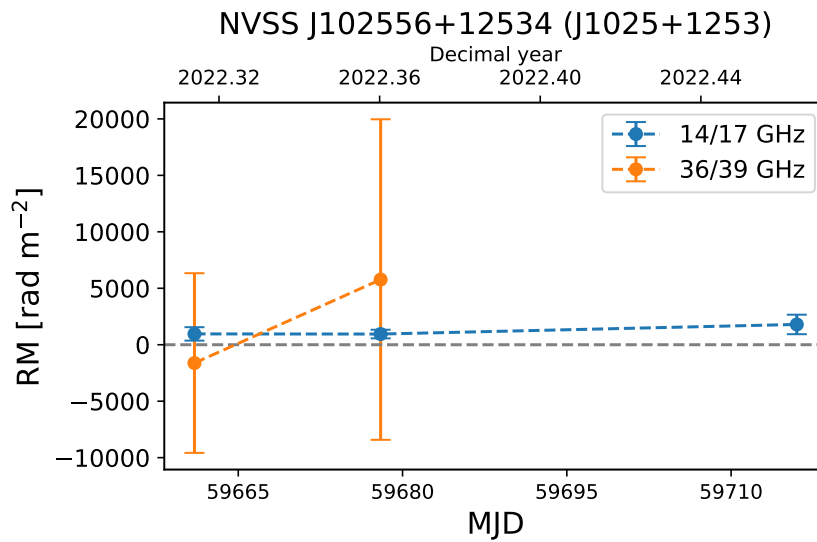


Figure E.10: Rotation measures of NVSS J102556+12534 (J1025+1253).

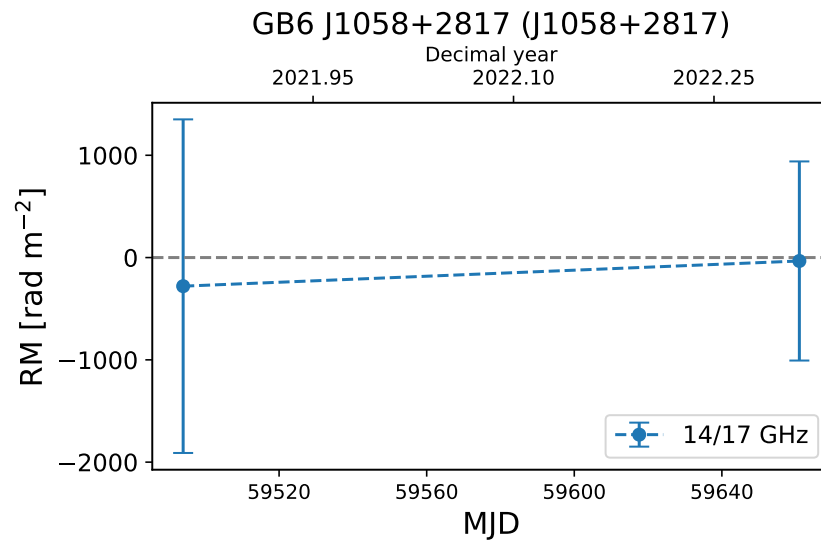


Figure E.11: Rotation measures of GB6 J1058+2817 (J1058+2817).

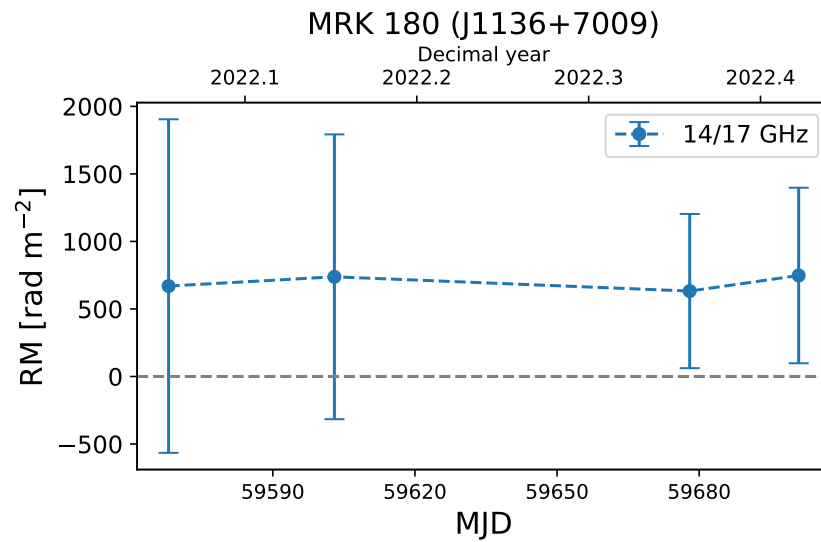


Figure E.12: Rotation measures of MRK 180 (J1136+7009).

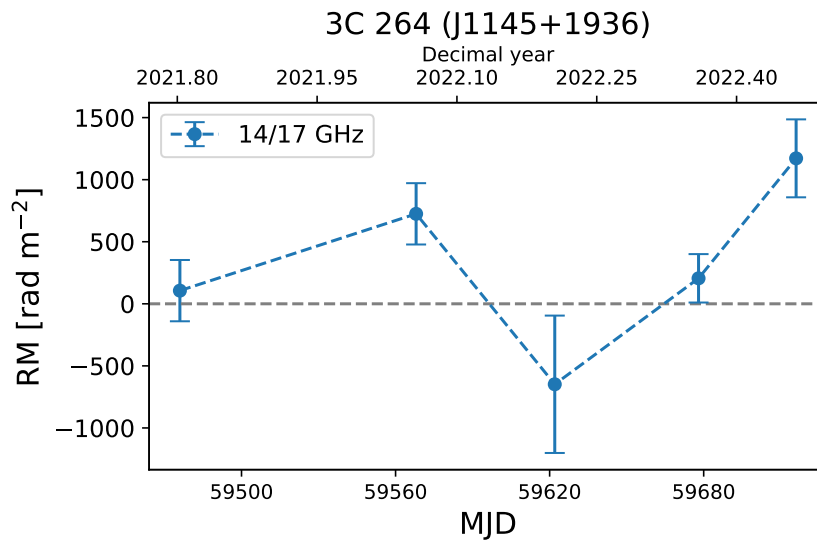


Figure E.13: Rotation measures of 3C 264 (J1145+1936).

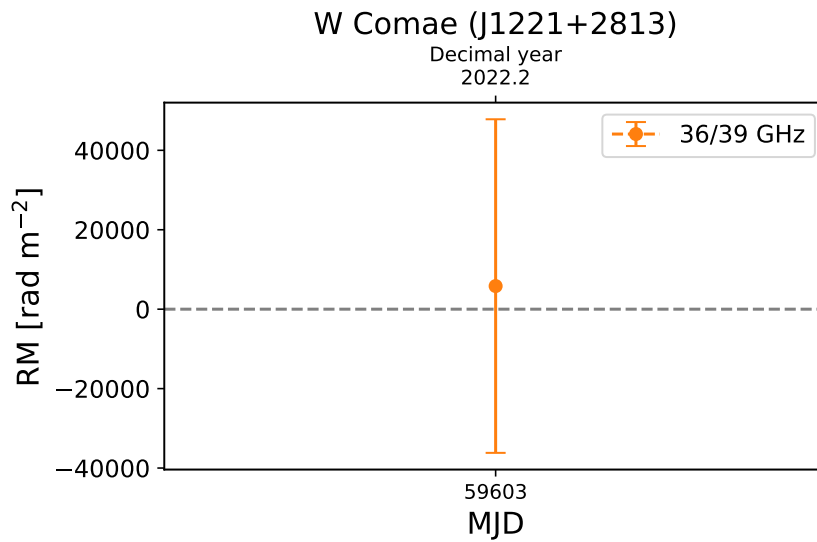


Figure E.14: Rotation measures of W Comae (J1221+2813).

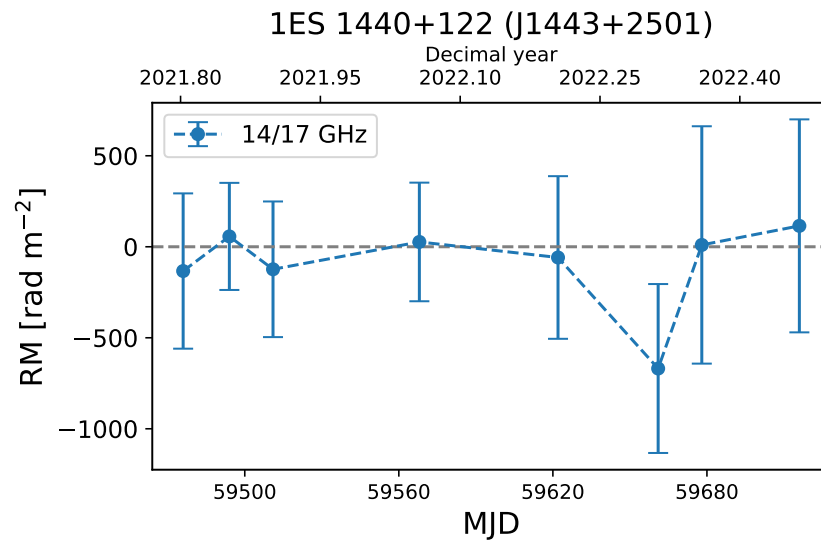


Figure E.15: Rotation measures of 1ES 1440+122 (J1443+2501).

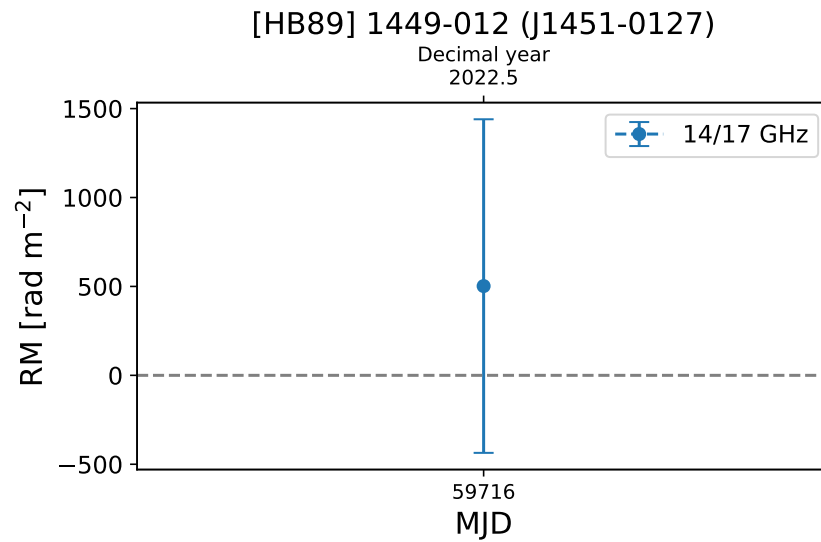


Figure E.16: Rotation measures of [HB89] 1449-012 (J1451-0127).

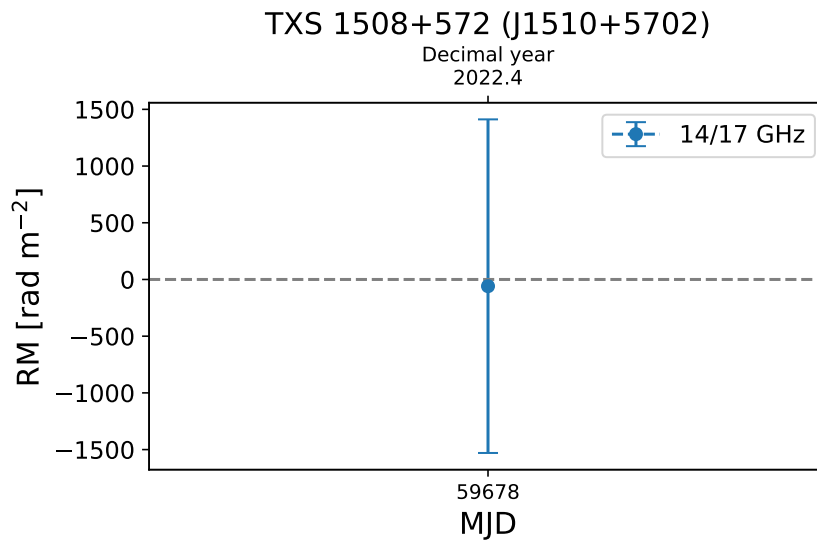


Figure E.17: Rotation measures of TXS 1508+572 (J1510+5702).

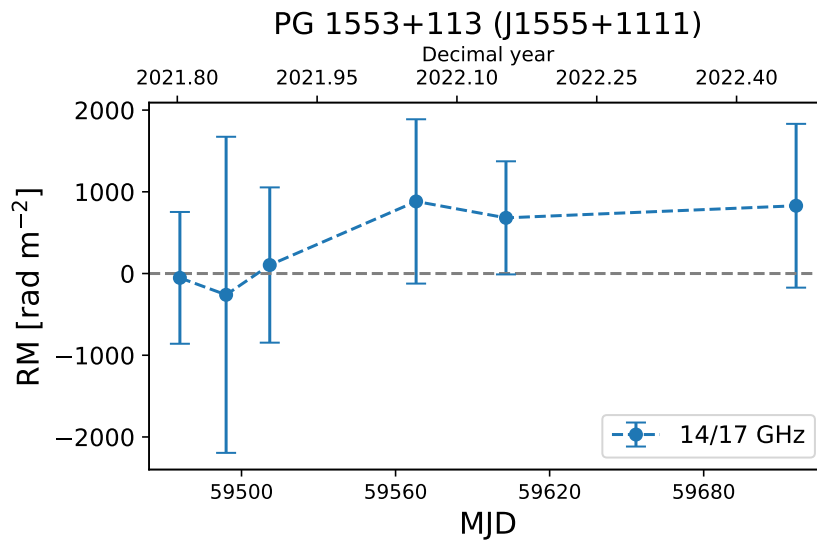


Figure E.18: Rotation measures of PG 1553+113 (J1555+1111).

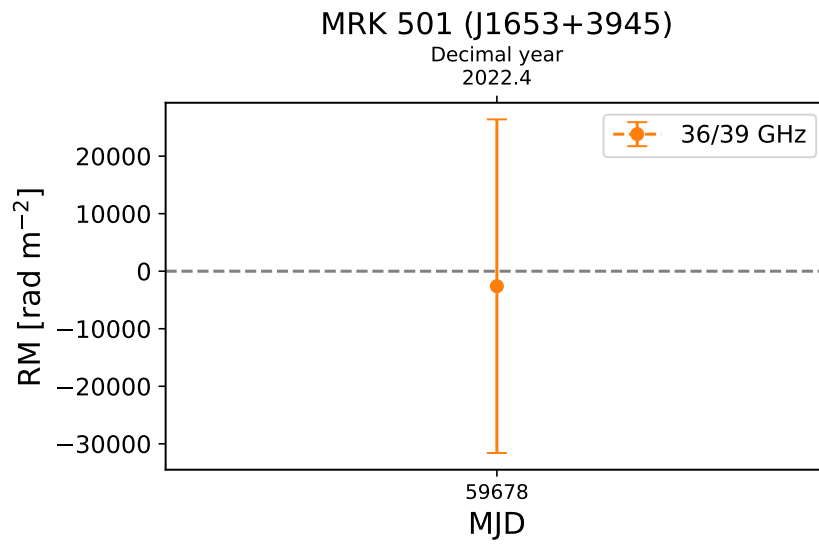


Figure E.19: Rotation measures of MRK 501 (J1653+3945).

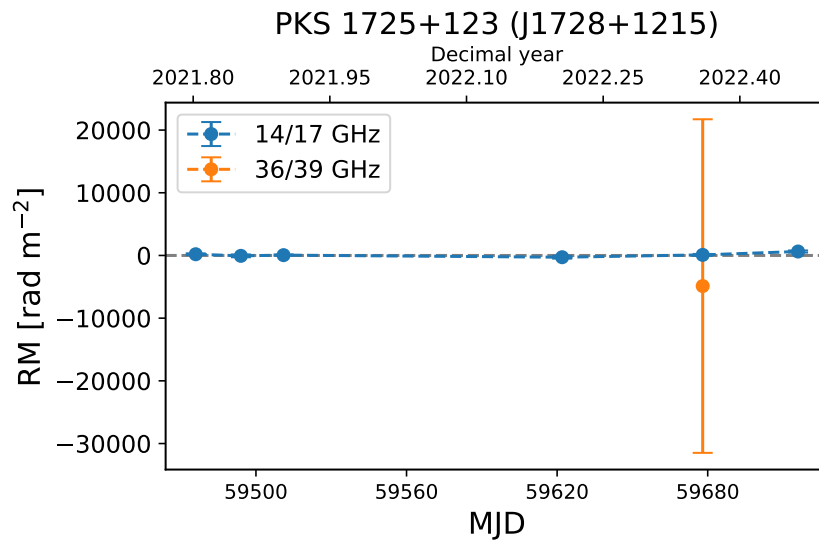


Figure E.20: Rotation measures of PKS 1725+123 (J1728+1215).

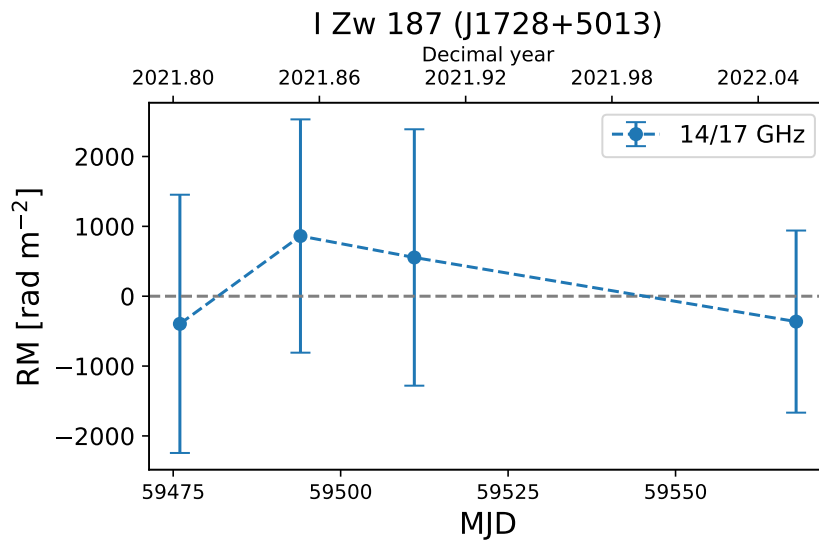


Figure E.21: Rotation measures of I Zw 187 (J1728+5013).

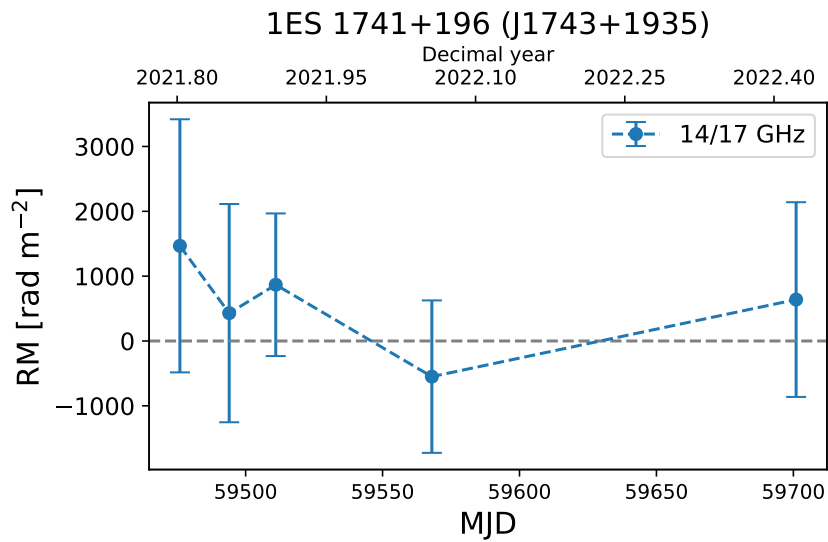


Figure E.22: Rotation measures of 1ES 1741+196 (J1743+1935).

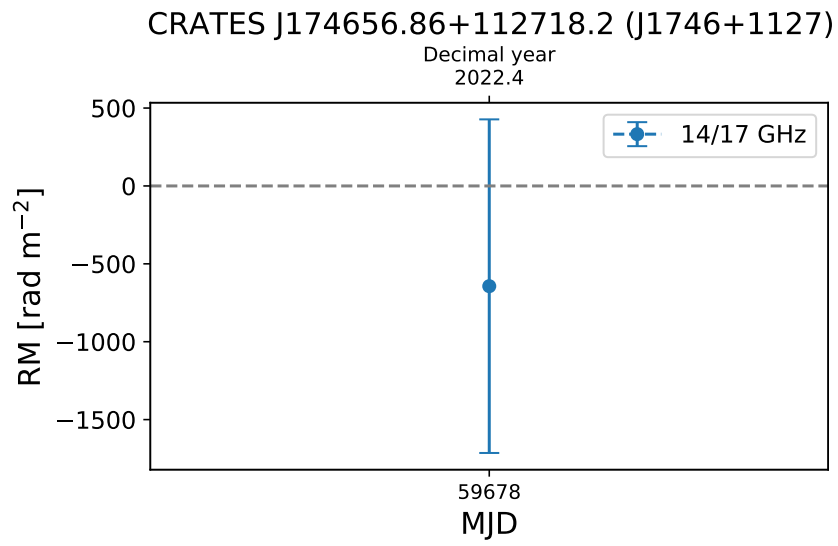


Figure E.23: Rotation measures of CRATES J174656.86+112718.2 (J1746+1127).

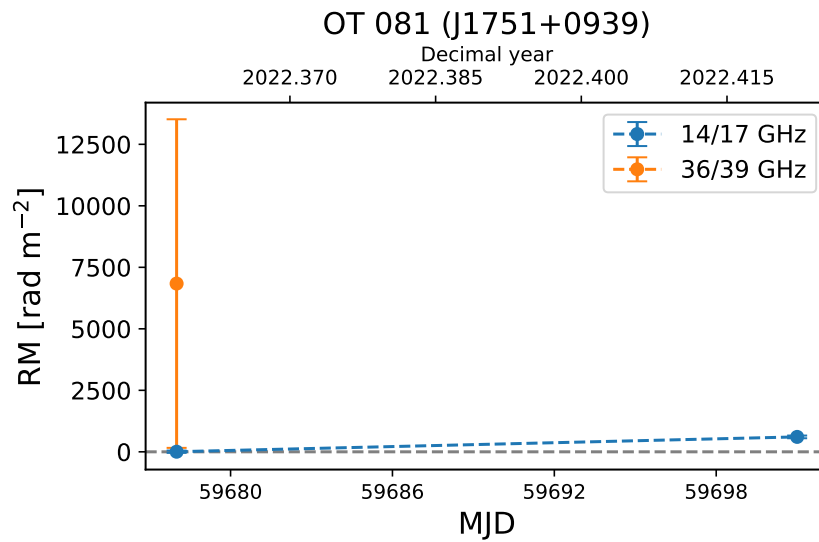


Figure E.24: Rotation measures of OT 081 (J1751+0939).

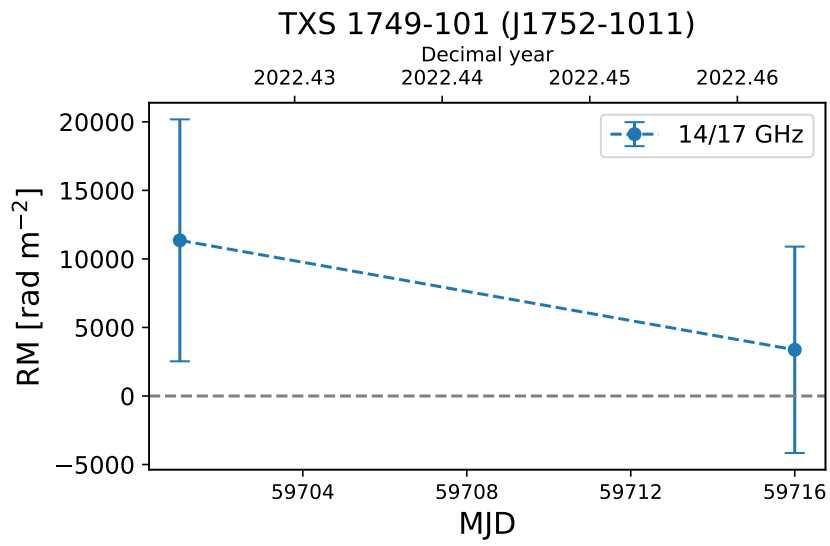


Figure E.25: Rotation measures of TXS 1749-101 (J1752-1011).

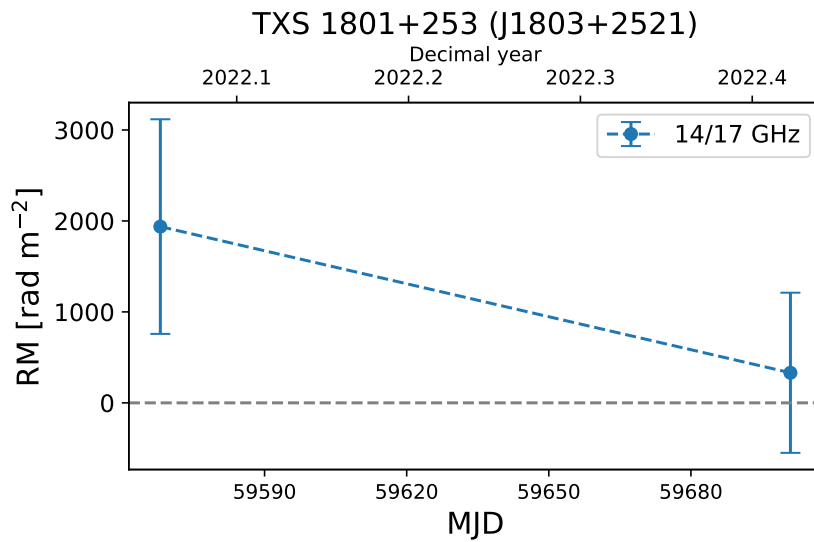


Figure E.26: Rotation measures of TXS 1801+253 (J1803+2521).

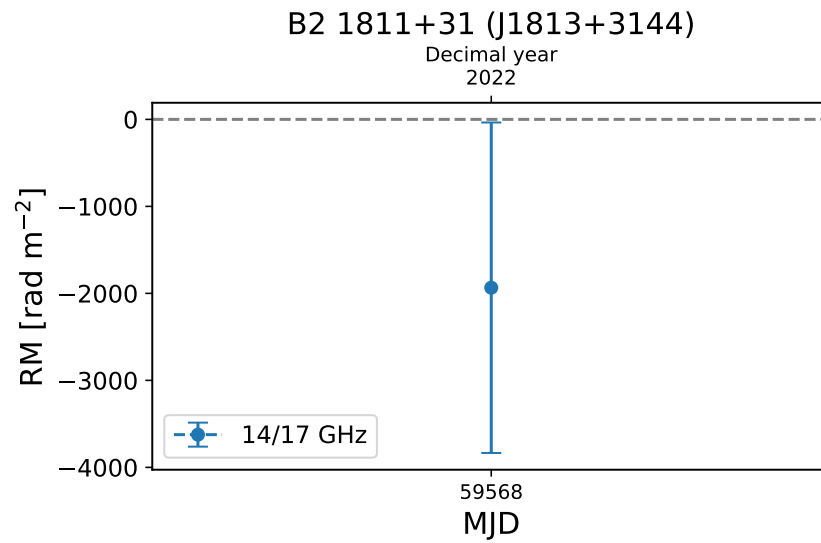


Figure E.27: Rotation measures of B2 1811+31 (J1813+3144).

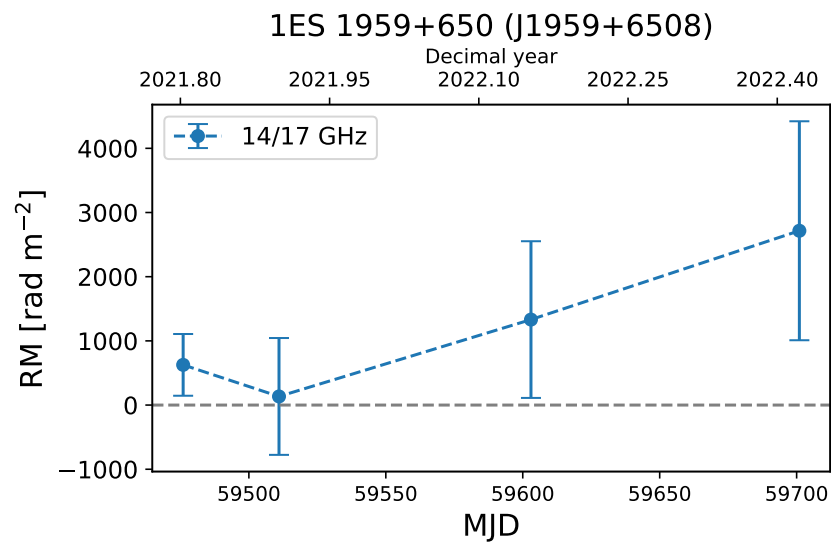


Figure E.28: Rotation measures of 1ES 1959+650 (J1959+6508).

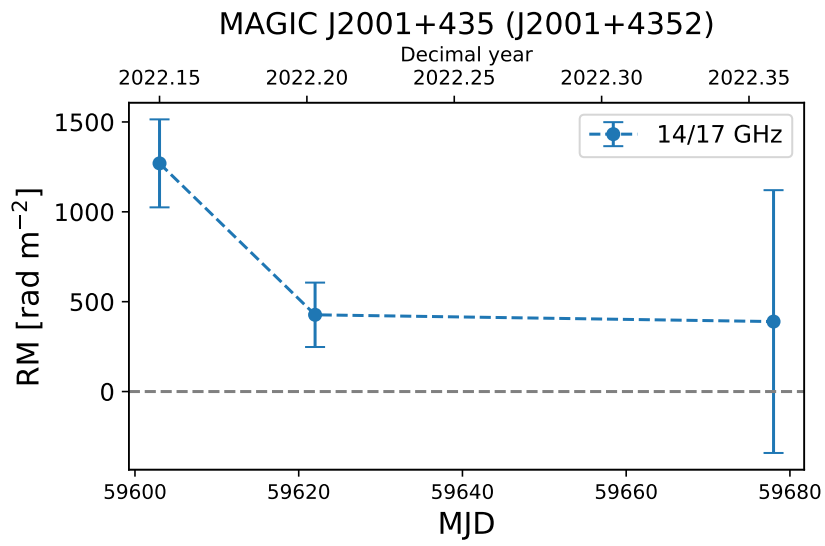


Figure E.29: Rotation measures of MAGIC J2001+435 (J2001+4352).

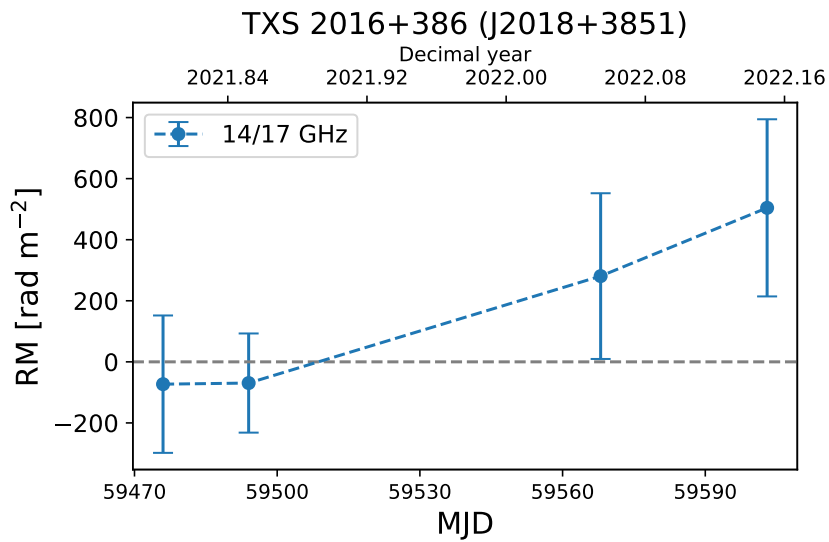


Figure E.30: Rotation measures of TXS 2016+386 (J2018+3851).

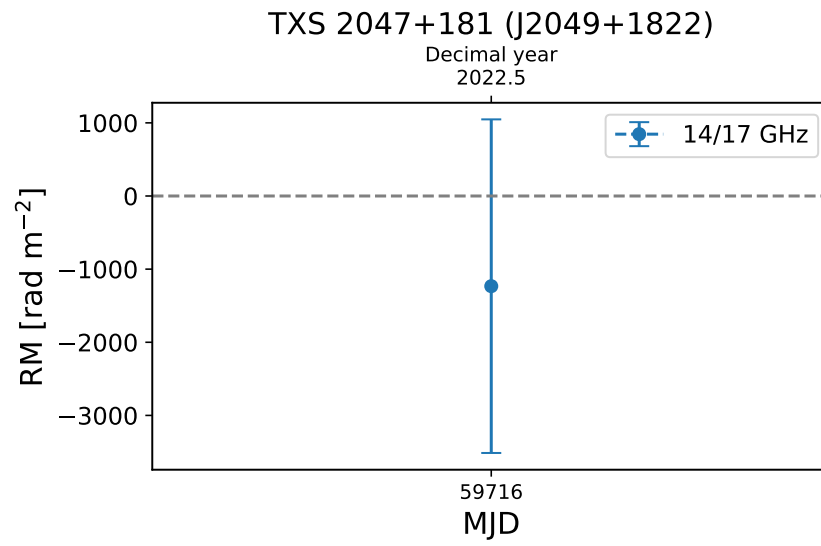


Figure E.31: Rotation measures of TXS 2047+181 (J2049+1822).

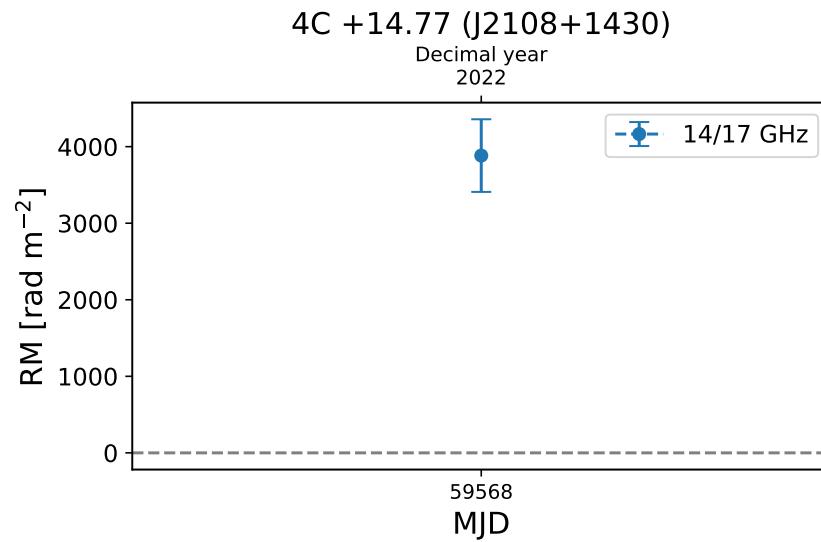


Figure E.32: Rotation measures of 4C +14.77 (J2108+1430).

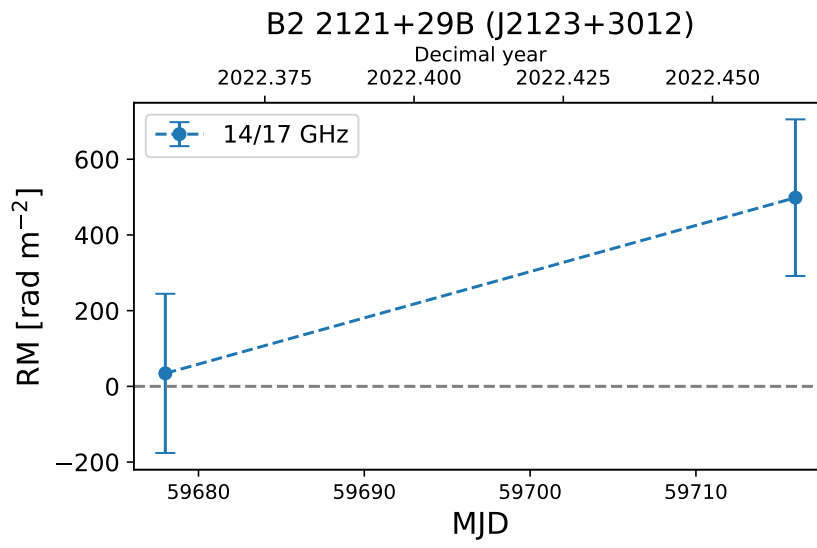


Figure E.33: Rotation measures of B2 2121+29B (J2123+3012).

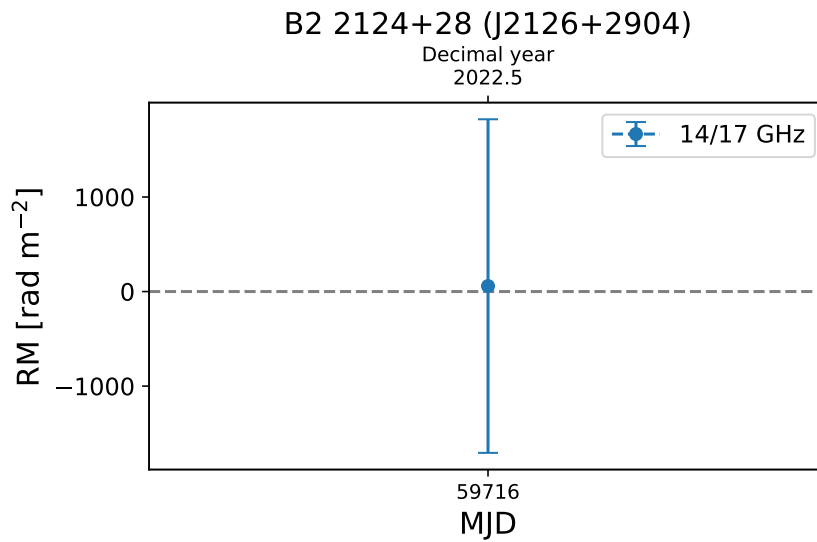


Figure E.34: Rotation measures of B2 2124+28 (J2126+2904).

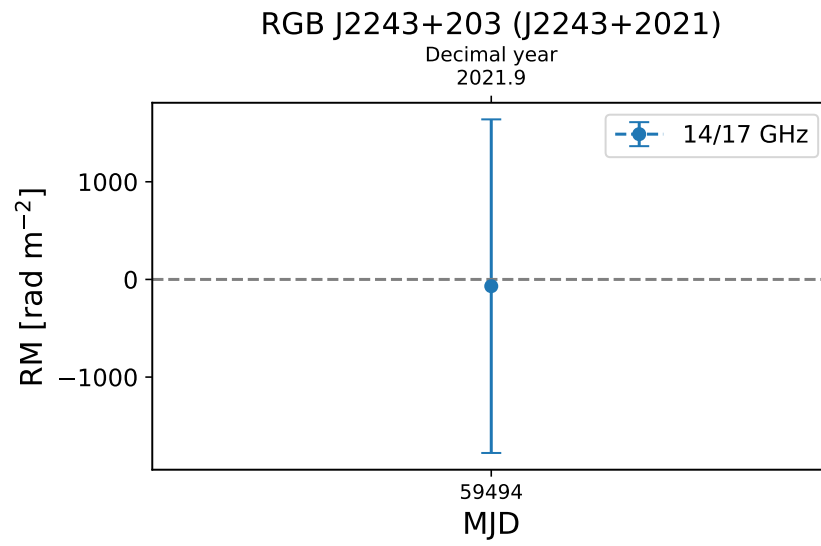


Figure E.35: Rotation measures of RGB J2243+203 (J2243+2021).

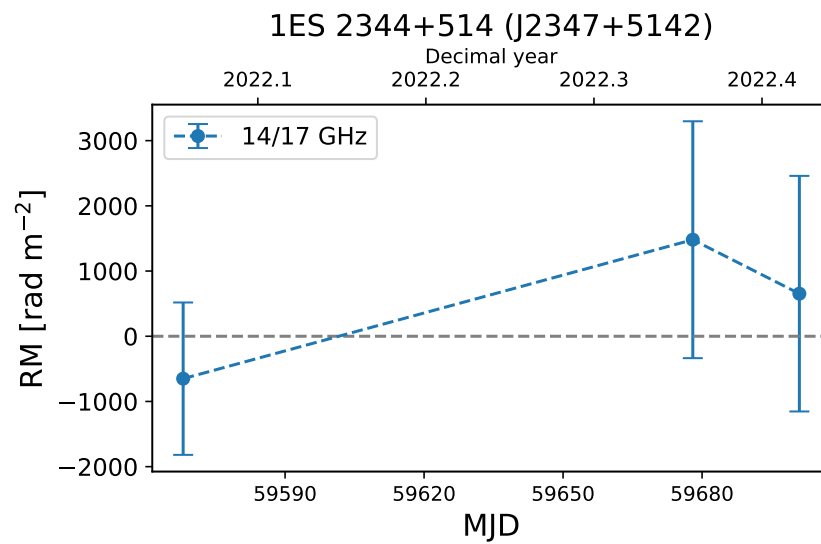


Figure E.36: Rotation measures of 1ES 2344+514 (J2347+5142).

Acknowledgments

First and foremost I would like to thank Prof. Dr. Matthias Kadler for entrusting me with writing not only one but two first-of-a-kind theses on TELAMON data. Working on this project was a great experience that will certainly benefit me in future ventures.

This endeavor would not have been possible without Dr. Alex Kraus from the MPIfR. He helped setting up the observations with the SPECPOL in the first place and always had an open ear for my questions about the analysis process of the polarization data. He also provided me with analysis scripts that made the data reduction a lot easier. For that, I am very grateful.

Many thanks go to all the TELAMON observers: Petra Benke, Florian Eppel, Andrea Gokus, Dana Kirchner, Georgios Filippou Paraschos, Florian Rösch, Jonas Sinapius and Philip Weber. Without them, it would not have been possible to collect all the data presented in this thesis. Huge thanks go to Florian Eppel for proofreading this thesis and giving me very helpful comments about the presentation of the data. Also, the semi-automatic analysis tool developed in the framework of his master thesis was of great help in the data reduction process.

Zum Schluss möchte ich noch meinen Eltern danken, die mich immer in meinen Zielen unterstützt haben.

Based on observations with the 100-m telescope of the MPIfR (Max-Planck-Institut für Radioastronomie) at Effelsberg.

This research has made use of data from the MOJAVE database that is maintained by the MOJAVE team ([Lister et al., 2018](#))

Declaration of authorship

I, Jonas Heßdörfer, declare that this thesis titled, 'High-frequency polarization studies of high-energy emitting AGN jets' and the work presented in it are my own. I confirm that:

- This work was done wholly or mainly while in candidature for a research degree at this University.
- Where any part of this thesis has previously been submitted for a degree or any other qualification at this University or any other institution, this has been clearly stated.
- Where I have consulted the published work of others, this is always clearly attributed.
- Where I have quoted from the work of others, the source is always given. With the exception of such quotations, this thesis is entirely my own work.
- I have acknowledged all main sources of help.

Signed: _____

Date: _____